

**SYSTEM-LEVEL APPROACHES FOR IMPROVING
PERFORMANCE OF CANTILEVER-BASED CHEMICAL SENSORS**

A Dissertation
Presented to
The Academic Faculty

by

Christopher John Carron

In Partial Fulfillment
of the Requirements for the Degree
Doctor of Philosophy in the
School of Electrical and Computer Engineering

Georgia Institute of Technology
December 2015

COPYRIGHT © 2015 BY CHRISTOPHER JOHN CARRON

SYSTEM-LEVEL APPROACHES FOR IMPROVING PERFORMANCE OF CANTILEVER-BASED CHEMICAL SENSORS

Approved by:

Dr. Oliver Brand, Advisor
School of Electrical and Computer Engineering
Georgia Institute of Technology

Dr. Muhannad Bakir
School of Electrical and Computer Engineering
Georgia Institute of Technology

Dr. A. Bruno Frazier
School of Electrical and Computer Engineering
Georgia Institute of Technology

Dr. A. Fatih Sarioglu
School of Electrical and Computer Engineering
Georgia Institute of Technology

Dr. Peter Hesketh
The George W. Woodruff School of Mechanical
Engineering
Georgia Institute of Technology

Date Approved: Nov 9, 2015

To Tressa

ACKNOWLEDGEMENTS

I wish to thank Dr. Oliver Brand for his patient and unwavering support. These last several years have been very trying for my family and me, and he has been patient, kind, and understanding throughout. Additionally, I thank Drs. Muhannad Bakir, Bruno Frazier, Peter Hesketh, and Fatih Sarioglu for their willingness to serve on my committee and offer their feedback and guidance. I also wish to thank the IEN staff – especially Gary Spinner, Tran-Vinh Nguyen, John Pham, Mikkel Thomas, and Eric Woods – for their technical support and advice, and Luke Beardslee for his disciplined and thorough training in the cleanroom. I would specifically like to thank Harley Hayden and C.S. Pai for their help in improving several aspects of the metal deposition processing used in this work. I would also like to specifically thank Ben Hollerbach for his help in developing the partial dicing technique, David Gottfried for his help with inkjet printing, and Richard Shafer for his help in developing the laser-cut package vias. Special thanks are also in order for Patrick Getz, who improved the measurement capabilities of our custom gas system, and for Mingu Kim and his help and encouragement in developing the first ‘no flow’ pre-concentration tests. Many thanks to other group members, past and present – Safak Demirci, Stuart Truax, Jin-Jyh Su, Karl Peterson, Spyridon Pavlidis, Hommood Alrowais, and Choong-soon Kim. Additional thanks to Purnima Sharma for her help with remote paperwork and administration, and to the NSF, AFRL, and GTRI organizations for funding the majority of this research. I also wish to thank my parents, David and Shawna, for encouraging and supporting me in my educational pursuits, and my friend, Chris Wampler, for his encouragement and help. Finally, my deepest gratitude to God,

and to Tressa and my children who gave me hope and courage to soldier on through this the most difficult and terrifying period of my life.

TABLE OF CONTENTS

	Page
ACKNOWLEDGEMENTS	iv
LIST OF TABLES	ix
LIST OF FIGURES	x
LIST OF EQUATIONS	xix
LIST OF SYMBOLS AND ABBREVIATIONS	xx
SUMMARY	xxi
CH 1 – INTRODUCTION TO CHEMICAL SENSING	1
Key Metrics for Chemical Sensors	3
Common Sensor Technologies	5
Cantilever-based MEMS Chemical Sensors	7
Resonant Cantilever Design	11
Resonant Cantilever Operation	20
Improvements to Prior State-of-the-Art	23
CH 2 – LOCALIZED POLYMER DEPOSITION	26
Inkjet Printing	28
Integrated Recess Structure	31
Finite Element Analysis	36
Resonance Frequency and Quality Factor	39
Chemical Measurements	41
Shadow Masking	43
CH 3 – TRANSIENT SIGNAL OPERATION	48
Valve Generated Transients	48
Measurement Setup	50
Sorbent Polymer Permeation Theory	53
Data Analysis	55
Design & Simulation	62
Device Operation	67
Chemical Measurements	68

CH 4 - ANALYSIS OF THERMAL TRANSIENTS	73
Transients Stemming from Variable Heating Pulse Length	75
Finite Element Simulation of Analyte Diffusion into Polymer Film	81
Temperature-induced Transients for Different Analytes	91
CH 5 – PRE-CONCENTRATOR THEORY & DESIGN	95
Pre-concentrator Design & Simulation	102
Thermal Design	104
Final Pre-Concentrator Design	107
CH 6 – SMART PRE-CONCENTRATOR FABRICATION	118
Heater Design	121
Ridge and Pillar Placement	125
Process Development	136
SOI Fabrication Development	137
Cantilever Fabrication	141
Initial Fabrication Results	142
CH 7 – PRE-CONCENTRATOR CHARACTERIZATION	148
Electrical Measurements	148
Oven Measurements	149
Self-Heating	154
Thermal Transient Behavior	159
CH 8 – PRE-CONCENTRATOR PACKAGING & CHEMICAL TESTING	161
Sorbent Coating	161
Packaging Concept	165
Chemical Measurements	172
CH 9 – OUTLOOK & FUTURE WORK	179
Integrated Recess Structure	179
Transient Signal Generation & Analysis	180
Pre-Concentration	181
APPENDIX A – SUPREME SIMULATION CODE	185
APPENDIX B – COMSOL SIMULATION CODE EXAMPLE	188
APPENDIX C – ARDUINO CODE USED FOR THERMAL PULSES	196

APPENDIX D – EXAMPLE RAW DATA OF THERMALLY-GENERATED TRANSIENTS	198
REFERENCES	199

LIST OF TABLES

Page

Table 1 - Diffusion coefficients D and partition coefficients K for alcohols in PECH and aromatic hydrocarbons in PIB.	57
Table 2 – Summary of simulation results for final designs, featuring bent-leg geometries and incorporating high aspect-ratio features on the suspended membranes.....	116
Table 3 - Summary of die specifications present in final mask layout.	128
Table 4 - Summary of electrical and thermal measurement results, compared with the values expected from simulation and theory.	149

LIST OF FIGURES

	Page
Figure 1 - Typical process flow for suspended resonant cantilever-based sensors formed from epitaxial silicon substrates. Device thickness is controlled with an electro-chemical etch stop [74, 89].....	13
Figure 2 – SEM images of hammerhead (left) and rectangular (right) cantilevers following fabrication. These devices are representative of prior state-of-the-art [62]. The white region near the tip of each device pictured is a thin gold layer, formed in anticipation of functionalization with a self-assembled monolayer (SAM) for biological sensing.....	15
Figure 3 – SEM image (left) and schematic illustration (right) of resistor arrangements for Wheatstone bridge and thermal excitation near cantilever base [93].....	16
Figure 4 – Illustration of how the integrated Wheatstone bridge responds as cantilever beam bends in x-y plane during resonant operation. Due to the arrangement of the piezoresistors, and alignment to the <100> direction, bending of the cantilever beam produces an amplified voltage difference from points Va – Vb, which can be read out electronically to track shifts in the resonance frequency [93].	17
Figure 5 – Illustration of OOP bending of cantilever beam, and its effect on piezoresistance changes in Wheatstone bridge. Due to the arrangement of the resistors in the Wheatstone bridge, OOP mode bending results in a suppressed output signal [93]. .	18
Figure 6 – Block diagram of PLL circuit for driving cantilevers at resonance and monitoring frequency shifts over time.	21
Figure 7 - Photograph (top) and schematic diagram (bottom) of custom gas setup. Flow rates are controlled by precision mass flow controllers (MFCs) and known VOC concentrations are generated by flowing carrier gas through a temperature-controlled bubbler and diluting with carrier gas. A pneumatic 4-way valve enables rapid switching between reference carrier and analyte gas streams [12, 90].	22
Figure 8 - Stroboscopic images (left) taken during inkjet printing of a solution of polyisobutylene (PIB) dissolved in o-xylene and (right) array of droplets deposited via inkjet printing from a solution of sucrose dissolved in water. Printing was performed on a MicroFab JetLab II inkjet printer located in the IEN cleanroom facilities at Georgia Tech.	29
Figure 9 – Inkjet printing, stray satellite droplets.	30
Figure 10 - Optical microscope (left) and enhanced 3D (center, right) images of printed EPCO film exhibiting the coffee ring effect. The image on the left shows the evolution of the coffee ring effect as printed film thickness increases. Printing was performed on a MicroFab JetLab II inkjet printer. Enhanced 3D images were obtained using the LEXT confocal microscope, located in the IEN cleanroom facilities at Georgia Tech.....	31
Figure 11 – Optical microscope images (left) of thin polymer films printed onto suspended micro-cantilever structures. As film thickness increases, the ‘coffee ring effect’ becomes more substantial (right).....	31
Figure 12 - SEM micrographs of (a) uncoated hammerhead resonator with 12- μ m total thickness and recess of 5- μ m etched into the head structure and (b) hammerhead resonator after filling the recess with polyvinylacetate (PVAc) as localized chemically sensitive film via ink-jet printing [89].	32

Figure 13 – SEM images of rectangular cantilevers featuring integrated recess structures. The cantilevers have been filled by inkjet printing to varying degrees with PVAc sorbent dissolved in DMSO as a solvent.	33
Figure 14 - Process flow diagram for hammerhead cantilevers with integrated recess structures.	35
Figure 15 – FEA simulation showing before (top) and after (bottom) coating resonance frequencies.	37
Figure 16 - Finite element modal analysis of 9- μm thick hammerhead resonator with 5- μm recess. The figure shows the stress in x-direction at the fundamental in-plane mode ($f = 489\text{ kHz}$); blue represents regions under compressive stress, red regions under tensile stress, while green indicates “stress-free” regions.	38
Figure 17 - Piezoresistive output signal as a function of excitation frequency of recessed hammerhead device, coated with $\sim 7\text{ }\mu\text{m}$ PVAc via ink-jet printing: (left) frequency range from 100-500 kHz showing two flexural modes with the desired in-plane mode at 410 kHz having the strongest signal; (right) close-up of amplitude and phase transfer characteristic of in-plane mode with $Q = 1910$	40
Figure 18 - Experimentally observed frequency shift of PIB-coated recessed resonator as a function of time; the microsensor is subsequently exposed to different toluene concentrations (3400-6800-10200-13600-13600-10200-6800-3400 ppm). Between successive toluene exposures, the chamber is flushed with nitrogen as carrier gas. A linear drift of 0.3 Hz/min has been subtracted from the data.	42
Figure 19 - Experimentally observed frequency shift for PIB-coated recessed resonator as a function of the toluene concentration.	43
Figure 20 – Design and rendering of (left) fixture for securing shadow masks in place during spray coating and (right) array of individual shadow masks of varying shapes and sizes. The inset on the right shows a magnified image of a single shadow mask designed for use with the integrated chemical sensors.	44
Figure 21 – Photographs of (left) spray-coating fixture machined from steel, with accompanying shadow mask and die to be spray coated, and (right) vapor atomizer used for spray coating.	45
Figure 22 – Photograph of resonator coated with PECH via shadow masking.	45
Figure 23 – Photographs of array (center) of resonators with integrated recesses, where each device (optical microscope images, labeled around perimeter of figure) is coated with a different type of sorbent. The coating of the devices in the array employed both shadow masking and inkjet printing.	46
Figure 24 - Frequency change Δf of a PECH-coated microresonator ($h = 4.6\text{ }\mu\text{m}$) to four 10-minute exposures to ethanol with concentrations of 7500, 15000, 22500 and 30000 ppm. In-between each analyte exposure, the chip is exposed to carrier gas (N_2) in order to desorb the analyte from the PECH.	51
Figure 25 - Relative frequency loss $\Delta f/\Delta f_{\text{max}}$ of microresonator coated with a 4.6 μm PECH film as a function of time upon exposure to methanol (50000 ppm), ethanol (22500 ppm) and isopropanol (17000 ppm).	52
Figure 26 - Relative frequency loss $\Delta f/\Delta f_{\text{max}}$ of microresonator coated with a 5.9 μm PECH film as a function of square root of time upon exposure to methanol (50000 ppm), ethanol (22500 ppm) and isopropanol (17000 ppm).	56

Figure 27 - Relative frequency loss $\Delta f/\Delta f_{\max}$ of resonator coated with a 5.9 μm PECH film as a function of time upon exposure to iso-propanol (17000 ppm); Circles: measurement data; Solid line: Fit using Equation 5 with $\tau = 53.1$ sec; Dashed line: Fit using Equation 7; Triangles: Difference fit using Equation 5 and data.	57
Figure 28 - Sorption transients of four subsequent exposures of PECH-coated microresonator ($h = 4.6$ μm) to 15000 ppm ethanol.	58
Figure 29 - SEM micrograph of resonant microstructure with semicircular head with 200 μm outer radius supported by a 75 μm wide and 100 μm long cantilever. Resistors for thermal excitation and piezoresistive detection of in-plane flexural vibrations are located at the cantilever base. Three heating resistors for rapid thermal modulation, connected in series, are clearly visible on the semicircular head.	61
Figure 30 - Thermal-modal analysis of resonant microstructure using COMSOL. The applied heating power of 100 mW causes a 71°C temperature elevation of the head structure (see color coding). The simulated in-plane resonant frequency of the heated structure is 776.19 kHz, a shift of -610Hz from the unheated structure.	64
Figure 31 - (Left) Amplitude transfer characteristic of in-plane resonant mode as a function of the applied heating power. (Right) Resonant frequency as a function of the applied heating power with a slope of -10.1Hz/mW or -13ppm/mW.....	65
Figure 32 - Screen capture of oscilloscope showing the square-wave signal applied to the three series heating resistors on the head region of the resonator, and the voltage across the piezoresistors at a constant current of 1 mA. The extracted thermal time constant is 1.1 ms.....	66
Figure 33 - In-plane resonance frequency of 25 μm thick microstructure subject to various levels of applied heating power; the PIB-coated resonator is exposed initially to pure carrier gas (N_2) and then to a constant toluene concentration of 6800ppm; Blue lines represent analyte absorption phases, red lines analyte desorption phases.	69
Figure 34 - Normalized frequency change vs. square-root of time for absorption transients induced by on-chip heating/cooling ($P = 40$ mW, red symbols) and analyte switching using a gas set-up (black symbols); the slope of the linear portion (solid line) is proportional to \sqrt{D} and yields a diffusion coefficient, $D = 2.4 \times 10^{-9}$ cm^2/s [10]. The heating-induced transient agrees very well with the gas-switching-enabled transient.	70
Figure 35 - Normalized frequency change vs. square-root of time for the initial portion of the absorption transients induced by on-chip heating/cooling ($P_{\text{applied}} = 18.8$ mW) for resonator coated with an 11 μm thick PIB film exposed to varying concentrations of toluene; the slope of the linear portion is proportional to \sqrt{D} and independent of concentration, for low concentration levels.	72
Figure 36 - Series of normalized desorption/absorption transients for increasing heating powers. The resonator was coated with a 2 μm thick polyepichlorohydrin (PECH) film and exposed to a continuous toluene concentration of 10800ppm. The transients are normalized with respect to their maximum frequency change, and frequency changes caused solely by a temperature change have been removed from these data through a differential measurement.	74
Figure 37 - Thermally generated transients based on pulsed-mode operation with 200ms heating pulses, resulting in an average heating power consumption of 900 μW per cycle.	75

Figure 38 - Signal transients, i.e. frequency change as a function of time, for 32.8s heating pulse: (1) Blue curve: signal transient in carrier gas; (2) Red curve: signal transient in analyte-loaded gas; (3) Green curve: differential transient representing analyte sorption effects only.	76
Figure 39 - Signal transients, i.e. frequency change as a function of time, for 256ms heating pulse: (1) Blue curve: signal transient in carrier gas; (2) Red curve: signal transient in analyte-loaded gas; (3) Green curve: differential transient representing analyte sorption effects only.	78
Figure 40 - Overlaid signal transients, i.e. frequency change as a function of time, for heating pulse lengths of 256ms (green), 1024ms (blue), 4096ms (purple) and 32768ms (red).	79
Figure 41 - Overlaid analyte re-absorption transients, i.e. frequency change as a function of time, for heating pulse lengths of 8ms (cyan), 256ms (green), 1024ms (blue), 4096ms (purple) and 32768ms (red). The frequency data are normalized by the maximum frequency shift at the given heating power.	81
Figure 42 - Comparison of simulated (grey lines) and experimental (black line) re-absorption transients after a 32s heating pulse. For the COMSOL simulation, the diffusion coefficients used were $D = 4e^{-9}, 6e^{-9}, 8e^{-9}, 1e^{-8}, 2e^{-8}, 4e^{-8} \text{ cm}^2/\text{s}$. The graph on the top shows the frequency axis in a linear scale, the bottom graph shows the same data using a logarithmic frequency axis.	83
Figure 43 - Comparison of simulated (grey lines) and experimental (black line) re-absorption transients after a 32s heating pulse. For the COMSOL simulation, the diffusion coefficients used were $D = 4e^{-9}, 6e^{-9}, 8e^{-9}, 1e^{-8}, 2e^{-8}, 4e^{-8} \text{ cm}^2/\text{s}$. The graph also shows the switching-valve induced absorption transient (red line) normalized to the same maximum frequency change as the heating-induced transient.	85
Figure 44 - Comparison of simulated (grey lines) and experimental (black line) desorption and re-absorption transients for a 256ms heating pulse. For the COMSOL simulation, the diffusion coefficients used were $D = 4e^{-9}, 6e^{-9}, 8e^{-9}, 1e^{-8}, 1.5e^{-8}, 2e^{-8} \text{ cm}^2/\text{s}$. The simulation were done using a constant D over the full 10s period.	87
Figure 45 - Comparison of simulated (grey lines) and experimental (black line) desorption (top graph) and re-absorption (bottom graph) transients for a 256ms heating pulse. During the heating pulse, a diffusion coefficient $D = 2.2 \cdot 10^{-8} \text{ cm}^2/\text{s}$ was applied, while the diffusion coefficients used during non-heating phases were $D = 4e^{-9}, 6e^{-9}, 8e^{-9}, 1e^{-8}, 2e^{-8}, 4e^{-8} \text{ cm}^2/\text{s}$	88
Figure 46 - Relative analyte concentration throughout the polymer film for a simulated heating pulse of (top) 256ms and (bottom) 32.8s. The heating pulse is simulated by a concentration drop from 1 to 0 at 1s. At the end of the heating pulse, the surface concentration jumps back from 0 to 1. The figure features 101 concentration profiles, equally spaced in time and simulated over the time of 10 s and 50 s for the 250 ms and 32.8 s pulse. The diffusion coefficient was set to $2 \times 10^{-8} \text{ cm}^2/\text{s}$ during “heating” and $8 \times 10^{-9} \text{ cm}^2/\text{s}$ outside of the “heating” pulses.	91
Figure 47 – Normalized valve-generated transients for PECH coated resonator exposed to 23400ppm benzene, 10,700ppm toluene, and 2400ppm xylene.	92
Figure 48 – Normalized thermally generated re-absorption transients following a 4 sec heating pulse for PECH coated resonator exposed to 23400ppm benzene, 10,700ppm toluene, and 2400ppm xylene.	92

Figure 49 – Normalized thermally-generated re-absorption transients following a 256 msec heating pulse for PECH coated resonator exposed to 23,400ppm benzene, 10,700ppm toluene, and 2400ppm xylene.	93
Figure 50 – Normalized desorption transients during a 4 sec heating pulse for PECH coated resonator exposed to 23,400ppm benzene, 10,700ppm toluene, and 2400ppm xylene.	94
Figure 51 – Graphical representation demonstrating how chemical pre-concentration can improve the effective LoD for chemical sensors, enabling detection of sub-LoD concentration levels that would otherwise be undetectable by the sensor alone.	96
Figure 52 - Graphical representation of pre-concentrator concept, with array of micro hotplate structures, inlet and outlet ports, and integrated mass-sensitive chemical sensors.	103
Figure 53 - Thermal simulation of a 1 mm x 1 mm x 20 μ m membrane with sorbent ridges included.	108
Figure 54 - Thermal simulation of transient response of a 1 mm x 1 mm x 20 μ m membrane with sorbent ridges included.	109
Figure 55 - Gravitational deflection of 1 mm x 1 mm x 20 μ m membrane with ridges and additional 5 mg of sorbent mass included (ridges not pictured).	109
Figure 56 - Pressure drop across an array of three 1 mm x 1 mm x 20 μ m membranes with sorbent ridges included.	110
Figure 57 - Fluid flow through an array of three 1 mm x 1 mm x 20 μ m membranes with sorbent ridges included.	110
Figure 58 - Thermal simulation of a 2 mm x 1 mm x 20 μ m membrane with sorbent ridges included.	111
Figure 59 - Thermal simulation of transient response of a 2 mm x 1 mm x 20 μ m membrane with sorbent ridges included.	112
Figure 60 - Pressure drop across an array of three 2 mm x 1 mm x 20 μ m membranes with sorbent ridges included.	112
Figure 61 - Fluid flow through an array of three 2 mm x 1 mm x 20 μ m membranes with sorbent ridges included.	113
Figure 62 - Thermal simulation of a 2 mm x 2 mm x 20 μ m membrane with sorbent ridges included.	114
Figure 63 - Thermal simulation of transient response of a 2 mm x 2 mm x 20 μ m membrane with sorbent ridges included.	114
Figure 64 - Pressure drop across an array of two 2 mm x 2 mm x 20 μ m membranes with sorbent ridges included.	115
Figure 65 - Fluid flow through an array of two 2 mm x 2 mm x 20 μ m membranes with sorbent ridges included.	115
Figure 66 - Detail from final mask layout of current-carrying metal traces (green) on support legs and membrane (blue). The traces make contact to the diffused heaters (purple) by way of arrays of contact vias (red). The white bars show the placement of high aspect-ratio ridges on the back surface of the pre-concentrator membrane, and the black areas indicate the areas of the silicon handle wafer that are removed by a DRIE step from the back of the wafer.	121
Figure 67 - Result of SUPREM simulation for boron diffusion and drive-in sequence, performed during manufacture of diffused heaters. Prior to drive-in, the simulated	

junction depth is approximately 0.45 μm ; following drive-in, the junction has deepened to approximately 1.2 μm with a simulated sheet resistance of 248 Ω/\square	122
Figure 68 - Detail from final mask layout showing placement of two diffused heaters (purple) on suspended 2 mm x 1 mm pre-concentrator membrane (blue). Electrical traces (green) make contact to the heaters and measurement resistors by way of arrays of contact vias (red). The white bars show the placement of high aspect-ratio ridges on the back surface of the pre-concentrator membrane.	123
Figure 69 - Example of cross-domain SIMULINK model (top) of a feedback system controlling the micro hotplate temperature, and μTPC temperature (bottom) as a function of time demonstrating control of μTPC temperature (the model is based on experimental data obtained from the 2 mm x 2 mm pre-concentrators).	125
Figure 70 - Screenshot from final mask layout, illustrating design of die with array of three 1 mm x 1 mm μTPC devices. Non-heated sensors and 120 μm ridge spacing on the back surface of the suspended membranes.	129
Figure 71 - Screenshot from final mask layout, illustrating design of die with array of three 2 mm x 1 mm μTPC devices. Non-heated sensors and 70 μm pillar spacing on the back surface of the suspended membranes.	129
Figure 72 - Screenshot from final mask layout, illustrating design of die with array of two 2 mm x 2 mm μTPC devices. Non-heated sensors and 35 μm pillar spacing on the back surface of the suspended membranes.	130
Figure 73 - Detail from final mask layout illustrating placement of cantilever-based chemical sensor pairs (blue semi-circular areas, mid-center) adjacent to inlet and outlet ports (blue rectangular area, top-center). The proximity of the sensor pair to the suspended pre-concentrator membrane (bottom-center) is also shown.	131
Figure 74 - Detail from final mask layout, illustrating 1 mm x 1 mm pre-concentrator device adjacent to two un-heated resonant sensors located at the integrated inlet/outlet port.	132
Figure 75 - Detail from final mask layout, illustrating 2 mm x 1 mm pre-concentrator device adjacent to two un-heated resonant sensors located at the integrated inlet/outlet port.	132
Figure 76 - Detail from final mask layout, illustrating 2 mm x 2 mm pre-concentrator device adjacent to two un-heated resonant sensors located at the integrated inlet/outlet port.	133
Figure 77 - Screenshot from final mask layout, illustrating placement of several die. The solid green rectangle surrounding each μTPC array is a capping piece formed on the separate packaging wafer, which is used to seal the chamber from the top surface. The bright pink features – near the bottom of the four die on the lower right side of the figure – are a series of alignment marks used as aides during photolithography.	134
Figure 78 - Screenshot of entire wafer layout, with a total of 88 pre-concentrator dies (6.5 mm x 9 mm each) and 28 cantilever-only dies (4.5 mm x 6.5 mm each), placed vertically down the center column. The center die (marked with four red X's) is used for wafer centering.	135
Figure 79 - Process flow diagram showing fabrication steps for μTPC devices formed on SOI substrates. The process sequence is compatible with existing resonant cantilever-based sensors. Red text indicates modifications to the previous process flow, which was based on epitaxial substrates.	138

Figure 80 – Process flow diagram for cantilevers with integrated heating units. Red text signifies new process development.....	141
Figure 81 - SEM images illustrating results of initial DRIE development for ridges and pillars. Further refinement was necessary to reduce the undercutting and improve the sidewall angle.....	143
Figure 82 - SEM image of a released 1 mm x 2 mm pre-concentrator with ridge-type structures imaged from back surface. Also visible are the mass-sensitive resonator structures at the bottom of the image. These initial devices were fabricated without the use of an etch stop, resulting in membranes that were approximately 70 μm thick.	143
Figure 83 - SEM images of a released 1 mm x 1 mm pre-concentrator with pillar-type structures imaged from back surface. These initial devices were fabricated with an improved DRIE recipe but without the use of an etch stop, resulting in membranes that were approximately 35 μm thick and with poor thickness uniformity across the wafer.	144
Figure 84 - SEM image of a released 2 mm x 2 mm pre-concentrator with pillar-type structures imaged from top surface. Also visible are the mass-sensitive resonator structures at the bottom of the image. These improved devices were fabricated from SOI substrates where the BOX layer was used as an etch stop for DRIE, resulting in membranes that were precisely 25 μm thick.	144
Figure 85 - SEM image of array of released 2 mm x 1 mm μTPC devices with pillar-type structures imaged from top (top) and back (bottom) surfaces. These improved devices were fabricated from SOI substrates where the BOX layer was used as an etch stop for DRIE, resulting in membranes that were precisely 25 μm thick.	145
Figure 86 - SEM image of array of released 1 mm x 1 mm μTPC devices with pillar-type structures imaged from top (left) and back (right) surfaces. These improved devices were fabricated from SOI substrates where the BOX layer was used as an etch stop for DRIE, resulting in membranes that were precisely 25 μm thick.	146
Figure 87 - SEM image of heated (top) and non-heated (bottom) integrated chemical sensors. The sensors were fabricated on-chip with the μTPCs , resulting in a device thickness of precisely 25 μm	147
Figure 88 - Photographs of a 2 mm x 1 mm μTPC die mounted in ceramic DIL package.	148
Figure 89 - Photograph of custom-built temperature-resistant PCB, connected to external measurement equipment by way of a feedthrough in the environmental chamber.	150
Figure 90 - Measured resistance as a function of ambient temperature for the measurement resistor of a 1 mm x 1 mm μTPC device. The resistance was measured both with (orange) and without (blue) a +10 V DC bias applied to the substrate.	151
Figure 91 - Calibration data for the heating resistors on 1 mm x 1 mm, 2 mm x 1 mm, and 2 mm x 2 mm μTPC devices, measured with no bias applied to the substrate.....	152
Figure 92 - Normalized resistance change as a function of the chamber temperature for all three heater designs (using data from Figure 43).....	152
Figure 93 – Absolute resistances as a function of chamber temperature for all three measurement resistors, without applied substrate bias.	153
Figure 94 - Calibration data for the measurement resistors on 1 mm x 1 mm, 2 mm x 1 mm, and 2 mm x 2 mm μTPC devices, measured with and without bias applied to the substrate.	153

Figure 95 – Absolute resistance values for all three heaters as a function of heating power.....	155
Figure 96 - Normalized resistance values for all three heaters as a function of heating power.....	155
Figure 97 – Absolute resistance values for all three measurement resistors as a function of applied heating power.	156
Figure 98 - Normalized resistance values for all three measurement resistors as a function of applied heating power.....	156
Figure 99 - Estimated membrane temperatures for 1 mm x 1 mm (blue), 2 mm x 1 mm (orange), and 2 mm x 2 mm (gray) μ TPC devices, measured with a +10 V DC bias applied to the substrate. The temperatures are estimated by measuring the temperature-dependent resistance during self-heating and comparing this value with the temperature calibration data.	157
Figure 100 - Normalized thermal transients for all three designs. To extract the thermal time constant of the μ TPC devices, a DC bias current of 100 μ A was applied to the measurement resistor. A 200-mW heating pulse was then applied to the heating resistors while simultaneously measuring the voltage change across the biased measurement resistor.	159
Figure 101 – SEM micrographs of silicon ridge structures coated with PIB by drop-coating of the polymer solution (toluene was used as solvent) from a micro-pipette. ...	162
Figure 102 –SEM image of an array of 1 mm x 1 mm μ TPC membranes spray-coated with PIB.	164
Figure 103 - SEM image of thin PIB coating, which was deposited with a shadow mask onto a suspended 2 mm x 1 mm μ TPC membrane. As seen in the figure, the location of the coating can be precisely controlled, allowing sorbent to be deposited only in regions useful for pre-concentration.	164
Figure 104 - SEM image of thick (approximately 50 μ m) OV-1 sorbent coating deposited by shadow masking onto a suspended 2 mm x 2 mm μ TPC membrane. As shown in the image on the right, the location of the coating can be precisely controlled.....	164
Figure 105 - Profile view of μ TPC packaging concept. A silicon capping piece (light gray) diced from a separately-processed packaging wafer is bonded to a μ TPC die (dark gray) with epoxy. The bottom surface of the μ TPC die is bonded with epoxy to the ceramic DIL package (gold) with the inlet/outlet ports on the die aligned to the laser-cut vias on the ceramic DIL package. The packaging results in a dead volume of approximately 10 μ L and is designed to be gas-tight with chamber walls that are inert with respect to VOC sorption.	166
Figure 106 - Detail from mask layout for 2 mm x 1 mm μ TPC die, showing placement of the packaging wafer die onto the μ TPC die. The green ring surrounding the μ TPC array represents the raised silicon ridge on the packaging wafer capping piece.	167
Figure 107 - Process flow diagram showing full fabrication sequence for μ TPC packaging wafer. If the capping pieces are to be bonded individually by hand, the process sequence can be simplified to a single mask step where DRIE of silicon is used to form the raised silicon rings.	168
Figure 108 - Photographs of several diced die (left) from completed packaging wafer, and single die bonded to glass slide with epoxy (right). To seal the top surface of the μ TPC	

die, epoxy is applied to the raised silicon ring of a capping die, which is subsequently bonded to the μ TPC die.	169
Figure 109 - Views from the top surface (left) and bottom surface (right) of ceramic DIL package, which has been laser-cut in preparation for packaging of a μ TPC die. The laser-cut vias are designed to align with the inlet and outlet ports on the μ TPC die.....	170
Figure 110 - Photograph of fully-packaged μ TPC die, which has been placed over the laser-cut vias and bonded with epoxy on the bottom surface. The top surface of the die has been sealed by bonding a silicon capping piece with epoxy. As can be seen from the figure, the packaging has been designed to allow wire-bonding between the die and package.	171
Figure 111 - Photograph (top) and schematic diagram (bottom) of custom gas setup. Flow rates are controlled by precision mass flow controllers (MFCs) and known VOC concentrations are generated by flowing carrier gas through a temperature-controlled bubbler and diluting with carrier gas. A pneumatic 4-way valve enables rapid switching between reference carrier and analyte gas streams.	173
Figure 112 - Experimentally observed frequency shift of PECH-coated resonator as a function of time (top); the microsensor is subsequently exposed to different toluene concentrations (3600-7200-10800-14400 ppm). Between successive toluene exposures, the chamber is flushed with nitrogen as carrier gas. The response of the sensor with respect to toluene concentration is reversible and very linear (bottom).	174
Figure 113 - Experimental test setup for measuring pre-concentration factor. The μ TPC and chemical sensors are first exposed (left) to a constant toluene concentration until equilibrium is reached. Once in equilibrium, the inlet/outlet ports to the chamber are quickly sealed (right) with a mechanical clamp, trapping a fixed volume of toluene inside the chamber. Applying heating power to the μ TPC during thermal desorption drives sorbed analyte molecules out of the μ TPC sorbent, which raises the ambient toluene concentration inside the chamber. Analyte uptake into the chemical sensors then increases due to the increased ambient concentration.	176
Figure 114 - Experimentally observed pre-concentration factor. (Top) shows a comparison between the sensor signal when the μ TPC is exposed to N_2 only for (blue curve) and 5000 ppm of toluene for (orange curve). The plot (bottom) shows the aggregate response, where temperature effects have been removed leaving only the response to toluene. The response of the sensor alone (i.e. without the μ TPC connected) was approximately 100 Hz when exposed to 5000 ppm of toluene; thus, an additional increase of 50 Hz due to pre-concentration has boosted the signal by 50%. Thermal desorption was performed by applying 100mW of heating power to the μ TPC for 30 sec.	177

LIST OF EQUATIONS

	Page
Equation 1 – Resonance frequency for classical mass-spring-dashpot system.	9
Equation 2 – Spring constant for a mechanical beam.	9
Equation 3 – Q-factor for resonant cantilever beam.	9
Equation 4 – Limit of detection (LoD) for resonant cantilever-based chemical sensor. ..	10
Equation 5 – Relative weight gain/loss of 1-dimensional sorbent film, assuming ideal Fickian diffusion.	53
Equation 6 – Characteristic diffusion time constant for ideal Fickian diffusion into thin sorbent film.	53
Equation 7 – Approximation for initial relative weight gain/loss for ideal Fickian diffusion into thin sorbent film.	54
Equation 8 – Measured relative frequency change and relative mass change.	54
Equation 9 – Henry’s law, governing partitioning of permeate across diffusion interface.	54
Equation 10 – Permeability coefficient for sorbent polymer.	55
Equation 11 – Fick’s law of diffusion.	81
Equation 12 – Limit of detection for resonant cantilever sensors.	95
Equation 13 – Temperature elevation as a function of heating power.	105
Equation 14 – Thermal resistance.	105
Equation 15 – Thermal time constant.	105
Equation 16 – Equation of fit for normalized heating resistance change as a function of temperature (in degrees Celsius).	154

LIST OF SYMBOLS AND ABBREVIATIONS

BOX	buried oxide
DCM	dichloromethane
DIL	dual in-line
DMM	digital multimeter
DRIE	deep reactive ion etching
EPCO	ethylene co-propylene
FEA	finite element analysis
GC	gas chromatography
KOH	potassium hydroxide
LoD	limit of detection
μ-	micro-
μTPC	micro thermal pre-concentrator
MEMS	micro electro-mechanical systems
MFC	mass flow controller
PDMS	polydimethylsiloxane
PECH	polyepichlorohydrin
PIB	polyisobutylene
PVAc	poly-vinyl acetate
SEM	scanning electron microscope
SiO ₂	silicon dioxide
SOI	silicon-on-insulator
VOC	volatile organic compound

SUMMARY

This work presents the development of different technologies and techniques for enhancing the performance of cantilever-based MEMS chemical sensors. The developed methods address specifically the sensor metrics of sensitivity, selectivity, and stability.

Different techniques for improving the quality and uniformity of deposited sorbent polymer films onto MEMS-based micro-cantilever chemical sensors are presented. A novel integrated recess structure for constraining the sorbent polymer layer to a fixed volume with uniform thickness was developed. The recess structure is used in conjunction with localized polymer deposition techniques, such as inkjet printing and spray coating using shadow masking, to deposit controlled, uniform sorbent layers onto specific regions of chemical sensors, enhancing device performance. The integrated recess structure enhances the stability of a cantilever-based sensor by constraining the deposited polymer layers away from high-strain regions of the device, reducing Q-factor degradation. Additionally, the integrated recess structure enhances the sensitivity of the sensor by replacing chemically-inert silicon mass with ‘active’ sorbent polymer mass. Finally, implementation of localized polymer deposition enables the use of sensor arrays, where each sensor in the array is coated with a different sorbent, leading to improved selectivity.

In addition, transient signal generation and analysis for mass-sensitive chemical sensing of volatile organic compounds (VOCs) in the gas phase is investigated. It is demonstrated that transient signal analysis can be employed to enhance the selectivity of individual sensors leading to improved analyte discrimination. As an example, elements of a simple alcohol series and elements of a simple aromatic ring series are distinguished with a single sensor (i.e. without an array) based solely on sorption transients. Transient signals

are generated by the rapid switching of mechanical valves, and also by thermal methods. Thermally-generated transients utilize a novel sensor design which incorporates integrated heating units onto the cantilever and enables transient signal generation without the need for an external fluidic system. It is expected that the thermal generation of transient signals will allow for future operation in a pulsed mode configuration, leading to reduced drift and enhanced stability without the need for a reference device.

Finally, A MEMS-based micro thermal pre-concentration (μ TPC) system for improving sensor sensitivity and selectivity is presented. The μ TPC enhances sensor sensitivity by amplifying low-level chemical concentrations, and is designed to enable coarse pre-filtering (e.g. for injection into a GC system) by means of arrayed and individually-addressable μ TPC devices. The system implements a suspended membrane geometry, enhancing thermal isolation and enabling high temperature elevations even for low levels of heating power. The membranes have a large surface area-to-volume ratio but low thermal mass (and therefore, low thermal time constant), with arrays of 3-D high aspect-ratio features formed via DRIE of silicon. Integrated onto the membrane are sets of diffused resistors designed for performing thermal desorption (via joule heating) and for measuring the temperature elevation of the device due to the temperature-dependent resistivity of doped silicon.

The novel system features integrated real-time chemical sensing technology, which allows for reduced sampling time and a reduced total system dead volume of approximately 10 μ L. The system is capable of operating in both a traditional flow-through configuration and also a diffusion-based quasi-static configuration, which requires no external fluidic flow system, thereby enabling novel measurement methods and applications. The ability

to operate without a forced-flow fluidic system is a distinct advantage and can considerably enhance the portability of a sensing system, facilitating deployment on mobile airborne platforms as well as long-term monitoring stations in remote locations. Initial tests of the system have demonstrated a pre-concentration factor of 50% for toluene.

CH 1 – INTRODUCTION TO CHEMICAL SENSING

We live in an information-rich era that has come to expect ubiquitous on-demand data delivered at low cost to mobile platforms. This drive for ever-increasing amounts and types of data has expanded to include chemical and biological information, with the hope that such data hold keys to improving our lives. As a result of this motivation, recent years have seen increased interest and activity in the area of micrometer-sized chemical sensors, which are both portable and low-cost [1-14]. The purpose of this research is to develop MEMS-based chemical sensing systems suitable for use in mobile platforms, to meet the growing need for real-time on-site chemical analyses.

Currently, many standard measurement systems for chemical analysis consist of bulky desktop equipment (e.g., gas chromatography [3, 15-18], mass spectrometry [15, 16, 19, 20]), requiring costly and complex external support systems to process and treat samples with additional reagents and control fluids. Such systems are often expensive and difficult to transport, requiring them to be located at a fixed position in a centrally located facility. Additionally, extensive personnel training is required due to both operational complexity of the equipment and interpretation of the results [19]. Thus, many such standard tests require samples to be transported off-site to a designated testing facility for processing and analysis, which introduces significant time delays and can even lead to inaccuracies in the interpreted results due to sample degradation or mishandling [21-23]. In instances where the sample analysis leads to a time-sensitive decision (e.g., clinical decision, quarantine of a contaminated location), such delays severely limit the efficacy of the information being

gathered. In these cases, the on-site real-time nature of data provided by low-cost mobile MEMS-based sensors can prove more valuable than the superior accuracy of traditional techniques, leading to applications where ‘good enough,’ in terms of measurement resolution, can be a preferable alternative [18, 23-25].

Low-cost portable sensors offer further the possibility of automated personalized healthcare within a patient’s home [26-28], potentially offloading many routine tasks from the looming shortage of primary-care physicians [29]. Leveraging the distributed nature of the Internet of Things (IoT) and machine learning technology [30, 31], such sensor systems can be designed for operation by an individual with minimal training or scientific knowledge [19, 32]. For example, significant functionality could be offered through the use of a mobile sensor platform coupled with software running on a patient’s tablet or cellular phone, which can access powerful databases and computational resources via the IoT. This application is especially attractive for the elderly and disabled, who may have difficulty traveling to a physician, and holds potential to save both lives and expense by enabling preventative treatments for conditions that would otherwise be discovered ‘too late’ [27, 28, 33].

While widespread personalized home healthcare enabled *via* low-cost mobile (bio)chemical sensors is not yet a reality, demonstrable progress has been made in other areas. For example, portable chemical sensors can be employed to assess blood alcohol concentration (BAC) from the breath of suspect drivers during roadside stops [1, 8, 34, 35], and by the military to improve the efficiency and quality of security checkpoints [9, 18, 23]. Additionally, MEMS-based sensors can be deployed for environmental monitoring [2, 25, 36-39] in remote [32, 40, 41] or hazardous locations [3, 9, 18, 21] that would

otherwise prove difficult to monitor by conventional means. As a final example, mobile sensors have also been employed in the food industry to measure ripening and reduce spoilage [42, 43].

In the applications described above, analysis of volatile organic compounds (VOCs) in the gas phase can yield much of the desired information [10, 44]. For example, analysis of exhaled breath samples has been shown to reveal information about the general health of a patient [45] and can be used to gauge sedation level during medical procedures [46, 47] or reveal exposure to toxic chemicals [48]. VOCs can be readily extracted from the saturated headspace over a liquid sample, extending the abilities of gas-phase technology for use in monitoring water contamination [2, 19, 43]. In general, many real-world applications such as these require the ability to reliably detect gas-phase VOC concentrations below 1 part-per-million (ppm). These applications further demand the ability to discriminate between similar compounds (e.g. benzene vs. toluene) in the presence of other interfering compounds. As an example, the threshold limit value (TLV) in the United States for benzene in ambient air is 500 ppb [3]. Thus, to monitor the safety of workers at risk of exposure to benzene, sensors are required which are capable of detecting benzene concentrations below 500 ppb levels even amidst other similar compounds that are present at higher concentrations.

Key Metrics for Chemical Sensors

When designing chemical sensors to address these challenges, there are several key metrics to consider. The most important of these have been referred to as “the four S’s” –

sensitivity, selectivity, speed, and stability [31, 49]. The first, sensitivity, is a measure of the change in sensor output signal per unit change in concentration for a given analyte. Selectivity measures how well the sensor is able to detect concentration changes in target analytes while simultaneously rejecting interfering signals from unwanted compounds. The time required for a sensor to complete and report a measurement is captured in the speed metric, while the stability metric gauges the reliability of reported measurements over time. The limit of detection (LoD) for a chemical sensor is defined as the minimum detectable analyte concentration, and is determined by both the sensor noise and the stability metrics for a given sensitivity [31]. In addition to these sensor metrics, there are two others that pertain more directly to the system as a whole and are crucial in the design of low-cost mobile platforms – size and scalability. While the size of an individual MEMS-based sensor itself is often minimal due to the capabilities of MEMS fabrication, the support systems necessary to operate the sensor are typically much larger and determine the total footprint of the platform [50]. Thus, care must be taken when designing a sensor so that the total system size (and power consumption) is minimized. This is especially relevant for systems designed to operate independently for extended periods of time or in remote locations. Lastly, the scalability metric is a measure of how well a given sensor/system design lends itself to being produced at scale (i.e. cost and ease of production as quantity increases). As the many applications are remarkably diverse there is no single ‘perfect’ sensor design, and a balance which is tailored to each specific application must be struck among the six ‘S’ metrics.

Common Sensor Technologies

Various approaches involving MEMS-based chemical sensing systems have been explored [21, 51-54], and can be broadly classified into the following categories based on fundamental sensing mechanism – electrochemical [4, 55, 56], thermal [57, 58], optical [13], and mechanical [24, 31, 52, 59-62]. Electrochemical sensing involves converting a change in chemical concentration to a subsequent change in electrical properties in the sensitive region of the device. Examples include potentiometric [63], amperometric [64], conductometric [4], and capacitive-type sensors [6, 55]. Electrochemical sensors can be very sensitive to specific classes of compounds, leading to enhanced chemical selectivity, and fabrication can be very simple and straightforward.

Thermal sensors, on the other hand, operate by transducing a chemical change into a corresponding change in thermal properties, which is then converted into an electrical signal [57]. This technique is often non-destructive – as opposed to e.g. a flame ionization detector (FID) in a GC system – to the chemical sample, which allows for further downstream processing by other sensing techniques and can enable multi-dimensional measurements leading to enhanced selectivity and discrimination amidst interfering compounds. The resolution of thermal sensors, however, can be sensitive to both the properties of the carrier gas (e.g., helium vs. nitrogen) and to how well the temperature of the carrier fluid can be controlled. Furthermore, the requirement of a carrier gas can lead to increased system cost and the use of a constant heating source to maintain temperature control can impact the system's power budget significantly, especially when considering use in long-term remote sensing applications. A thermal conductivity detector (TCD) is an

example of a simple but effective thermal chemical sensor that has found use in many MEMS-based sensing systems [65-67].

Optical sensors correlate a change in chemical concentration with a change in optical properties in the sensitive region. In some applications, the optical properties of a fluid containing the sample are directly observed (e.g. fluorescence), whereas in other cases sorption of the analyte onto a sensitive surface induces electro-optical changes in the surface, which are then read out electronically. Examples of optical sensors include waveguide, IR absorption, and Raman spectroscopy devices [13]. While optical sensors are capable of delivering the highest possible sensitivity – even single-molecule detection has been demonstrated with optical techniques [68] – they typically require the use of more exotic, optically-active materials which can lead to increased cost and can restrict their direct integration with CMOS circuitry for data processing and readout. Furthermore, optical chemical sensors typically require precise alignment of optical elements and can be sensitive to unwanted vibrations in the environment, leading to significantly increased total system size.

The focus of this work is on mechanical chemical sensors, which convert a change in chemical concentration into a corresponding change in the mechanical or motional properties of the sensor itself, which is then read out electronically. The most prominent examples of mechanically-based chemical sensors include surface acoustic wave (SAW) [31, 48, 59, 69-71] and cantilever devices [8, 9, 12, 62, 72-75]. SAW devices have proven to be very effective chemical sensors, and have seen use in many different types of miniaturized chemical sensing systems. However, SAW devices typically require the use of piezoelectric materials, which can increase overall processing cost and complexity, and

can limit their direct integration with CMOS processing circuitry. Additionally, the use of piezoelectric materials often requires poling at elevated temperatures during fabrication, and the presence of relatively high voltages during operation, which can further limit integration with low-power, low-noise measurement circuitry [76].

Cantilever-based MEMS Chemical Sensors

Of the many available sensor technologies discussed above, mass-sensitive cantilever-based sensors functionalized with sorptive coatings are an attractive technology to explore for several reasons [77-79]. First, the design and theory of cantilever sensors is well understood, and their fabrication via standard MEMS processing techniques is well established. This maturity is evidenced by their widespread use in scanning probe microscopy (SPM) [80, 81] and inertial sensing [82]. Second, the interface circuitry necessary for measuring frequency shifts in resonant sensors is mature and well documented [83]. Third, all molecules possess mass, which allows for the potential detection of any target species with a mass-sensitive approach and the sensor directly measure the mass of the analyte sorbed by the sensing film. This can also prove a disadvantage, however, as it can be difficult to distinguish between similar compounds based solely on mass (i.e. selectivity). Lastly, CMOS-compatible processes can be employed in the fabrication of cantilevers formed from silicon substrates, which enable the cantilevers to be integrated directly on-chip (i.e. on the same substrate) with drive and sense circuitry [84]. Such integration can dramatically reduce the total system footprint and

power consumption, enhancing system portability. Compatibility with CMOS processing further enables the possibility of scaling future sensor production to quantities of scale.

Cantilever-based mechanical sensors are typically operated in either a static [8, 9, 72] or dynamic mode [12, 62, 74, 75, 84, 85]. In the static mode, the cantilever is coated with an appropriate sorbent film sensitive to analytes of interest and when exposed to a chemical concentration the ad/absorption of analyte into or onto the sorbent layer induces surface stresses, which cause the cantilever beam to bend. The amount of displacement can be measured with capacitive, piezoresistive, or optical methods. Such sensors have demonstrated detection capabilities in the femtogram range for VOCs [86] and in the μM range for biological compounds [87].

The focus of this work, however, is on cantilevers operating in a dynamic mode [12, 62, 73, 74, 88-90]. In the dynamic mode of operation, the cantilever is actively driven into resonance and the corresponding resonance frequency and phase for a particular resonance mode are tracked electronically. The resonance frequencies of the device are determined by geometry and material properties. As the material properties (e.g., the overall mass due to sorption of gas molecules, or the Young's modulus due to temperature elevation) of the cantilever change upon exposure to a chemical concentration, correspondingly the resonance frequency also changes. With careful design, the nature of this frequency shift can ultimately be correlated with a change in chemical concentration surrounding the sensor. For cantilevers formed from silicon substrates and operated in the linear regime, resonant operation of the device can be modeled as a classical mass-spring-dashpot system [91]. Thus, the angular resonance frequency is given by

$$w_0 = \sqrt{\frac{k_{eff}}{m_{eff}}}$$

Equation 1 – Resonance frequency for classical mass-spring-dashpot system.

where k is the effective spring constant of the cantilever beam, and m is the effective mass.

The spring constant of a mechanical beam (subject to a tip force) can be calculated from

$$k = \frac{F}{x} = \frac{Ewt^3}{4L^3}$$

Equation 2 – Spring constant for a mechanical beam.

where F is the applied force to the tip of the cantilever beam, x is the corresponding displacement of the beam tip in the direction of the force, E is the Young's modulus of the beam material, and w , t , and L are the dimensions of the cantilever beam – width, thickness, and length, respectively. It is important to note that the thickness dimension is defined to be the dimension in the plane of motion or bending. Another important metric for resonant cantilevers is the quality factor, Q , which is the ratio of energy stored over energy dissipated, per cycle. It is given by

$$Q = \frac{f_0}{\Delta f_{3dB}} = \frac{w_0 \cdot m}{b} = \frac{k}{w_0 \cdot b}$$

Equation 3 – Q-factor for resonant cantilever beam.

where f_0 is resonance frequency, Δf_{3dB} is the 3 dB width of the resonance peak, w_0 is angular resonance frequency, m is the effective mass of the beam, k is the effective spring constant, and b is the effective damping present in the system. When used as a chemical sensor, the cantilever beam has a corresponding limit of detection (LoD), which is defined as three times the noise-equivalent analyte concentration, which in turn can be approximated by

$$LoD = 3 \frac{\Delta f_{min}}{S}$$

Equation 4 – Limit of detection (LoD) for resonant cantilever-based chemical sensor.

where Δf_{min} is the lowest detectable frequency change (determined by the noise and stability) and S is the sensitivity metric (determined by properties of the sorbent coating and the mechanical sensor), as discussed previously [92]. From Equation 4, it would seem that the LoD (i.e. minimum detectable concentration) of a resonant cantilever-based sensor can be improved by increasing either the Q (i.e. by decreasing Δf_{min}) or the sensitivity, or both, and that an arbitrarily low LoD can be achieved by doing so.

In practice, however, detection of a specific target analyte in real-world applications can be complicated by the presence of interfering compounds, and the effective Q-factor is often reduced during fabrication and packaging by the application of a polymer-based sorbent layer necessary for increased chemical sensitivity. Thus, the Q and the sensitivity are generally in direct conflict with one another, limiting the maximum attainable LoD. All three of these issues – chemical selectivity, Q-factor degradation, and sensitivity – can be approached simultaneously through improvements to the chemically-sensitive sorbent

layer that is typically applied to the surface of mass-sensitive cantilever-based sensors. For example, by coating arrays of sensors, where each individual sensor is coated with a separate class of sorbent, the ensemble response of the array can be interpreted as a multidimensional measurement. This multidimensional approach of detecting specific target analytes by characteristic chemical fingerprints across the sensor array offers the potential to improve analyte discrimination (i.e. selectivity) even in the presence of interfering compounds [30, 31]. Additionally, careful selection of sorbent materials that are disproportionately sensitive to target analytes can significantly enhance the sensitivity of the sensor, which in turn improves the signal-to-noise ratio and ultimately the LoD. Finally, the effective, post-coating Q-factor (i.e. reduction in Q-factor degradation) can be improved considerably through the use of localized polymer deposition. The exploration of techniques for improving sensitivity, selectivity, and stability by means of enhancements to the sorbent layer will be discussed in more detail in Chapter 2.

Resonant Cantilever Design

The cantilevers discussed in this work are designed to operate in an in-plane, flexural resonance mode and feature both rectangular and semicircular suspended geometries. Devices with a semicircular ‘hammerhead’ geometry were found previously to have superior performance when compared to the simpler rectangular designs, due to increased surface area for chemical sorption without a correspondingly significant increase in viscous damping in air or liquid [62, 73, 74]. The hammerhead sensors exhibit relatively low Q-

factors for out-of-plane modes, due to increased viscous damping from the large surface area of the head region. Operating the devices in an in-plane flexural mode, however, enhances the Q-factor as the beam effectively slices through the surrounding medium, experiencing significantly reduced energy loss from viscous damping despite its large surface area in the plane. Exciting the hammerhead sensors in an in-plane mode allows even liquid-phase operation with reasonably high Q-factors [62].

Due to their superior performance, the emphasis of this work is primarily on the hammerhead-style devices consisting of a semicircular head portion with inner and outer radii of 100- μm and 200- μm , respectively, supported by a 45-75 μm wide and 100- μm long cantilever beam. At its supported end, each hammerhead structure has embedded silicon resistors for electrothermal excitation and piezoresistive detection of in-plane flexural vibrations (Figure 2). A typical fabrication process flow for devices representing prior state-of-the-art is highlighted below (Figure 1). The devices are formed from silicon substrates using a six-mask CMOS-compatible process flow.

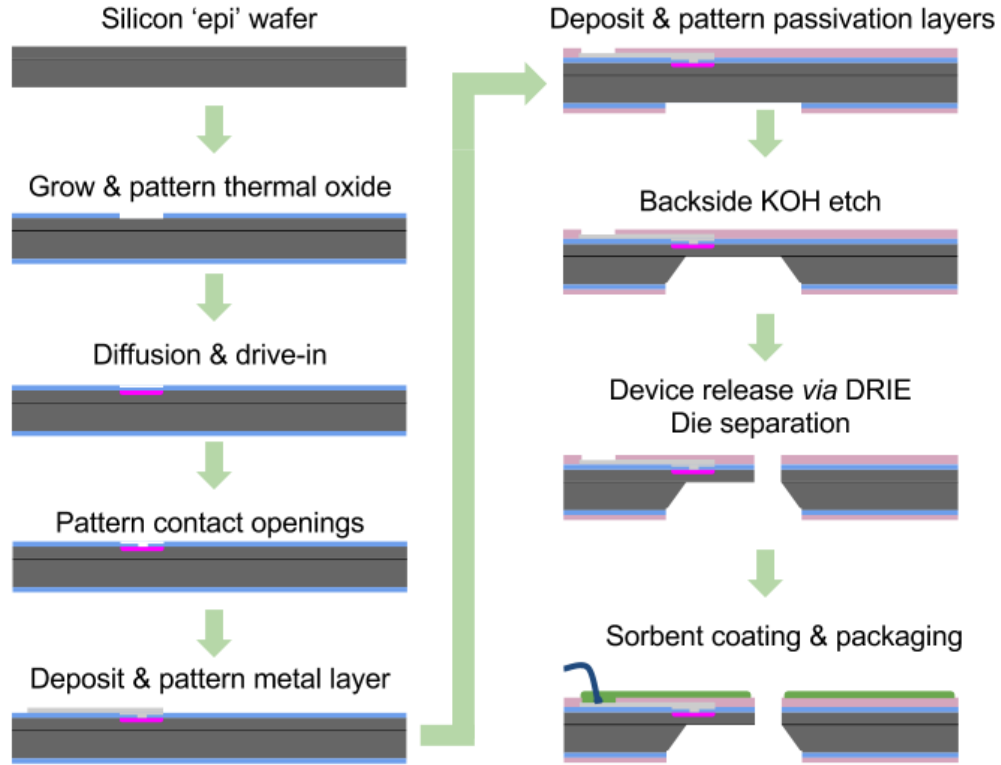


Figure 1 - Typical process flow for suspended resonant cantilever-based sensors formed from epitaxial silicon substrates. Device thickness is controlled with an electro-chemical etch stop [74, 89].

Fabrication begins with thermal oxidation of an epitaxial silicon wafer, where the thickness of the epitaxial layer defines the final thickness of the released cantilevers. The thermally grown oxide is then patterned and dry-etched down to the silicon surface to open diffusion windows. High-temperature boron diffusion through the oxide windows into the exposed silicon, followed by a drive-in step, is used to form the heating resistors and piezoresistive Wheatstone bridge necessary for operation of the completed sensors. Electrical contact is made to the diffused resistors *via* contact openings to the silicon and a thin aluminum metallization layer is deposited and patterned to define electrical traces and bond pads suitable for wire-bonding to an external circuit. Nitride passivation is deposited

and patterned on the front surface of the wafer to protect the devices from scratches and corrosion, and to enable operation in conductive environments without short-circuiting adjacent metal traces. Additional dielectric thickness necessary for a sufficiently durable hard mask is deposited and patterned on the back surface of the wafer, and the wafer is then placed in a KOH etch bath for several hours to remove the silicon exposed through the patterned dielectric mask on the back surface. The KOH etch is controlled with an electrochemical etch stop that inhibits the etch mechanism once it reaches the reverse-biased PN-junction formed between the P-type bulk layer and the N-type epitaxial layer. Completion of the KOH etch step results in thin, suspended membranes, which are subsequently patterned and etched *via* DRIE from the front side to release the suspended cantilevers. The importance of a reliable and accurate etch stop in this process cannot be overstated, as the thickness of the suspended cantilevers has a considerable effect on device performance (e.g. resonance frequency, Q-factor). By inhibiting the KOH etch electrochemically, the thickness of the epitaxial layer can be used to precisely control the thickness and uniformity of the released cantilevers resulting in consistent, optimal sensor performance. Figure 2 highlights images of both hammerhead and rectangular cantilevers, following fabrication. Once fabricated, the sensors are coated with a sorbent polymer layer, which is sensitive to target compounds of interest.

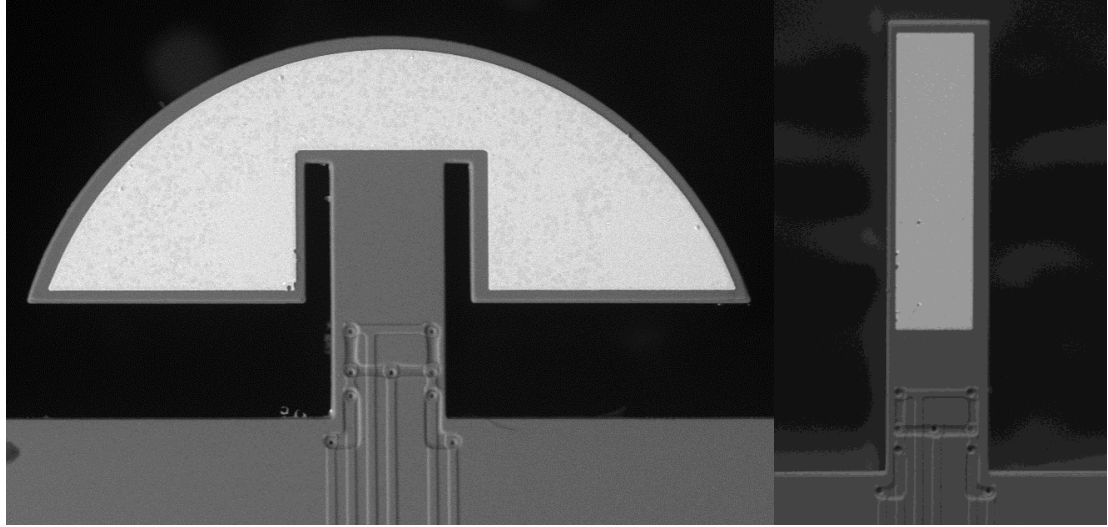


Figure 2 – SEM images of hammerhead (left) and rectangular (right) cantilevers following fabrication. These devices are representative of prior state-of-the-art [62]. The white region near the tip of each device pictured is a thin gold layer, formed in anticipation of functionalization with a self-assembled monolayer (SAM) for biological sensing.

Forming the cantilevers from silicon substrates has several advantages. This approach allows for the use of many existing processes employed in standard IC fabrication (e.g. thermal oxidation, dopant diffusion), leveraging decades of accumulated experience and technology. Furthermore, building atop existing IC fabrication techniques renders the cantilever process readily compatible with CMOS circuitry, enabling direct integration of the sensors with drive and measurement circuitry. Such integration can lead to significant reductions in power consumption and total system size, while simultaneously enhancing signal-to-noise ratio (SNR) and speed. Ultimately, direct integration of sensors and circuitry enhances overall system portability, which is the primary advantage of a MEMS-based chemical sensing approach.

Additionally, building from silicon substrates enables the use of the piezoresistive effect in monitoring beam motion as the cantilever vibrates at resonance. This approach is

explained in detail in prior state-of-the-art [74, 85]. For example, when precisely aligned to the appropriate crystal planes, silicon piezoresistors can exhibit significant resistance changes under strain conditions resulting from beam motion. When the piezoresistors are arranged in a Wheatstone bridge configuration, as shown in Figure 3, the total differential resistance change can be increased still further as opposite sides of the bending cantilever beam experience opposite strain.

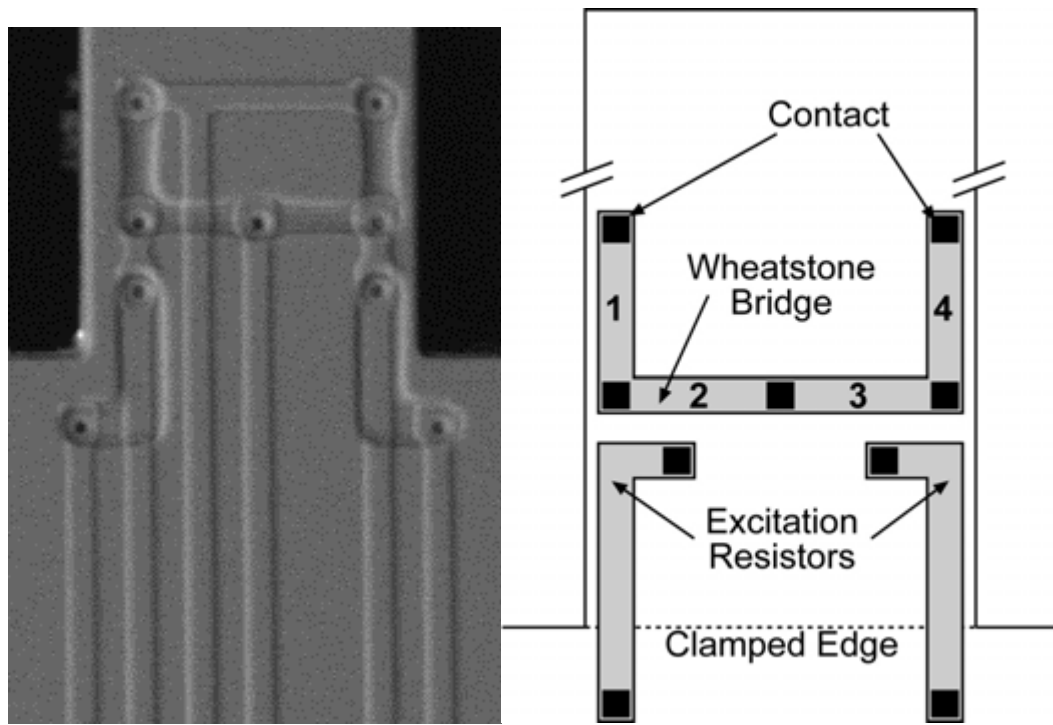


Figure 3 – SEM image (left) and schematic illustration (right) of resistor arrangements for Wheatstone bridge and thermal excitation near cantilever base [93].

For example, during beam bending one side of the beam experiences tensile stress while the opposite side experiences compressive stress (Figure 4). As a result, the piezoresistors running along the long axis of the beam (resistors 1 & 4 in Figure 4) experience opposite resistance changes, so that one resistor increases its resistance while

the other decreases its resistance. Similarly, the piezoresistors running perpendicular to the long axis of the beam (resistors 2 & 3 in Figure 4) also experience opposite changes in resistance, so that one resistor increases in resistance while the other decreases. In the case of a beam bending in the x-y plane, as illustrated in Figure 4, resistors 1 & 4 experience longitudinal stresses while resistors 2 & 3 experience transverse stresses. For the cantilevers in this work, the piezoresistors in the Wheatstone bridge are aligned to be parallel to the $\langle 110 \rangle$ direction on a (100) wafer.

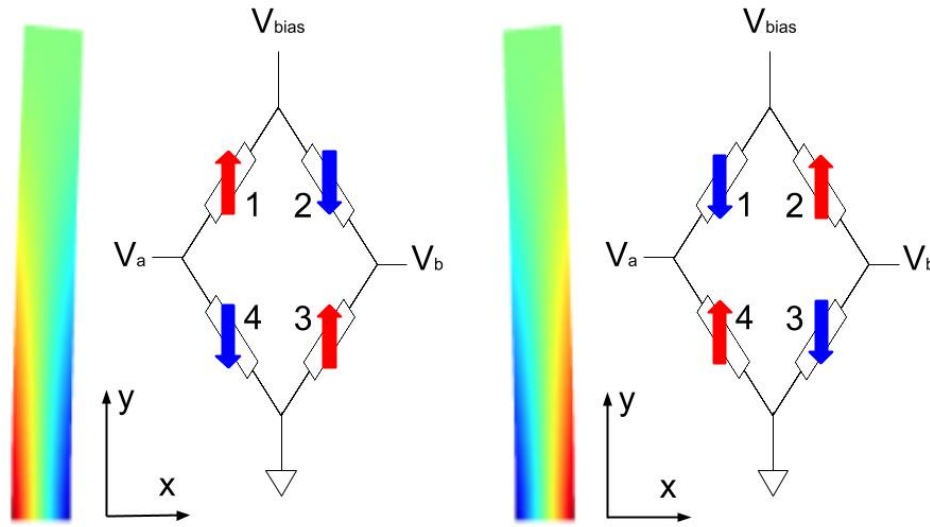


Figure 4 – Illustration of how the integrated Wheatstone bridge responds as cantilever beam bends in x-y plane during resonant operation. Due to the arrangement of the piezoresistors, and alignment to the $\langle 100 \rangle$ direction, bending of the cantilever beam produces an amplified voltage difference from points $V_a - V_b$, which can be read out electronically to track shifts in the resonance frequency [93].

The piezoresistive coefficients for p-type (boron) diffusion in the $\langle 110 \rangle$ direction in silicon are such that the magnitude of the relative resistance change for piezoresistors undergoing transverse stress is similar to that of piezoresistors undergoing longitudinal stress, but with opposite sign [91]. Thus, as resistors 1 & 3 both increase in resistance in tandem under beam bending, resistors 2 & 4 will decrease in resistance in tandem. The net effect of this

behavior as the cantilever beam vibrates – and when a DC bias current is sourced through the Wheatstone bridge from V_{cc} to ground – is to produce an amplified periodic voltage difference appearing between points V_a and V_b on the Wheatstone bridge.

Thus, the time-dependent change in piezoresistance as the beam resonates and experiences changing stresses produces a time-dependent voltage difference across the resistor arrangement that can be read out electronically. This periodic, time-varying voltage signal can then be monitored with various frequency-counting schemes to precisely track the resonance frequency of the vibrating cantilever beam.

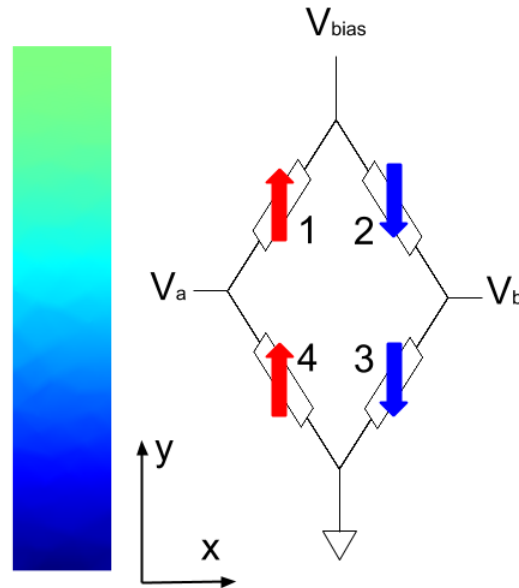


Figure 5 – Illustration of OOP bending of cantilever beam, and its effect on piezoresistance changes in Wheatstone bridge. Due to the arrangement of the resistors in the Wheatstone bridge, OOP mode bending results in a suppressed output signal [93].

Arrangement of the resistors into a Wheatstone bridge configuration has the additional advantage of reducing common mode noise on the piezoresistors, as common mode noise does not result in a change in differential signal between nodes V_a and V_b on the

Wheatstone bridge. Additionally, this design approach results in the suppression of spurious unwanted signals due to out-of-plane (OOP) beam bending. As illustrated in Figure 5, OOP beam motion causes resistors 1 & 4 to both increase in resistance and by the same amount. Similarly, resistors 2 & 3 both decrease in resistance and by a similar amount as resistors 1 & 4 as a consequence of the piezoresistive coefficients for transverse and longitudinal stresses discussed above. As a result of this response, the voltages at points V_a and V_b do not vary significantly from their quiescent points and the voltage difference between V_a and V_b remains fairly constant during OOP beam motion.

Movement of the cantilever beam is accomplished *via* thermal actuation. Thermal actuation involves dissipating electrical power in the thermal excitation resistors near the base of the cantilever beam (Figure 3), which causes the beam to bend away from the heated resistor due to thermal expansion. By pulsing the excitation resistors with heating power waveforms at the desired in-plane resonance frequency of the cantilever beam, the beam will begin to vibrate back and forth in the xy-plane. In practice, a DC-shifted sine wave voltage signal is used to drive the cantilever at resonance, so that the effective power dissipated in the excitation resistors varies from a low quiescent value to P_{peak} over each cycle. Due to the large Q-factors exhibited by the cantilever devices in this work, driving the sensor in a corresponding resonance mode results in efficient operation as very low driving power is necessary to achieve substantial beam motion. For example, the driving power necessary for continuous thermal actuation at resonance for a device operating at 765 kHz was experimentally determined to be approximately 40 mW. This level of continuous power dissipation equates to approximately 50 nJ of energy per actuation cycle. It is suggested for future work that pulsed operation schemes be investigated, which could

remove the requirement of driving the resonator continuously, enabling lower power consumption per measurement. As a final note, it has been observed that it is not necessary to utilize both excitation resistors – driving the device with only one excitation resistor is sufficient, and results in lower power consumption.

Resonant Cantilever Operation

Various circuit techniques have been studied for driving a cantilever at its resonance frequency and simultaneously monitoring shifts or deviations from this frequency. Prior state-of-the-art employed a closed-loop feedback system based on the Schmitt-trigger topology to operate cantilever-based sensors at resonance [12, 62, 73, 74]. Other work has utilized a phase-locked loop (PLL) approach to drive cantilevers in an OOP resonance mode at frequencies in the low tens of kHz range [94, 95]. However, the use of a PLL system to operate in-plane cantilever sensors featuring integrated drive and sense resistors at frequencies approaching 1 MHz has not been observed in the literature. As a result, a closed-loop feedback circuit for driving the sensors at resonance and tracking chemical concentration-dependent frequency shifts over time was developed as part of this work. Figure 6 is a block diagram of the completed circuit.

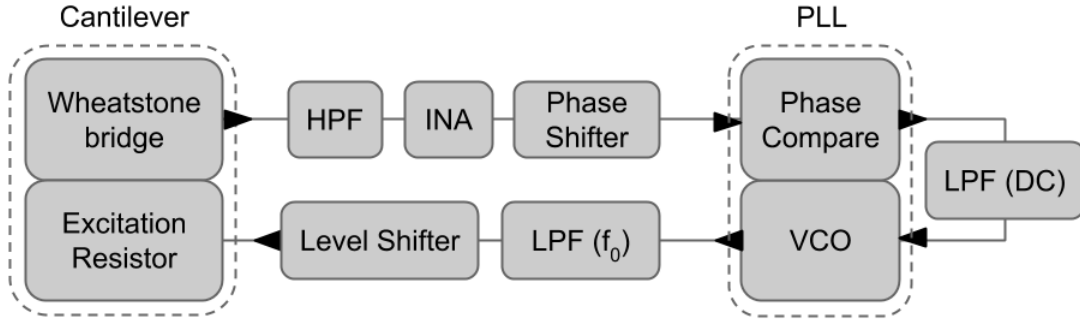


Figure 6 – Block diagram of PLL circuit for driving cantilevers at resonance and monitoring frequency shifts over time.

Initially, the voltage-controlled oscillator (VCO) of the PLL is idling at its baseline frequency – which is significantly less than the cantilever’s resonance frequency – and the cantilever is essentially at rest. To excite the cantilever into resonance, the oscillation frequency of the VCO is increased by external control until it reaches the cantilever’s resonance frequency. At resonance, the driving signal passed through the level shifter and into the excitation resistor results in a large-displacement, sustained vibration of the cantilever, which is subsequently transduced into a differential output signal from the Wheatstone bridge. This output signal is high-pass filtered (HPF) and fed into a high-speed instrumentation amplifier (INA), which both amplifies the differential signal further and also suppresses common mode noise. Cascaded below the INA is a phase shifter, which adjusts the driving signal to be 90° out of phase with the sense signal from the Wheatstone bridge. The phase-shifted output signal is then compared by the PLL, which adjusts the VCO frequency to match that of the incoming phase-shifted signal, leading to a condition where the loop is ‘locked’ to the frequency of this signal. Once locked, the frequency of the VCO driving signal will track any changes in the phase-shifted output signal and the circuit will adjust so that the cantilever is continuously vibrating at its resonance frequency.

In this way, as the cantilever resonance frequency changes (e.g., due to mass uptake, or heating) the output of the circuit can be measured electronically and correlated to the changing properties of the cantilever. As the VCO outputs a square wave, this signal must be low-pass filtered (LPF) so as to drive the cantilever with a sine wave. The level shifter serves to adjust both the amplitude and DC bias of the driving signal.

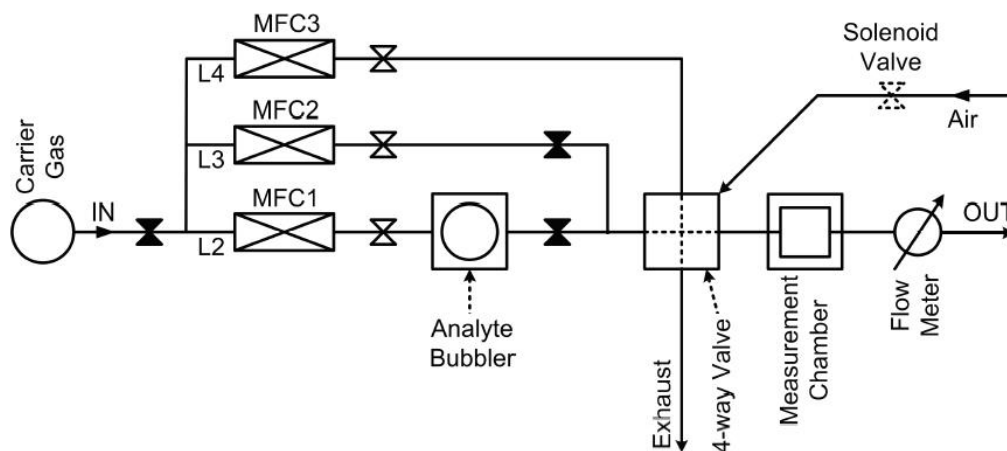
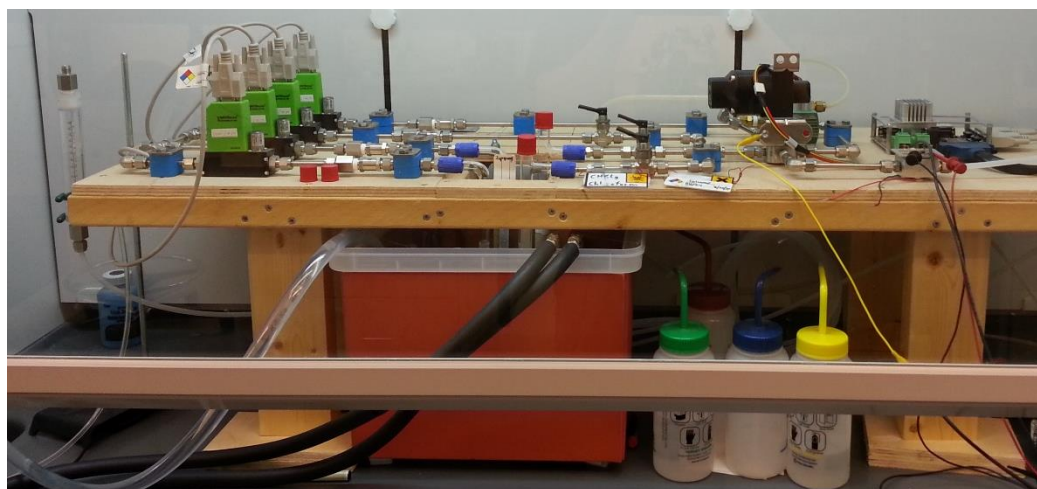


Figure 7 - Photograph (top) and schematic diagram (bottom) of custom gas setup. Flow rates are controlled by precision mass flow controllers (MFCs) and known VOC concentrations are generated by flowing carrier gas through a temperature-controlled bubbler and diluting with carrier gas. A pneumatic 4-way valve enables rapid switching between reference carrier and analyte gas streams [12, 90].

Once locked at resonance, a typical chemical measurement involves exposing the cantilever to varying concentrations of analytes while monitoring shifts in the cantilever's resonance frequency. The concentrations are produced and controlled by means of a custom gas-flow system, as shown in Figure 7. The analyte-loaded gas stream introduced to the sensor is generated by flowing nitrogen carrier gas through a temperature-controlled bubbler containing analyte-soaked quartz sand. The analyte vapor pressure in the gas stream can then be determined from Antoine's equation for a given bubbler temperature [90]. After leaving the bubbler, the analyte-loaded gas stream is subsequently diluted downstream by mixing with pure carrier gas before the mixture is drawn through the gas-tight measurement chamber where the sensor is located (Figure 7). Mass-flow controllers (MFCs) control the flow through the different gas lines in the custom setup, thereby controlling the analyte concentration presented to the sensor in the chamber.

Improvements to Prior State-of-the-Art

Building on the foundation laid by previous work, various techniques for improving the quality of deposited sorbent polymer films onto MEMS-based micro-cantilever chemical sensors are explored in the following chapters. First, the development of a novel integrated recess structure for constraining the sorbent polymer layer to a fixed volume with uniform thickness is presented. The recess structure is used in conjunction with localized polymer deposition techniques, such as inkjet printing and shadow masking, to deposit controlled, uniform sorbent layers onto specific regions of chemical sensors,

enhancing device performance. Specifically, the integrated recess structure results in enhanced sensitivity and frequency stability.

Additionally, the investigation of transient signal generation and analysis at the system level is presented for mass-sensitive chemical sensing of VOCs in the gas phase. It is demonstrated that transient signal analysis can be employed to enhance the selectivity of individual sensors leading to improved analyte discrimination. Transient signals are generated by the rapid switching of mechanical valves, and also by thermal methods. Thermally-generated transients utilize a novel sensor design which incorporates integrated heating units onto the cantilever beam and enables transient signal generation without the need for an external fluidic system.

Finally, A MEMS-based micro thermal pre-concentration (μ TPC) system for enhanced detection of gas phase VOCs is presented. The system implements a suspended membrane geometry, enhancing thermal isolation and enabling high temperature elevations even for low levels of heating power. The membranes have a large surface area-to-volume ratio but low thermal mass (and therefore, low thermal time constant), with arrays of 3-D high aspect-ratio features formed via DRIE of silicon. Integrated onto the membrane are sets of diffused resistors designed for performing thermal desorption (via joule heating) and for measuring the temperature elevation of the device due to the temperature-dependent resistivity of doped silicon.

The novel system features integrated real-time chemical sensing technology, which allows for reduced sampling time and a reduced total system dead volume of approximately 10 μ L. The system is capable of operating in both a traditional gas-flow setup and also in a static atmosphere which requires no external fluidic flow system, thereby enabling novel

measurement methods and applications. The ability to operate without a forced-flow fluidic system is a distinct advantage and can considerably enhance the portability of a sensing system, facilitating deployment on mobile airborne platforms as well as long-term monitoring stations in remote locations.

CH 2 – LOCALIZED POLYMER DEPOSITION

In some designs, prior state-of-the-art employed a uniform blanket approach to the application of sorbent coatings, where all devices in the array were coated simultaneously and with an identical uniformly-deposited sorbent layer [73]. Other approaches involved the use of drop-casting or inkjet printing, as a way of achieving localized polymer deposition [96, 97]. The application of a blanket coating was accomplished through the use of spray coating (with an atomizer) of polymer-based sorbents dissolved in a suitable solvent, or through the use of alkane-thiol chemistry to produce self-assembled monolayers (SAM) on the exposed gold surfaces (Figure 2) of the sensors [62]. Such blanket techniques, however, limit considerably the possibility of coating adjacent sensors in an array with different sorbent layers, limiting the potential for analyte discrimination in the presence of interfering compounds. Furthermore, the addition of a uniformly applied polymer sorbent layer over the entire cantilever structure can dramatically degrade a device's mechanical and electrical characteristics. For example, it has been observed that a uniformly-applied sorbent coating can degrade a given sensor's initial, uncoated Q-factor by as much as an order of magnitude when operated in air [73]. Thus, the ability to confine the sorbent layer near the tip of the beam offers the advantage of preserving the desirable mechanical properties of the silicon beam in high-strain regions (e.g. near the beam anchor), which in turn preserves the Q-factor. As the LoD is proportional to the Q-factor, minimizing Q-factor degradation ultimately improves the LoD and resolution of the sensor. Additionally, localized deposition enables sorbent to be placed precisely in regions where it is most effective in detecting mass loading (e.g. near the beam tip), and allows for thicker

sorbent layers to be used without compromising the post-coating Q-factor. These factors combine to enhance the effective sensitivity of the coated device when compared with blanket coating techniques. In other words, the localized deposition of the sensing film in areas near the beam tip allows for thicker sensing films without significant Q-factor degradation compared to uniformly coated resonators. This typically far compensates for the loss in sensitivity by not coating the full surface area of the resonator, especially if one considers that the regions at the beam tip contribute more to the sensitivity than region close to the cantilevers clamped edge.

Thus, improvements to three of the previously-discussed ‘S metrics’ – sensitivity (and even more so the LOD), selectivity, and stability – can be approached simultaneously through improvements in the chemically-sensitive sorbent layer that is typically applied to the surface of mass-sensitive cantilever-based sensors. For example, by coating arrays of sensors, where each individual sensor is coated with a separate class of sorbent, the response of the array can be interpreted as a multidimensional measurement [30, 31]. This multidimensional approach offers the potential of detecting specific target analytes by characteristic chemical fingerprints across the sensor array even in the presence of interfering compounds. Additionally, careful selection of sorbent materials that are disproportionately sensitive to target analytes can significantly enhance the sensitivity of the sensor, which in turn improves the signal-to-noise ratio and LOD.

Looking at a single sensor, the localized coating allows for thicker sensing films without significant Q-factor degradation, which can improve sensitivity and minimal detectable frequency change simultaneously, compared to uniformly coated sensors, and

thus is expected to improve the LOD. Finally, the sensor stability might be improved by not coating the high-strain regions near the cantilever's clamped edge with polymer.

In the following, different techniques for the localized deposition of the sensing film have been investigated.

Inkjet Printing

The use of inkjet printing as a possible coating technique was explored as it has been demonstrated to be capable of achieving localized polymer deposition onto silicon microstructures [22, 89, 98]. With this approach, the sorbent polymer is typically dissolved in a suitable solvent and subsequently ejected onto the substrate through a micro-nozzle *via* ultrasonic piezoelectric actuation (Figure 8). This versatile technique allows for polymer deposition onto non-planar substrates, and can be used to print precise, arbitrary patterns (Figure 8) through the use of software scripting. To investigate this possibility, initial feasibility experiments made use of an ink-jet printing platform (Microfab, JetLab) available in the IEN cleanrooms at Georgia Tech, and consisted of printing simple patterns of poly-isobutylene (PIB) dissolved in xylene (0.1wt%) onto both planar silicon surfaces and 3D high aspect-ratio ridge and pillar test structures.

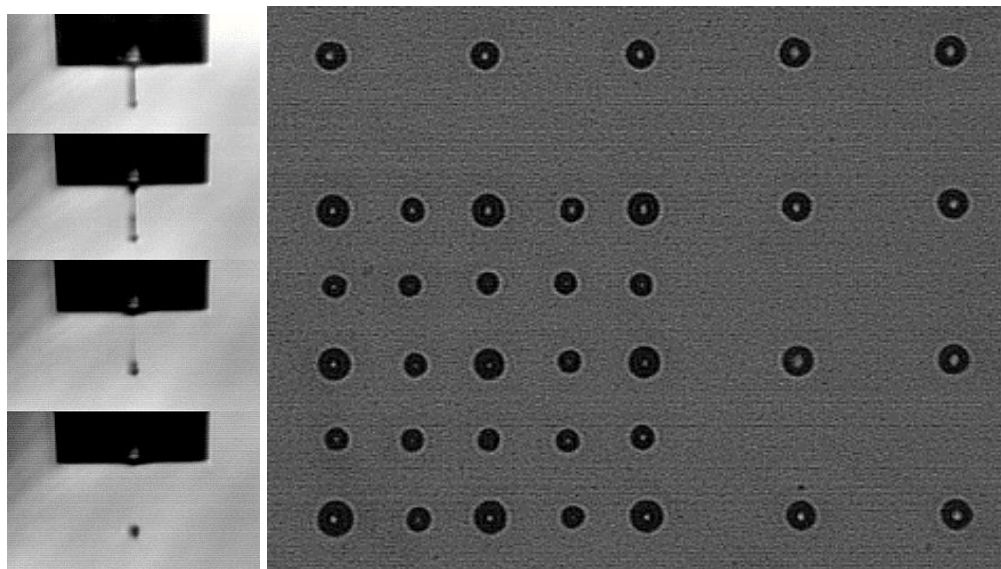


Figure 8 - Stroboscopic images (left) taken during inkjet printing of a solution of polyisobutylene (PIB) dissolved in o-xylene and (right) array of droplets deposited via inkjet printing from a solution of sucrose dissolved in water. Printing was performed on a MicroFab JetLab II inkjet printer located in the IEN cleanroom facilities at Georgia Tech.

Additional experiments involved printing of relatively thick (1-2 μm) PIB, ethylene co-propylene (EPCO), and polyvinylacetate (PVAc) patterns, and demonstrated basic feasibility of inkjet printing as a method for coating individual MEMS devices. In an effort to avoid nozzle clogging, dimethyl sulfoxide (DMSO) was used as a solvent for PVAc, and xylene as a solvent for EPCO and PIB, due to their relatively high boiling points and thus slow rate of evaporation during the ink-jetting process [89].

It was observed, however, that the deposition of high-quality sorbent polymer films with inkjet printing can prove difficult for a variety of reasons. For example, the range of suitable solvents can be limited by incompatibility with the printing nozzle itself. In the case of the Jetlab inkjet printer, solvents such as chloroform and dichloromethane cannot be printed as they readily dissolve the adhesive used in the nozzle's construction. This limitation precludes the use of polymers dissolved by these solvents (e.g. PEUT, PECH), and thus restricts the range of available sensing films. Additionally, the formation of stray

‘satellite’ droplets (Figure 9) can result in undesirable polymer deposition in unintended areas.

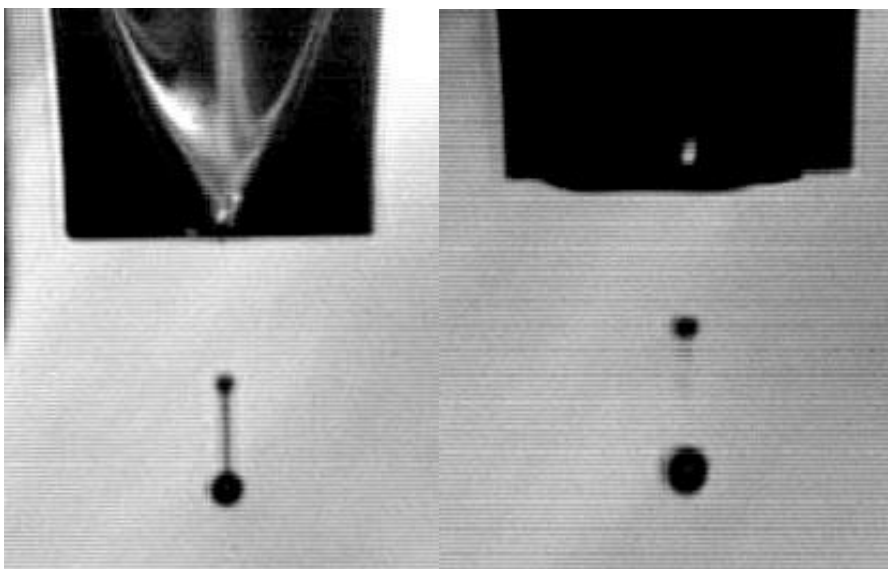


Figure 9 – Inkjet printing, stray satellite droplets.

It has also been observed that certain polymer/solvent combinations result in non-uniform films, where the deposited polymer film is considerably thicker near the edges of the film and thinner in the center (“coffee ring” effect), as illustrated in Figure 10 [89]. The effect becomes more pronounced with increasing film thickness, leading to severely non-uniform films when coating in excess of a few microns. When considering the use of inkjet printing in conjunction with cantilever-based chemical sensors, it would be desirable to overcome these difficulties and leverage the unique advantages of inkjet printing to deposit different classes of sorbent films onto arrays of sensors, with each sorbent film being uniform and localized near the tip of the cantilever beam, away from high-strain regions near the beam support.

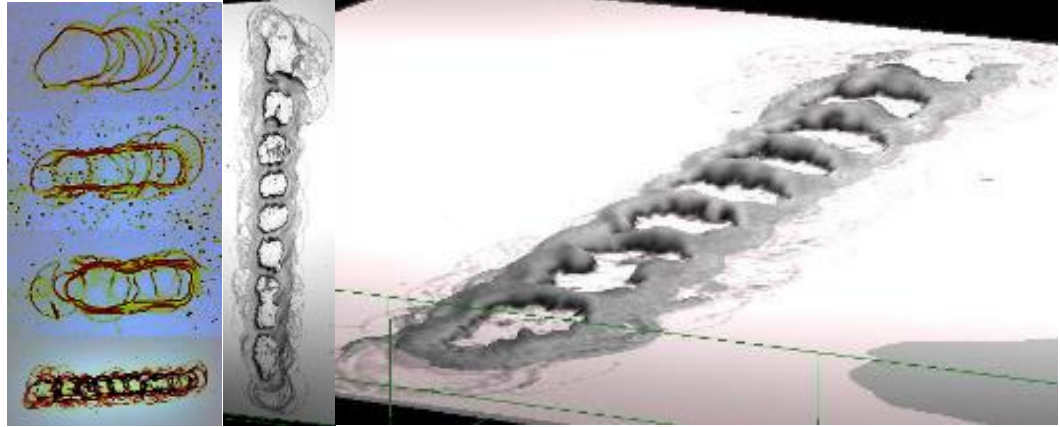


Figure 10 - Optical microscope (left) and enhanced 3D (center, right) images of printed EPCO film exhibiting the coffee ring effect. The image on the left shows the evolution of the coffee ring effect as printed film thickness increases. Printing was performed on a MicroFab JetLab II inkjet printer. Enhanced 3D images were obtained using the LEXT confocal microscope, located in the IEN cleanroom facilities at Georgia Tech.

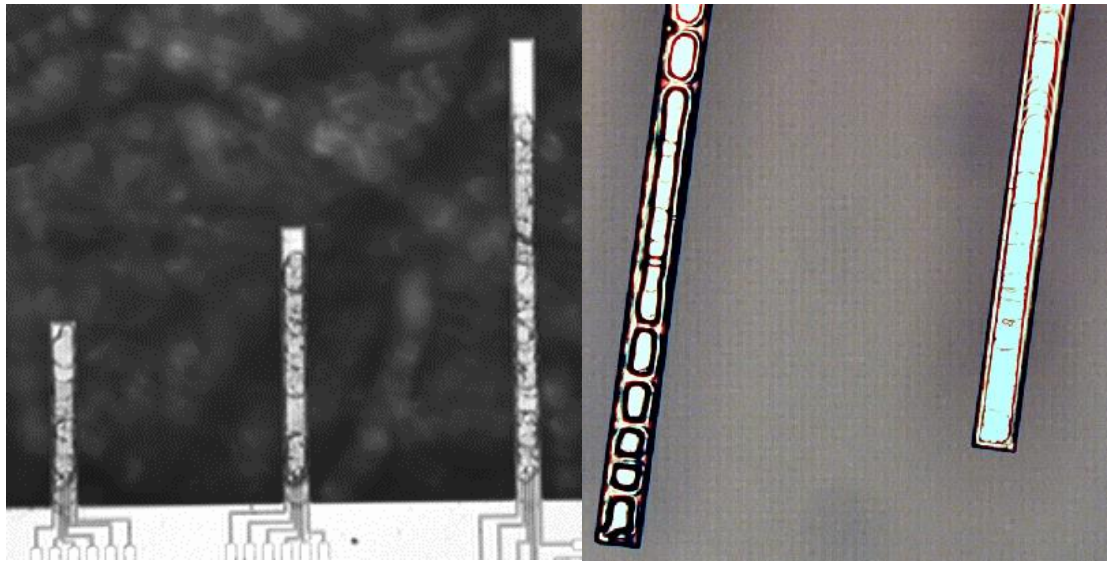


Figure 11 – Optical microscope images (left) of thin polymer films printed onto suspended micro-cantilever structures. As film thickness increases, the ‘coffee ring effect’ becomes more substantial (right).

Integrated Recess Structure

To this end, a novel technique for improving the quality of deposited sorbent films with significantly reduced Q-factor degradation for resonators operated in air was

developed. The technique consists of forming an integrated recess structure into the tip region of silicon cantilevers designed to resonate in an in-plane flexural mode. The sorbent film is deposited via inkjet printing and is localized in the recess structure, a significant distance away from high-strain areas of the cantilever support beam. The benefits of the etched recess in conjunction with ink-jet deposition are:

- Improved film uniformity and confinement – reduced splattering of polymer, reduced coffee ring effect
- Improved sensor sensitivity – silicon mass is replaced by ‘active’ polymer sensing material
- Improved Q-factor – polymer is confined to un-strained regions of the resonator

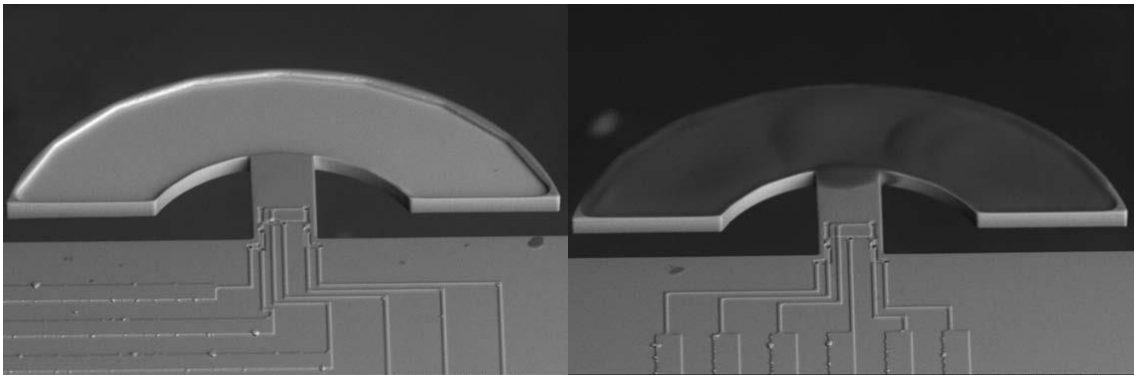


Figure 12 - SEM micrographs of (a) uncoated hammerhead resonator with 12- μm total thickness and recess of 5- μm etched into the head structure and (b) hammerhead resonator after filling the recess with polyvinylacetate (PVAc) as localized chemically sensitive film via ink-jet printing [89].

The hammerhead resonators developed in this endeavor consist of a semicircular head portion with inner and outer radii of 100- μm and 200- μm , respectively, supported by a 45- μm wide and 100- μm long cantilever beam. At its supported end, each hammerhead

structure has embedded silicon resistors for electrothermal excitation and piezoresistive detection of in-plane flexural vibrations.

In addition to hammerhead devices, the effects of the integrated recess structure on localized polymer deposition were also explored for traditional rectangular microcantilevers. Figure 13 shows a progression of rectangular cantilevers which have been partially-filled to varying degrees with PVAc.

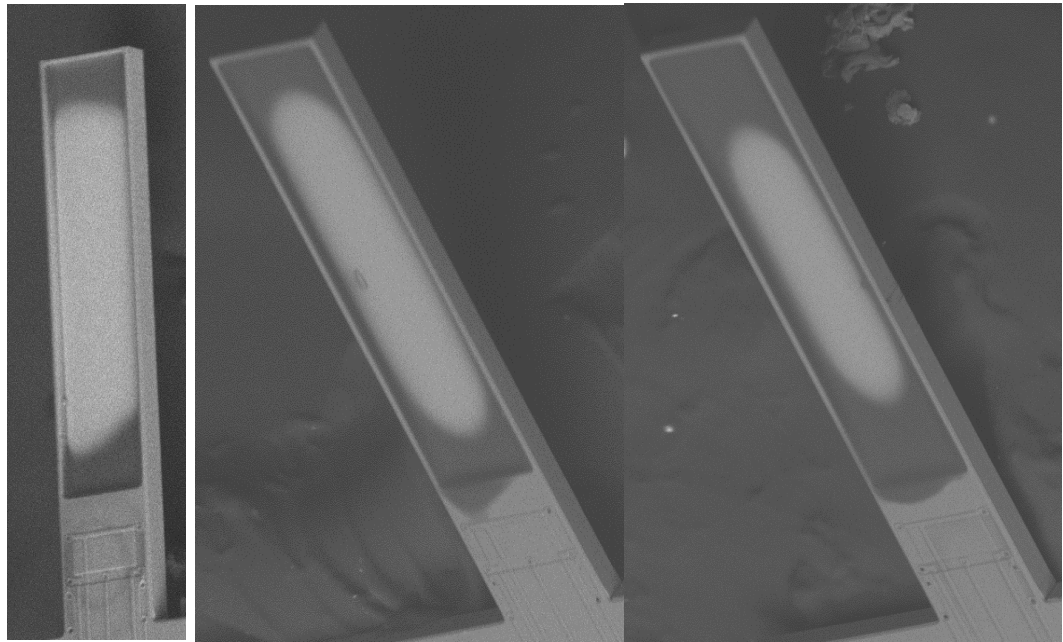


Figure 13 – SEM images of rectangular cantilevers featuring integrated recess structures. The cantilevers have been filled by inkjet printing to varying degrees with PVAc sorbent dissolved in DMSO as a solvent.

The basic fabrication process for the cantilever-based microstructures is highlighted in the previous chapter, however, integration of the recess structures onto the cantilever tips requires additional processing (Figure 14). Using reactive ion etching, an approximately 5- μm deep recess was etched into the head area of the silicon cantilevers, the latter having a nominal thickness of 9-12 μm (Figure 12). This recess slightly reduces the Q-factor of the in-plane mode as the resonator mass and thus the kinetic energy is decreased while keeping

surface losses to the surrounding fluid approximately the same. Prior to mounting the chip containing eight recessed resonators into a dual-in-line package, ink-jet printing (Microfab JetLab II) was used to fill the recess of select resonators with a sorbent polymer layer. Each resonator was coated individually with only one type of sorbent polymer – in the present work, either polyvinylacetate (PVAc) or polyisobutylene (PIB) – which serves as the chemically sensitive film. Various parameters such as solvent to polymer mass ratio, jet nozzle orifice diameter, and the jet nozzle's piezoelectric voltage levels and timing influence the accuracy and quality of the deposited films. Bursts of drops were deposited at various locations in the recess, allowed to evaporate, and followed by another burst until the recess was completely filled.

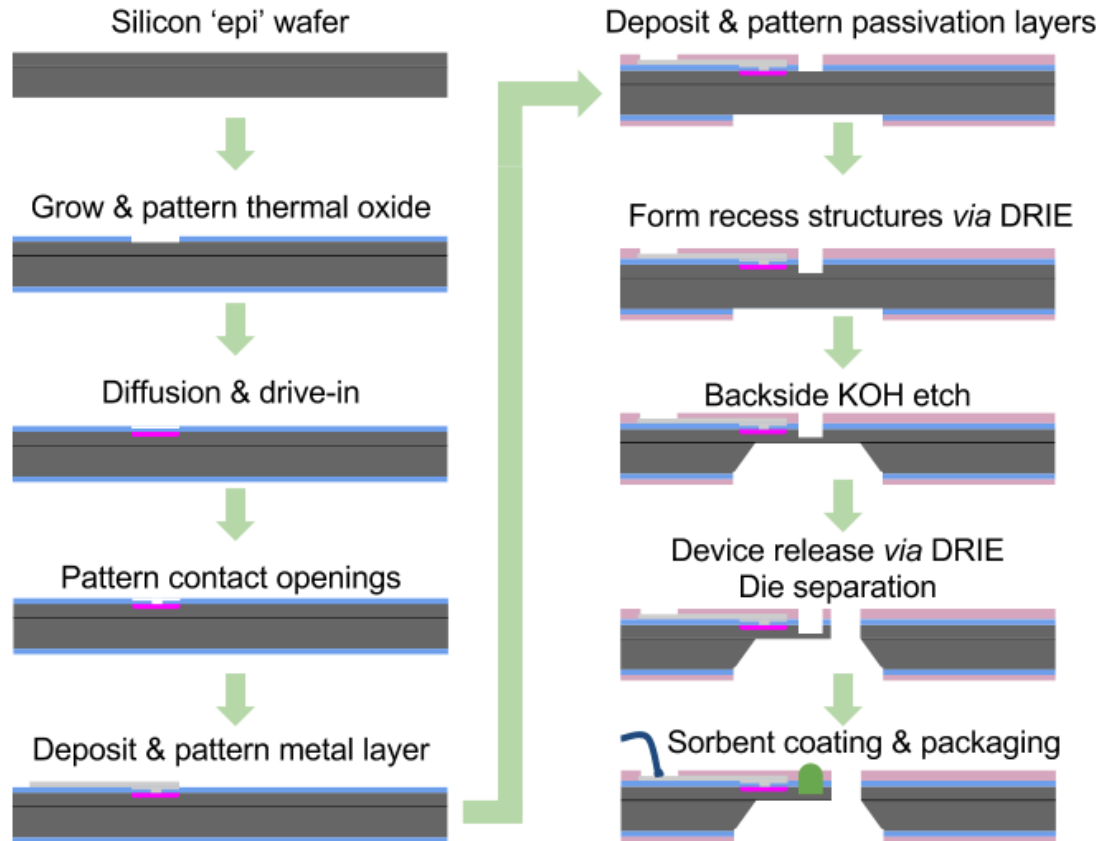


Figure 14 - Process flow diagram for hammerhead cantilevers with integrated recess structures.

To counter the high boiling point of the solvents and allow for more frequent bursts, the JetLab stage was heated. In this way the recesses could be completely filled with polymer (Figure 12) without covering any of the support beam. Moreover, the recess structure reduces undesirable solvent splattering – due to droplets impacting the substrate surface with high velocity – and nicely confines the deposited polymer within the defined region. Examination of the images in Figure 12, in addition to analysis of the resonance frequency before and after coating, indicate that the recess structure is filled with approximately 3- μg of PVAc.

It is evident from Figures 12-13 that the integrated recess structure functions well in containing the deposited polymer into a smooth, uniform, and localized film near the beam tip. In addition to mitigating the coffee ring effect and improving the uniformity of the sorbent layer, the sorbent-filled recess structure enhances overall device sensitivity by effectively replacing silicon with sorbent layer “active mass” that is chemically sensitive. Thus, a hammerhead sensor with integrated recess is inherently more sensitive, for a given cantilever and polymer thickness, than a non-recessed device.

Finite Element Analysis

The effect of the integrated recess structure on the device performance was initially modeled using finite element analysis (COMSOL Multiphysics). Simulation indicated that the introduction of a 5- μm integrated recess structure into an uncoated 9- μm thick hammerhead device resulted in an expected fundamental in-plane resonance frequency of 489 kHz for the hammerhead device (Figure 15).

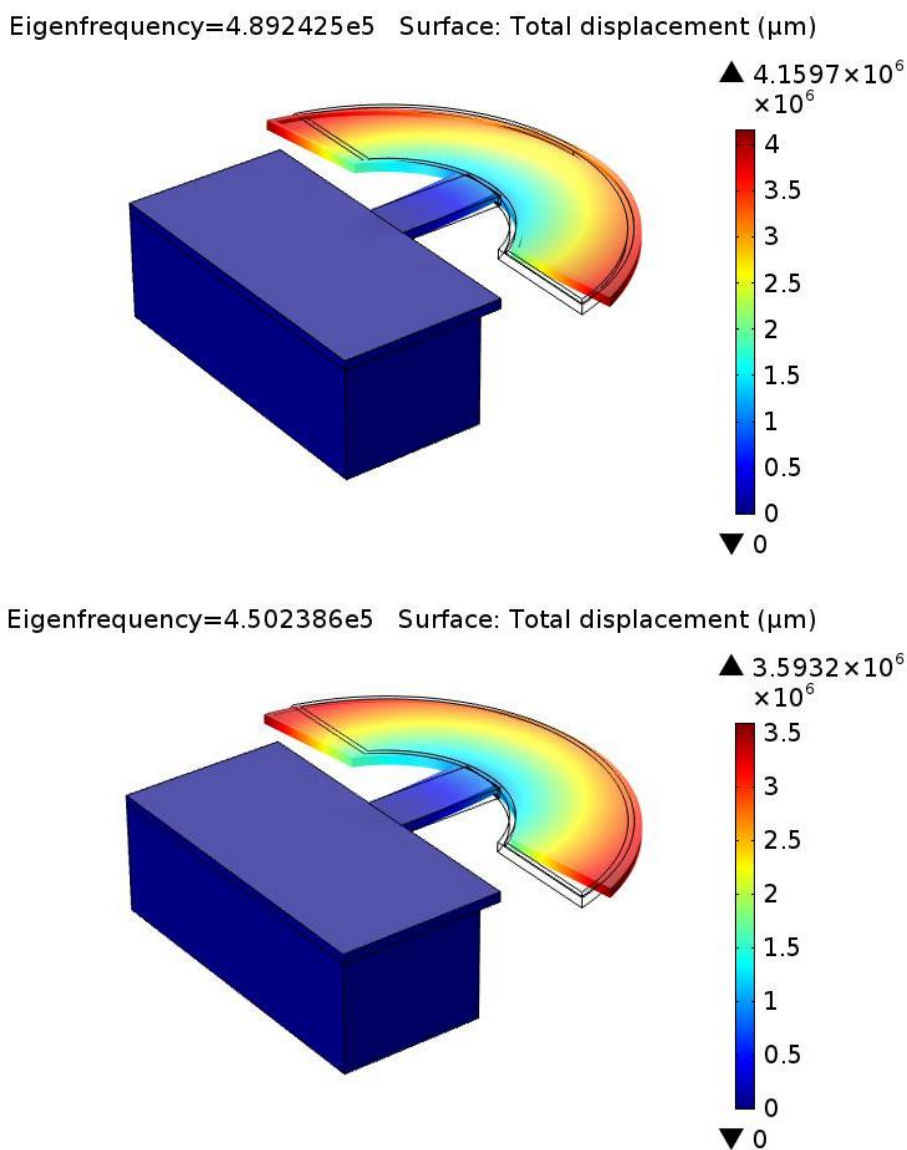


Figure 15 – FEA simulation showing before (top) and after (bottom) coating resonance frequencies.

Simulation further showed that the localized deposition of 5- μm of PIB into the recess structure resulted in a resonant frequency drop to 450 kHz due to the added mass of the sorbent polymer layer. The simulations were found to be in close agreement with experimental data: the recessed 9- μm hammerhead structure exhibited a measured in-plane resonance frequency of approximately 483 kHz prior to coating. Localized deposition of

5- μm of PIB via inkjet printing lowered the resonance frequency to 445 kHz. In case of the device coated with 7- μm PVAc, the simulation yielded an in-plane resonance frequency of 420 kHz, while the measured frequency was 410 kHz (see Figure 15).

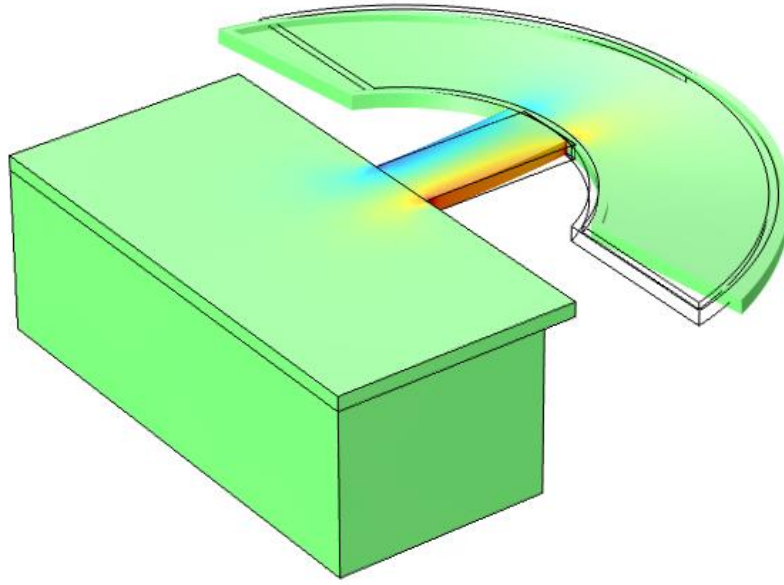


Figure 16 - Finite element modal analysis of 9- μm thick hammerhead resonator with 5- μm recess. The figure shows the stress in x-direction at the fundamental in-plane mode ($f = 489$ kHz); blue represents regions under compressive stress, red regions under tensile stress, while green indicates “stress-free” regions.

The finite element simulations also confirm that the recess aids in confining the polymer to areas away from the strained region of the microstructure (see stress distribution in Figure 16). As can be seen from the figure, almost no strain occurs in the head region where the polymer is deposited. Ultimately, this localization of polymer away from high-strain regions leads to an enhanced LoD for a given chemical sensor due to reduced Q-factor degradation. Finally, the sensitivity of the device to changes in the polymer density (i.e., the change in frequency per change in polymer density [84]) was explored: a 9- μm

thick hammerhead without recess coated with a uniform 5- μm PIB film exhibits a simulated sensitivity of 36 Hz/(kg/m³), while the 9- μm hammerhead with a 5- μm recess filled completely with PIB shows a sensitivity of 46 Hz/(kg/m³). Even though not all of the available surface area on the device is coated with polymer, the fact that previously inactive silicon is locally replaced by polymer capable of analyte uptake improves the so-called gravimetric sensitivity of the recessed device. At the same time, as discussed previously, the post-coating Q-factor in air is improved by the localized polymer deposition and, both the sensitivity and Q-factor improvements lead to better limits of detection in a chemical sensing application.

Resonance Frequency and Quality Factor

The transfer characteristics of uncoated recessed hammerhead devices were compared to those of recessed devices with ink-jet printed coatings, as illustrated in Figure 17, and to those of non-recessed devices with spray-coated sorbent layers. Previous work has shown that uniform deposition of a 7- μm sorbent film over an entire resonator structure (including the highly strained regions near the support) can lead to Q-factor degradation of one order of magnitude due to damping induced by periodically deforming the polymer [85]. This reduction in Q-factor is highly undesirable, as Q-factor is directly correlated with sensing resolution (i.e., LoD). Through application of the integrated recess structure with a localized polymer deposition, the Q-factor degradation of the coated devices was significantly reduced, leading to an enhanced limit of detection.

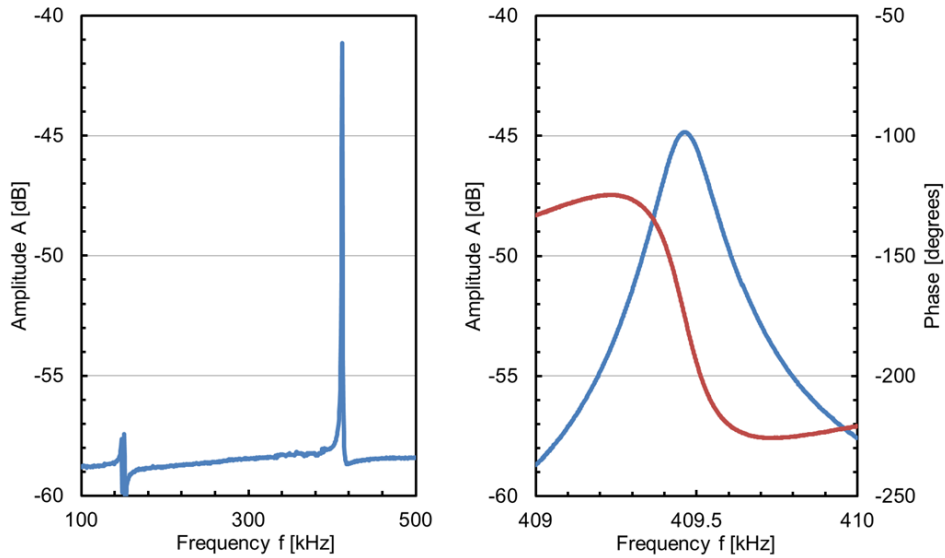


Figure 17 - Piezoresistive output signal as a function of excitation frequency of recessed hammerhead device, coated with $\sim 7\ \mu\text{m}$ PVAc via ink-jet printing: (left) frequency range from 100-500 kHz showing two flexural modes with the desired in-plane mode at 410 kHz having the strongest signal; (right) close-up of amplitude and phase transfer characteristic of in-plane mode with $Q = 1910$.

For example, a localized $5\text{-}\mu\text{m}$ PIB film deposited into the recess structure *via* inkjet printing resulted in a Q-factor decrease of $\sim 40\%$, and a $7\text{-}\mu\text{m}$ film of PVAc deposited in the same way resulted in a Q-factor drop of only $\sim 1.5\%$. These data confirm that confining polymer deposition away from the high-strain areas of the support beam through the use of the integrated recess structure and inkjet printing enables relatively thick sorbent layers to be applied to a device while still maintaining a high Q-factor in air. This improvement in post-coating Q-factor (i.e., reduction in Q-factor degradation due to sorbent coating), while simultaneously allowing the application of relatively thick sorbent films which can accumulate more captured analyte mass, leads to enhanced frequency stability and sensor sensitivity when compared to uniformly coated devices. Ultimately, these factors combine

to improve the effective LoD of the sensor, leading to enhanced detection resolution in chemical sensing applications.

Chemical Measurements

Following the open-loop characterization, the sorbent-coated sensors were evaluated as chemical sensors. To this end, coated resonators were embedded into an amplifying feedback loop and exposed alternately to pure nitrogen carrier gas and defined concentrations of gas-phase volatile organic compounds (VOCs) in a custom gas set-up. As an example, Figure 18 shows the frequency response of a PIB-coated resonator to different concentrations of toluene. The data were collected at a constant temperature of 19 °C and a flow rate of 80 ml/min through the measurement chamber. Between successive exposures to the analyte-loaded gas stream, the gas flow over the resonator is changed to pure nitrogen carrier gas. A four-way valve enables fast switching and allows the investigation of signal transients as well. From the baseline frequency data (see final 500 seconds in Figure 18), a short-term frequency stability of 2×10^{-8} was extracted using the Allan variance method.

An analysis of the measured frequency data reveals that the sensors exhibit a linear response with respect to toluene concentration (Figure 19). Using the observed chemical sensitivity of 0.15 Hz/ppm for toluene and the Allan variance of 2×10^{-8} , limits of detection below 1 ppm can be expected for these devices. It is suggested for future work that these LOD values be confirmed by measurements at ppm-level analyte concentrations. This could be accomplished, for example, with the use of a permeation tube system capable of generating low ppm-level concentrations. Another important observation from the gas

measurement data is that the sensor's response is fully reversible with time constants well below 1 minute even for relatively thick polymer films. A reversible response is advantageous, as it enables the sensor to be refreshed between measurements. In this way, a sensor can be operate without maintenance or replacement for long periods of time, enabling the sensor to be deployed for extended periods of time or in remote locations. Additionally, the response of the sensor is in real-time, with tens of seconds being all that is required for a measurement to stabilize upon exposure to analyte concentration.

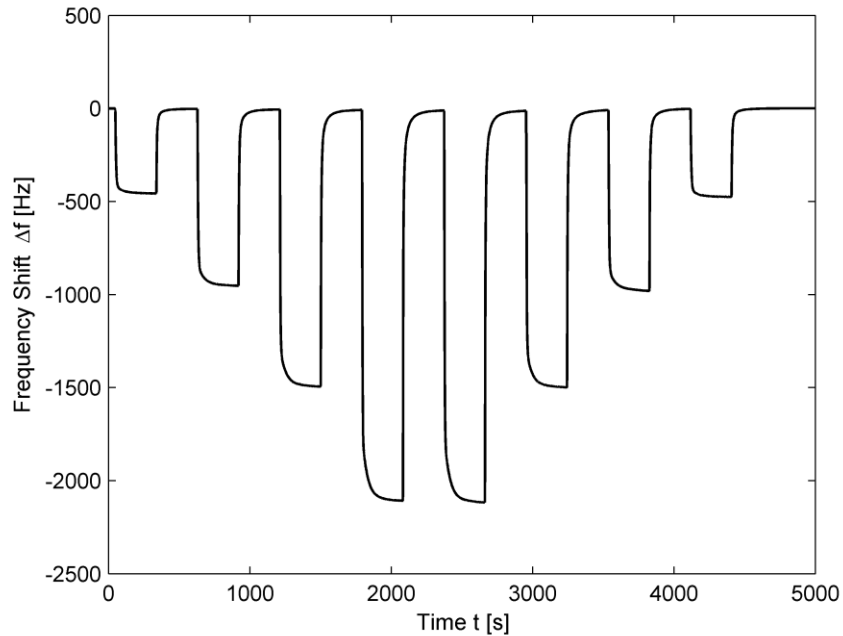


Figure 18 - Experimentally observed frequency shift of PIB-coated recessed resonator as a function of time; the microsensor is subsequently exposed to different toluene concentrations (3400-6800-10200-13600-13600-10200-6800-3400 ppm). Between successive toluene exposures, the chamber is flushed with nitrogen as carrier gas. A linear drift of 0.3 Hz/min has been subtracted from the data.

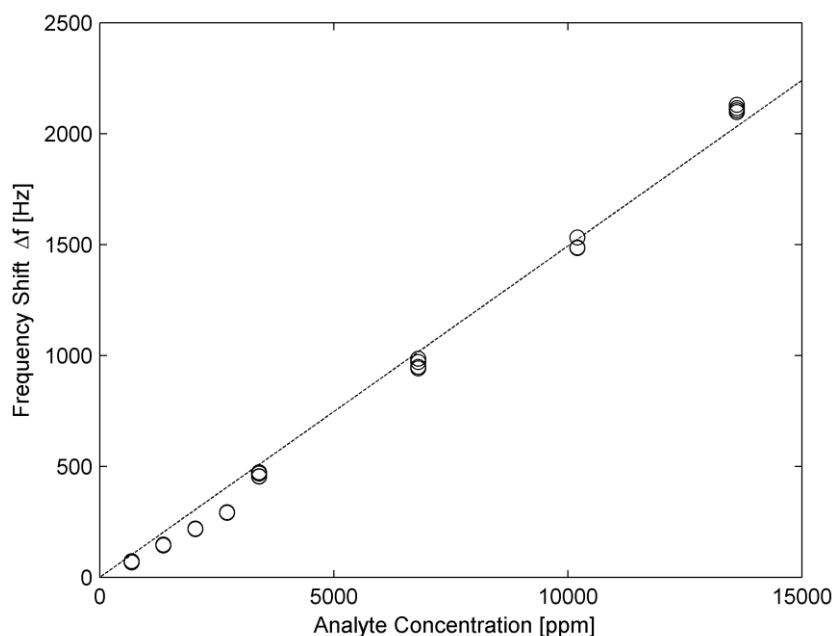


Figure 19 - Experimentally observed frequency shift for PIB-coated recessed resonator as a function of the toluene concentration.

Shadow Masking

While the integrated recess structure has been shown to improve sorbent film quality by mitigating coffee ring effects and effectively constraining the sorbent film near the beam tip, inkjet printing can suffer from a host of additional difficulties such as nozzle-clogging, misalignment, and the undesirable formation of secondary droplets (Figure 9). To minimize clogging of the nozzle during printing, low-viscosity mixtures are often necessary but this reduction in viscosity comes at the expense of increased printing time required to deposit a given film thickness on the substrate. Since viscosity is typically lowered by dissolving less polymer into a given amount of solvent, the result is that less polymer is deposited per printed droplet, requiring patterns to be repeated multiple times to achieve a given

thickness in the deposited film. Furthermore, inkjet printing is an inherently serial process and presents significant difficulties at scale.

As an alternative to inkjet printing, a spray-coating technique was investigated for accomplishing localized sorbent deposition in a more cost-effective, scalable manner. This technique employs the use of a vapor atomizer in conjunction with laser-cut shadow masks (Figure 20) to achieve localized polymer deposition similar to that just described. As with inkjet printing, the sorbent polymer is dissolved in a suitable solvent and the mixture is sprayed out of the nozzle of the atomizer (Figure 21). The shadow mask is placed against the top surface of the die and aligned to the underlying devices. Once aligned, the mask is locked in place with a custom-built fixture (Figures 20-21) and subsequently placed in the vapor stream from the atomizer until the desired film thickness has been achieved. Sorbent film deposition rate can be controlled by the viscosity of the sorbent/solvent solution, the adjustable aperture of and nitrogen flow through the atomizer, and distance between the aperture and the target. The shadow masks were designed with CAD software (Figure 20) and laser-cut with the Resonetics IR Laser located in the IEN facilities.

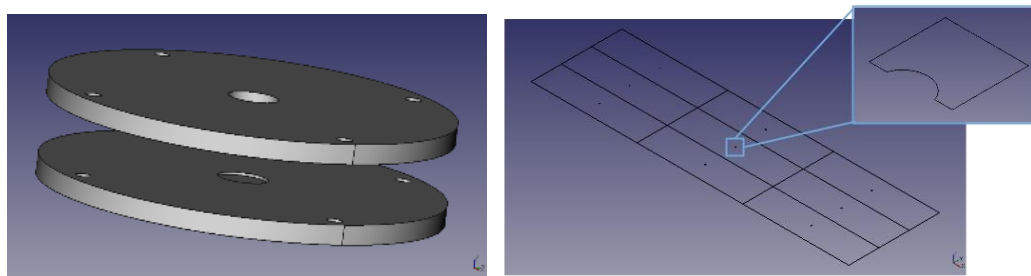


Figure 20 – Design and rendering of (left) fixture for securing shadow masks in place during spray coating and (right) array of individual shadow masks of varying shapes and sizes. The inset on the right shows a magnified image of a single shadow mask designed for use with the integrated chemical sensors.

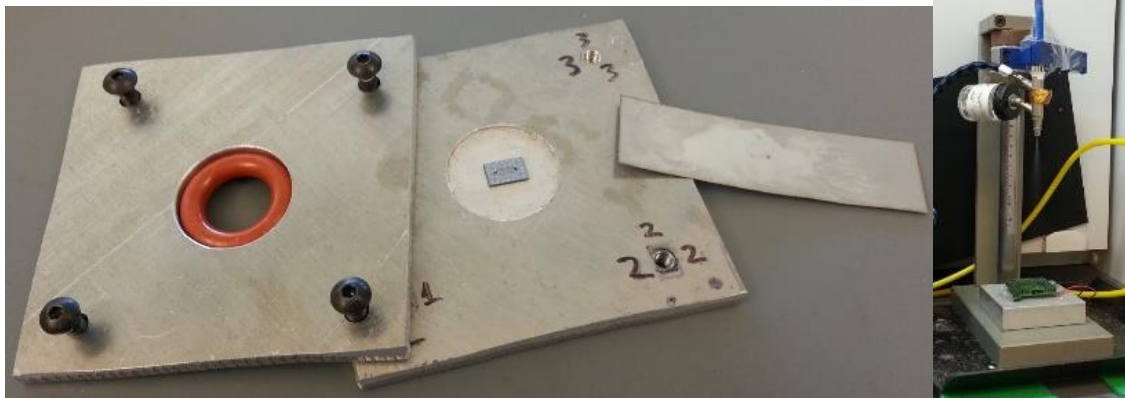


Figure 21 – Photographs of (left) spray-coating fixture machined from steel, with accompanying shadow mask and die to be spray coated, and (right) vapor atomizer used for spray coating.

As demonstrated in Figure 22 the shadow masking technique proved very effective at depositing a sorbent layer onto the tip of the chemical sensors and prevents polymer deposition in masked areas near the beam anchor.

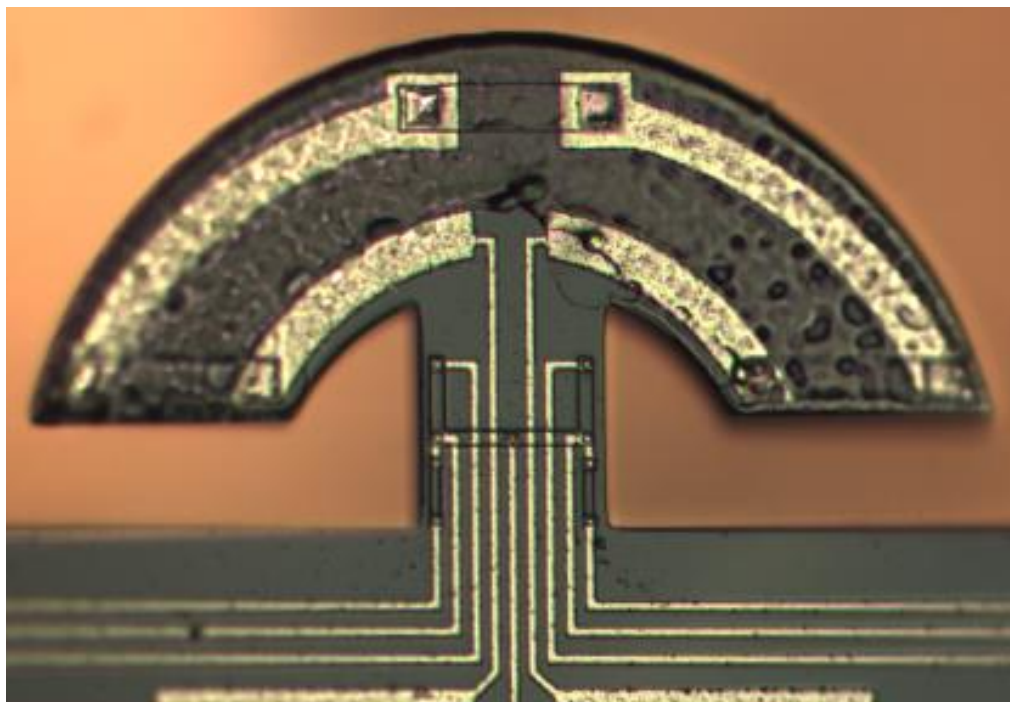


Figure 22 – Photograph of resonator coated with PECH via shadow masking.

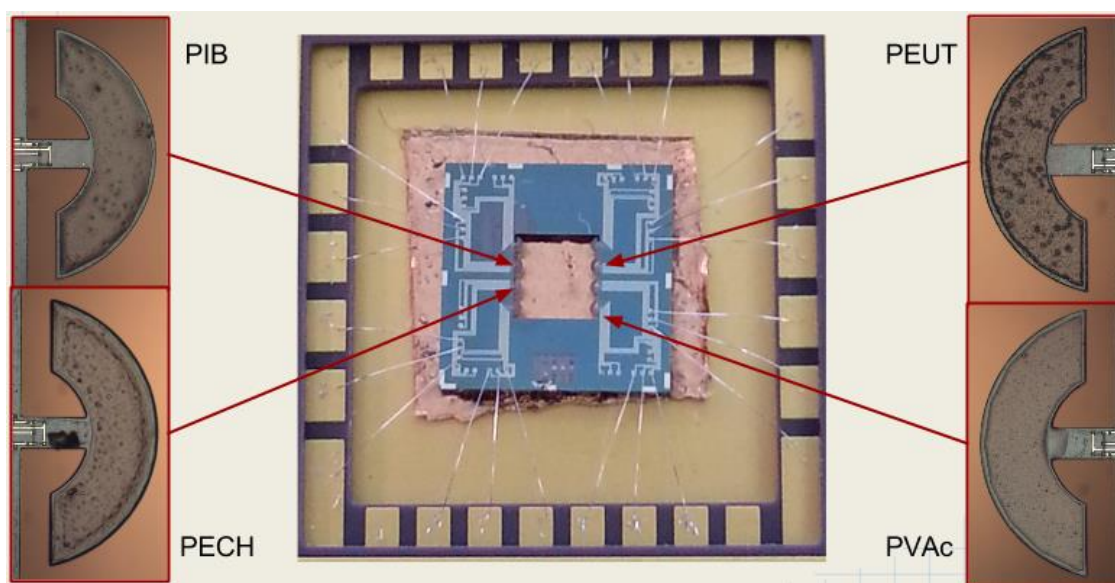


Figure 23 – Photographs of array (center) of resonators with integrated recesses, where each device (optical microscope images, labeled around perimeter of figure) is coated with a different type of sorbent. The coating of the devices in the array employed both shadow masking and inkjet printing.

The result is a quickly deposited, relatively uniform film that is constrained away from high-strain regions of the device. Film quality is high, even without the use of the integrated recess structure as spray coating is not as susceptible to the coffee ring effect. The shadow masking technique can, however, be combined with the integrated recess structure to offer increased sensitivity due to silicon replacement with active sorbent material (Figures 12-13). Shadow masking has been demonstrated previously in the literature as an effective method for coating individual devices [55], but has not been combined with an integrated recess structure as a way of improving film uniformity and enhancing sensitivity. Furthermore, the shadow masking approach confers several additional advantages when compared with inkjet printing. One such advantage is flexibility in solvent choice. Since the atomizer is of metallic and glass construction, nearly any solvent used to dissolve polymer-based sorbents now becomes available for use. This not only lowers cost by

enabling the use of less expensive solvents, but also expands new possibilities for the deposition of previously unavailable sorbents (due to solvent incompatibility with the ink-jet printer). In short, this improvement is not a difference of degree but of kind. For example, spray-coating in this way enables devices to be coated with PECH or Tenax TA, which cannot be readily inkjet-printed due to the aggressive solvents (e.g. chloroform, dichloromethane) necessary for polymer dissolution. Furthermore, this method does not require the additional fabrication complexity necessary to form the integrated recess structure (although it can be combined with the recess structure for additional increased device sensitivity), lowering total cost. Finally, the shadow masking technique can be easily scaled to coat multiple devices at the wafer level, in parallel. When these considerations are taken into account, shadow masking offers significant potential, especially for low-cost applications at scale. With the use of high concentration solutions and multiple coating steps, film thicknesses in excess of 200 μm on planar surfaces can be achieved in less than an hour. While films this thick are not typically suitable for resonant cantilever-based sensors, the ability to rapidly coat with very thick uniform films can be desirable for other applications such as the coating of chemical pre-concentrators (Chapter 8).

CH 3 – TRANSIENT SIGNAL OPERATION

While improvements to the sorbent layer through the use of inkjet printing and shadow masking with the integrated recess structure have been shown to improve an individual sensor's performance by minimizing Q-factor degradation and increasing overall sensitivity by replacing non-sorbing silicon near the beam tip with 'active' sorbent mass, these advancements do not directly improve the overall system's ability to distinguish target compounds in the presence of interfering compounds. One approach to address this aspect of chemical sensing is to develop an array of sensors where each sensor is coated with a different class of sorbent [75]. This can be achieved through appropriate use of localized polymer deposition, as previously discussed and as demonstrated in the literature [89, 98]. In addition to considering arrayed devices, it has also been shown that analysis of signal transients from *individual* sensors can improve analyte discrimination [55, 75, 90].

Valve Generated Transients

As discussed previously, sorption of low-molecular-weight substances into polymeric sorbent materials is ubiquitous in chemical sensing of VOCs. As such, the sorption kinetics of analyte into the sorbent layer can either limit or enhance the sensor's overall performance. When polymers are used as coatings in microelectronics packaging [99], the designer tries to minimize gas permeability by using polymers that feature low diffusion

and partition coefficients for the gases of interest. On the other hand, when the polymer is used as the sensitive sorbent layer in a chemical sensor [83, 100], it should exhibit large partition coefficients to achieve high sensitivity and large diffusion coefficients for the analytes of interest to achieve a rapid response for a given measurement (i.e. sensor ‘speed’ metric). Additionally, it is shown that sensor selectivity can be improved simply through the use of transient-signal analysis of standard sorption curves. This enhancement to sensor selectivity is the result of different analytes diffusing into the sorbent polymer film at different rates, and remarkably does not require modification of the sensor itself but rather is implemented at the system level.

To perform the polymer sorption experiments, microresonators were spray-coated with PECH and PIB dissolved in chloroform and toluene, respectively. To assess the influence of the polymer thickness on the sorption characteristics, multiple layers were coated in sequence and the additional film thickness was measured on a test sample with a contact profilometer. In this way, PECH films with thicknesses up to 6 μm were evaluated. In the case of PIB films, only a single 1.5 μm thick layer was studied.

The particular resonator used in this study is a hammerhead-style cantilever (see Figure 2), which comprises a semicircular disk (the hammerhead) with an outer radius of 200 μm attached to a cantilever beam. The excitation and detection elements are located close to the clamped edge of the resonator. The tested resonators have a silicon thickness of approximately 19 μm and are coated with a 1.3 μm thick stack of dielectric films used for passivation and metal interconnect routing. Without a polymer coating, the fundamental in-plane resonance frequency of these resonators was experimentally determined to be

approximately 380 kHz. These resonators – which do not feature integrated recess structures — exhibit excellent characteristics in air with Q-factors up to 4000 [74].

Measurement Setup

Initially, transient signal analysis was investigated using a pneumatically controlled 4-way valve to rapidly switch between an analyte-loaded gas stream and a reference carrier gas stream [90]. The gas flow was kept constant at 80 ml/min, ensuring that the volume of the small measurement chamber (≈ 0.2 ml) is exchanged several times per second. Figure 24 shows an example measurement using a PECH-coated microresonator exposed to ethanol. The sensor is subjected to four different ethanol concentrations, with each 10-minute exposure subsequently followed by a 10-minute purge with nitrogen carrier gas. Upon analyte exposure, ethanol is readily absorbed into the PECH film and the resonance frequency of the resonator decreases proportionally to the mass uptake. During the measurement, the resonator is embedded in an amplifying feedback loop and the resonance frequency is recorded every second using a frequency counter. Subjected to 22500 ppm of ethanol, the resonance frequency decreases by 343 Hz at a base frequency of 350 kHz, which corresponds to a mass uptake of approximately 4.3 ng.

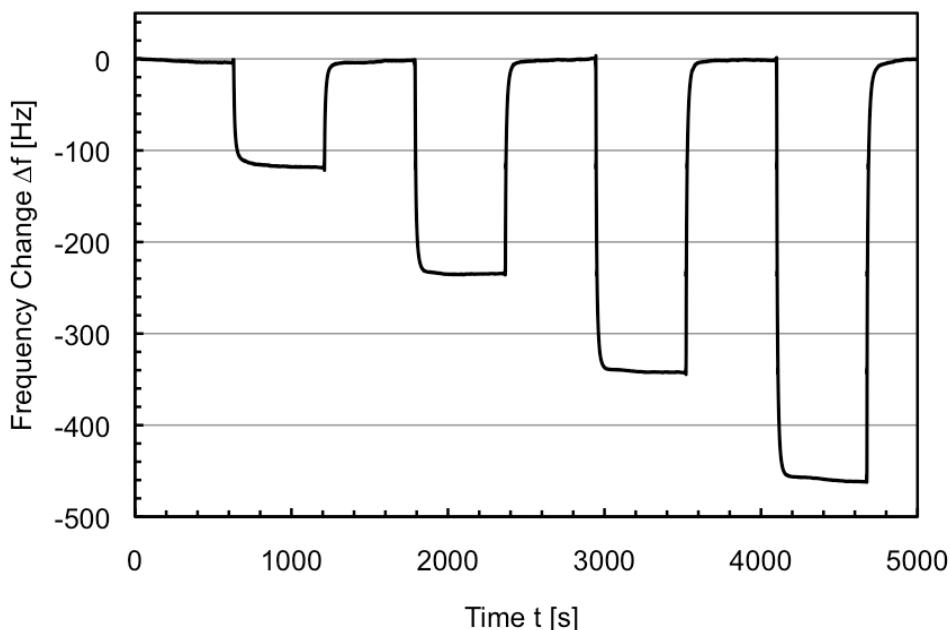


Figure 24 - Frequency change Δf of a PECH-coated microresonator ($h = 4.6 \mu\text{m}$) to four 10-minute exposures to ethanol with concentrations of 7500, 15000, 22500 and 30000 ppm. In-between each analyte exposure, the chip is exposed to carrier gas (N_2) in order to desorb the analyte from the PECH.

Of particular interest to this work are the signal transients after the 4-way valve is switched. Figure 25 compares the signal transients when exposing the PECH-coated microresonator to a simple alcohol series consisting of methanol, ethanol and isopropanol. The measured frequency change is thereby normalized by the maximum frequency change, Δf_{max} , at the end of the given 10-minute exposure step. Different time constants associated with the different diffusion coefficients of the analytes in PECH are clearly visible; as expected, the analyte diffusion speed is reduced with increasing size of the alcohol under test (methanol, $\text{CH}_3\text{OH} \rightarrow$ ethanol, $\text{C}_2\text{H}_5\text{OH} \rightarrow$ isopropanol, $(\text{CH}_3)_2\text{CHOH}$).

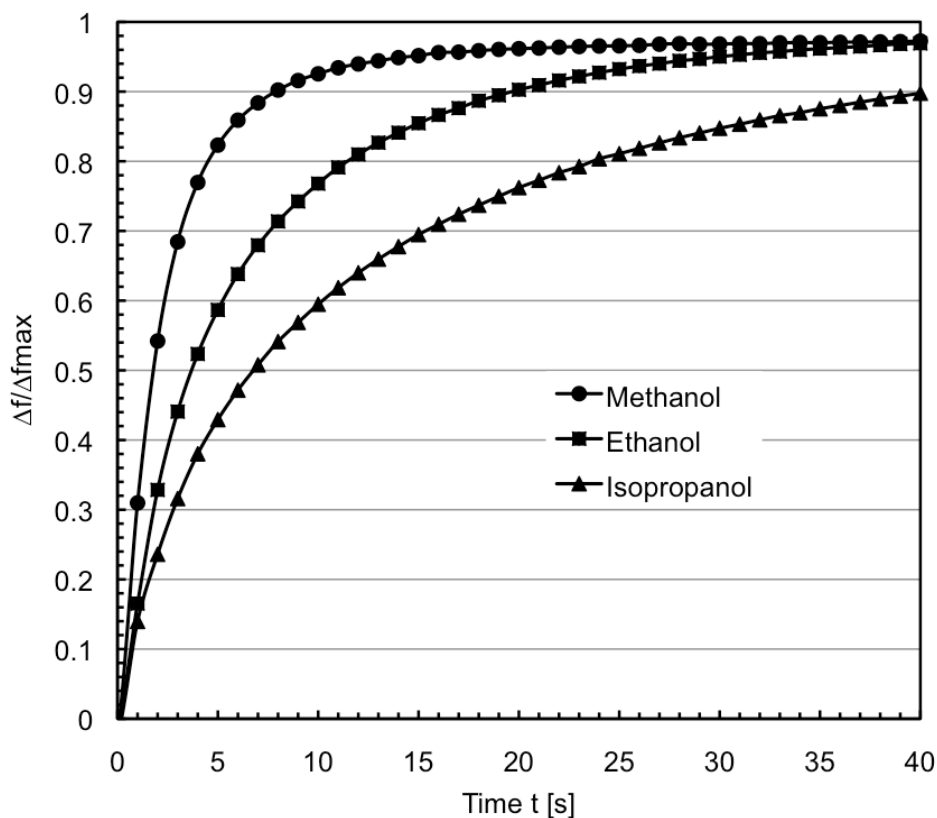


Figure 25 - Relative frequency loss $\Delta f/\Delta f_{max}$ of microresonator coated with a 4.6 μm PECH film as a function of time upon exposure to methanol (50000 ppm), ethanol (22500 ppm) and isopropanol (17000 ppm).

Since the diffusion time constants are characteristic for a particular polymer-analyte combination, the obtained transient signal can be used for improved analyte discrimination (i.e. selectivity). As such, it carries additional (and often complementary) information to the steady-state sensor response, which is dependent on the partition coefficient, K .

Sorbent Polymer Permeation Theory

Using the theory for permeation into a one-sided “terminated” film [101, 102], the signal transients can be analyzed. Assuming ideal 1-dimensional Fickian diffusion into the thin polymer film, the relative weight gain or loss of the film is given by

$$\frac{M_t}{M_\infty} = 1 - 8 \sum_{n=0}^{\infty} \frac{1}{[(2n+1) \cdot \pi]^2} e^{\left(\frac{-t}{4\tau}\right) \cdot [(2n+1) \cdot \pi]^2}$$

Equation 5 – Relative weight gain/loss of 1-dimensional sorbent film, assuming ideal Fickian diffusion.

where M_t is the weight gain/loss at time, t , M_∞ is the equilibrium weight gain/loss and τ is the characteristic diffusion time constant

$$\tau = \frac{h^2}{D}$$

Equation 6 – Characteristic diffusion time constant for ideal Fickian diffusion into thin sorbent film.

which depends on the polymer thickness, h , and the diffusion coefficient, D . Moreover, the *initial* relative weight gain/loss is described by

$$\frac{M_t}{M_\infty} = \frac{2}{h} \sqrt{\frac{D \cdot t}{\pi}}.$$

Equation 7 – Approximation for initial relative weight gain/loss for ideal Fickian diffusion into thin sorbent film.

In the case of ideal Fickian diffusion, Equation 7 is valid approximately for $M_t/M_\infty \leq 0.5$. Thus, by plotting M_t/M_∞ as a function of \sqrt{t} , the diffusion coefficient D can be extracted from the slope in the initial linear region.

Since it is the case that for uniformly-coated micro-resonators the measured relative frequency change is directly proportional to the relative (effective) mass change

$$\frac{\Delta f}{f} = -\frac{1}{2} \frac{\Delta m}{m}$$

Equation 8 – Measured relative frequency change and relative mass change.

we can also use Equations 5-7 to analyze the ratio of frequency change Δf_t at time, t , to the equilibrium frequency change, Δf_{max} (see e.g. Figure 26).

In addition, Henry's law applies to the interface between polymer and surrounding medium and governs the partitioning of the permeate across the interface

$$K = \frac{c_{polymer}}{c_{gas}}$$

Equation 9 – Henry's law, governing partitioning of permeate across diffusion interface.

with the dimensionless partition coefficient, K , and the permeate concentrations at the polymer surface and in the surrounding gas, $c_{polymer}$ and c_{gas} , respectively. If the gravimetric

sensitivity, G , of the resonator [83] – i.e. the ratio of the measured frequency change to the density change in the polymer – is known (e.g. through FEM simulations), the partition coefficient, K , can be extracted from the measured equilibrium frequency change, Δf_{\max} for a given analyte concentration step.

Once K and D have been determined, the permeability coefficient, P , for the permeate in the particular polymer is simply given by

$$P = K \cdot D$$

Equation 10 – Permeability coefficient for sorbent polymer.

Data Analysis

In this work, the diffusion coefficients of alcohols and aromatic hydrocarbons in PECH and PIB have been extracted in two ways: (i) by fitting the transient signal response for $0 \leq \Delta f_t / \Delta f_{\max} \leq 0.8$ using Equation 5, thus obtaining τ and subsequently D using Equation 6 and (ii) by plotting $\Delta f_t / \Delta f_{\max}$ as a function of \sqrt{t} , evaluating the slope of the resulting linear relationship for $0 \leq \Delta f_t / \Delta f_{\max} \leq 0.5$, and subsequently calculating D using Equation 7. An example of the latter approach for absorption of methanol, ethanol and isopropanol into a 5.9 μm PECH film is shown in Figure 26.

Figure 27 compares the fits according to Equations 5 & 7 for the case of sorption of isopropanol into a 5.9 μm layer of PECH. While Equation 5 describes the signal transient well for the first 50 seconds, significant deviations are found beyond this initial analyte

uptake, which indicate deviations from the case of ideal Fickian diffusion. Table 1 summarizes the diffusion coefficients for the alcohols obtained both ways in PECH films with different thicknesses. From the equilibrium frequency changes Δf_{\max} and the gravimetric sensitivities G (obtained by FEM), the partition coefficients, K , were also extracted.

In the plot in Figure 26, the frequency shifts for a similar measurement from a different PECH-coated sensor are plotted against the square root of time, revealing an initial linear region during each sorption curve. The slope of these linear regions can be used to extract the characteristic diffusion coefficient for each alcohol into PECH.

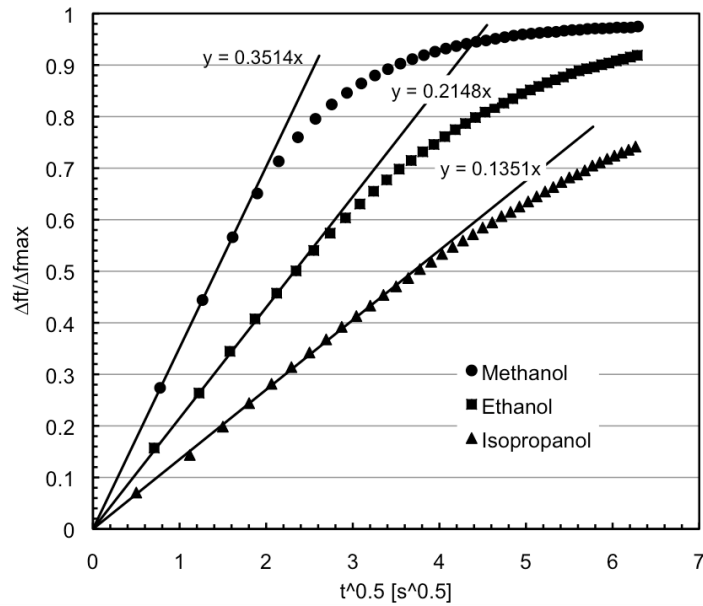


Figure 26 - Relative frequency loss $\Delta f/\Delta f_{\max}$ of microresonator coated with a 5.9 μm PECH film as a function of square root of time upon exposure to methanol (50000 ppm), ethanol (22500 ppm) and isopropanol (17000 ppm).

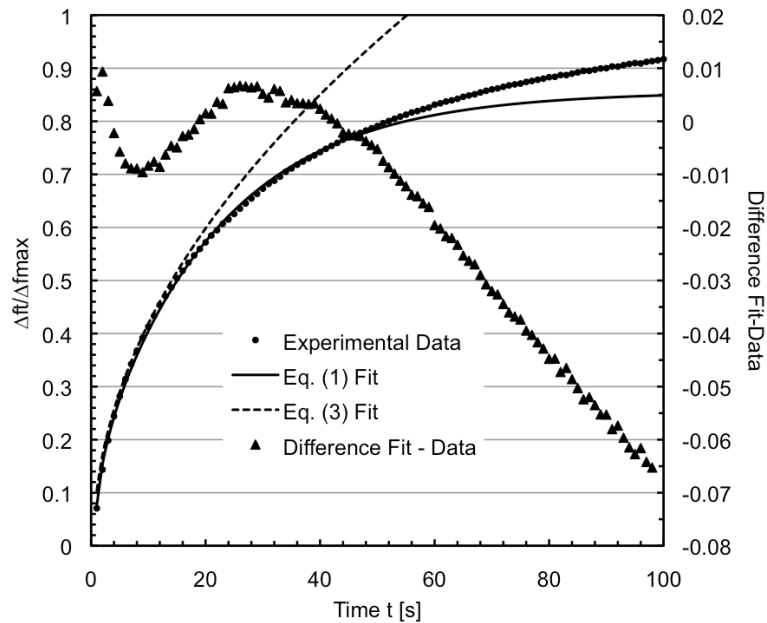


Figure 27 - Relative frequency loss $\Delta f/\Delta f_{\max}$ of resonator coated with a 5.9 μm PECH film as a function of time upon exposure to iso-propanol (17000 ppm); Circles: measurement data; Solid line: Fit using Equation 5 with $\tau = 53.1$ sec; Dashed line: Fit using Equation 7; Triangles: Difference fit using Equation 5 and data.

Table 1 - Diffusion coefficients D and partition coefficients K for alcohols in PECH and aromatic hydrocarbons in PIB.

	Analyte	h [μm]	D [cm^2/s] via Eq. (1)	D [cm^2/s] via Eq. (3)	K
PECH	Methanol 50000 ppm	2.3 ± 0.4	1.8×10^{-8}	—	—
		4.6 ± 0.6	3.9×10^{-8}	3.1×10^{-8}	369
		5.9 ± 0.7	3.9×10^{-8}	3.4×10^{-8}	442
	Ethanol 22500 ppm	2.3 ± 0.4	0.92×10^{-8}	0.85×10^{-8}	—
		4.6 ± 0.6	1.8×10^{-8}	1.3×10^{-8}	546
		5.9 ± 0.7	1.6×10^{-8}	1.3×10^{-8}	583
	Isopropanol 17000 ppm	2.3 ± 0.4	0.43×10^{-8}	0.36×10^{-8}	—
		4.6 ± 0.6	0.89×10^{-8}	0.67×10^{-8}	452
		5.9 ± 0.7	0.66×10^{-8}	0.50×10^{-8}	513
PIB	Benzene 5500 ppm	1.5	11.9×10^{-10}	9.0×10^{-10}	—
	Toluene 4400 ppm	1.5	10.4×10^{-10}	7.4×10^{-10}	—
	m-Xylene 2000 ppm	1.5	8.2×10^{-10}	6.0×10^{-10}	—

While the repeatability of the signal transients is generally excellent (four subsequent signal transients are shown in Figure 28), the variation in the obtained diffusion and partition coefficients (see Table 1) is still considerable and possible reasons for the observed data variability are discussed briefly.

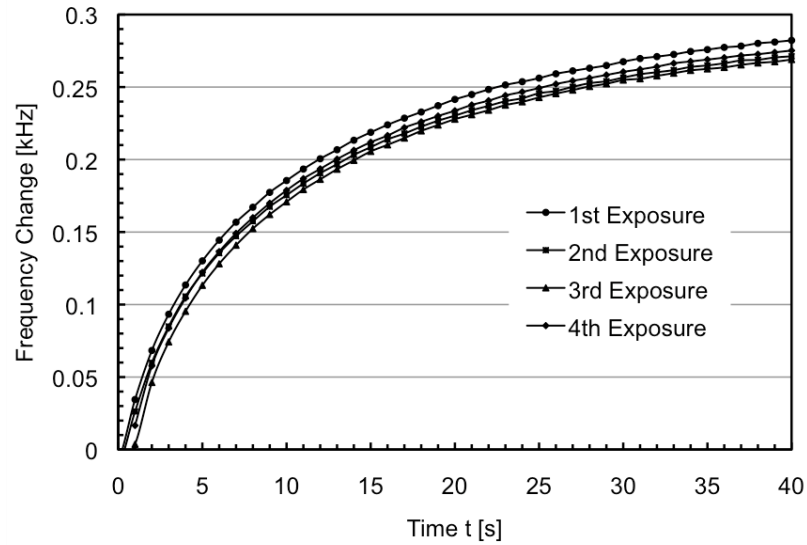


Figure 28 - Sorption transients of four subsequent exposures of PECH-coated microresonator ($h = 4.6 \mu\text{m}$) to 15000 ppm ethanol.

The comparison of measurement and model in Figure 27 highlights that the permeate diffusion into the polymer does not exhibit ideal Fickian behavior, contrary to the assumption stated previously. It appears that with increasing permeate concentration in the sorbent film more permeate can diffuse into the layer (this explains the generally higher D values obtained using Equation 5 compared to Equation 7). The origin for this non-ideal behavior can either be a concentration dependent diffusion coefficient or the fact that the high permeate concentration in the film leads to relaxation in the polymer (because of increased polymer chain mobility) [103], which allows more permeate to be absorbed in

the film. To investigate this in more detail, it is suggested for future work that additional experiments with lower permeate concentrations be performed.

Considering the data analysis by itself, the primary challenges are the proper measurement of the polymer thickness, h , and the number of data points recorded during the signal transient. At the time of acquiring this data, the data acquisition was limited to one frequency measurement per second, which was not sufficient for the fastest permeates, e.g. methanol in case of a PECH film. The measurement capabilities of the test setup have since been expanded to enable frequency measurements approximately every 50 msec, enhancing time resolution by a factor of 20. It is suggested for future work that these experiments be revisited using the higher resolution measurement setup. Even more important, however, is an accurate film thickness measurement, as h affects the diffusion coefficient values in a quadratic fashion. Film thickness is currently measured using a stylus-type surface profiler on separately coated control samples. It is believed that the variation of D with the film thickness is largely due to uncertainties in the polymer thickness. An optical technique to determine film thickness on the actual device used for testing is suggested for future work. It is also suggested that the integrated recess structure discussed in Chapter 2 be utilized to constrain the film to a readily measurable known volume. For example, the integrated recess structure has a well-known fixed volume determined by precision processing and easily verified by independent measurement prior to coating. Once coated, it is trivial to see when the volume of the recess structure has been completely filled, allowing one to know precisely the volume of sorbent polymer occupying the space.

Despite these limitations at the time of the reported experiments, the obtained diffusion

coefficients for the alcohols in PECH compare well with literature values obtained using capacitive microsensors [55]. Compared to [55], the present work directly assesses the mass uptake and the sensor response is independent of the location of permeate within the polymer film. The results presented here have been demonstrated for fast permeates – common for chemically sensitive layers – however, the method is also applicable to slow permeates, and could also be used to investigate polymers used in packaging applications. Finally, in a chemical sensing application, a sensor would anyway require an initial calibration step during which the characteristic time constants for different analytes would be recorded. In this case, accurate measurement of h would not be necessary, as the goal is not to precisely determine D , but to distinguish between different analytes.

Thermally Generated Transients

While the results from valve-generated transient analysis demonstrate the potential to improve sensor performance in the face of interfering compounds, they require, however, additional power consumption and system complexity in the form of mechanical valves, MFCs, and pressurized gas cylinders. Such complexity presents significant size and cost constraints on the design of a truly mobile field-deployable platform. To address these issues of mobility, a novel resonant cantilever platform with integrated temperature modulation was developed. The embedded heating elements enable rapid thermal cycling of individual resonant microstructures and, thus, allow for analysis of signal transients, which contain information about the real-time sorption kinetics of analytes into the sensing film on the resonator surface [55, 56]. By generating the signal transients through

temperature modulation with integrated heating units, this mode of operation can eliminate the need for an external microfluidic setup to switch between analyte and reference gas streams. Additionally, the rapid temperature modulation potentially enables intrinsic drift compensation without the need for a reference resonator – and corresponding support circuitry – and generates measurement data in real-time. Combining these two advantages – no need for an external flow system or a reference resonator – can dramatically reduce the complexity and cost of the total system, leading to increased portability in the field as part of low-power mobile platforms.

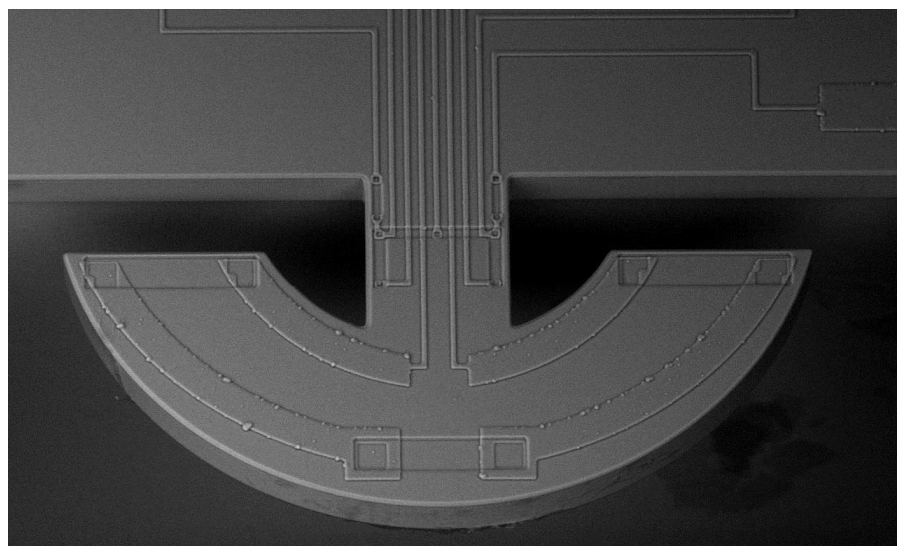


Figure 29 - SEM micrograph of resonant microstructure with semicircular head with 200 μm outer radius supported by a 75 μm wide and 100 μm long cantilever. Resistors for thermal excitation and piezoresistive detection of in-plane flexural vibrations are located at the cantilever base. Three heating resistors for rapid thermal modulation, connected in series, are clearly visible on the semicircular head.

Design & Simulation

Figure 29 shows an SEM micrograph of a fabricated micro-resonator consisting of a semicircular head region with inner and outer diameters of 100 μm and 200 μm , respectively, supported by a 75 μm wide and 100 μm long cantilever beam. Three integrated heating resistors, connected in series, are defined around the perimeter of the semicircular head region and were formed via high-temperature boron diffusion through an oxide mask. As the thermal excitation resistors as well as the piezoresistive sensing resistors connected in a Wheatstone bridge are formed in like manner, the integration of the embedded heating resistors does not require any additional process steps. These devices are formed from silicon-on-insulator (SOI) substrates, which represents a departure from the design of previously-discussed cantilevers (i.e. those released *via* KOH etching from epitaxial silicon substrates) and required a considerable amount of new process development. While this transition to a new process sequence introduces additional complexity into the fabrication of the heated cantilevers when compared to previous work, it also offers the ability to define high-aspect-ratio features onto the reverse-side of the die (e.g. *via* DRIE, with the SOI BOX layer serving as etch stop), making possible novel future designs. The fabrication process flow for these devices is discussed in detail in Chapter 6, in conjunction with the fabrication development for a micro thermal pre-concentration system that was designed to be integrated on-chip with these heated cantilevers and was made possible by use of the modified process flow arrangement.

The total series resistance of the embedded heating unit was designed to have a value of approximately 1 $\text{k}\Omega$, allowing for significant temperature elevation while requiring only modest applied heating current in the low milliamp range. The overall resonator structure

was further designed to allow for rapid and uniform heating of the head area with a minimal thermal time constant. Reduction of the thermal rise time of the heated cantilever head region is crucial, as the ideal transition from reference temperature to desorption temperature would appear as an ideal step function. In this way, the sorbed analyte experiences a rapid change in ambient conditions, similar to the scenario introduced by switching between a reference gas and analyte gas *via* mechanical valves.

Prior to fabrication, the device performance was simulated and the device geometry was optimized *via* Finite Element Analysis (FEA). For a 25 μm thick resonator, finite element simulations indicate a maximum temperature elevation of 71°C at 100 mW of applied heating power and a uniform temperature profile across the heated head area of the cantilever (Figure 30). This simulated result compares well with experiment: for an applied heating power of 100 mW, the observed temperature increase of the device was ~85°C in air. This result was obtained by placing the device in a temperature-controlled chamber while continuously monitoring the change in resistance of the three series-connected heating resistors as a function of the chamber temperature, and subsequently comparing these data to the change in resistance as a function of applied heating power due to self-heating of the embedded heaters.

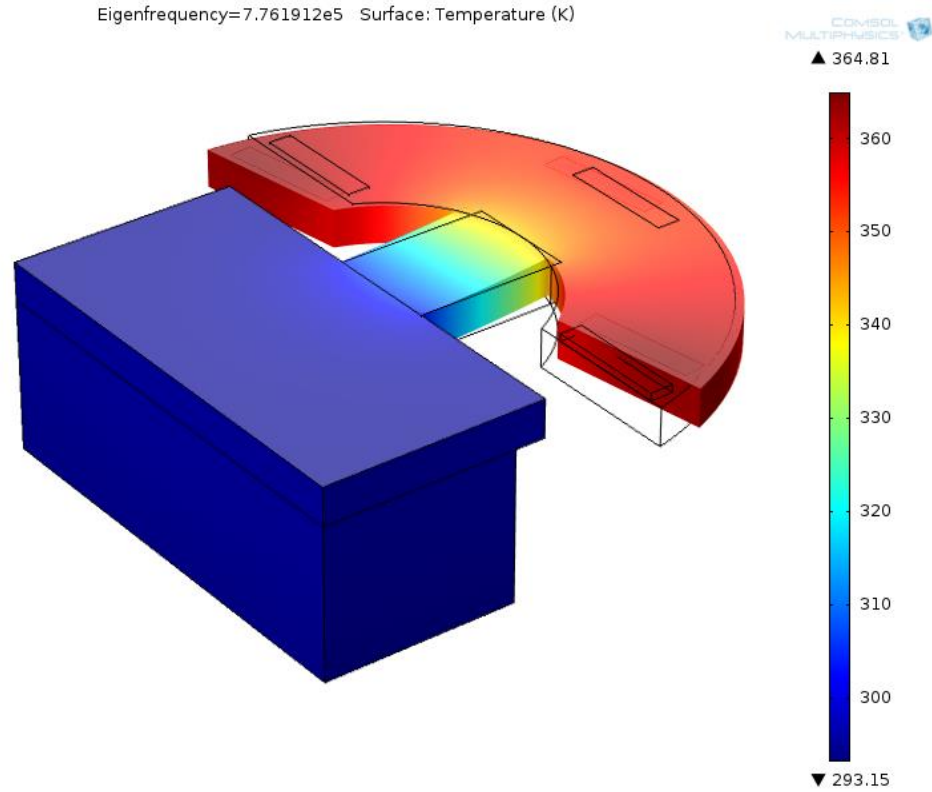


Figure 30 - Thermal-modal analysis of resonant microstructure using COMSOL. The applied heating power of 100 mW causes a 71°C temperature elevation of the head structure (see color coding). The simulated in-plane resonant frequency of the heated structure is 776.19 kHz, a shift of -610Hz from the unheated structure.

The discrepancy between the simulated and observed temperature elevations is approximately 15% and can be explained by taking into account differences between the simulated model and the physical device (e.g. thickness variations, dielectric layers). Figure 31 shows the open-loop amplitude transfer characteristic of the fundamental in-plane mode as a function of the applied heating voltage. The resulting frequency drop is linear with the heating power with a slope of -10.1 Hz/mW, or -13 ppm/mW. Typical Q-factors for these devices are approximately 3000 in air.

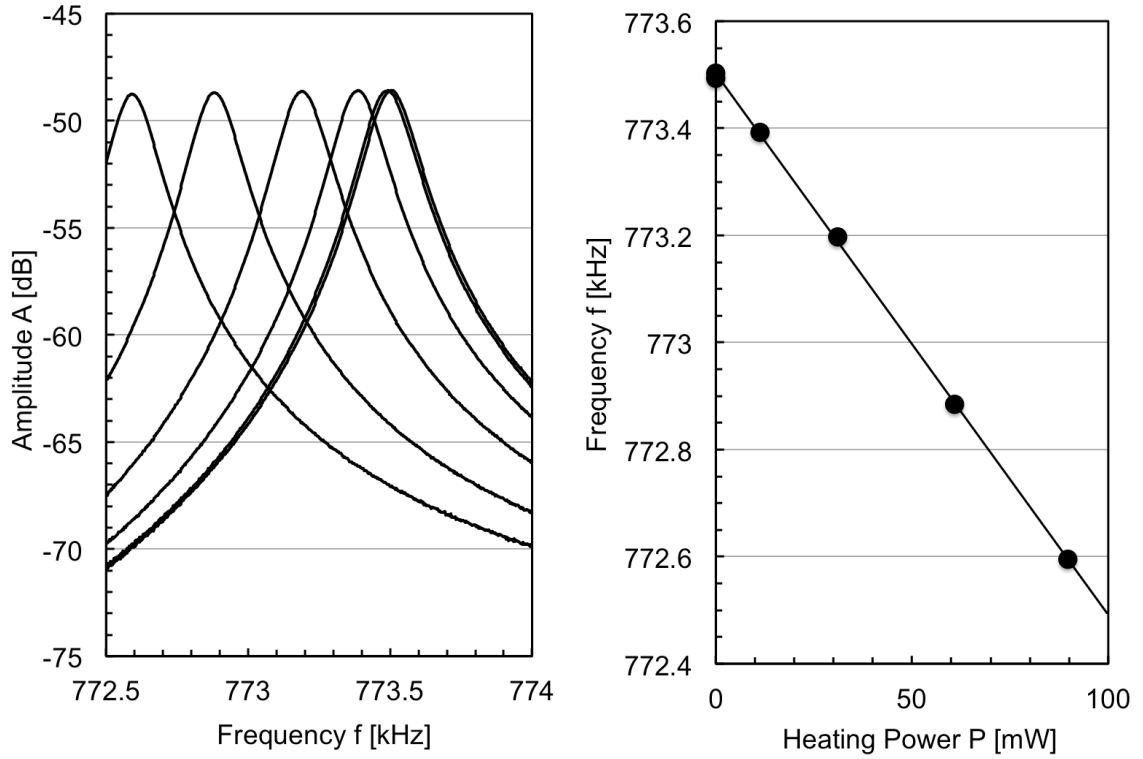


Figure 31 - (Left) Amplitude transfer characteristic of in-plane resonant mode as a function of the applied heating power. (Right) Resonant frequency as a function of the applied heating power with a slope of -10.1Hz/mW or -13ppm/mW.

The thermal time constant of the heated resonator can also be estimated using finite element modeling and was simulated to be approximately 1.2 ms for a 25 μm -thick resonator. By applying a square-wave heating pulse with a frequency of 100 Hz to the three series-connected heating resistors and measuring the temperature-dependent resistance change across the Wheatstone bridge, a thermal time constant of 1.1 ms was experimentally observed (Figure 32), confirming the simulated results.

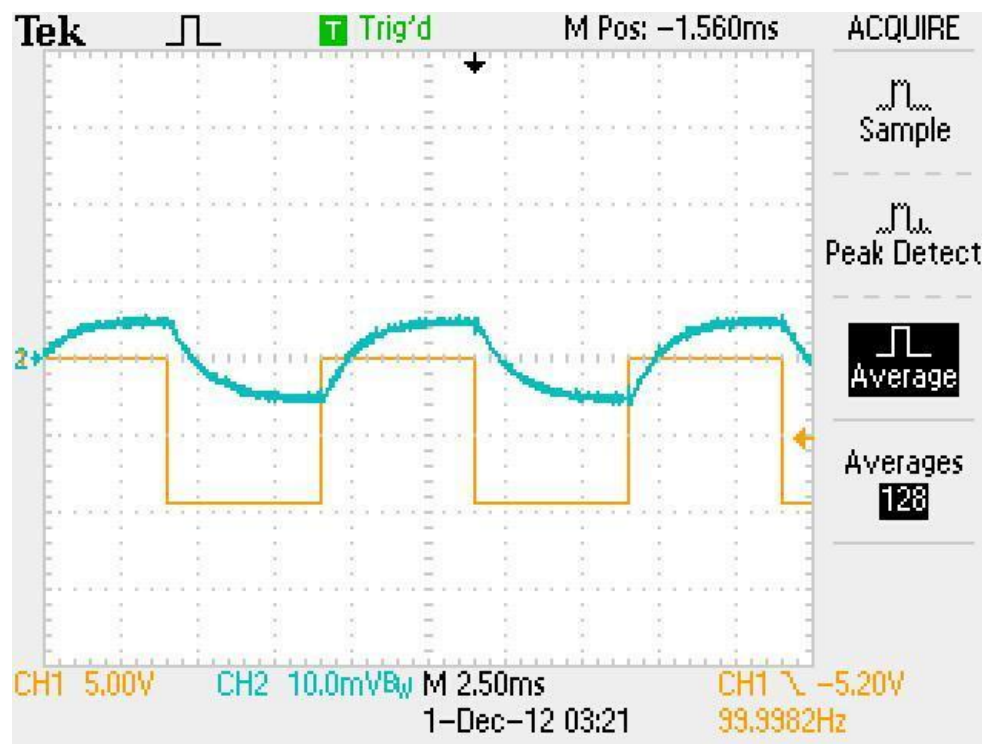


Figure 32 - Screen capture of oscilloscope showing the square-wave signal applied to the three series heating resistors on the head region of the resonator, and the voltage across the piezoresistors at a constant current of 1 mA. The extracted thermal time constant is 1.1 ms.

It is important to note that this thermal time constant is 2-3 orders of magnitude shorter than typical analyte diffusion times into polymeric sensing films with micrometer thicknesses (Figures 24-25) [90]. As a result, the resonators can be quickly heated to desorb the analyte out of the polymer film and then rapidly cooled to monitor the analyte absorption back into the polymer in real time. As a result of the rapid cooling of the device, the resonator quickly returns to its original temperature (i.e. the baseline temperature of the device, prior to generating the self-heating transient) and analyte absorption into the polymer sorbent film takes place essentially at room temperature. Because the analyte sorption is recorded at the original baseline operating temperature, the unavoidable frequency shift associated with heating the resonator does not affect the measurement.

Device Operation

Despite the integration of the on-chip heating units, basic device operation remains similar to that of previous work [89, 90, 93]. The resonator is embedded into an amplifying feedback loop and driven at its fundamental in-plane resonance mode using the aforementioned diffused silicon excitation resistors at the base of the cantilever beam. Four piezoresistors arranged in a U-shaped Wheatstone bridge configuration generate a sensing signal at the desired in-plane mode and enable closed-loop operation of the resonator at its in-plane resonance frequency of approximately 780 kHz.

In addition to the closed-loop feedback circuitry used for driving the sensors at resonance and tracking chemically-induced frequency shifts, a separate circuit driven by a low-power microcontroller was developed for pulsing the integrated heating units. The circuit used for applying power to the heating resistors consisted of an operational amplifier driven by an 8-bit digital-to-analog converter (DAC), which was in turn controlled digitally by the microcontroller. This setup allowed for the application of 256 different heating power levels – with a step size of approximately 40 mV – that are controlled with the digital precision and timing of the microcontroller. Additionally, the programmable microcontroller enables complex heating patterns to be applied in an automated and consistent way. An example program run by the setup is found in Appendix C.

Chemical Measurements

Following fabrication, and subsequent electrical and thermal characterization, several micro-resonators were coated with sorbent polymer layers and evaluated for performance as gas-phase chemical sensors. Building on previous work [89], sorbent polymer layers were applied via localized polymer deposition through a shadow mask onto the semicircular head region only. By functionalizing the device in this way, the effective post-coating quality factor is preserved, even in the case of relatively thick sorbent layer films. As discussed previously, this reduction in Q-factor degradation results from the coated polymer layer's localization away from high strain regions of the device. Since deformation in the head region is negligible, the overall chemical sensitivity can be improved by applying a thick sorbent coating without compromising on operational quality factor. The coated resonators were then embedded into an amplifying feedback loop and exposed to defined concentrations of volatile organic compounds (VOCs) in the custom gas-flow setup.

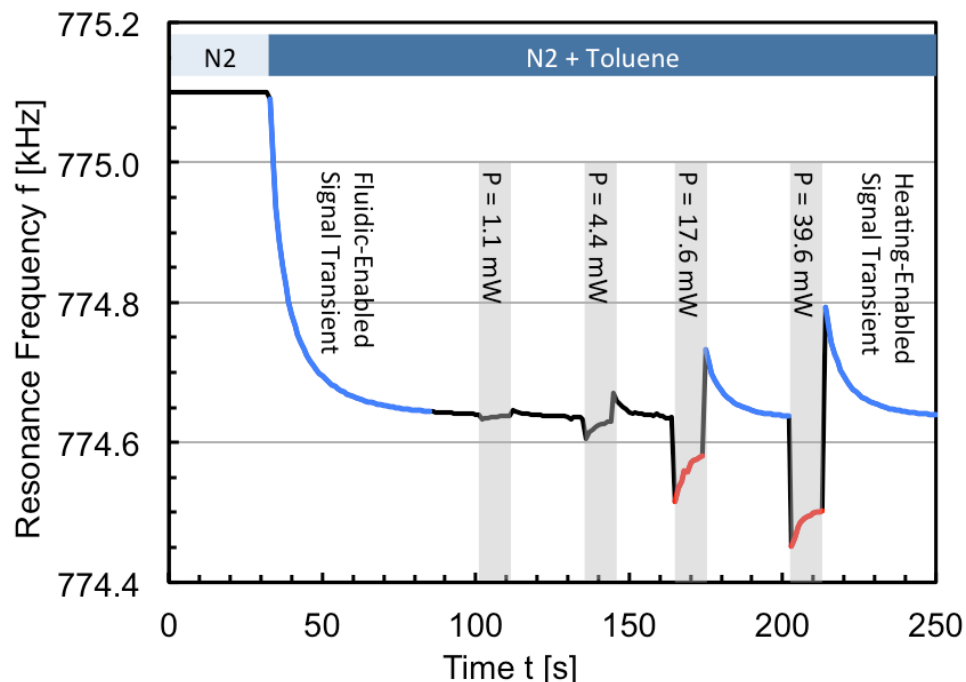


Figure 33 - In-plane resonance frequency of 25 μ m thick microstructure subject to various levels of applied heating power; the PIB-coated resonator is exposed initially to pure carrier gas (N₂) and then to a constant toluene concentration of 6800ppm; Blue lines represent analyte absorption phases, red lines analyte desorption phases.

Figure 33 summarizes a typical chemical measurement performed with a 25 μ m thick heated resonator coated with a 2 μ m thick polyisobutylene (PIB) sorbent polymer layer. After exposing the microstructure to pure carrier gas (N₂), it was subjected to a continuous flow (80 ml/min) of toluene at a concentration of 6800 ppm, at a constant temperature of 20°C. The resulting initial frequency drop of ~1.2 kHz is due to absorption of toluene into the PIB sensing film. While exposing the sensor to a constant toluene concentration, heating pulses of varying power were applied to the three series-connected resistors located on the head region of the resonator, and the resonance frequency of the device was continuously monitored and recorded. As can be seen in Figure 33, the resonance frequency drops quickly when heating power is initially applied due to a rapid increase in the device temperature, which reduces the stiffness of the cantilever beam (due

to the temperature dependence of the Young's modulus). Almost immediately after the heating pulse is applied, the frequency slowly begins to increase as analyte is desorbed from the heated polymer film. After the heating power is turned off, the frequency rapidly shifts upward due to the temperature decrease as device and polymer return to their initial state (as demonstrated previously, the thermal time constant is approximately 1.1 ms) and then slowly decreases again as analyte is re-absorbed into the polymer layer.

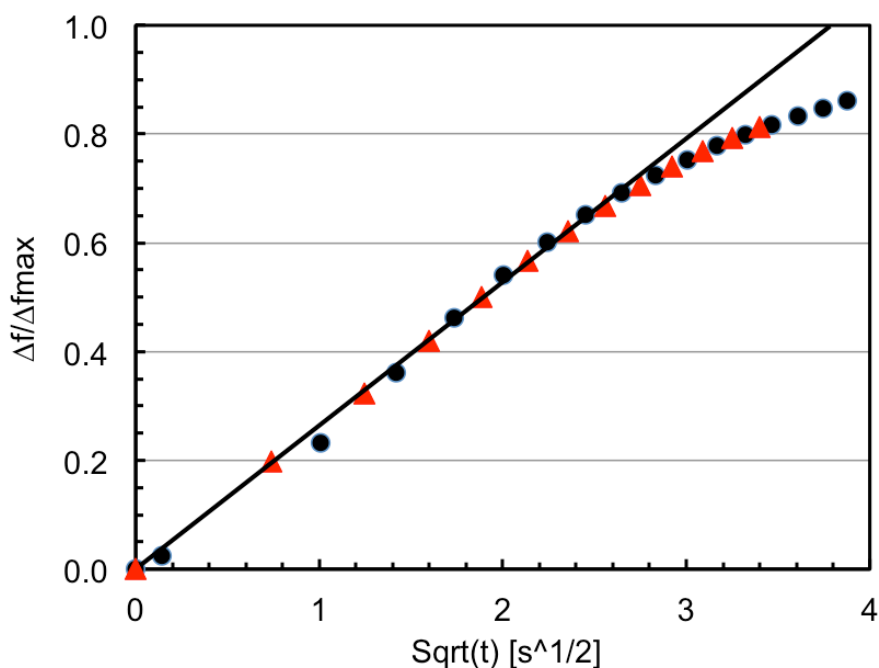


Figure 34 - Normalized frequency change vs. square-root of time for absorption transients induced by on-chip heating/cooling ($P = 40$ mW, red symbols) and analyte switching using a gas set-up (black symbols); the slope of the linear portion (solid line) is proportional to \sqrt{D} and yields a diffusion coefficient, $D = 2.4 \times 10^{-9}$ cm²/s [10]. The heating-induced transient agrees very well with the gas-switching-enabled transient.

The observed sorption transients (blue sections in Figure 33) can be analyzed further to improve analyte discrimination, as the associated diffusion coefficients are specific to the particular polymer-analyte pair [90], as illustrated in Figure 26. This plot of

normalized frequency change vs. square-root of time compares transients induced by modulation of the integrated heating resistors with a conventional transient induced by rapidly switching between analyte-loaded gas and reference gas streams with a mechanical valve. By plotting (for the three blue absorption cycles in Figure 33) the ratio of the frequency change to the maximum frequency change versus the square-root of time, the initial slopes of the transients, which are proportional to the square-root of the diffusion coefficient, D [90], are observed to agree within 5% (Figure 34). Thus, signal transients generated via modulation of the on-chip heating units are nearly indistinguishable from those generated due to sudden changes in analyte concentration (e.g. switching via valve between analyte and pure carrier gas streams). As such, heater-generated transients carry virtually identical information as the conventional transients and can be used in like manner for enhancing selectivity for chemical sensing of VOCs in the gas-phase. The extracted diffusion coefficient for toluene into PIB is $2.4 \times 10^{-9} \text{ cm}^2/\text{s}$. Since the transients are generated in a constant-concentration environment, operation in this mode does not require an external flow system for switching between analyte and reference gas streams, thereby reducing cost and complexity in the total sensing platform.

As another example, Figure 35 represents a series of measurements performed with a resonator coated with an 11 μm thick PIB film exposed to varying concentrations of toluene. The measurements were each performed using the previously-mentioned gas-flow setup, with a constant flow rate of 80 ml/min and at a constant temperature of 20°C. In each case, 18.8 mW of heating power were applied to the device for a duration of 30 sec once the resonator became saturated with the given toluene concentration. As can be seen from

the figure, the slopes of the transients agree very closely and are independent of the analyte concentration for relatively low analyte concentration levels.

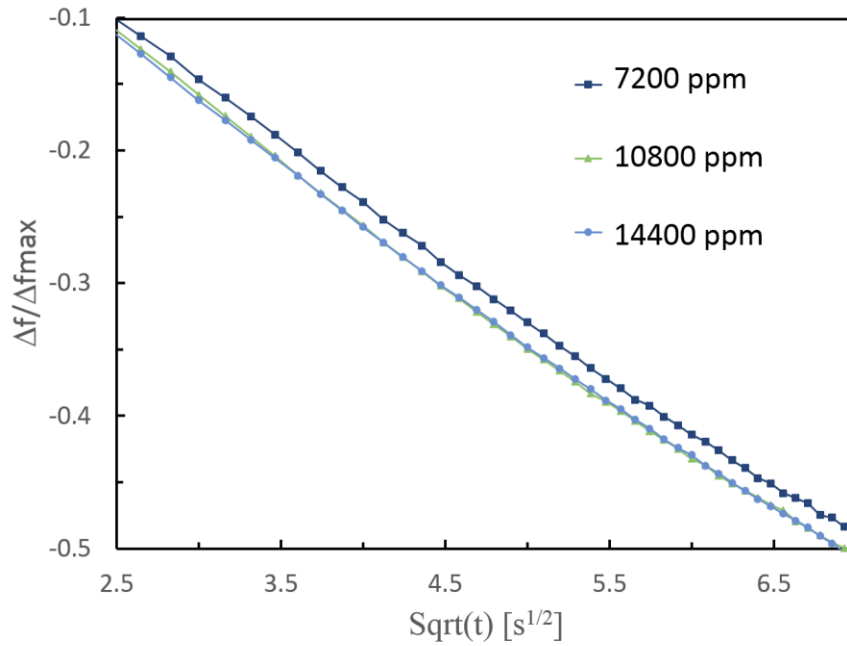


Figure 35 - Normalized frequency change vs. square-root of time for the initial portion of the absorption transients induced by on-chip heating/cooling ($P_{\text{applied}} = 18.8 \text{ mW}$) for resonator coated with an $11 \text{ }\mu\text{m}$ thick PIB film exposed to varying concentrations of toluene; the slope of the linear portion is proportional to \sqrt{D} and independent of concentration, for low concentration levels.

Analysis of the measured frequency shifts reveals that the sensors exhibit a linear response with respect to toluene concentration. Another important observation from the data is that the sensor's response is fully reversible and the measurements are made in real-time due to the rapid generation of heating transients.

CH 4 - ANALYSIS OF THERMAL TRANSIENTS

The temperature-induced analyte sorption into polymeric sensing films can be studied further by separating temperature effects from analyte diffusion effects. To begin this investigation, a stair-step pattern of precisely timed heating powers was applied to the polymer-coated resonator first in a pure nitrogen environment and subsequently in a constant atmosphere of toluene. The resulting frequency shifts in the N₂-only atmosphere (which represent the sensor's response to temperature alone) were then subtracted from the corresponding shifts obtained in the analyte-loaded atmosphere and normalized with respect to maximum frequency shift for a given heating power (Figure 36). In this way, the temperature response of the sensor stemming from the temperature-dependence of the Young's modulus can be removed leaving only the response due to analyte sorption. As can be seen in Figure 36, the analyte desorption is temperature-dependent (because the diffusion coefficient depends on temperature), while the normalized rate of re-sorption (which occurs at the same temperature in all cases, because the sensor cools so quickly) is independent of the heating power. This is important to note if the re-absorption transients are used to distinguish analytes by their characteristic diffusion times: in case of relatively long heating pulses, the re-absorption is independent of the heating power and, thus, analyte discrimination can potentially be achieved at any heating power that generates a sufficiently large signal transient.

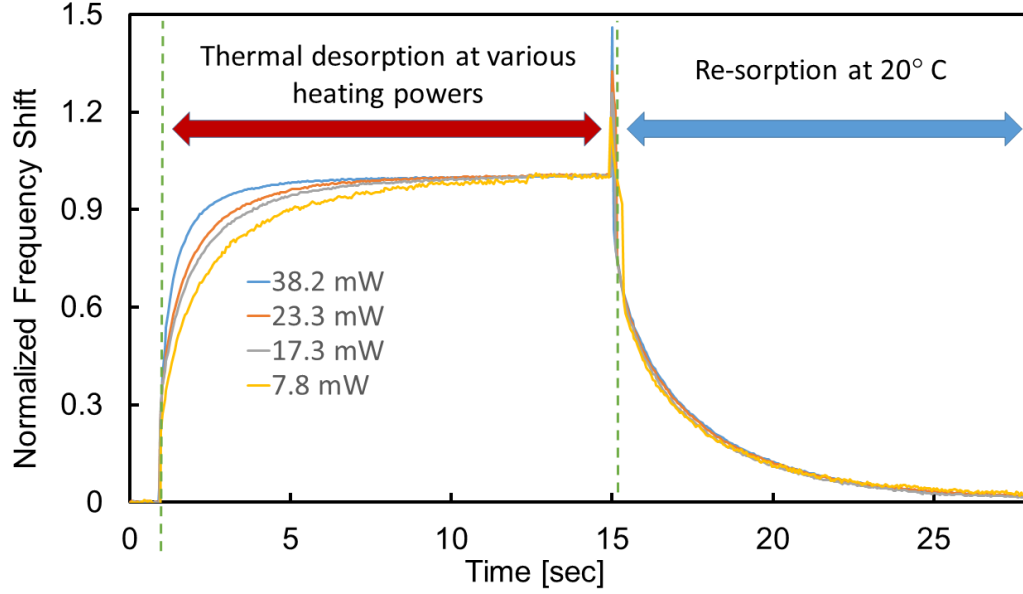


Figure 36 - Series of normalized desorption/absorption transients for increasing heating powers. The resonator was coated with a 2 μm thick polyepichlorohydrin (PECH) film and exposed to a continuous toluene concentration of 10800ppm. The transients are normalized with respect to their maximum frequency change, and frequency changes caused solely by a temperature change have been removed from these data through a differential measurement.

As a result of the rapid heating, even short-duration heat pulses are sufficient to generate the transients. Figure 37 illustrates a pulsed-mode operation that was performed using the previously discussed low-power digital-to-analog converter (DAC) and microcontroller to apply precise heating powers to the resonator for 200 ms durations. As can be seen from the figure, signal transients are generated that require an average total heating power consumption of 900 μW per measurement cycle. The generation of low-power transient signals without the use of an external fluidic system introduces novel measurement techniques, and lends itself well to mobile sensing applications.

In the following sections, the temperature-induced signal transients are investigated in more detail for the cases of long and short heating pulses.

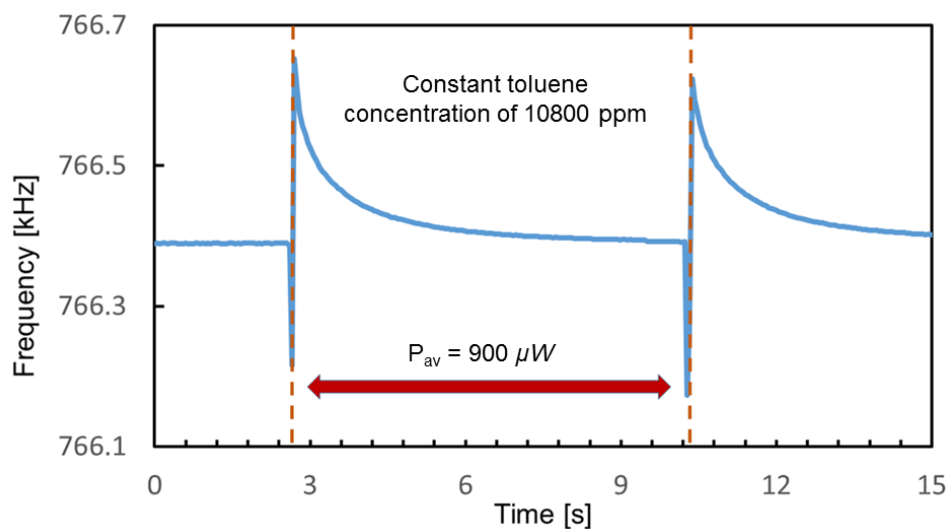


Figure 37 - Thermally generated transients based on pulsed-mode operation with 200ms heating pulses, resulting in an average heating power consumption of 900 μ W per cycle.

Transients Stemming from Variable Heating Pulse Length

To investigate the impact of the heating pulse duration (as opposed to the heating power) on the signal transients, a heated cantilever structure coated with approximately 2 μ m of PECH was subsequently exposed to N₂ carrier gas only and approximately 10,800 ppm toluene in N₂, while heating pulses with variable pulse length but constant heating power were applied. The recorded frequency data was analyzed as follows (see example in Figure 38): (1) all signal transients are referenced to $t = 0$ sec at the time the heating pulse starts; (2) for each heating pulse duration, the signal transient due to temperature only (recorded in carrier gas) is subtracted from the signal transient due to analyte and temperature (recorded in analyte-loaded gas). The differential transient (green signal in

Figure 38) should thus only stem from analyte sorption out of and into the sensing film and not be affected by changes in the resonator's stiffness due to the temperature changes.

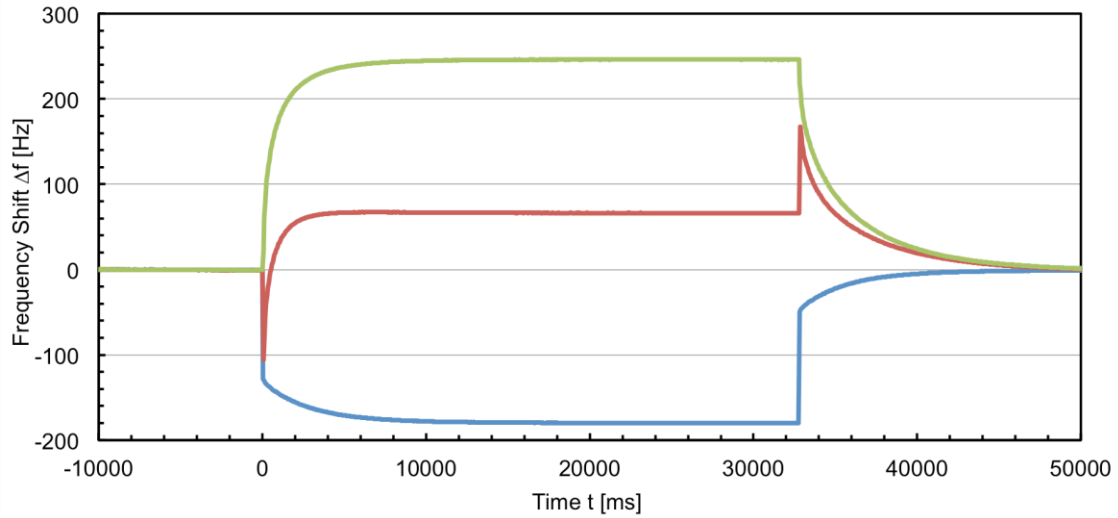


Figure 38 - Signal transients, i.e. frequency change as a function of time, for 32.8s heating pulse: (1) Blue curve: signal transient in carrier gas; (2) Red curve: signal transient in analyte-loaded gas; (3) Green curve: differential transient representing analyte sorption effects only.

Upon analyzing the signal transients recorded in carrier gas only, two time constants are clearly visible. During heating, the frequency drops nearly instantaneously at first and then continues to drop at a significantly reduced rate. It is believed that the initial drop is due to the rapid heating of the cantilever structure itself, while the second, slower time constant stems from heating either the whole chip or the chip and package together. The result of this chip/package heating is that the analyte re-absorption at the end of the heating pulse does not happen at the initial baseline temperature. Rather, re-absorption occurs at slightly elevated temperature, thus affecting the shape of the re-absorption transients. To avoid this undesirable heating of the chip, it is suggested for future work that improvements be made to the thermal properties of the packaged sensor. For example, the chip could be connected

to a heat sink capable of effectively sinking the heating power from the pulses, or the measurement protocol could be modified to work with shorter heating pulses. Analysis of the signal transients stemming from a 256 msec heating pulse (see Figure 39) reveals minimal heating of the chip (and package), which signifies that the analyte re-absorption is essentially occurring at room temperature. At the same time, the power/energy consumption associated with heating is significantly reduced if it is assumed that measurements are taken at fixed time intervals. However, as will be demonstrated shortly, due to the short heating pulses the analyte distribution within the polymer is not constant at the end of the heating pulse, which renders the re-absorption transient dependent on the heating pulse length.

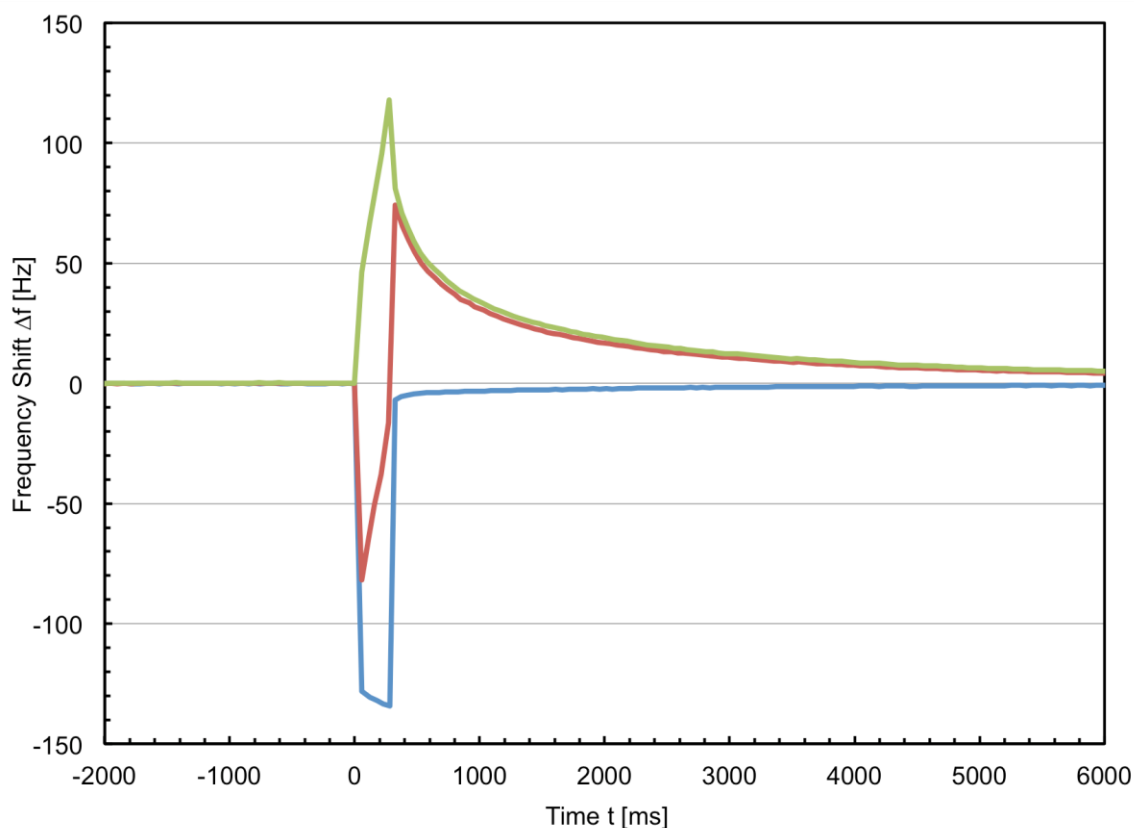


Figure 39 - Signal transients, i.e. frequency change as a function of time, for 256ms heating pulse: (1) Blue curve: signal transient in carrier gas; (2) Red curve: signal transient in analyte-loaded gas; (3) Green curve: differential transient representing analyte sorption effects only.

Following analysis of the signal transients for individual heating pulse lengths, it now becomes possible to compare (i) the analyte desorption transients and (ii) the analyte re-absorption transients for different pulse lengths. Figure 40 combines the signal transients for 256 ms, 1.02 s, 4.1 s and 32.8 s long heating pulses into a single graph. As can be readily observed in Figure 40, the desorption transients coincide for the different heating pulse lengths, due to (1) the temperature during the desorption phase being the same regardless of the heating pulse length and (2) the analyte within the polymer film having reached equilibrium before the heating pulse is applied. The only effect of the heating pulse

length, then, is that individual desorption transients are stopped at different times. By plotting the ratio of the measured frequency change and the maximum frequency change ($\Delta f_{\max} = 246 \text{ Hz}$) as a function of the square root of the time, the initial part of the transient can be described by Equation 7 with a slope of approximately $0.88 \text{ s}^{-1/2}$. Assuming a polymer thickness of $2 \mu\text{m}$ yields a diffusion coefficient of $D = 2.4 \cdot 10^{-8} \text{ cm}^2/\text{s}$ for the toluene-PECH combination. It should be noted that this does not correspond to the room-temperature diffusion coefficient but rather to the diffusion coefficient at the temperature of the heated cantilever. For a heating power of 40 mW , this is approximately 29°C above room temperature.

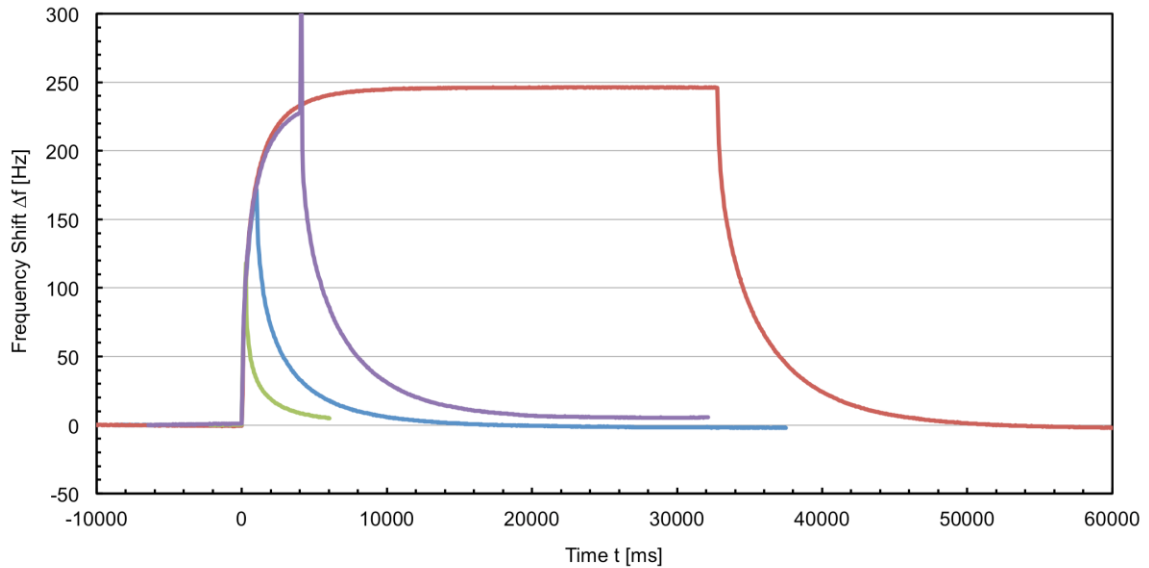


Figure 40 - Overlaid signal transients, i.e. frequency change as a function of time, for heating pulse lengths of 256ms (green), 1024ms (blue), 4096ms (purple) and 32768ms (red).

Figure 41 shows a similar comparison for the re-absorption transients. In this case, the frequency shift is normalized by the maximum frequency shift for a particular heating pulse length and timed so that the end of the heating pulse coincides with $t=0\text{s}$ in each case.

Clearly, only the re-absorption transients for 4 s and 32 s heating pulses coincide. For shorter pulse durations, the transients become shorter and shorter. This result was initially not expected, as the analyte re-absorption essentially takes place at room temperature because of the fast cooling of the micro-resonator. However, as mentioned before, the analyte distribution in the polymer does not reach equilibrium for pulses shorter than approximately 4 s and, thus, the underlying assumptions for the theory highlighted in Chapter 3 are no longer fulfilled. The analyte distribution reaches equilibrium within the polymer when the frequency no longer changes, i.e., after approximately 10 s in Figure 40. For heating pulses shorter than 4 s, desorption during heating preferentially happens from the surface areas of the polymer and, thus, the reabsorption again must occur primarily in the volume closest to the sorbent surface. Thus, this re-absorption at the surface can happen more quickly than the re-absorption into the ‘deeper’ levels of the polymer film. As a result, the re-absorption event occurs more quickly with decreasing pulse length, as observed in Figure 41.

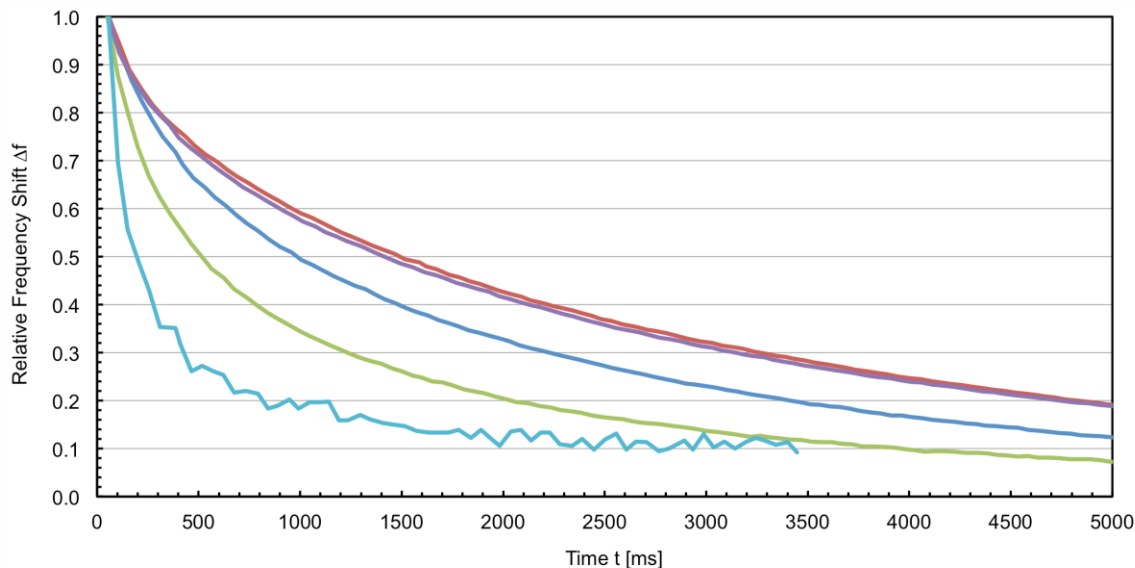


Figure 41 - Overlaid analyte re-absorption transients, i.e. frequency change as a function of time, for heating pulse lengths of 8ms (cyan), 256ms (green), 1024ms (blue), 4096ms (purple) and 32768ms (red). The frequency data are normalized by the maximum frequency shift at the given heating power.

Finite Element Simulation of Analyte Diffusion into Polymer Film

To better understand this effect, diffusion of the analyte into the polymer film was simulated using the finite element software, COMSOL. For this simulation, the analyte diffusion is described by Fick's diffusion law

$$\frac{dC}{dt} = D \frac{d^2C}{dx^2}$$

Equation 11 – Fick's law of diffusion.

and simulated in COMSOL using time-dependent heat transfer in solids. In this case, the temperature becomes the analyte concentration and the ratio of the thermal conductivity, k , [W/(mK)] and the specific heat per volume [J/(Km³)] becomes the thermal diffusivity, D , [m²/s]. Assuming that the lateral extension of the polymer is much larger than the thickness, the problem reduces to a 1-dimensional diffusion problem along the thickness direction. In COMSOL, a 2D problem was actually simulated and the heating pulse is simulated by presenting a concentration pulse to the top surface of the polymer. Thereby, the concentration, C , can be given as an absolute concentration (in units ppm, or g/cm³), a relative concentration C/C_{ref} (dimensionless from 0 to 1), or even as an equivalent frequency change (i.e., multiplying the concentration by the sensor sensitivity, S , [Hz/ppm]). Using this approach, it should be possible to observe signal transients similar to the measured ones, but it will not be possible to simulate desorption and re-absorption at different temperatures. Instead, both sorption processes will happen with a constant (temperature-independent) diffusion coefficient. However, COMSOL allows implementing time-dependent material properties. In this way, different material properties during heating and non-heating can be defined using a piecewise function similar to the way the concentration step/profile is defined at the surface.

Figure 43 compares experimental and simulation results for the re-absorption transient after a 32.8 s heating pulse. Thereby, the “concentration” step applied to the surface of the simulated film varied from 0 to 245 [K] to match the experimentally observed maximum frequency change of 245Hz. The gray lines in Figure 43 represent simulated transients assuming diffusion coefficients of $D = 4\text{e-}^9$, 6e-^9 , 8e-^9 , 1e-^8 , 2e-^8 , 4e-^8 cm²/s with the rate of

frequency change increasing with increasing D . The black line represents the experimentally measured re-absorption transient of the heated cantilever.

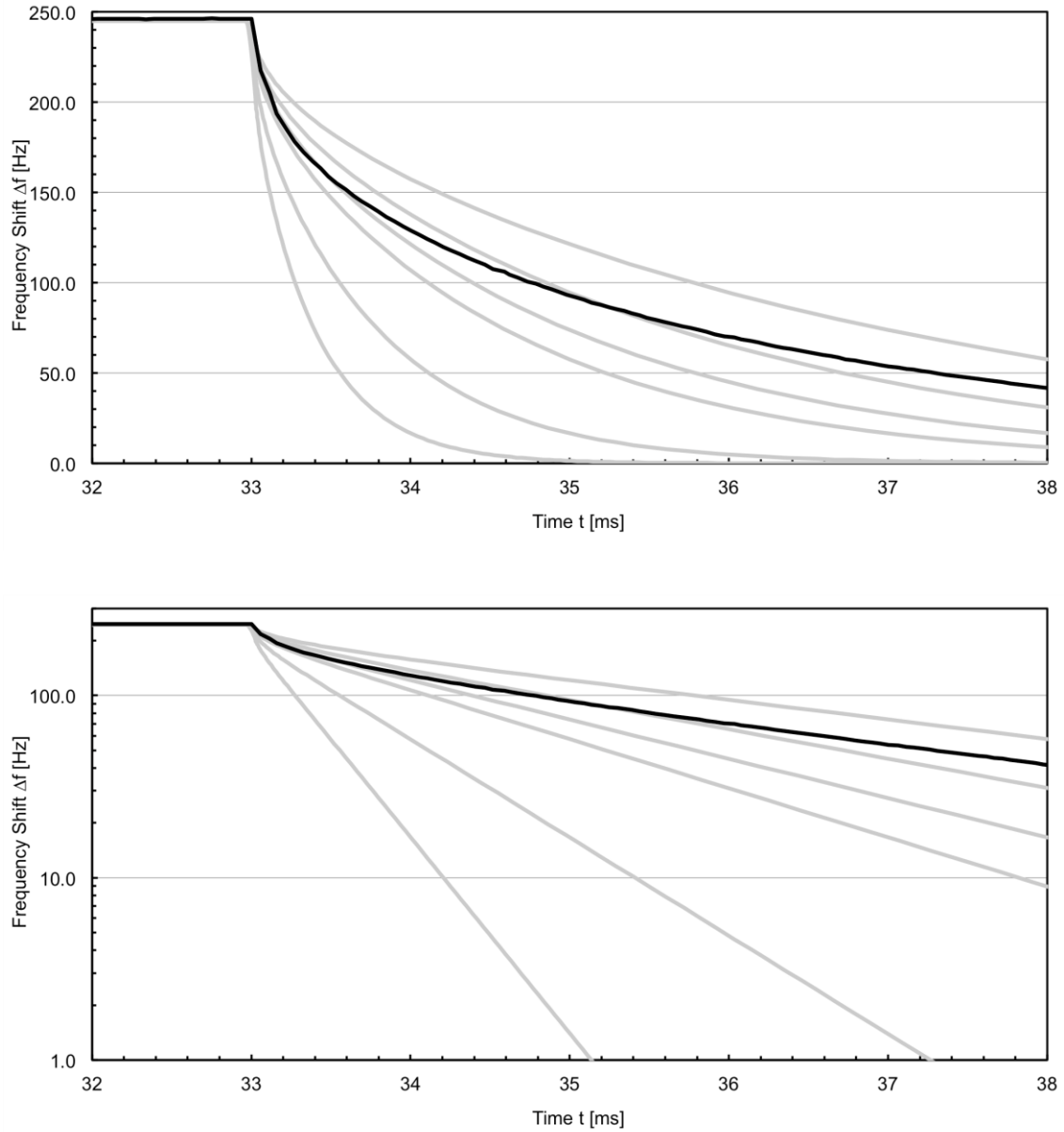


Figure 42 - Comparison of simulated (grey lines) and experimental (black line) re-absorption transients after a 32s heating pulse. For the COMSOL simulation, the diffusion coefficients used were $D = 4e^{-9}, 6e^{-9}, 8e^{-9}, 1e^{-8}, 2e^{-8}, 4e^{-8} \text{ cm}^2/\text{s}$. The graph on the top shows the frequency axis in a linear scale, the bottom graph shows the same data using a logarithmic frequency axis.

Clearly, the experimentally measured transient does not follow the transient expected by Fickian behavior with a constant diffusion coefficient: initially, the transient closely follows the simulated transient for $D = 8 \times 10^{-9} \text{ cm}^2/\text{s}$, but with time the effective D appears to decrease to values around $D = 4 \times 10^{-9} \text{ cm}^2/\text{s}$ (see especially the representation with logarithmic frequency axis). The most plausible explanation for this behavior is a temperature effect: due to chip heating, the temperature during analyte re-absorption is not constant at room temperature, but decreasing towards room temperature during the transient (see Figure 38). As a result, the effective diffusion coefficient is higher at the beginning of the transient and decreases throughout the transient. A second possible explanation would be a concentration-dependence of the diffusion coefficient, with D decreasing for increasing concentration. However, while concentration-dependent diffusion coefficients are often found in case of gas diffusion into polymers, the diffusion coefficient typically increases with increasing concentration and not *vice versa* [104].

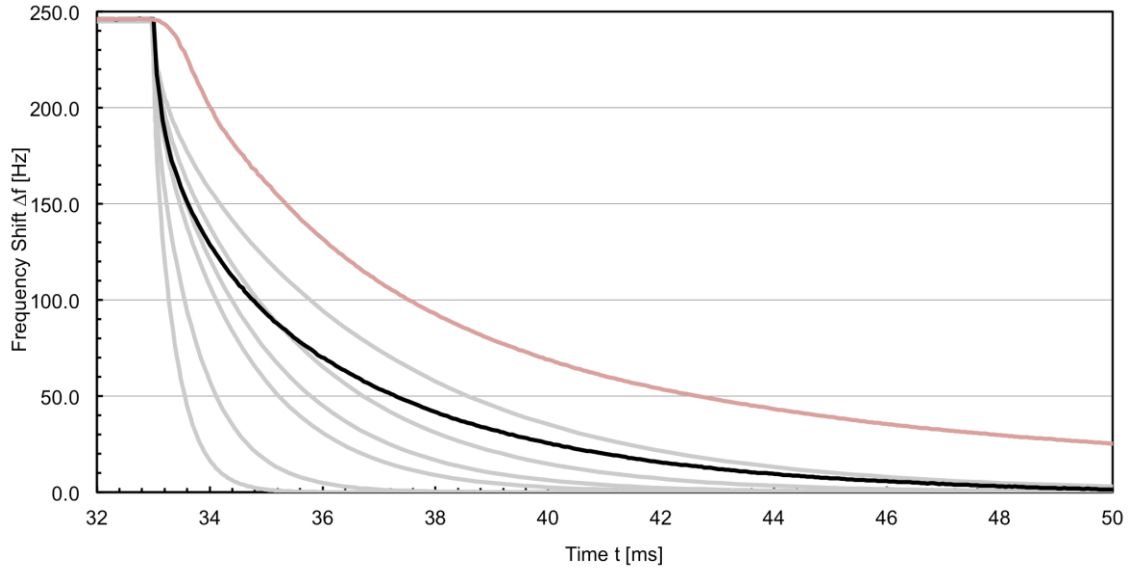


Figure 43 - Comparison of simulated (grey lines) and experimental (black line) re-absorption transients after a 32s heating pulse. For the COMSOL simulation, the diffusion coefficients used were $D = 4\text{e-}^9, 6\text{e-}^9, 8\text{e-}^9, 1\text{e-}^8, 2\text{e-}^8, 4\text{e-}^8 \text{ cm}^2/\text{s}$. The graph also shows the switching-valve induced absorption transient (red line) normalized to the same maximum frequency change as the heating-induced transient.

While the heating transients were recorded, an absorption transient induced by mechanical switching of the 4-way valve of the gas setup was recorded as well. In Figure 44, this switching-valve-induced transient is compared to the heating-induced transient. To this end, the switching-induced transient was normalized to the magnitude of the heating induced transient, which shows a maximum frequency change of 246 Hz. Surprisingly, both transients do not coincide. This is in contrast to earlier data published in [88]. One explanation could be the impact of the measurement chamber on the transient: at a flow rate of 80ml/min, the measurement chamber (approximate volume of 0.25 ml) is flushed about 5 times per second. As a result, the gas concentration in the chamber is expected to change quickly from carrier gas to 10,800ppm toluene, but certainly this transition is not

instantaneous. For example, laminar flow in the measurement chamber might further impede the rate with which the concentration changes at the surface of the sensing film. The effect of this concentration step with finite slope in the measurement chamber was not observed previously in [88], as data were only recorded every 1 s and due to the slower diffusion of toluene into PIB. Thus, the heating-induced transients likely represent a more accurate representation of the diffusion in the sensing film. However, it is suggested for future work that additional measurements be taken to confirm the conclusions of this result.

If the non-ideal re-absorption transient for the 32.8 s heating pulse is indeed affected by the undesired chip heating, the effect should be less pronounced for shorter heating pulses. Thus, the simulated and measured transients for the 256 ms heating pulse were further investigated. In this case, it is essential that the COMSOL simulation is performed using different diffusion coefficients during the “heating” and “non-heating” phases. Initially, the simulations were performed at a constant diffusion coefficient and the reabsorption phases were studied by normalizing the simulated frequency changes by the maximum frequency changes. Surprisingly, re-absorption transients became almost independent of D this way. However, upon further analysis, this is actually not surprising when the desorption phase is also considered: at higher D , more analyte desorbs, but then also re-absorbs more quickly, yielding D -independent normalized transients.

Simulations at constant diffusion coefficient can, however, be used to find the effective D during the heating pulse. Figure 45 shows a close-up of the desorption transient: while only 5-6 measurement points were recorded during the desorption transient, the measured data nicely follows the simulated desorption transient for a diffusion coefficient of $D = 2 \times 10^{-8} \text{ cm}^2/\text{s}$, which is consistent with desorption data for the 32.8 s heating pulse. Again, it

should be noted that desorption happens at elevated temperature and not at the baseline temperature. For the following simulations, D was set to $2.2 \times 10^{-8} \text{ cm}^2/\text{s}$ during the heating pulses.

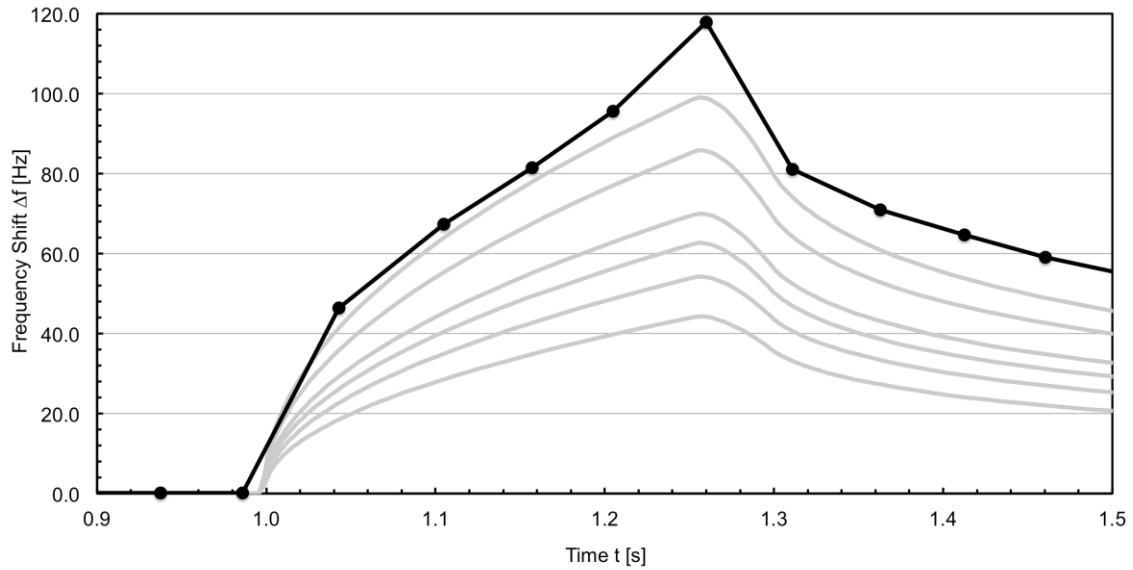


Figure 44 - Comparison of simulated (grey lines) and experimental (black line) desorption and re-absorption transients for a 256ms heating pulse. For the COMSOL simulation, the diffusion coefficients used were $D = 4\text{e}^{-9}$, 6e^{-9} , 8e^{-9} , 1e^{-8} , 1.5e^{-8} , $2\text{e}^{-8} \text{ cm}^2/\text{s}$. The simulation were done using a constant D over the full 10s period.

Figure 46 compares the simulated and measured re-absorption transients. For this simulation, a “piecewise function” was defined in COMSOL to simulate differing diffusion coefficients during “heating” and “non-heating” periods. During heating, i.e. during the concentration pulse, $D = 2.2 \times 10^{-8} \text{ cm}^2/\text{s}$ was applied, while the diffusion coefficient during the non-heating phases was varied from $D = 2\text{e}^{-9}$, 4e^{-9} , 6e^{-9} , 8e^{-9} , 1e^{-8} , 2e^{-8} , $4\text{e}^{-8} \text{ cm}^2/\text{s}$. Similar to the findings for the long heating pulses, the effective diffusion coefficient

appears to decrease during the re-absorption phase. Initially, $D \approx 1\text{-}2 \times 10^{-8} \text{ cm}^2/\text{s}$, while towards the end it is observed that $D = 4\text{-}6 \times 10^{-9} \text{ cm}^2/\text{s}$.

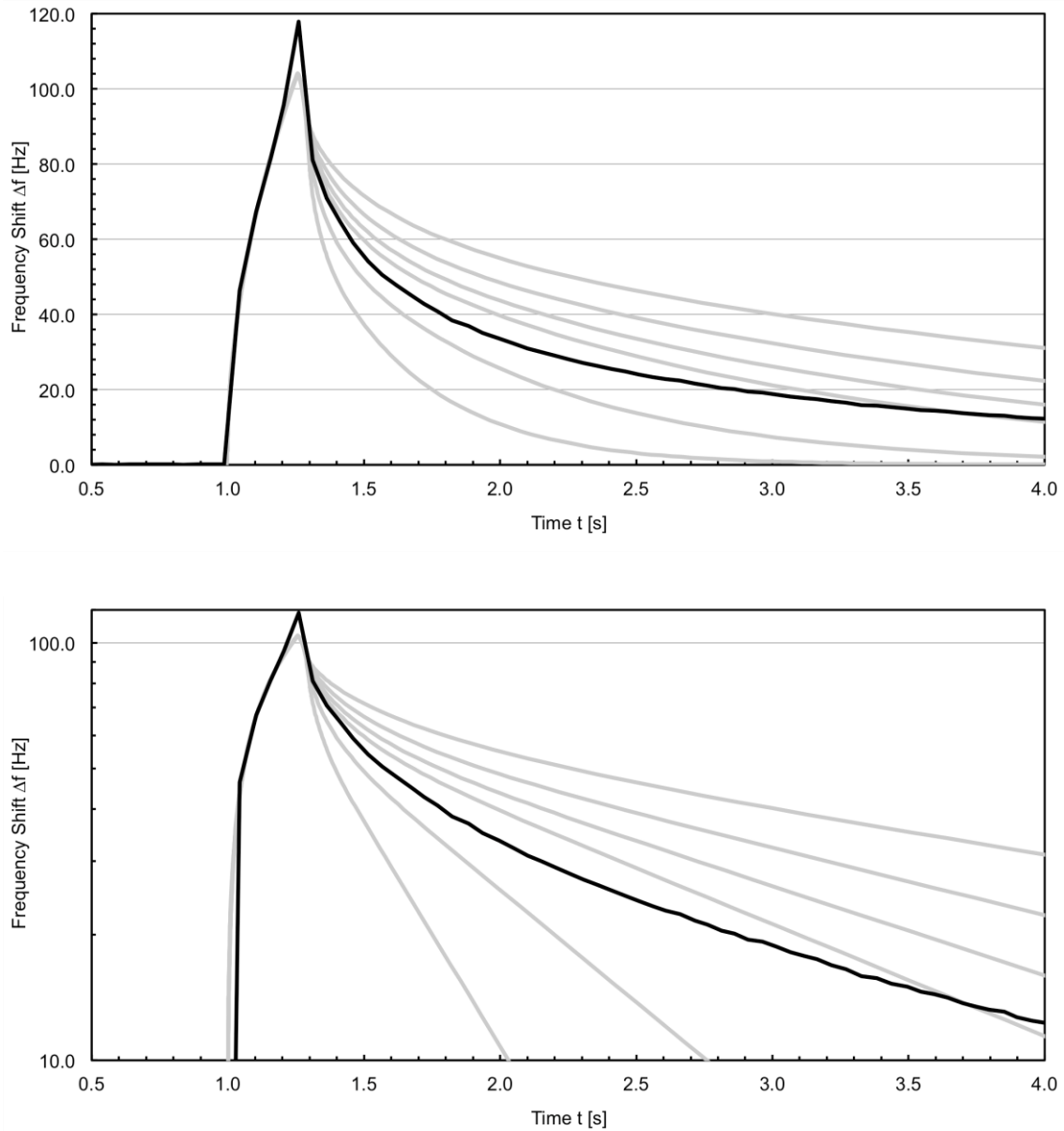


Figure 45 - Comparison of simulated (grey lines) and experimental (black line) desorption (top graph) and re-absorption (bottom graph) transients for a 256ms heating pulse. During the heating pulse, a diffusion coefficient $D = 2.2 \cdot 10^{-8} \text{ cm}^2/\text{s}$ was applied, while the diffusion coefficients used during non-heating phases were $D = 4e^{-9}, 6e^{-9}, 8e^{-9}, 1e^{-8}, 2e^{-8}, 4e^{-8} \text{ cm}^2/\text{s}$.

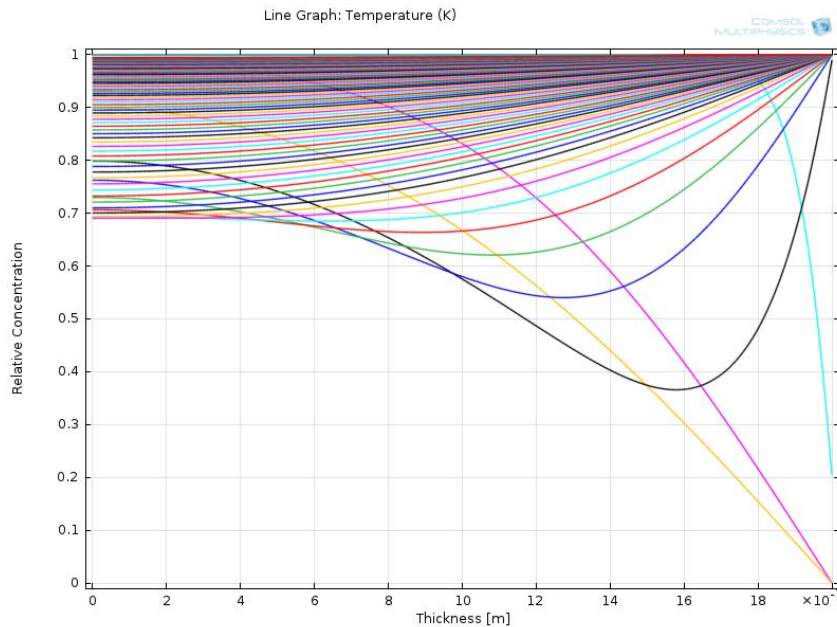
Overall, the change of the effective D during analyte re-absorption is potentially more pronounced for the short pulse than for the long pulse. This suggests, that it might not be caused by the undesired temperature variation of the chip/package. It is interesting that the diffusion coefficient during the re-absorption phase is initially very similar to the diffusion coefficient during the heating phase, which may suggest that the material properties that affect D (polymer plasticity, etc.) might relax more slowly than the rapid temperature decrease (due to the short thermal time constant of the device).

In summary, it has been observed that shorter heating pulses are preferable over longer pulses due to reduced heating power and reduced undesirable chip/package heating. However, it might be difficult to determine the true diffusion coefficient for the particular polymer-analyte combination from the analyte transients, as the effective D appears to change during analyte re-absorption.

It is also interesting to further visualize the simulation results for the analyte diffusion into the polymer film and compare the results for long heating pulses (reaching steady-state analyte distribution in the polymer) and short heating pulses. Figures 46a and 46b show the relative concentration profile through the thickness of the polymer film for different times in the case of the 256 ms and 32.8 s long heating pulses, respectively. The heating pulse is simulated by a (relative) concentration drop from 1 to 0 at 1 s. At the end of the heating pulse, the surface concentration jumps back from 0 to 1. The figures feature each 101 concentration profiles, equally spaced in time and simulated over the time of 10 s and 50 s for the 250 ms and 32.8 s pulse. The diffusion coefficient was set to 2×10^{-8} cm²/s during “heating” and 8×10^{-9} cm²/s outside of the “heating” pulses.

While the concentration profile within the film reaches equilibrium (i.e., a relative concentration of 1 throughout the film) in case of the 32.8 s heating pulse, the analyte profile never reaches equilibrium in the case of the short pulse. In case of the 250 ms heating pulse, the concentration at the bottom of the polymer only reduces to approximately 70% of the equilibrium concentration during the simulated heating pulse. In this case, analyte desorbs and re-absorbs principally from the polymer volume close to the polymer surface, which explains the observed faster signal transients in the case of short pulses.

The effect of the heating pulse length on the observed signal transients suggests investigating the effect of a periodic heating with increasing frequency on the analyte sorption. It is expected that the sensor response exhibits a low-pass characteristic in this situation, where the cut-off frequency somehow depends on the polymer film thickness and the analyte diffusion coefficient in a particular polymer.



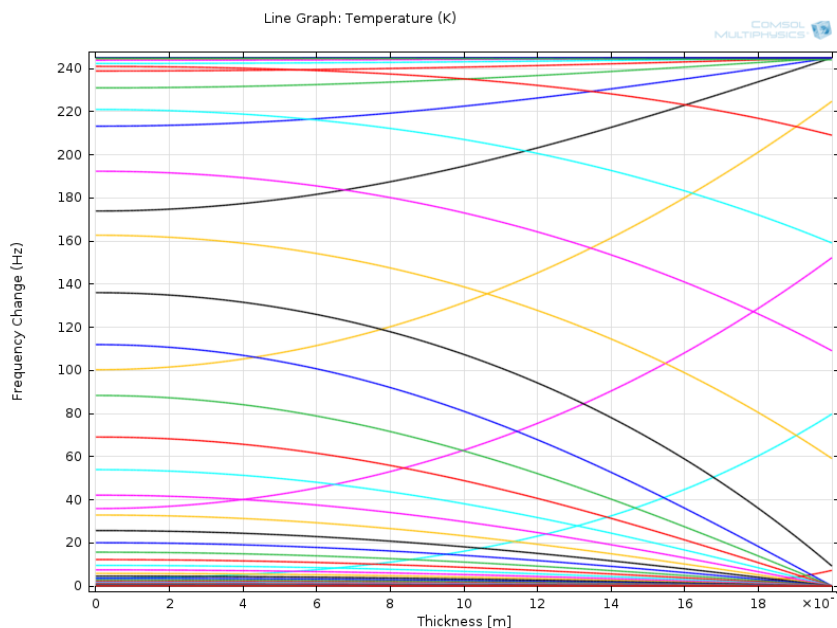


Figure 46 - Relative analyte concentration throughout the polymer film for a simulated heating pulse of (top) 256ms and (bottom) 32.8s. The heating pulse is simulated by a concentration drop from 1 to 0 at 1s. At the end of the heating pulse, the surface concentration jumps back from 0 to 1. The figure features 101 concentration profiles, equally spaced in time and simulated over the time of 10 s and 50 s for the 250 ms and 32.8 s pulse. The diffusion coefficient was set to $2 \times 10^{-8} \text{ cm}^2/\text{s}$ during “heating” and $8 \times 10^{-9} \text{ cm}^2/\text{s}$ outside of the “heating” pulses.

Temperature-induced Transients for Different Analytes

Additionally, thermally-generated transient signals were employed as an approach to improve sensor selectivity, similar to the previously-demonstrated work with valve-generated transient signals in the previous chapter. In this case, a hammerhead sensor coated with approximately $2 \mu\text{m}$ of PECH was exposed to a series of aromatic hydrocarbons – benzene, toluene, and mixed xylenes – where each compound was held at a fixed concentration and flow rate during the measurements. Once at equilibrium, the sensor was heated with pulses of approximately 17mW of heating power and varying durations. Figure 47 shows the normalized absorption due to valve-generated transients for

the aromatic series, and Figure 48 shows the normalized re-absorption transients following exposure to a 4 sec heating pulse.

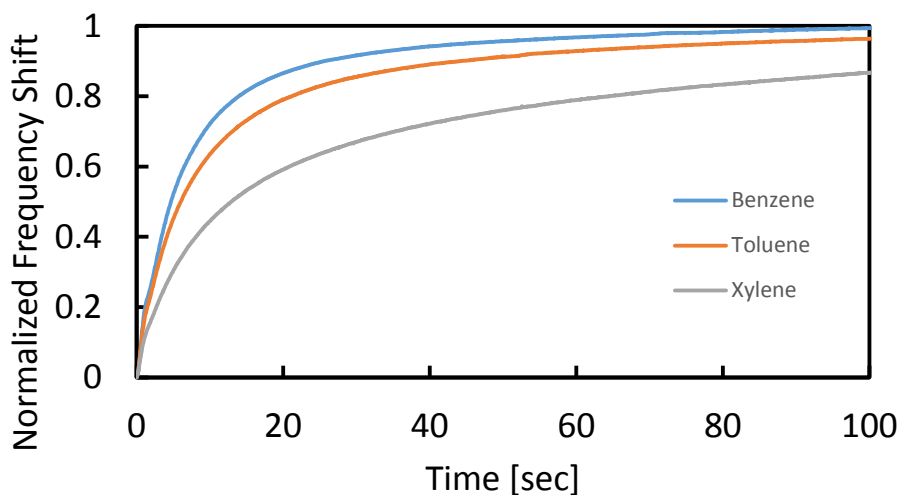


Figure 47 – Normalized valve-generated transients for PECH coated resonator exposed to 23400ppm benzene, 10,700ppm toluene, and 2400ppm xylene.

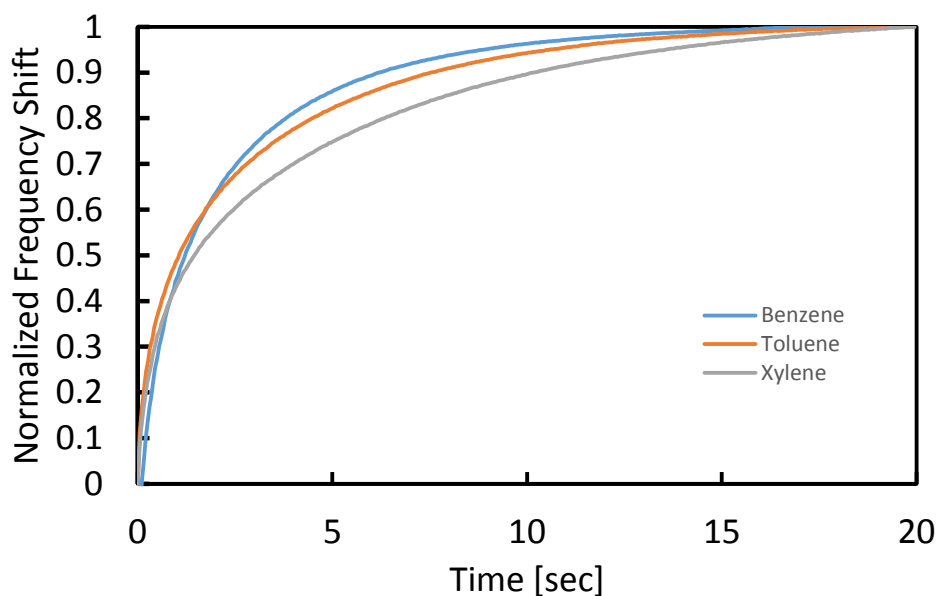


Figure 48 – Normalized thermally generated re-absorption transients following a 4 sec heating pulse for PECH coated resonator exposed to 23400ppm benzene, 10,700ppm toluene, and 2400ppm xylene.

From a comparison of Figures 47-48, it is clear that the diffusion rates differ for the case of valve transients and the case of the thermally-generated transients. This is likely due to the many effects discussed in the previous sections (e.g., preferential surface desorption, chip/package heating, diffusion through stagnant gas layer to reach the sensing film). It is also clear, however, that relative rates of absorption for the compounds in the aromatic series agree with the relative molecular weight of each compound, as seen with the alcohol series in the previous chapter. Thus, these data indicate potential enhancing sensor selectivity through the use of thermally-generated transients. For comparison, Figure 49 shows the normalized re-absorption transients following exposure to a 256 msec heating pulse.

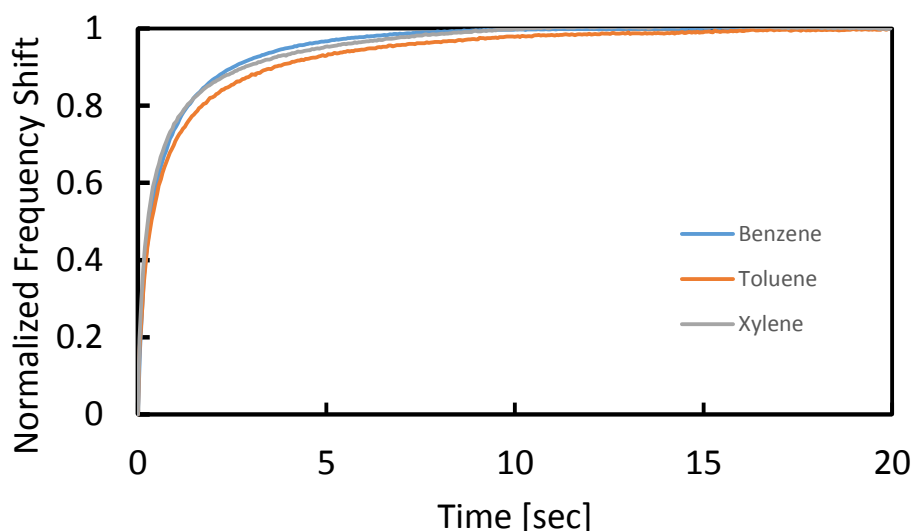


Figure 49 – Normalized thermally-generated re-absorption transients following a 256 msec heating pulse for PECH coated resonator exposed to 23,400ppm benzene, 10,700ppm toluene, and 2400ppm xylene.

It is clear from comparing Figures 48 and 49 that the sorption curves converge as the pulse duration is reduced. This seems to confirm the previous analysis, which concluded that short pulses of insufficient duration do not drive the sorbent layer to equilibrium and result in preferential desorption from a thin surface layer only. As a final example, Figure 50 shows the normalized desorption transients for the sensor during a 4 sec heating pulse.

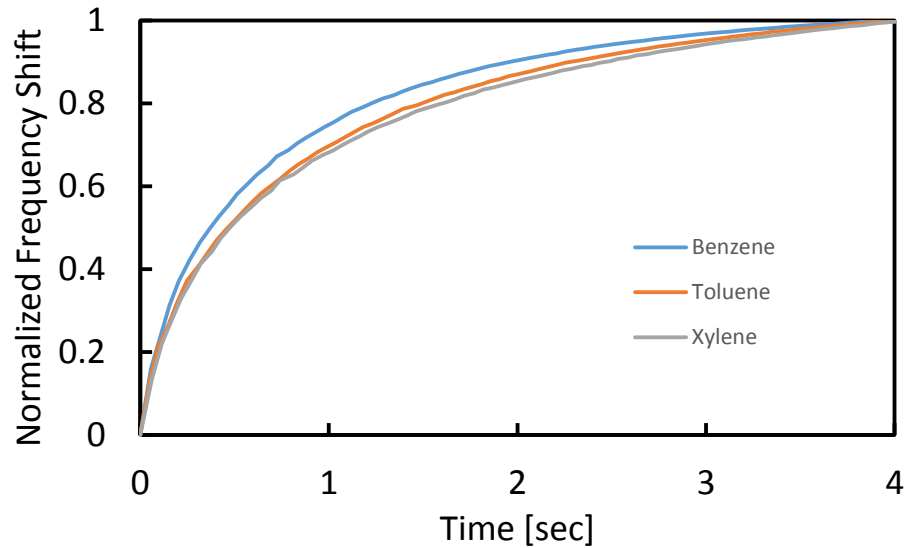


Figure 50 – Normalized desorption transients during a 4 sec heating pulse for PECH coated resonator exposed to 23,400ppm benzene, 10,700ppm toluene, and 2400ppm xylene.

CH 5 – PRE-CONCENTRATOR THEORY & DESIGN

In addition to the work demonstrated regarding cantilever-based chemical sensors, this research also presents the development of a MEMS-based micro thermal pre-concentration (μ TPC) system for enhanced detection of volatile organic compounds (VOCs) in the gas phase. The novel system features integrated chemical sensing technology, which can be used to improve the performance of previously developed cantilever-based resonant micro-sensors and enables novel modes of operation without the need of an external fluidic system.

As discussed previously, all chemical sensors are constrained by an inherent limit of detection (LoD), and are incapable of reliably detecting chemical species at concentrations below this limit [3, 4, 18, 42, 46, 105, 106]. As stated in Chapter 1, the LoD for a cantilever-based resonant chemical sensor is defined as three times the noise-equivalent analyte concentration (Equation 1), which can be approximated by

$$LoD = 3 \frac{\Delta f_{min}}{S}$$

Equation 12 – Limit of detection for resonant cantilever sensors.

where Δf_{min} is the lowest detectable frequency change (determined by the noise and stability) and S is the sensitivity determined by sorption into a sorbent coating [92]. From Equation 12, it is clear that the LoD (i.e. minimum detectable concentration) can be

improved by increasing either the Q-factor of the resonator (i.e. by decreasing Δf_{min}) or the sensitivity, or both, and that an arbitrarily low LoD can be achieved by doing so. The results of the preceding chapters have demonstrated various approaches to improving the performance of individual sensors by utilizing localized coatings or novel operation modes.

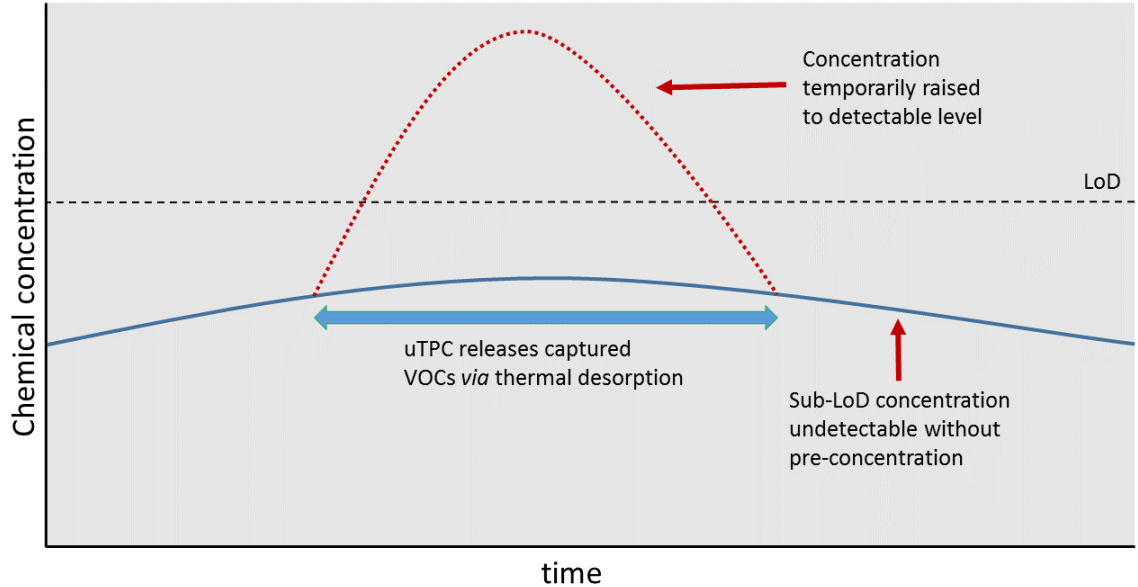


Figure 51 – Graphical representation demonstrating how chemical pre-concentration can improve the effective LoD for chemical sensors, enabling detection of sub-LoD concentration levels that would otherwise be undetectable by the sensor alone.

Alternatively, chemical pre-concentration systems can improve the effective LoD of chemical sensors by accumulating target chemical species at sub-LoD concentrations over time and rapidly releasing them within the vicinity of the chemical sensor [3, 4, 36, 44, 105-108]. This rapid release of captured analytes can temporarily raise the chemical concentration above the sensor's inherent LoD, enabling measurement (Figure 51). Through analysis of the accumulation and release cycle times and the measured concentration spike, the previously undetectable sub-LoD concentration can be deduced,

effectively enabling the system to detect concentrations below the theoretical LoD of the chemical sensor alone [3, 4, 36, 42, 46, 105-108].

Various chemical and biological pre-concentration systems have been developed by several groups in the academic and commercial communities, for a wide range of applications [1, 3, 4, 18, 36, 42, 44, 46, 107-109]. This work focuses on those that can be categorized as μ TPCs used to enhance detection of VOCs in the gas phase. Specifically, a μ TPC in this context is a MEMS-based chemical pre-concentration device which utilizes rapid thermal cycling to purge target chemical compounds from an active sorbent layer, in a process known as thermal desorption [3, 4, 22, 36, 42, 46, 108, 110]. Thermal desorption is typically performed just prior to the μ TPC reaching full saturation, to maximize the amount of VOCs -- and thus the concentration -- released into the vicinity of the corresponding chemical sensor. The term ‘dead volume’ is often used to refer to the fixed volume surrounding the sensor, which includes the chamber volumes of the sensor and μ TPC as well as the adjacent volumes introduced by interconnect tubing and valves due to interfacing with an external gas flow system [3, 4, 22, 36, 37, 44, 46, 107, 111].

A key objective of μ TPC design is to minimize the dead volume so that the transient concentration spike due to thermal desorption is maximized [37, 108, 111]. Minimizing the thermal time constant of the μ TPC is also preferable, as this reduces the temporal width of the thermal desorption event, which in turn maximizes the peak height of the concentration spike [39, 112-116]. Other design considerations include minimizing the pressure drop across the device – so that it can operate without the need for a high-pressure gas cylinder – and maximizing the ‘breakthrough volume’ [14, 18, 111, 117]. The breakthrough volume refers to the volume of analyte-loaded gas at a fixed concentration

that must pass over the μ TPC before it becomes saturated [4, 22, 36, 44, 111, 118, 119]. The breakthrough volume can be maximized by increasing the sorbent-coated inner surface area that comes into contact with the analyte-loaded gas stream, and by using sorbent materials with either high partition coefficients or high specific surface area, as discussed below [3, 4, 22, 36, 44, 46, 47]. For a given fixed device volume, there is often a compromise between decreasing the pressure drop and increasing the breakthrough volume as it becomes increasingly difficult to force gas flow through areas of densely packed sorbent material which are necessary for capturing large amounts of VOCs. Finally, the most important metric for μ TPC design is the pre-concentration factor, which is defined as the ratio of the peak concentration during thermal desorption to the original concentration during accumulation [3, 4, 42, 44, 110, 120, 121].

Typically, the specific target application determines the desired thermal desorption temperature, as various gas-phase species desorb at different temperatures from a given sorbent based on the vapor pressure and boiling point of the compounds and interaction between the analyte and sorbent [3, 22, 30, 37, 111, 116, 118, 122-127]. This property also enables arrays of μ TPC devices to perform coarse pre-filtering of samples by coating each device in the array with a sorbent which targets a specific class of VOC compounds [2, 22, 30, 111, 116]. When a complex gas mixture is introduced into the array, individual compounds segregate and partition by class into separate devices in the array. Individual addressing of devices during thermal desorption enables the various classes of compounds to be desorbed at different times, thereby accomplishing an initial rough temporal separation prior to chemical measurement. In applications where the μ TPC is used for injection into a GC system, coarse pre-filtering in this manner can enhance separation of

co-eluting compounds and improve the overall performance of the system [19, 20, 25, 30, 32, 47, 51, 112, 116, 128-130].

The choice of sorbent materials used in a μ TPC device can vary widely, and depends on the properties of the target VOC analytes, desired thermal desorption temperature, and whether the pre-concentration approach is exhaustive or equilibrium-based [18, 19, 28, 30, 37, 45, 46, 105, 107, 112, 113, 131-135]. With an exhaustive μ TPC approach, the design goal is to capture all target VOCs in the sample volume, typically through the use of a high-surface area activated carbon sorbent layer, and perform thermal desorption once the sorbent layer approaches saturation [14, 18, 32, 36, 37, 39, 50, 105, 111, 114-117, 125, 127, 130, 135-139]. Equilibrium μ TPCs are also designed to initiate thermal desorption just prior to saturation, but no attempt is made to capture all of the VOCs flowing past the device. Rather, thermal desorption is initiated when an equilibrium is reached between the sample concentration in the chamber and the concentration of VOCs in the sorbent layer of the μ TPC [19, 26-28, 30, 43, 45-47, 107, 129, 131-134, 140, 141]. This equilibrium point is determined by the partition coefficient of the given sorbent material and the corresponding target VOC concentrations as they diffuse into the sorbent [22, 43, 59, 69, 85, 90, 98, 106, 134]. Equilibrium μ TPCs typically utilize thin-film polymer-based sorbents, such as polydimethylsiloxane (PDMS) and Tenax TA, rather than the activated carbon sorbents employed in an exhaustive μ TPC system [18, 39, 50, 105, 114, 116, 135, 142].

Often, a μ TPC interfaces with a downstream gas chromatography (GC) system and serves to inject concentrated VOC samples into the GC separation column [19, 20, 24, 25, 30, 32, 38, 41, 116, 143, 144]. Operation of arrayed or cascaded μ TPC devices, in

combination with appropriate sorbent choices for target VOCs, can enable rough pre-filtering of sample analytes (e.g., based on vapor pressure differences) prior to analysis or injection into the GC system, which can improve measurement cycle time and precision of the system as a whole [47, 51, 112, 127-130]. Due to their small size, μ TPCs are capable of operating at relatively low power and can be combined directly with existing MEMS-based sensor technologies and micro-GC systems for deployment on mobile platforms, enabling novel applications for real-time on-site data collection [24, 32, 38-41, 50, 70, 116].

The specific focus of this work is to develop a novel equilibrium-based μ TPC system that is integrated on-chip with existing resonant cantilever-based chemical sensors developed at Georgia Tech. The integrated design improves the effective LoD of the cantilever-based chemical sensors, enhancing their effective sensitivity, and enables measurements to be completed within a few seconds of thermal desorption, improving significantly on reported measurement cycle times for state-of-the-art systems demonstrated in the literature. For example, subsequent analysis of VOCs via separation downstream in a conventional GC column can require the sample to be transported off-site to a dedicated testing facility, precluding applications where immediate real-time data is the highest priority (e.g., clinical monitoring of patient in critical condition, quarantine of a developing hazardous situation) [9, 18, 20, 32, 38-41, 46, 47, 50, 70, 105, 110, 116, 138, 145-147]. Portable GC systems have recently been demonstrated, but still require complex fluidic control systems with costly reagents, support fluids and high-pressure gas cylinders [18, 32, 36, 40, 105]. The integrated sensing platform presented in this work can perform measurements in less than 30 seconds and is capable of operating in both a traditional gas-

flow setup and also in a static atmosphere which requires no external fluidic flow system, thereby enabling novel measurement methods and applications. The ability to operate without a forced-flow fluidic system is a distinct advantage and can considerably enhance the portability of a sensing system, facilitating deployment on mobile airborne platforms as well as long-term monitoring stations in remote locations.

Furthermore, since ideal operation of a μ TPC requires thermal desorption to occur just below the saturation point of the sorbent-analyte combination, real-time knowledge of the VOC uptake rate into the sorbent of the μ TPC is desirable. The rapid measurement cycling of the proposed design enables more accurate tracking of the saturation state of the μ TPC, which can be used to improve overall system performance. For example, if multiple sequential measurement cycles reveal that the μ TPC was saturated when thermal desorption occurred, the next measurement can reduce the μ TPC accumulation time until the μ TPC is being operated just below full saturation. Since the cycle time for this system is on the order of seconds (rather than minutes or hours), the saturation loading state of the μ TPC can be tracked essentially in real-time, ensuring that the system is operating in an optimal state. Finally, the real-time measurement capabilities of the integrated chemical sensors allow for transient analysis of thermally generated signals, which has been demonstrated to improve analyte discrimination for VOCs without the need for a separation column or external fluidic system [55, 90].

Pre-concentrator Design & Simulation

To achieve the stated design goals necessary for optimal pre-concentration – low dead volume, high breakthrough volume, low thermal time constant, and high temperature elevation with low power consumption – the system demonstrated here implements a suspended membrane geometry formed from an SOI substrate. This design choice has the advantage of enhancing thermal isolation of the device and enabling relatively high temperature elevations even for low levels of applied heating power. The membrane is designed to have a large surface-area-to-volume ratio but low thermal mass (and therefore, low thermal time constant), with arrays of 3-D high aspect-ratio ridges and pillars on the back surface formed via DRIE of silicon. Integrated onto the front surface of the membrane are sets of diffused resistors which are designed for performing thermal desorption (via joule heating) and for measuring the temperature elevation of the device due to the temperature-dependent resistivity of doped silicon (Figure 52).

This approach combines into one cohesive whole the individual strengths from various μ TPC devices presented in the literature. For example, some groups have implemented a membrane structure – which provides excellent thermal isolation, enabling rapid heating and low-power operation – but did not incorporate high-aspect-ratio 3D features necessary to achieve a high surface-area-to-volume ratio [3, 148]. As a result, the pre-concentration factor for such designs is limited due to the low surface area available for sorbent placement. Other groups avoided a membrane structure and instead focused on fabrication simplicity, which in turn minimizes dead volume and maximizes surface area and sorbent capacity [18, 19, 30, 37, 46, 47, 105, 112, 113, 149]. This approach, however, has the disadvantage of increased thermal mass – which leads to longer thermal time constants –

and reduced thermal isolation which ultimately limits the practical thermal desorption temperature and requires higher power consumption to achieve the same thermal desorption temperature as a membrane-based device. Similar to both groups, the design presented here implements arrays of individually-addressable μ TPC devices which enables coarse pre-filtering by desorption of each device in the array one at a time. The final design resulted in a packaged dead volume (i.e. inner chamber volume) of approximately 10 μ L, a thermal time constant of less than one second and a temperature elevation in excess of 200°C for less than one Watt of applied heating power.

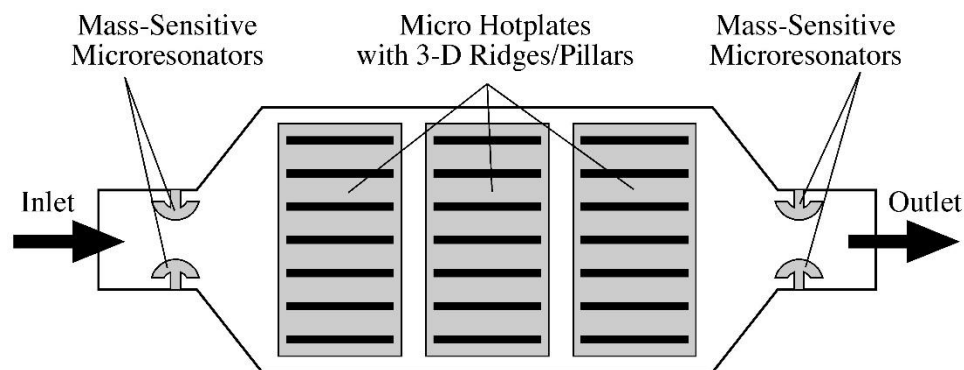


Figure 52 - Graphical representation of pre-concentrator concept, with array of micro hotplate structures, inlet and outlet ports, and integrated mass-sensitive chemical sensors.

Each die is designed to accommodate an array of two or three μ TPCs of varying sizes and four cantilever-based chemical sensors (Figure 52). The chemical sensors are placed at the inlet and outlet ports of the die to allow for monitoring of both upstream and downstream concentration levels when operated in a traditional gas-flow configuration. The system also has the capability of operating in a static atmosphere setup, where no external flow system is required. Two of the four sensors can remain uncoated as reference

devices in a differential setup to allow for the possibility of removing temperature effects in real-time during measurement.

The mass-sensitive micro-sensors, based on hammerhead-type resonator structures, which have been discussed previously in Chapters 2-4 [12, 62, 84, 85, 89, 90], have a mass resolution in the pico-gram regime, and are fabricated within the same process sequence as the μ TPC arrays. The direct, on-chip integration of cantilever-based chemical sensors into the same chamber as the μ TPC devices represents a novelty and has distinct advantages over systems which separate the two. For example, this arrangement results in a reduced total dead volume for the system as a whole (by reducing e.g. the interconnect volume for valves and tubing between sensors and μ TPCs), and reduced measurement cycle times. As discussed previously, the integrated sensors can monitor in real-time the loading state of the μ TPC and also enable novel modes of operation which can allow the system to be operated in a static atmosphere, without the need for an external fluidic system. The cantilever-based sensors are well-understood and feature the novel integrated heating units described in Chapter 3, which allow for the on-chip generation of thermal transients via temperature modulation of the heating units [88].

Thermal Design

Prior to the development of a suitable fabrication process flow that would be compatible at the wafer-level with the existing cantilever-based microsensors, the μ TPC devices were designed at a high level with a focus on making appropriate compromises among the several conflicting variables (e.g. pressure drop vs. breakthrough volume, thermal rise time vs. maximum temperature elevation vs. power consumption). The first design constraint examined was the target temperature elevation and thermal rise time during thermal desorption. External pre-existing system specifications required the design

to achieve a maximum temperature elevation of 200 °C in less than 1 second, with minimal power consumption. For example, data from Supelco sorbents show typical desorption temperatures greater than 200 °C for commonly-used VOCs [150]. From the theory of heat transfer, it can be shown that the temperature elevation for a given power dissipation in a system dominated by heat conduction is given by

$$\Delta T = Q \cdot R_{thermal}$$

Equation 13 – Temperature elevation as a function of heating power.

where ΔT is the temperature elevation, Q is the instantaneous power dissipation, and $R_{thermal}$ is the effective resistance to heat conduction given by

$$R_{thermal} = \frac{L}{k \cdot A}$$

Equation 14 – Thermal resistance.

where A , the cross-section, and L , the length over which the heat conduction occurs, are determined by the geometry of the system and k is the thermal conductance of the material. The thermal time constant, $\tau_{thermal}$, is given by

$$\tau_{thermal} = R_{thermal} \cdot \rho \cdot c_p \cdot V$$

Equation 15 – Thermal time constant.

where $\tau_{thermal}$ is the thermal time constant, $R_{thermal}$ is the equivalent thermal resistance of the system, ρ is the material density, C_p is the specific heat, and V is the volume. It should be noted that these equations assume that the system can be described by lumped elements, such as a uniformly heated volume V that is connected through a (massless) thermal

resistance R_{thermal} to a heat sink. From these equations it becomes clear that a theoretical maximum temperature elevation can be achieved by maximizing R_{thermal} and minimizing k , while the thermal time constant is minimized by reducing R_{thermal} and the thermal mass. To satisfy both conditions, however, a compromise must be made with regards to R_{thermal} . Additionally, for real devices there are practical, physical limits to the lower bounds of A and the upper bounds of L , and one is further constrained by k values offered from available materials (e.g. silicon, SiO_2). In addition to the external design specifications of achieving a maximum temperature elevation of 200°C in less than 1 second, the choice to integrate cantilever-based sensors on-chip with the μTPC requires that the silicon membrane thickness falls between $5\text{-}25\ \mu\text{m}$. Since both the sensors and the μTPC membranes will be fabricated together on the same SOI substrate and with the same process sequence, their suspended thicknesses will be identical. Previous work with the cantilever-based sensors has shown that ideal thicknesses for resonance fall between $5\text{-}25\ \mu\text{m}$, thus constraining the thickness of the μTPC membranes to this range. As a result of these constraints, initial designs focused on exploring – *via* finite element simulation – the practical membrane geometries that are physically realizable with current MEMS/IC fabrication techniques at Georgia Tech, while still optimizing for temperature elevation and thermal rise time.

For the various device geometries presented, static thermal analyses were undertaken to find the temperature elevation (and temperature uniformity across the membrane) for a given heating power, while transient thermal analyses were employed to extract thermal time constants. Additionally, mechanical analyses were used to find the resonance frequency and the membrane deformation under gravity (with sorbent mass included). Finally, fluidic analysis of the μTPC arrays, with simulated flow through inlet and outlet ports, were performed to optimize the fluid flow through the ridge and pillar structures (and, hence, the pressure drop across the μTPC module for a given sample flow). Especially in the case of the fluidic simulations, it was necessary to simplify the model geometry considerably due to limitations of available computing resources. Nonetheless, the results

gave important guidelines for the spacing of the ridge and pillar structures: too narrow a spacing resulted in the sample flow bypassing the ridge structures, while too wide a spacing had a negative effect on the effective surface area available for sorbent deposition. Thus, the fluidic simulations aided in the optimization of ridge and pillar arrangements, resulting in reduced impedance for sample flow through the device.

Final Pre-Concentrator Design

Using the finite element software COMSOL, the performance of various device geometries, including suspended membrane structures with and without 3D ridge and pillar structures, was investigated. In the following, however, we focus on the simulation results for the final designs. Thereby, the finite element simulations described below not only consider heat transfer by conduction through the silicon, but also heat transfer through the air by conduction. Initially, the air around the membrane was simulated using a thermal conductivity of $0.026 \text{ W}\cdot\text{m}^{-1}\text{K}^{-1}$. The resulting models are computationally demanding and, thus, in subsequent models heat transfer through the air was simulated using a heat transfer coefficient of $h = 50 \text{ [W}\cdot\text{m}^{-2}\cdot\text{K}^{-1}]$ applied to the surfaces of the membrane. This heat transfer coefficient corresponds to a conduction over approximately $500 \text{ }\mu\text{m}$ of air.

The first design features a $1 \text{ mm} \times 1 \text{ mm} \times 20 \text{ }\mu\text{m}$ membrane supported by four bent legs with total lengths of 1.3 mm each and cross-sections of $100 \text{ }\mu\text{m} \times 20 \text{ }\mu\text{m}$ (Figure 53). This design also features six high-aspect ratio ridges on the membrane, each having dimensions of $1 \text{ mm} \times 500 \text{ }\mu\text{m} \times 50 \text{ }\mu\text{m}$, yielding a total surface area of 7 mm^2 per device and a total surface area of 21 mm^2 for an array of three devices. The effective thermal

resistance of the four parallel support legs was calculated to be 997 K/W. For a simulated input power of 500 mW, τ_{thermal} was found to be 0.2 sec with a temperature elevation of 265 K. The mechanical properties of the design were also simulated *via* FEA, yielding a simulated fundamental resonance frequency of 5.9488 kHz and a deflection of 105 nm for an estimated additional sorbent mass of 5 mg. Finally, the fluidic properties of the design were simulated, revealing a relatively low estimated pressure drop of 35.6 Pa across an array of three devices. Note that the maximum temperature elevation is smaller than what would be expected from conduction along the support legs only, because thermal conduction through the air is considered as well.

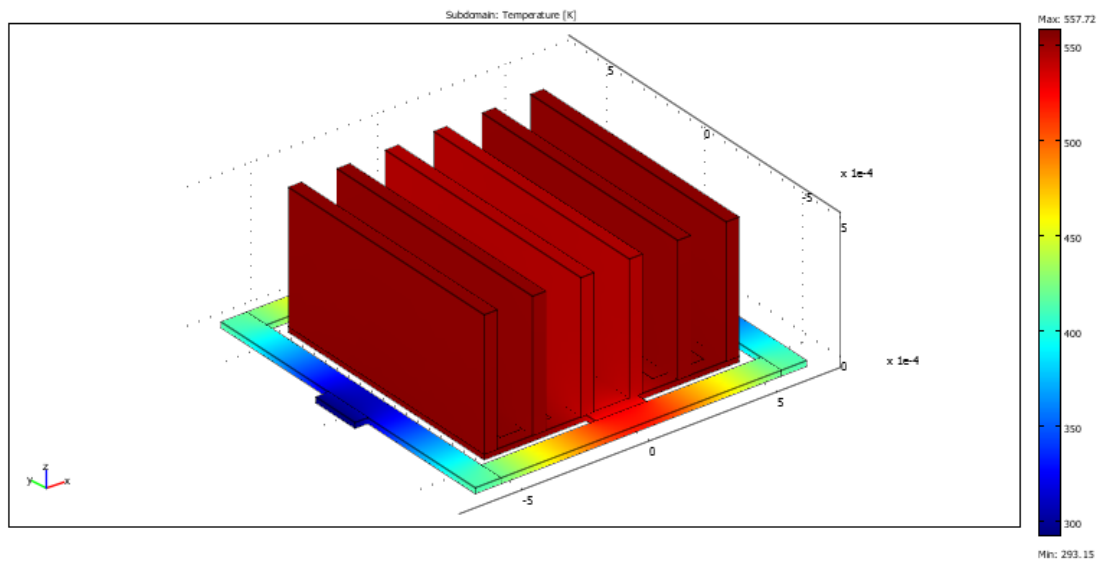


Figure 53 - Thermal simulation of a 1 mm x 1 mm x 20 μm membrane with sorbent ridges included.

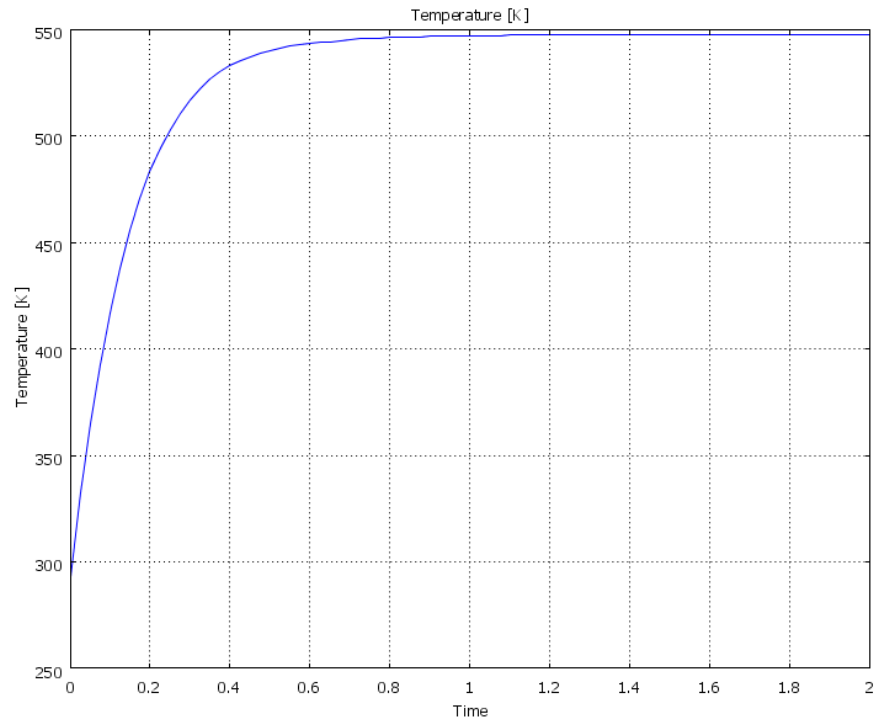


Figure 54 - Thermal simulation of transient response of a 1 mm x 1 mm x 20 μ m membrane with sorbent ridges included.

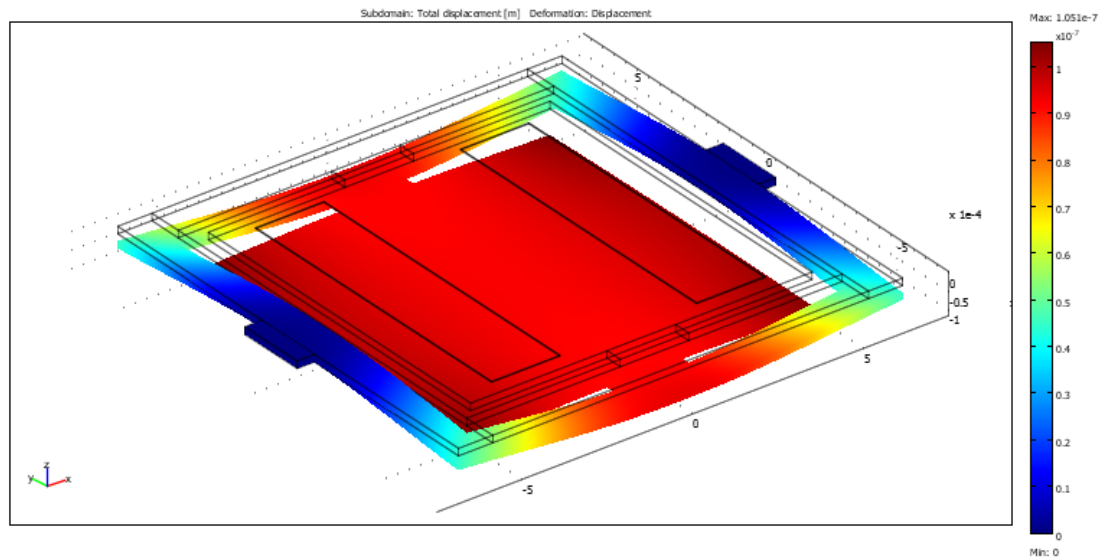


Figure 55 - Gravitational deflection of 1 mm x 1 mm x 20 μ m membrane with ridges and additional 5 mg of sorbent mass included (ridges not pictured).

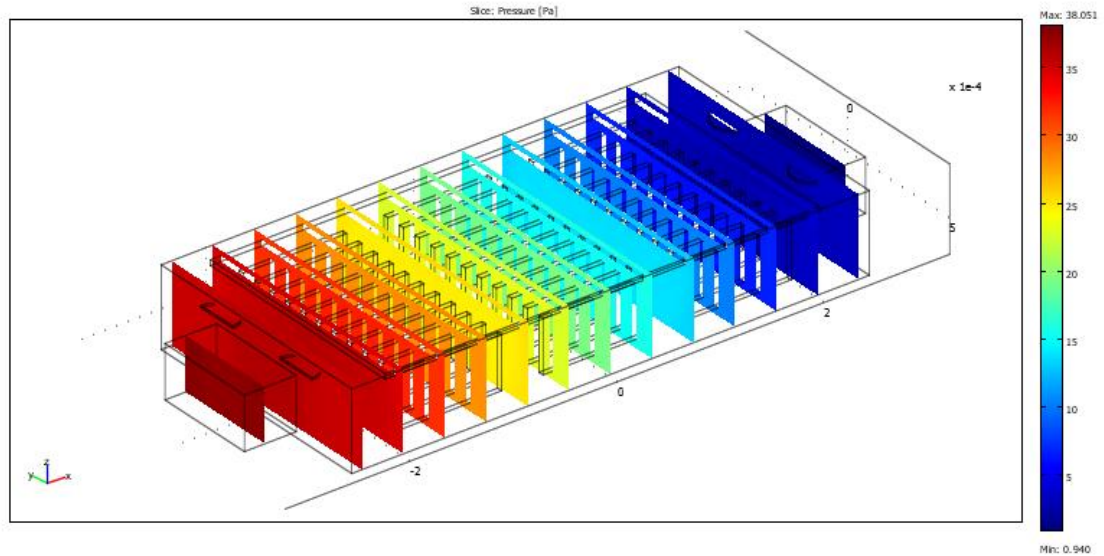


Figure 56 - Pressure drop across an array of three 1 mm x 1 mm x 20 μ m membranes with sorbent ridges included.

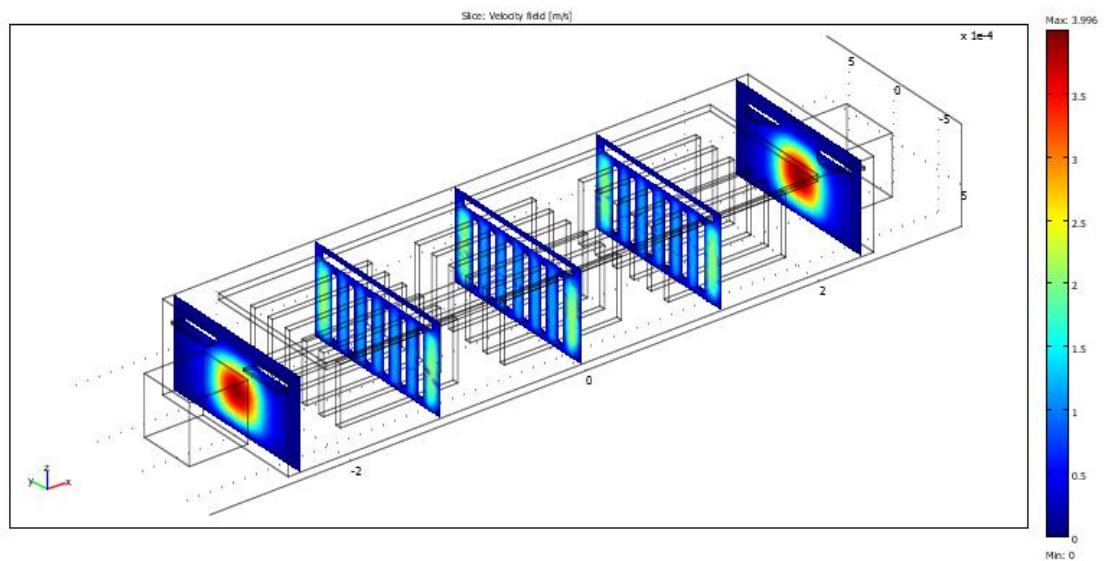


Figure 57 - Fluid flow through an array of three 1 mm x 1 mm x 20 μ m membranes with sorbent ridges included.

The second design features a larger 2 mm x 1 mm x 20 μ m membrane supported by four bent legs with total lengths of 1.8 mm each and cross-sections of 100 μ m x 20 μ m (Figure 58). This design also features eleven high-aspect ratio ridges on the membrane, each having dimensions of 1 mm x 500 μ m x 50 μ m, yielding a total surface area of 13

mm² per device and a total surface area of 39 mm² for an array of three devices. The effective thermal resistance of the four parallel support legs was calculated to be 1380 K/W. For a simulated input power of 500 mW, τ_{thermal} was found to be 0.4 sec with a temperature elevation of 229 K. The mechanical properties of the design were simulated *via* FEA, yielding a simulated fundamental resonance frequency of 2.3338 kHz and a deflection of 443 nm for an estimated additional sorbent mass of 5 mg. Finally, the fluidic properties of the design were simulated, revealing a relatively low estimated pressure drop of 40.7 Pa across an array of three devices.

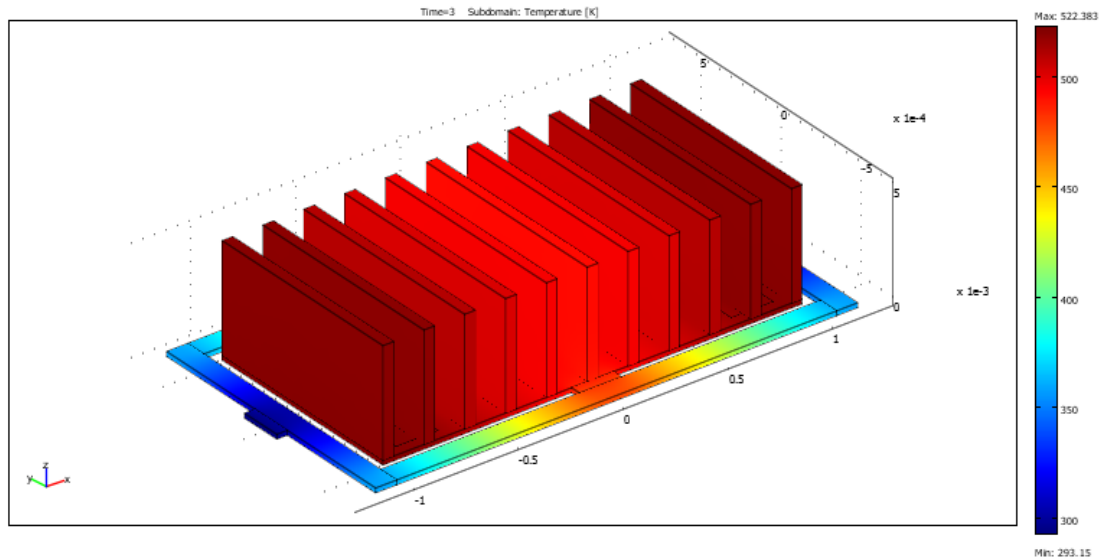


Figure 58 - Thermal simulation of a 2 mm x 1 mm x 20 μ m membrane with sorbent ridges included.

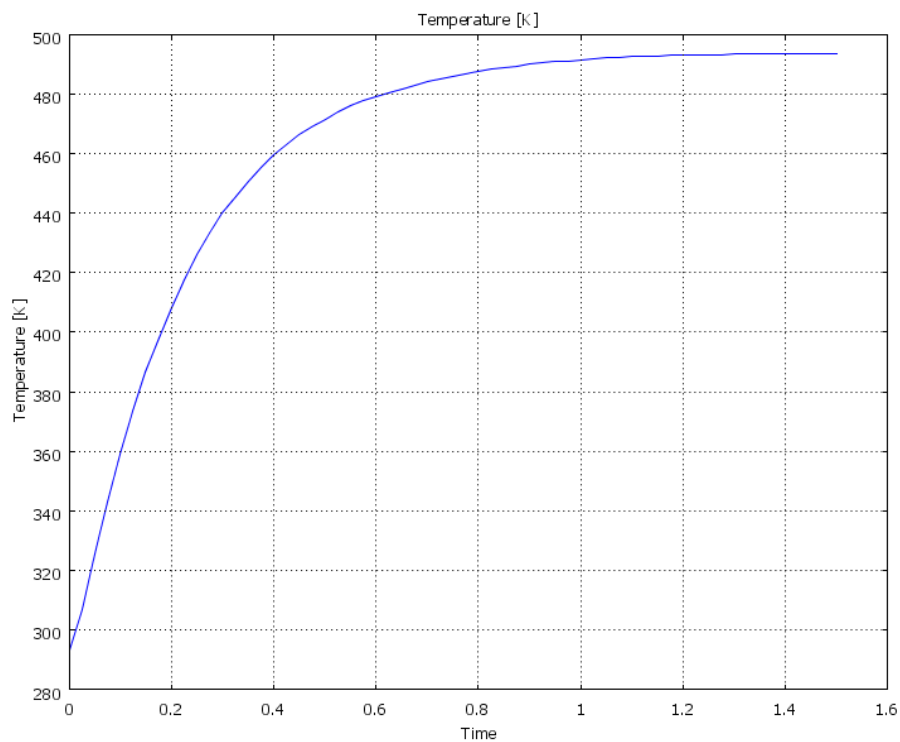


Figure 59 - Thermal simulation of transient response of a 2 mm x 1 mm x 20 μ m membrane with sorbent ridges included.

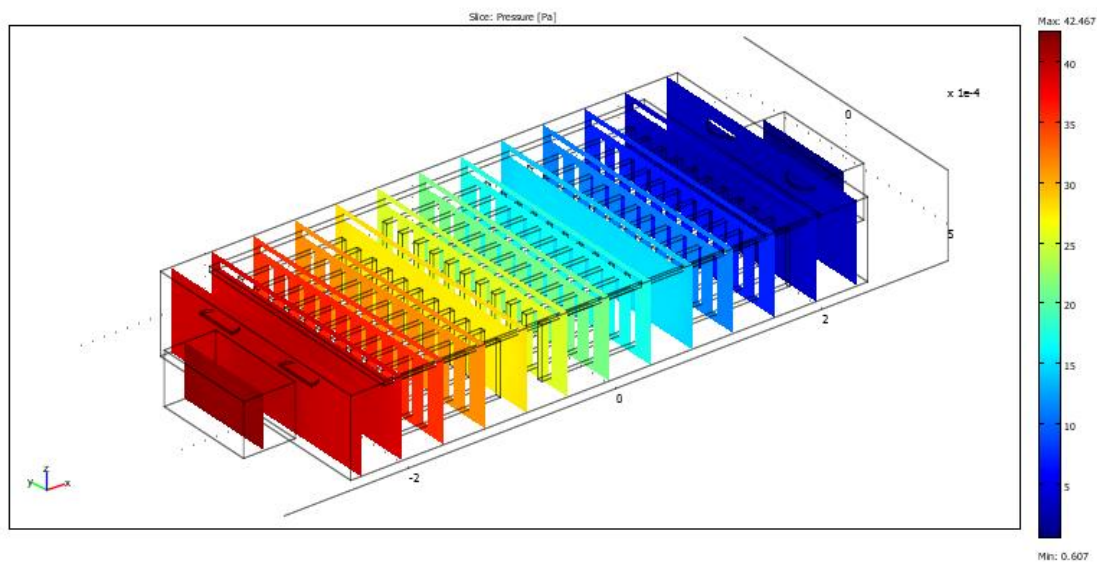


Figure 60 - Pressure drop across an array of three 2 mm x 1 mm x 20 μ m membranes with sorbent ridges included.

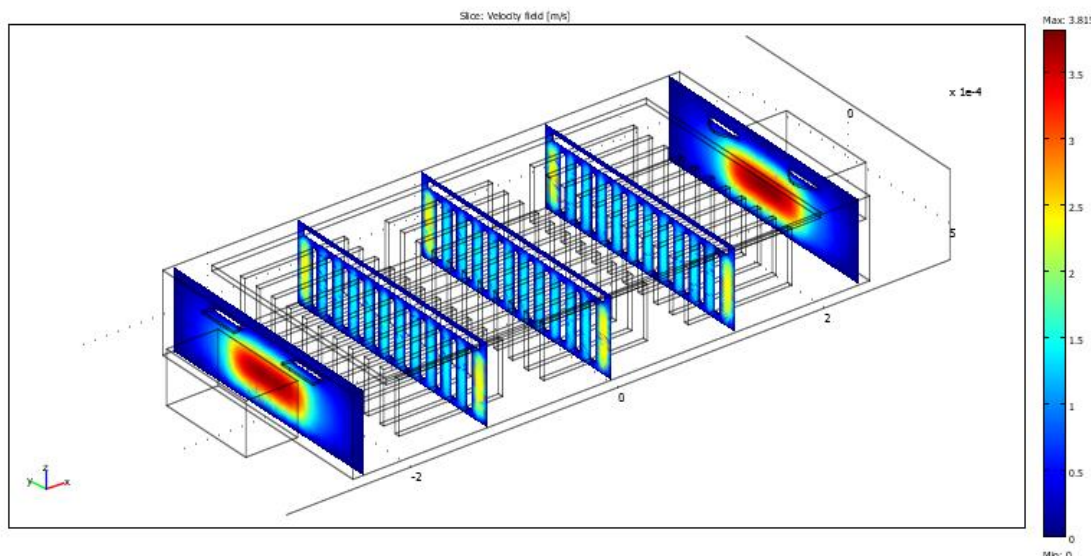


Figure 61 - Fluid flow through an array of three 2 mm x 1 mm x 20 μm membranes with sorbent ridges included.

The third and final design features an even larger 2 mm x 2 mm x 20 μm membrane supported by four bent legs with total lengths of 2.3 mm each and cross-sections of 100 μm x 20 μm (Figure 62). This design also features eleven high-aspect ratio ridges on the membrane, each having dimensions of 2 mm x 500 μm x 50 μm , yielding a total surface area of 26 mm² per device and a total surface area of 52 mm² for an array of two devices. The effective thermal resistance of the four parallel support legs was calculated to be 1763 K/W. For a simulated input power of 1 W, τ_{thermal} was found to be 0.6 sec with a temperature elevation of 271 K. The mechanical properties of the design were simulated *via* FEA, yielding a simulated fundamental resonance frequency of 1.3338 kHz and a deflection of 821 nm for an estimated additional sorbent mass of 5 mg. Finally, the fluidic properties of the design were simulated, revealing a relatively low estimated pressure drop of 52.0 Pa across an array of two devices.

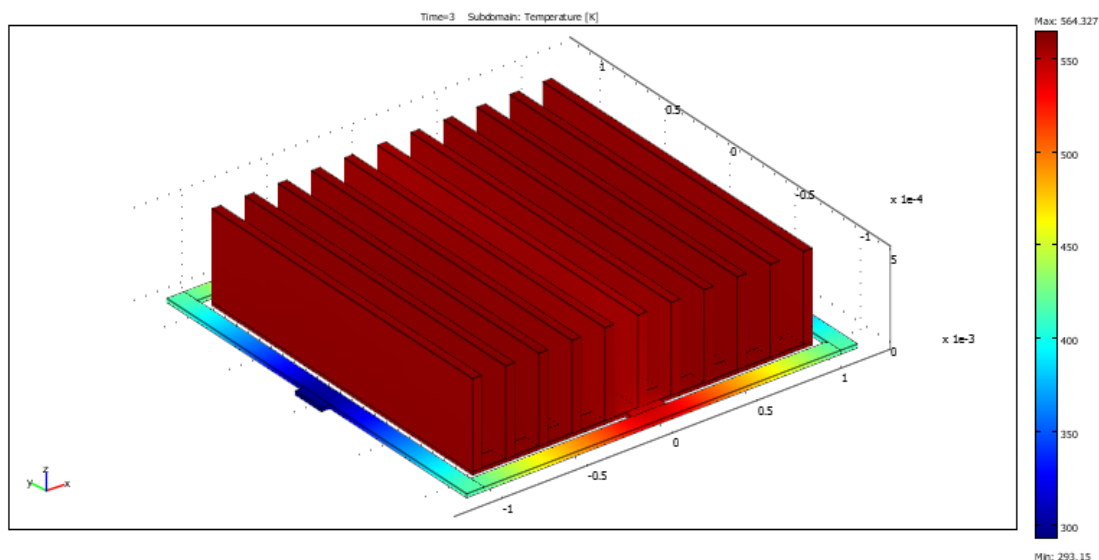


Figure 62 - Thermal simulation of a 2 mm x 2 mm x 20 μ m membrane with sorbent ridges included.

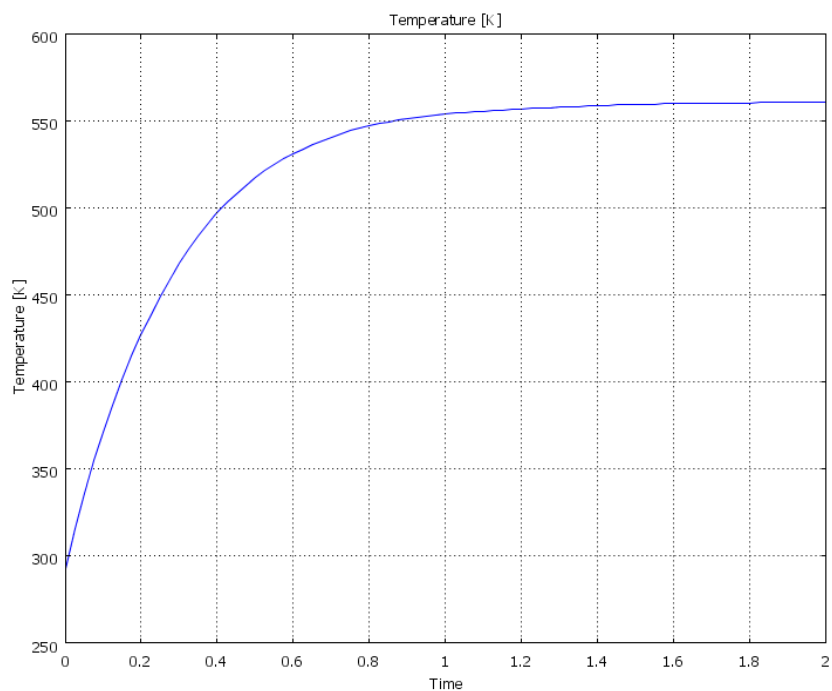


Figure 63 - Thermal simulation of transient response of a 2 mm x 2 mm x 20 μ m membrane with sorbent ridges included.

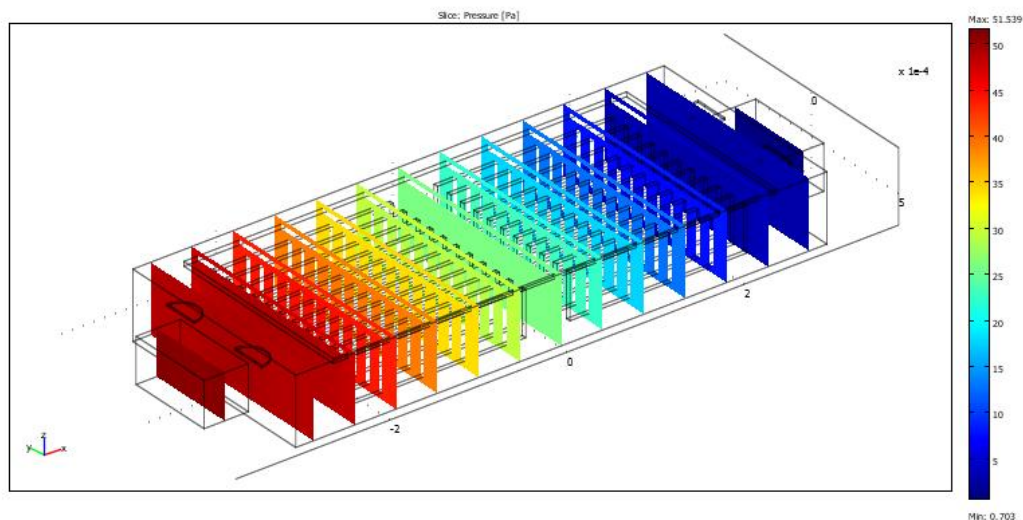


Figure 64 - Pressure drop across an array of two 2 mm x 2 mm x 20 μm membranes with sorbent ridges included.

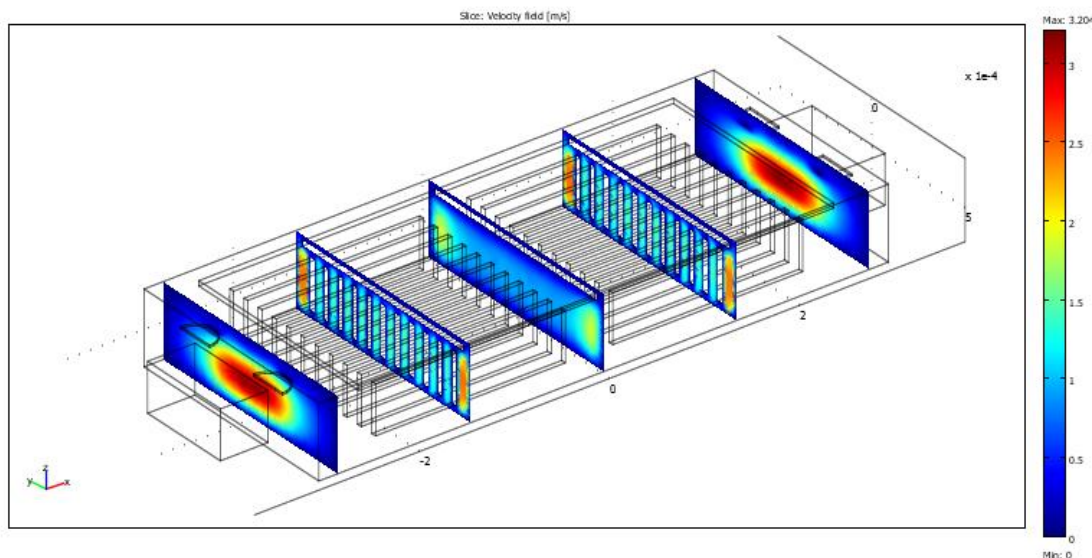


Figure 65 - Fluid flow through an array of two 2 mm x 2 mm x 20 μm membranes with sorbent ridges included.

The simulation results for these three designs are summarized in Table 2. In all three designs, the simulated fundamental resonance frequencies were designed to be orders of magnitude smaller than the resonance frequencies of the integrated resonant cantilever-based sensors. This difference in resonance frequencies is important, in order to minimize

mechanical coupling and interference between the sensors and μ TPCs during operation. The simulations also show that all three designs exhibit relatively uniform heating across the central membrane surfaces, and possess excellent thermal isolation enabling optimal temperature elevation for thermal desorption from the proposed sorbent coatings with minimal power dissipation. Additionally, the mechanical deflection due to gravitational forces acting on the μ TPC devices (including added sorbent mass) was found in all three designs to be negligible, indicating a low probability of mechanical failure during normal operation. Finally, Table 2 shows that these three designs meet the required thermal specifications discussed previously, with minimal on-chip footprint. The designs also cover a wide range of the target design space to allow for extensive “real-world” testing of the effects of the various parameters (e.g. surface area vs. τ_{thermal}) in anticipation of future designs based on knowledge gained from this work. Additionally, several other designs were simulated and evaluated which featured wide ranges of ridge and pillar densities, but the results of these are not included here for the sake of brevity.

Table 2 – Summary of simulation results for final designs, featuring bent-leg geometries and incorporating high aspect-ratio features on the suspended membranes.

	1 mm x 1 mm x 20 μm	2 mm x 1 mm x 20 μm	2 mm x 2 mm x 20 μm
Surface area per device [mm^2]	7	13	26
Surface area per die [mm^2]	21	39	52
Fundamental resonant mode [Hz]	5948.8	2333.8	1333.8
Gravitational deflection with 5 mg of added sorbent [nm]	105	443	821
Pressure drop across array [Pa]	35.6	40.7	52.0
Input power [mW]	500	500	1000
Maximum temperature elevation [K]	265	229	271
τ_{thermal} [15]	0.2	0.4	0.6

CH 6 – SMART PRE-CONCENTRATOR FABRICATION

Upon verification of viable thermal and mechanical designs, a compatible fabrication process flow for integration of the proposed μ TPC designs with existing cantilever-based sensor technology was developed, and corresponding photomasks were designed and manufactured (DeltaMask, Netherlands) using CAD layout software.

This deeper level of the development process saw the introduction of additional design constraints imposed both by fabrication limitations and also by the necessity of interfacing the completed devices with pre-existing, external circuitry required for performing chemical measurements and experiments. For example, the circuit board used to excite and track the resonance frequency shifts of the resonant chemical sensors was previously designed to accommodate a 28-pin ceramic DIL package. As a result of the package dimensions, the maximum practical die size for the μ TPCs was limited to 9 mm x 9 mm. Thus, the mask layout design is constrained to have die sizes below these dimensions, while simultaneously accommodating arrays of large-area membrane-based μ TPCs and also the large-area inlet and outlet ports necessary for introducing analyte gas concentrations into the measurement chamber.

Additionally, each die must have space to place four on-chip cantilever-based chemical sensors, with the many wire traces necessary to carry the signals that excite the sensors into resonance and perform chemical measurements. These wire traces must also terminate in bond pads of sufficient size near the edge of the die to allow for all 28 wirebonds between the ceramic DIL package and die to make connections without overlap or interference. As discussed previously, while large-area 4 mm x 4 mm membranes can be fabricated with current MEMS/IC fabrication techniques, such were deemed unsuitable

for this particular design due to the requirement for an arrayed pre-concentration system and the external constraints placed on die size and footprint. As a result of these restrictions, several smaller-footprint membrane-based pre-concentrators were designed and placed in arrays of two or three devices each, yielding a relatively large total surface area for the system while simultaneously offering reduced thermal time constants (due to reduced thermal mass of the individual membranes) and enabling the possibility of coarse pre-filtering of complex gas mixtures.

In addition to restrictions imposed on individual membrane footprint, an example of a design constraint introduced when considering the possibility of device failure is the support leg dimensions. As discussed previously, the legs must be capable of supporting the weight of the suspended membrane – with added sorbent mass – during manufacture, final packaging, and normal operation following final packaging. Simulations were performed to verify that device failure during normal operation is unlikely, but it is more difficult to accurately assess forces experienced during the fabrication and packaging process (e.g. shear forces due to rinsing the wafer in DI water). Thus, an examination of similarly-dimensioned suspended structures fabricated previously in the IEN cleanroom facilities at Georgia Tech was conducted and confirmed a reasonable likelihood of successful fabrication with high yield for the final designs discussed in Chapter 5.

In addition to supporting the weight of the suspended membrane, the legs must also carry long, thin metal traces with the capability of delivering fairly significant amounts of power without failure (e.g. 12.5 GW/m^3 in the $2 \text{ mm} \times 2 \text{ mm} \times 20 \text{ }\mu\text{m}$ membrane). Since this system is designed with the goal of mobile operation without the availability of high voltages, the power must be supplied primarily using a large current. Due to the thin

metallization layer required for processing the cantilever sensors, which are integrated into the same die and process sequence as the μ TPCs, this requirement results in a situation where the metal traces along the legs must be made as wide as possible to facilitate the delivery of high current to the membrane with minimal power dissipation in the traces (i.e. low resistance) and minimal likelihood of device failure due to overheating and electromigration. With these considerations taken into account, and based on an examination of the current-carrying capacity of the metal traces for previously-developed devices, it was determined that a trace width of 50 μm would exhibit sufficient current-handling capacity for the designs. Since this proposed trace width (including the additional setback tolerances from the edge necessary in manufactured devices) is much less than the 100 μm width of the support legs in the previously-discussed thermal designs, no change in leg dimensions was necessary to accommodate the high-current metal traces. Figure 66 shows a detail from the final mask layout, illustrating the implementation of the support legs from the thermal design stage, overlaid with the proposed metal traces.

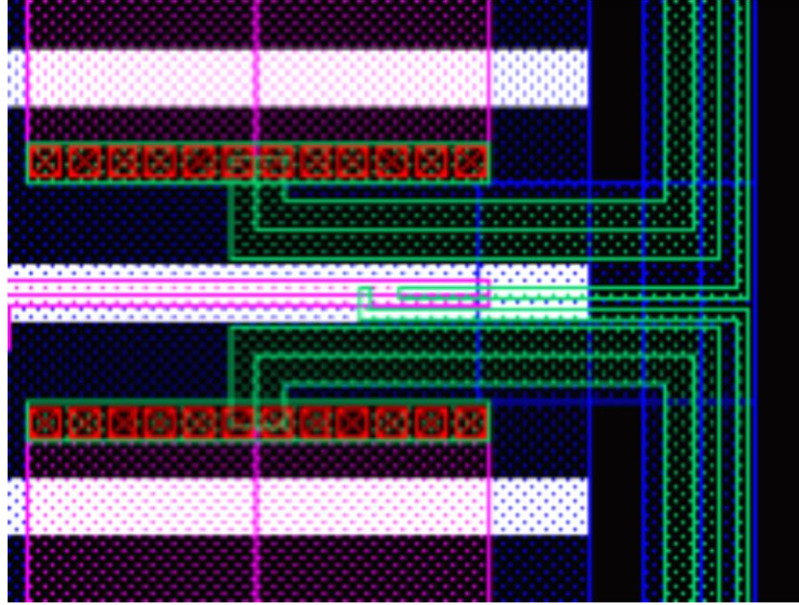


Figure 66 - Detail from final mask layout of current-carrying metal traces (green) on support legs and membrane (blue). The traces make contact to the diffused heaters (purple) by way of arrays of contact vias (red). The white bars show the placement of high aspect-ratio ridges on the back surface of the pre-concentrator membrane, and the black areas indicate the areas of the silicon handle wafer that are removed by a DRIE step from the back of the wafer.

Heater Design

With initial compatibility established between the thermal-mechanical designs and the proposed metallization and device placement on the die, development shifted to design of the integrated heating units. The heaters, which are formed as boron-doped diffused resistors in silicon, were designed to deliver efficient, localized power dissipation in the suspended membrane region *via* joule heating. Examination of the properties of the boron diffusion step in the cantilever sensor fabrication process revealed a sheet resistance of approximately $110 \Omega/\square$. This measured sheet resistance value was achieved *via* boron diffusion from solid sources boron sources into a silicon substrate in a conventional tube furnace at 930°C for 40 min with a constant nitrogen flow throughout. Prior to performing

the diffusion, the geometry of the resistors is defined by removal of the field oxide *via* dry etching of SiO₂ with C₄F₈ in the regions to be doped. Following diffusion, drive-in was performed in a tube furnace. In addition to measuring the sheet resistance of completed devices, the diffusion and drive-in process was also simulated in software *via* SUPREM (Figure 67).

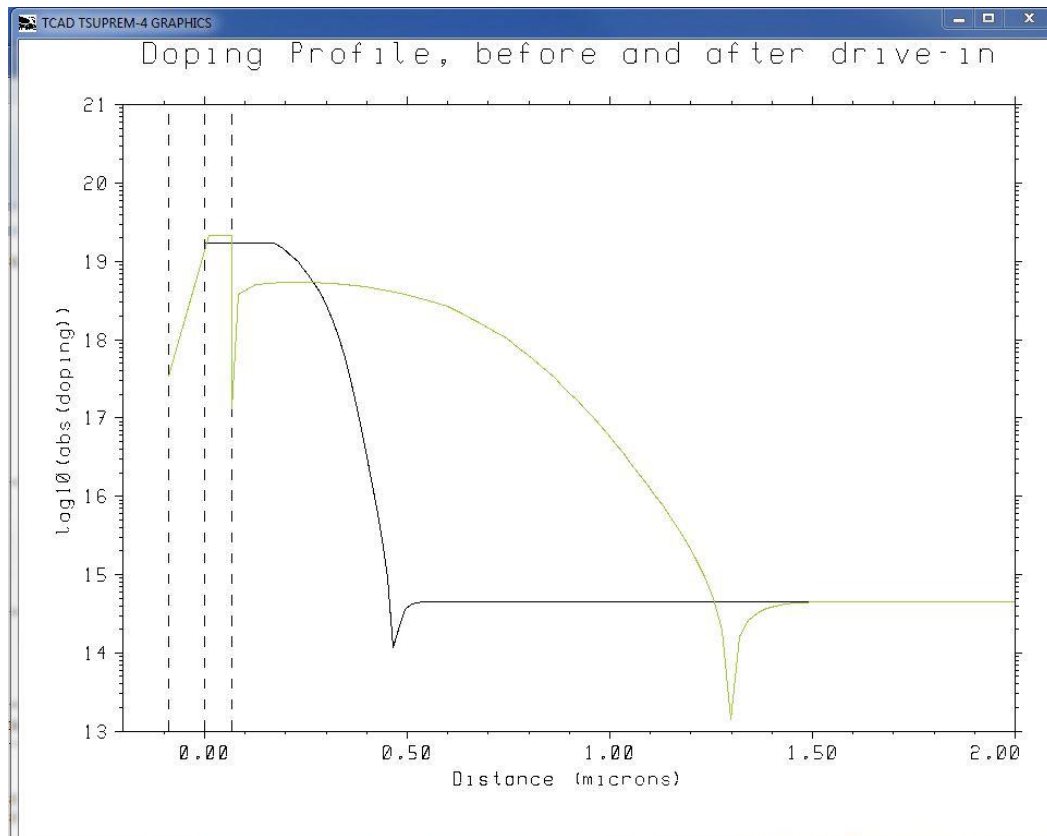


Figure 67 - Result of SUPREM simulation for boron diffusion and drive-in sequence, performed during manufacture of diffused heaters. Prior to drive-in, the simulated junction depth is approximately 0.45 μm ; following drive-in, the junction has deepened to approximately 1.2 μm with a simulated sheet resistance of 248 Ω/\square .

The code and file output for this simulation can be found in Appendix A. The simulation reveals that the initial diffusion results in a predicted junction depth of approximately 0.45

μm , with the drive-in moving the junction further into the silicon to approximately $1.2\ \mu\text{m}$. The simulated sheet resistance is $248\ \Omega/\square$.

With an estimated range of the expected sheet resistance for the diffused heaters, and a desire for mobile operation limiting heating voltages to less than 12 V, the integrated heaters were designed to have nominal resistances of approximately $500\ \Omega$. The aspect ratio required to achieve this resistance for each heater was approximately 5:1. The measurement resistors were designed to have resistances in the mid-k Ω range. During mask layout, the heaters were placed along the membrane edges most distant from the anchor points of the support legs, and two heaters were placed on each membrane (Figure 68). This placement is the same as that used in the previously-discussed thermal simulations, ensuring optimal thermal isolation and temperature uniformity across the entire membrane region.

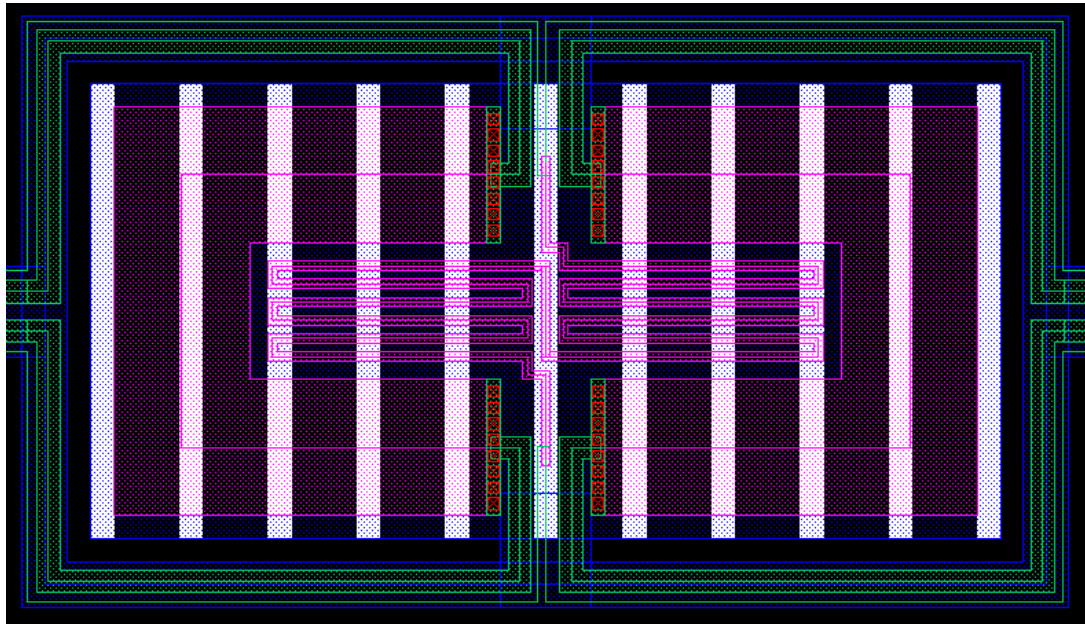


Figure 68 - Detail from final mask layout showing placement of two diffused heaters (purple) on suspended 2 mm x 1 mm pre-concentrator membrane (blue). Electrical traces (green) make contact to

the heaters and measurement resistors by way of arrays of contact vias (red). The white bars show the placement of high aspect-ratio ridges on the back surface of the pre-concentrator membrane.

The two heating resistors have separate electrical traces, and can therefore be wired in series or in parallel during packaging, lending flexibility for the system to adjust its equivalent resistance to match differing external interface requirements. For example, if higher voltages are available at the circuit level, the heaters can be wired in series in order to reduce the number of wire-bonds and external pin connections. If, however, voltages above 12 V are not available, the heaters can be wired in parallel to reduce the heating voltage necessary to achieve the same heating power.

In addition to the two heating resistors, each membrane was also equipped with a long, thin measurement resistor in the center (Figure 68) designed to gauge the real-time temperature of the membrane during heating. The measurement resistor was designed to be capable of performing an accurate 4-wire measurement and a high aspect-ratio geometry was chosen to result in maximum absolute resistance change with respect to temperature, further enhancing resolution of the temperature measurement. This integrated resistive temperature sensor allows the μ TPCs to be embedded in a simple feedback loop, so that an accurate desorption temperature can be maintained even under the presence of manufacturing variations. In addition, such a control loop allows for the implementation of more complex temperature profiles. An example of such a control loop is shown in Figure 69, where an operational amplifier controls the voltage applied across the heating resistor based on the voltage drop across the resistive temperature sensor. The cross-domain model for the resulting feedback system was implemented in Simulink using the experimental data from a fabricated 2 mm x 2 mm pre-concentrator. Figure 69 (b) shows how such a feedback signal can heat the membrane to approximately 150°C in about 0.4 seconds and

then maintain a constant temperature. The presented feedback model is based on a single operational amplifier (and a current source to bias the resistive temperature sensor).

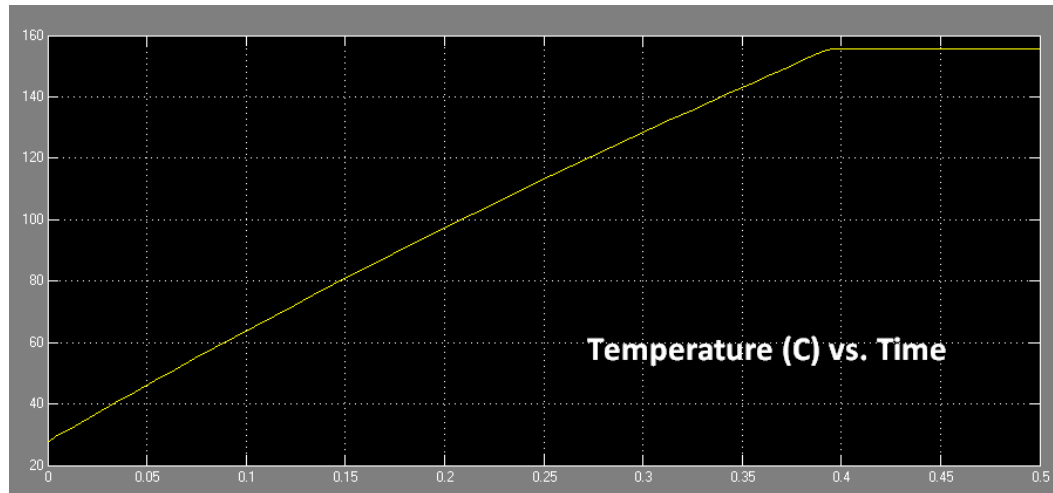
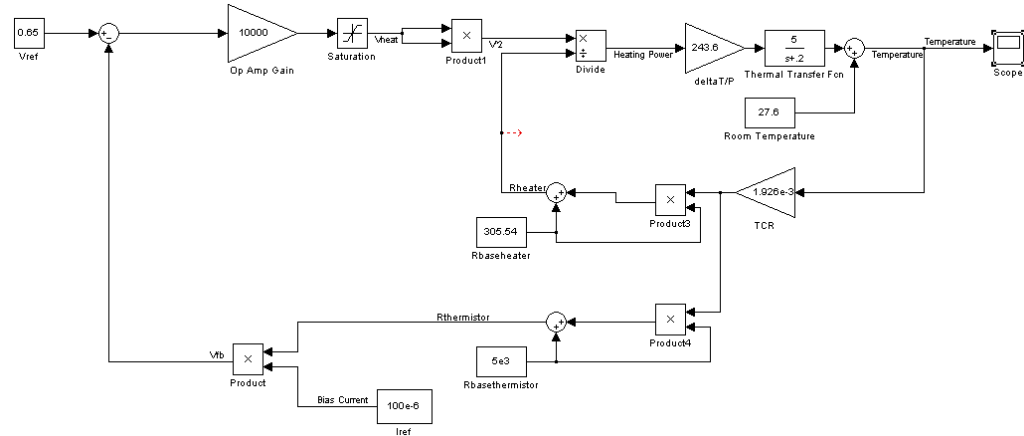


Figure 69 - Example of cross-domain SIMULINK model (top) of a feedback system controlling the micro hotplate temperature, and μ TPC temperature (bottom) as a function of time demonstrating control of μ TPC temperature (the model is based on experimental data obtained from the 2 mm x 2 mm pre-concentrators).

Ridge and Pillar Placement

In addition to integrated heaters, the final thermal-mechanical designs discussed in Chapter 5 incorporated arrays of high aspect-ratio ridges on the surface of the membrane

in order to increase the surface area available for sorbent coating, and in turn increase the sorption capacity of the μ TPC. Ultimately, a higher sorption capacity leads to a higher pre-concentration factor, as the dead volume remains fixed while more analyte will be released during thermal desorption. This increased amount of released analyte into a fixed volume results in an increased concentration peak, enhancing the effective sensitivity of the integrated chemical sensors.

Various densities and arrangements of ridges and pillars, with varying total surface areas, were designed for placement on the die during mask layout. Clearly, increasing the density and aspect-ratio for the arrays of pillars and ridges correspondingly increases the effective surface area of the device without increasing die footprint. There are practical limitations, however, to both the aspect-ratio and the density for these features. First, manufacturing capabilities limit the aspect ratio for a ridge or pillar formed *via* DRIE of silicon to be less than approximately 50:1. Furthermore, while 50:1 aspect-ratio pillars and ridges may be successfully fabricated, such features must also be sufficiently rugged to withstand sorbent coating and final packaging. As it can be difficult to estimate the forces present during sorbent coating (e.g. wetting/drying forces of the solvent/polymer mixes, air pressure from airbrush spray gun) a conservative design was chosen to ensure increased device yield during deposition of the sorbent layers. Finally, the effects of ridge and pillar density on airflow through the enclosed chamber must be considered. As density increases, flow through the chamber will be increasingly, and undesirably, shunted around the sides of the membrane and over the support legs rather than through the high surface-area regions of the ridges and pillars. Such a situation increases the pressure drop of the system and limits interaction between the gas sample and the device, reducing effective surface area.

Thus, as discussed in Chapter 5, fluidic simulations of various ridge and pillar densities were performed to ensure adequate interaction between the flowing gas sample and the sorbent-coated high aspect-ratio features on the membranes. When the device is operated in a static non-flowing atmosphere, however, gas-sorbent interactions are driven primarily by diffusion and not by forced flow, thereby allowing for the possibility of extremely high density arrangements to function without the reduced capacity (due to flow shunting) experienced by the forced flow approach. A summary of the ridge and pillar placements included in the final mask layout are listed in Table 3. In all cases outlined in the table, widths of both 20 μm and 50 μm for both the pillars and ridges were used.

Table 3 - Summary of die specifications present in final mask layout.

Membrane Area	Pillar vs. Ridge	Spacing	Heated Sensors?	# of Chips per Wafer
1 mm x 1 mm	Pillar	140 μm	Yes	4
	Ridge	120 μm	Yes	2
	Pillar	120 μm	Yes	2
	Pillar	50 μm	Yes	2
	Pillar	29 μm	Yes	2
	Ridge	140 μm	No	6
	Ridge	120 μm	No	2
	Pillar	120 μm	No	2
	Pillar	50 μm	No	2
	Pillar	29 μm	No	2
	Ridge	145 μm	Yes	2
	Pillar	145 μm	Yes	2
2 mm x 1 mm	Pillar	70 μm	Yes	4
	Ridge	145 μm	No	10
	Pillar	145 μm	No	8
	Pillar	70 μm	No	4
	Ridge	145 μm	Yes	2
	Pillar	145 μm	Yes	2
2 mm x 2 mm	Pillar	70 μm	Yes	4
	Ridge	145 μm	No	10
	Pillar	145 μm	No	10
	Pillar	70 μm	No	4
	Ridge	145 μm	No	10
	Pillar	70 μm	No	4

Figures 70-72 show several details from the final mask layout, demonstrating examples of die with either pillars or ridges placed on the arrays of suspended pre-concentrator membranes.

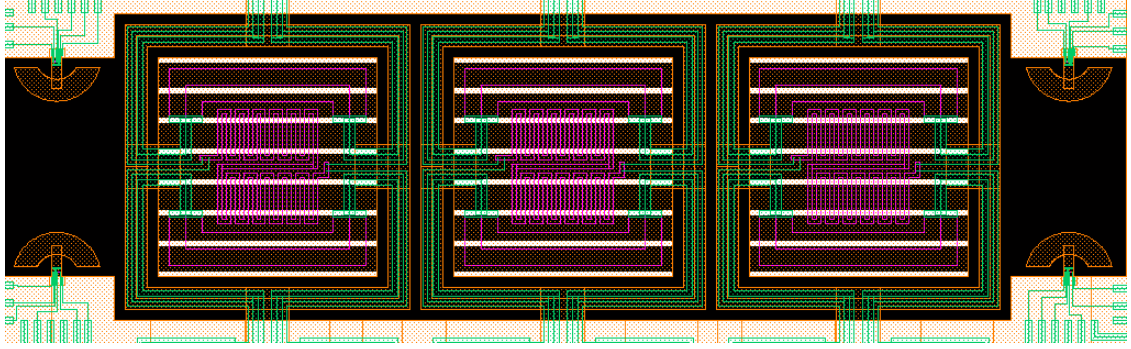


Figure 70 - Screenshot from final mask layout, illustrating design of die with array of three 1 mm x 1 mm μ TPC devices. Non-heated sensors and 120 μ m ridge spacing on the back surface of the suspended membranes.

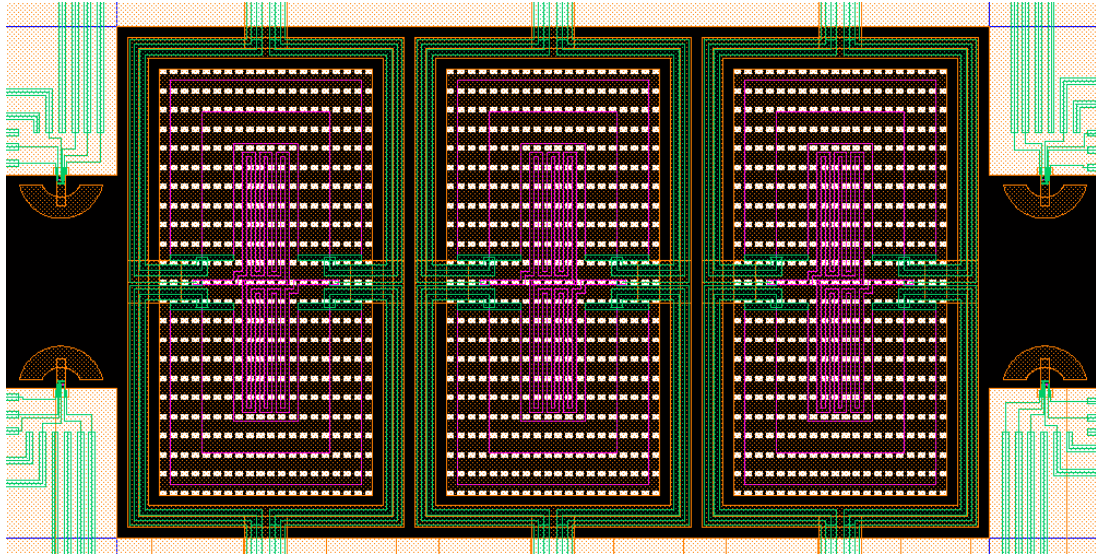


Figure 71 - Screenshot from final mask layout, illustrating design of die with array of three 2 mm x 1 mm μ TPC devices. Non-heated sensors and 70 μ m pillar spacing on the back surface of the suspended membranes.

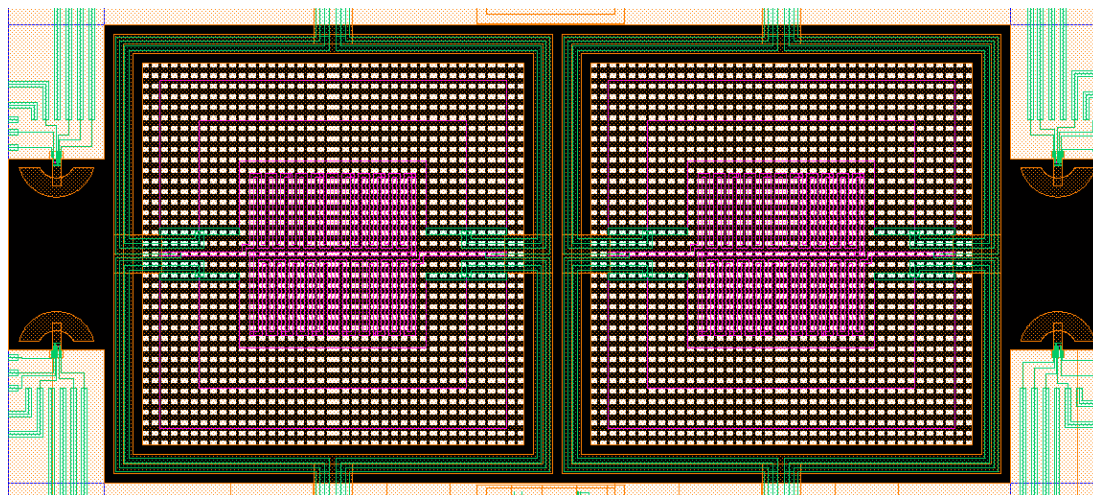


Figure 72 - Screenshot from final mask layout, illustrating design of die with array of two 2 mm x 2 mm μ TPC devices. Non-heated sensors and 35 μ m pillar spacing on the back surface of the suspended membranes.

With the pillar and ridge arrays determined, the bulk of the remaining mask layout process involved placement of the previously-discussed cantilever-based chemical sensors at each end of the pre-concentrator arrays (Figure 73). The sensors were placed in pairs, across from each other and adjacent to the 1 mm x 1 mm inlet and outlet ports arranged at each end of the chamber. In this configuration, one sensor pair is located upstream and one downstream so that loading of the pre-concentrator array can be monitored in real-time. Additionally, each sensor pair can be operated in a differential mode, where one sensor is coated with sorbent and one is uncoated, so that temperature effects can be filtered out in real-time. Shown in Figure 73 are non-heated designs of the mass-sensitive microsensors with six metallization lines connecting the two thermal excitation resistors and four piezoresistors in a Wheatstone bridge arrangement.

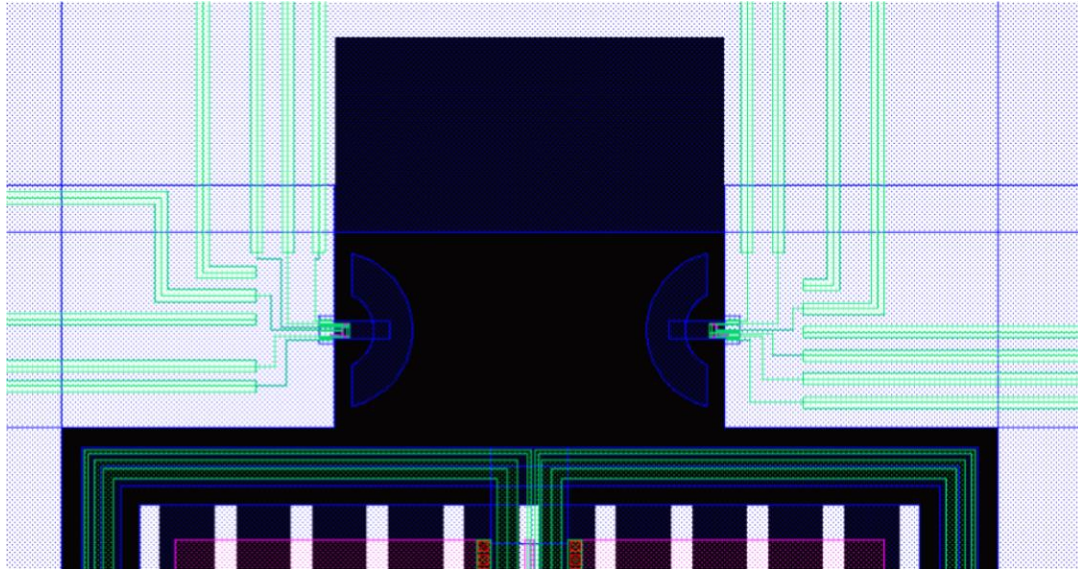


Figure 73 - Detail from final mask layout illustrating placement of cantilever-based chemical sensor pairs (blue semi-circular areas, mid-center) adjacent to inlet and outlet ports (blue rectangular area, top-center). The proximity of the sensor pair to the suspended pre-concentrator membrane (bottom-center) is also shown.

Figures 74-76 show several details of individual die from the completed mask design, illustrating examples of individual pre-concentrator membranes adjacent to a chemical sensor pair. Clearly visible in purple color are the diffused resistors on each μ TPC: the largest two are used as heating resistors, while the central one is for temperature monitoring (using a 4-contact measurement). Shown as white rectangles on each of the screen shots are the high aspect-ratio 3-D structures, in this case parallel ridges. The metallization lines connecting the diffused heating resistors are shown in green with small red squares highlighting the contacts between metallization and p-type resistors. The shape of the released microstructures is shown in blue against the black background. Finally the black areas indicate the areas of the silicon handle wafer that are removed by a deep reactive ion etching step from the back of the wafer.

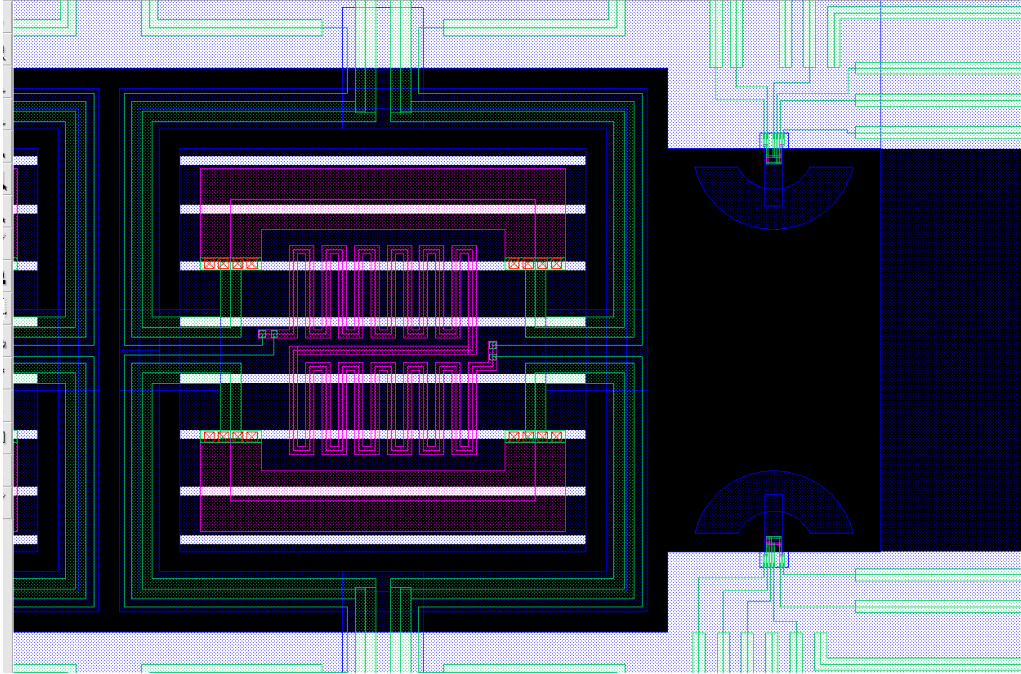


Figure 74 - Detail from final mask layout, illustrating 1 mm x 1 mm pre-concentrator device adjacent to two un-heated resonant sensors located at the integrated inlet/outlet port.

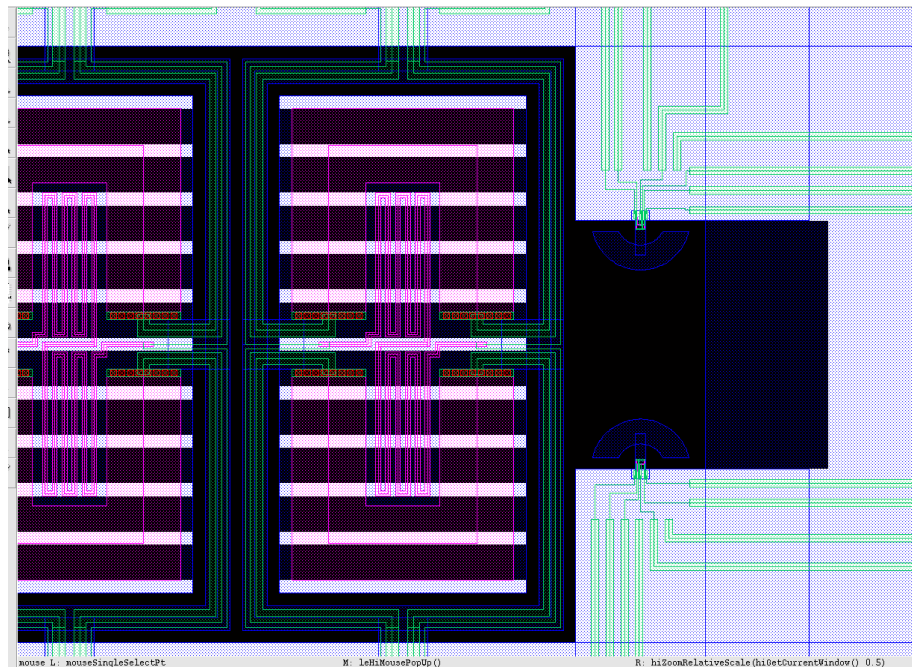


Figure 75 - Detail from final mask layout, illustrating 2 mm x 1 mm pre-concentrator device adjacent to two un-heated resonant sensors located at the integrated inlet/outlet port.

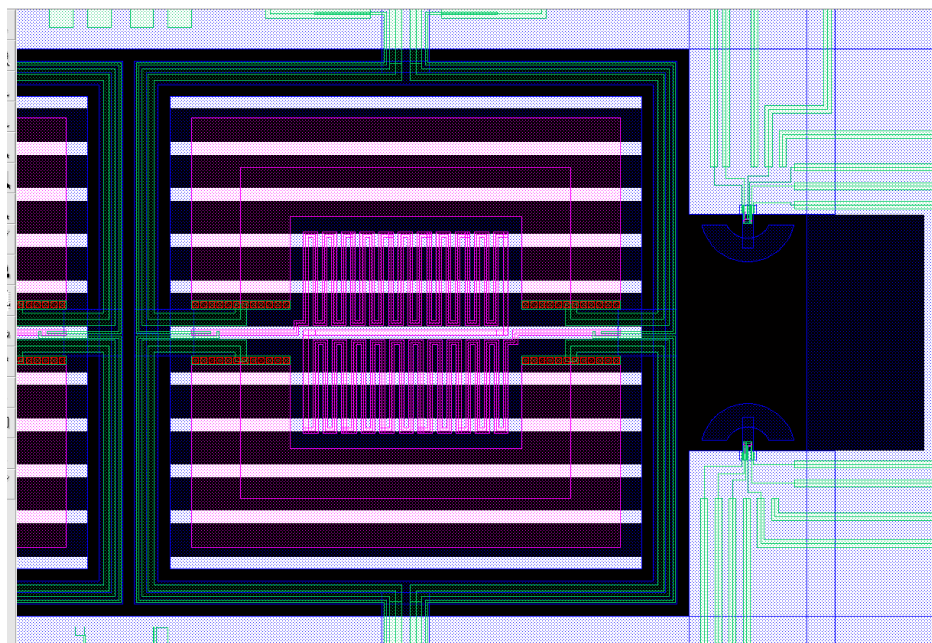


Figure 76 - Detail from final mask layout, illustrating 2 mm x 2 mm pre-concentrator device adjacent to two un-heated resonant sensors located at the integrated inlet/outlet port.

Figures 77 and 78 show large-area views of the final mask layout. The wafer-level die are grouped into three general groups, based on the size of the pre-concentration devices included on each die. Die also differ from one another according to the presence of a desorption heater on the embedded chemical sensors, and according to the number and spacing of high aspect ratio pillars/ridges on the back surface of the suspended membranes. Some die were included which feature only sensors (no pre-concentrators) for testing and characterization of the experimental on-board desorption heaters.

The final mask layout contains 1 x 1, 2 x 1 and 2 mm x 2 mm pre-concentrator designs, as listed in Table 3. Each pre-concentrator die has a size of 6.5 mm x 9 mm; in the case of the 1 mm x 1 mm and 2 mm x 1 mm designs, three μ TPC structures are located on each chip, in the case of the 2 mm x 2 mm designs, each chip comprises two μ TPC structures. In total, 88 pre-concentrator die are included on a 4-inch wafer (see Figure 78). In addition, the mask layout includes 28 die containing only arrays of mass-sensitive

microsensors, with dimensions of 4.5 mm x 6.5 mm. These cantilever die were used to characterize the mass-sensitive microsensors individually and separately from the μ TPC devices, and as arrays coated with different sensing films.

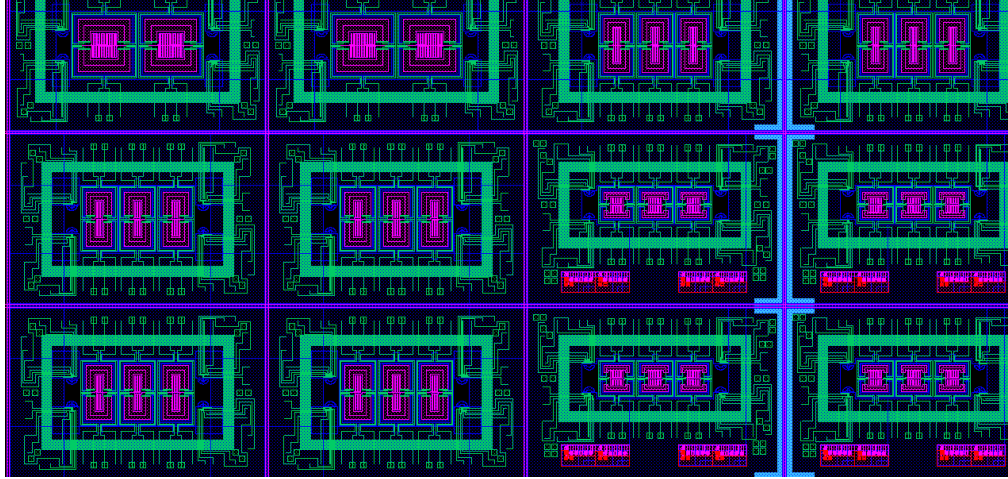


Figure 77 - Screenshot from final mask layout, illustrating placement of several die. The solid green rectangle surrounding each μ TPC array is a capping piece formed on the separate packaging wafer, which is used to seal the chamber from the top surface. The bright pink features – near the bottom of the four die on the lower right side of the figure – are a series of alignment marks used as aides during photolithography.

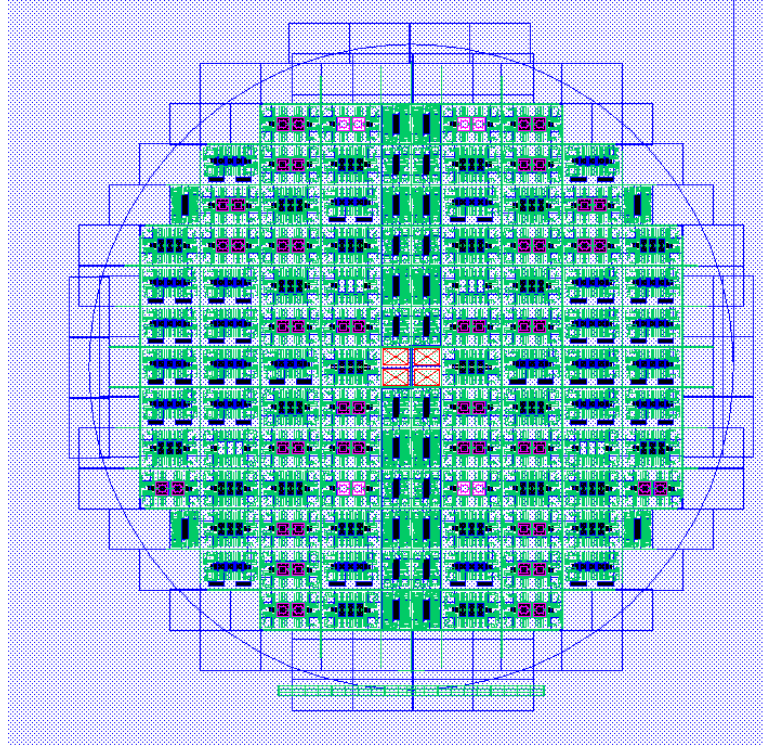


Figure 78 - Screenshot of entire wafer layout, with a total of 88 pre-concentrator dies (6.5 mm x 9 mm each) and 28 cantilever-only dies (4.5 mm x 6.5 mm each), placed vertically down the center column. The center die (marked with four red X's) is used for wafer centering.

The mask set also accounts for the fabrication of a packaging wafer to encapsulate the dies at the wafer-level, thereby minimizing device dead volume and improving future scalability. The complete process flow requires 6 photomasks for the device wafer and 2 photomasks for the packaging wafer, as summarized below:

- Mask 1 – Diffusion of p-doped resistors
- Mask 2 – Metal contact vias
- Mask 3 – Metallization lines
- Mask 4 – Device passivation
- Mask 5 – Device release
- Mask 6 – Backside DRIE etch of high-aspect ratio features

- Mask 7 – Capping ring structure for sealing top surface of μ TPC chamber
- Mask 8 – Alignment marks for alignment between device and packaging wafer

Process Development

In parallel with the mask layout design, a suitable fabrication sequence compatible with both the μ TPC arrays and the integrated cantilever-based sensors was developed. Due to the inter-related nature of and dependencies between the two, both the mask layout and the fabrication process design were developed simultaneously, in a cyclical and iterative manner. For example, the possibility of slight misalignment occurring during a lithography step requires the introduction of tolerances into the drawn layouts for sequential mask layers. Likewise, the design choice to implement a wet etch for defining the metal traces constrains the mask layout traces to be drawn wider than they actually appear on the completed device, due to undercutting that arises from the isotropic nature of the etch. Experience and knowledge gained from work on previous devices proved invaluable, and was leveraged as much as possible for the sake of speed and efficiency throughout this inter-dependent process.

In fact, the fabrication sequences for past sensors had already achieved a substantial level of complexity and maturity prior to the commencement of this work. These designs typically employed a 6-8 mask processing sequence, based on epitaxial silicon substrates [62, 73, 74, 89, 90]. An example processing sequence for cantilever-based resonant sensors is shown in Figure 79.

SOI Fabrication Development

Due to the crystal-direction-dependence of silicon etching using KOH solutions, however, the process sequences used for prior state-of-the-art cannot be readily adapted to form the high aspect-ratio pillars and ridges necessary to increase the surface area of the μ TPC membranes. Such features are possible on SOI substrates, however, where the buried oxide (BOX) layer is used as an etch stop in conjunction with DRIE of silicon. Thus, a design decision was made to modify the well-established and mature epitaxial substrate-based processing sequence so that it could be implemented on SOI substrates, enabling both pre-concentrators (with their large-area membranes and high aspect-ratio pillars and ridges) and mass-sensitive chemical sensors to be processed simultaneously on the same substrate. This modified fabrication process has been designed to be fully compatible with the existing chemical sensor designs so that sensor performance is not compromised by the switch to SOI. Figure 79 illustrates the modified fabrication sequence, requiring six masks for the device wafer.

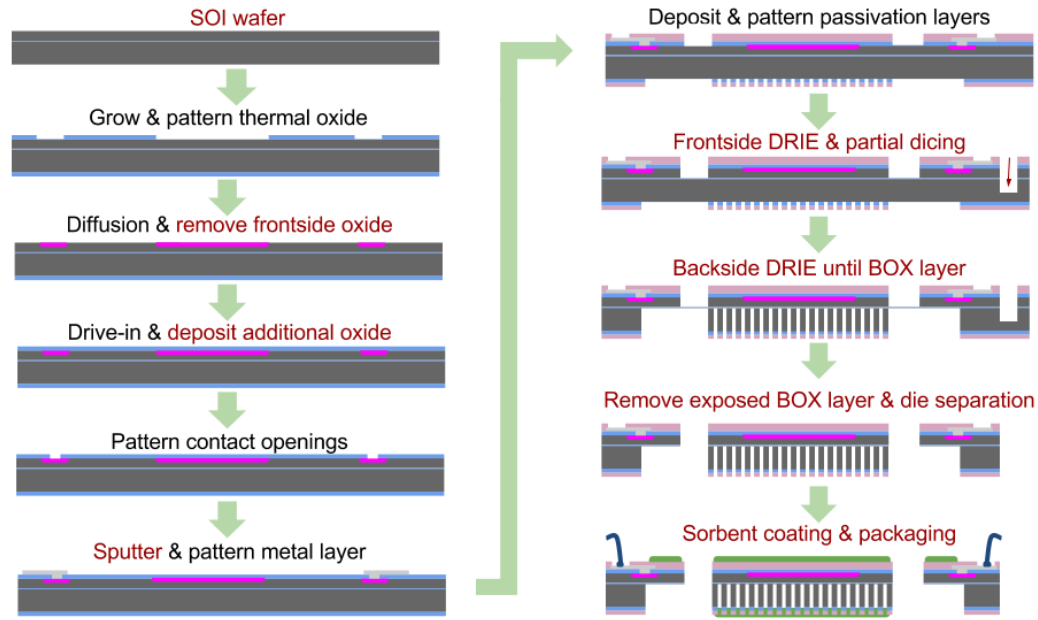


Figure 79 - Process flow diagram showing fabrication steps for μ TPC devices formed on SOI substrates. The process sequence is compatible with existing resonant cantilever-based sensors. Red text indicates modifications to the previous process flow, which was based on epitaxial substrates.

In the modified sequence, fabrication begins with thermal oxidation of an SOI wafer, where the thickness of the device layer defines the final thickness of the released cantilevers and μ TPC membranes while the thickness of the handle layer defines the height of the high aspect-ratio pillars and ridge structures. The thermally-grown oxide is then patterned and dry-etched down to the silicon surface to open diffusion windows, as before, and high-temperature boron diffusion through the oxide windows into the exposed silicon is used to form heating resistors and piezoresistors. In the modified sequence, however, all oxide is removed completely from the front surface prior to drive-in. This step serves to re-planarize the front surface of the wafer, reducing unnecessary topography and improving the yield for all subsequent processing steps. Following drive-in, additional oxide is deposited *via* PECVD in order to increase dielectric thickness and reduce the possibility of dielectric breakdown during μ TPC heating. Electrical contact is made to the diffused resistors *via*

contact openings to the silicon and a thin aluminum metallization layer is deposited and patterned to define electrical traces and bond pads suitable for wire-bonding to an external circuit. While the previous processing sequence employed e-beam evaporation of pure aluminum for the metallization layer, the modified sequence opted instead for sputtering of Al-Cu(1%). Sputter coatings generally exhibit enhanced step coverage over e-beam evaporation, and the introduction of copper into the metallization has been demonstrated to reduce electromigration effects. As before, nitride passivation is deposited and patterned on the front surface of the wafer to protect the devices from scratches and corrosion, and to enable operation in conductive environments without short-circuiting adjacent metal traces. Additional dielectric thickness necessary for a sufficiently durable hard mask is deposited and patterned on the back surface of the wafer, and the wafer is then patterned and etched from the front surface down to the BOX layer *via* DRIE to define the shape of the cantilevers and membranes.

A significant design choice was made at this point to reorder the processing sequence so that the dicing step could be accomplished prior to final device release. As was discussed in Chapter 5, the ideal membrane would be as thin as possible (for reduced thermal mass, and increased surface-area-to-volume ratio) but there are practical limits to the dimensions of a physically-realizable suspended membrane structure. These limits are determined by available fabrication and packaging technologies, and the corresponding decrease in yield imposed by reducing the thickness of a suspended membrane that is inherently fragile. In some cases, the choice of fabrication approach can dramatically affect the projected yield, with more fragile structures being more sensitive to manufacturing methods. For example, it is common practice to separate the die on a wafer with a dicing

saw at the end of the manufacturing process, upon completion of all other fabrication steps. This presents a problem for a delicate, suspended membrane structure, however, as the necessary slurry used during dicing can fracture the exposed membranes and significantly reduce yield. If the dicing step can be moved up in the sequence so that it occurs prior to final membrane release then the loss in yield due to dicing can be virtually eliminated, enabling the manufacture of more aggressive membrane dimensions. In the case of the modified SOI process flow, a *partial* dicing of the wafer occurs where the wafer is diced partway through the handle layer immediately following the front-side DRIE etch. This technique allows for the wafer to be handled as a complete wafer for the remaining fabrication steps, with die separation accomplished by gently fracturing off individual die following completion of all processing. In this way, the partial dicing technique allows for more aggressive membrane geometries to be targeted by dicing – with its accompanying destructive slurry – before the membranes are released and fragile, without compromising on dicing yield. Alternatively, die could be laser diced (i.e. without slurry) at the end of the processing sequence, but this capability is not available at Georgia Tech.

Following the partial dicing step, fabrication continues with a DRIE etch from the back surface of the wafer down to the BOX layer, with subsequent removal of the BOX layer *via* dry plasma etching of SiO₂. Due to the high selectivity (200:1) of the DRIE process for silicon vs. SiO₂, the BOX layer serves as a very effective etch stop resulting in all suspended features having uniform thicknesses despite non-uniformities in the DRIE etch rate across the wafer. Again, the use of a reliable and accurate etch stop to determine accurate thicknesses and maintain uniformity is critical for achieving high yield with consistent, optimal sensor performance.

Cantilever Fabrication

As the pre-concentrators and heated cantilevers were designed to be integrated onto the same die, their fabrication processing sequences must necessarily be the same. As discussed previously, the thickness of the suspended pre-concentrator membranes must thus be the same as the cantilever beam thickness, thereby constraining the design of both devices to 25 μm . While this process arrangement introduces additional complexity into the fabrication of the resonant devices when compared to previous work, it also offers the ability to define high-aspect-ratio features onto the reverse-side of the die, making possible novel future designs and enabling fabrication of the pre-concentrators. The fabrication process flow, from the perspective of the heated cantilevers, is illustrated in Figure 80.

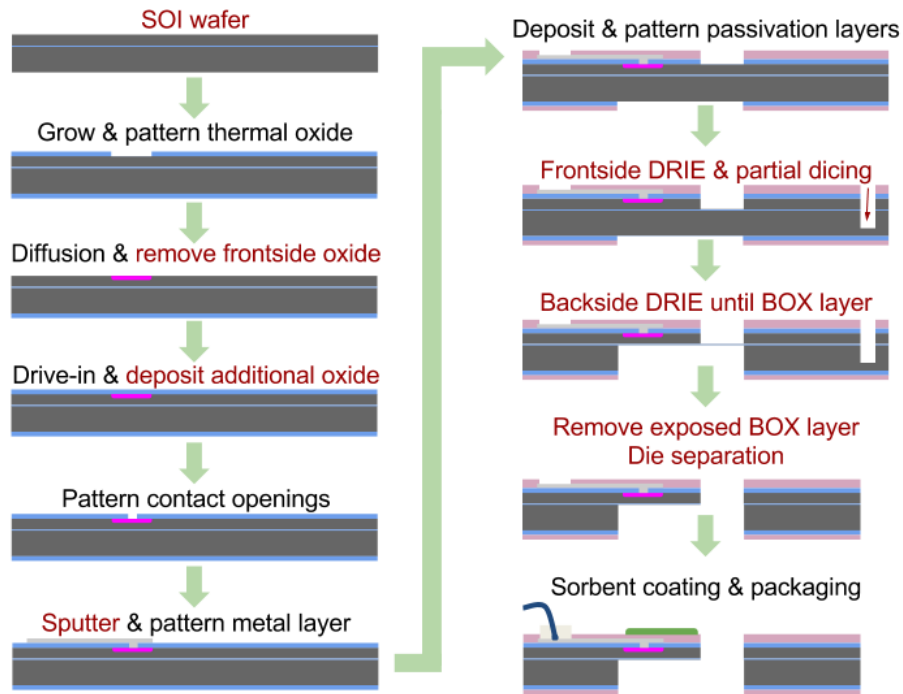


Figure 80 – Process flow diagram for cantilevers with integrated heating units. Red text signifies new process development.

Initial Fabrication Results

Prior to undertaking a complete processing sequence on costly SOI wafers, various aspects of the design were first qualified individually on less-expensive silicon prime wafers. For example, viability of the ridge and pillar dimensions was proven initially by processing only that particular mask with bare silicon wafers. Figures 82 and 83 illustrate some results from those initial experiments, demonstrating that the ridge and pillar arrays were capable of being formed as designed. It is clear, however, that the initial etching parameters were not optimized. For example, the pillar structures in Figure 81 show considerable under-etch stemming from non-90° sidewalls and would likely not survive sorbent coating. Nonetheless, with time the DRIE parameters were sufficiently optimized (e.g. by varying cycle times, RF power, gas pressures) to enable processing the DRIE mask in conjunction with the front-side device release mask on a bare silicon wafer. Due to the lack of a BOX layer – and a corresponding etch stop – the etch depths for these initial tests were controlled simply by monitoring the number of etch cycles and estimating depth. This lack of precise control resulted in released membranes that were relatively thick (70 μm), with thicknesses varying roughly 10-15% across the wafer due to non-uniformities in the etch rate across the wafer surface.

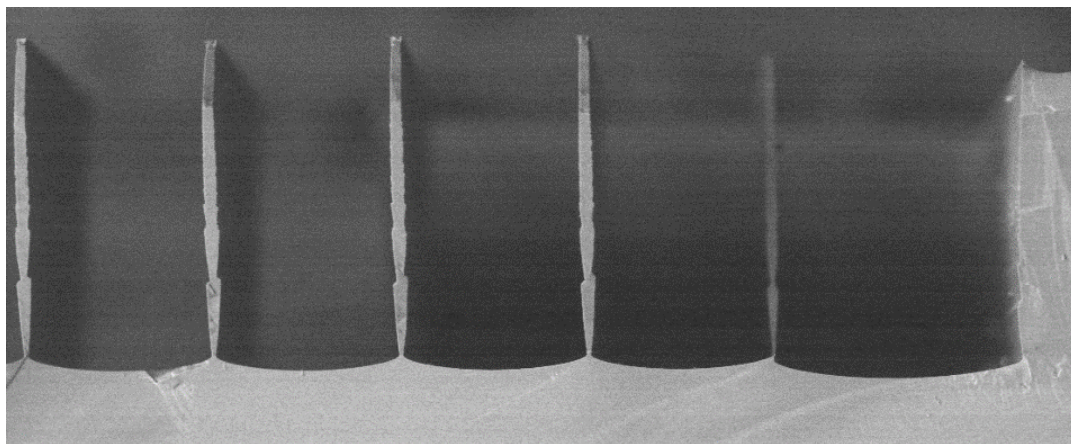


Figure 81 - SEM images illustrating results of initial DRIE development for ridges and pillars. Further refinement was necessary to reduce the undercutting and improve the sidewall angle.

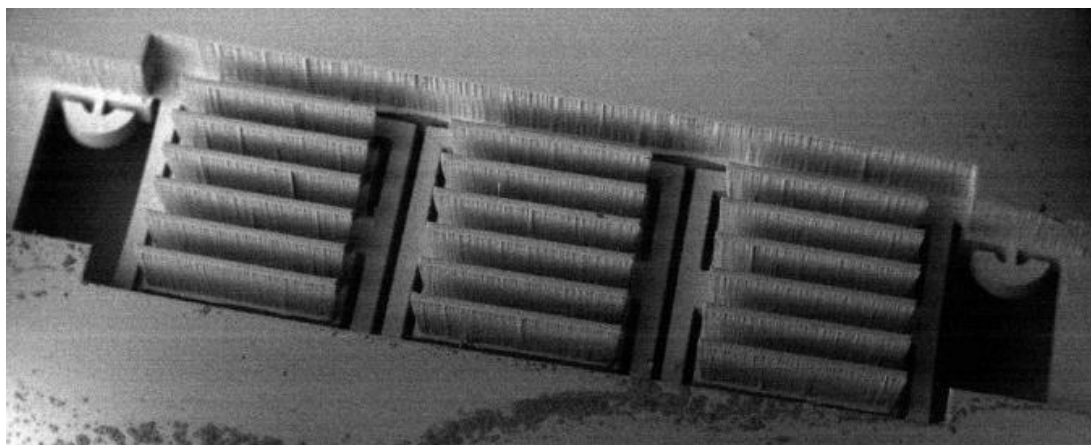


Figure 82 - SEM image of a released 1 mm x 2 mm pre-concentrator with ridge-type structures imaged from back surface. Also visible are the mass-sensitive resonator structures at the bottom of the image. These initial devices were fabricated without the use of an etch stop, resulting in membranes that were approximately 70 μm thick.

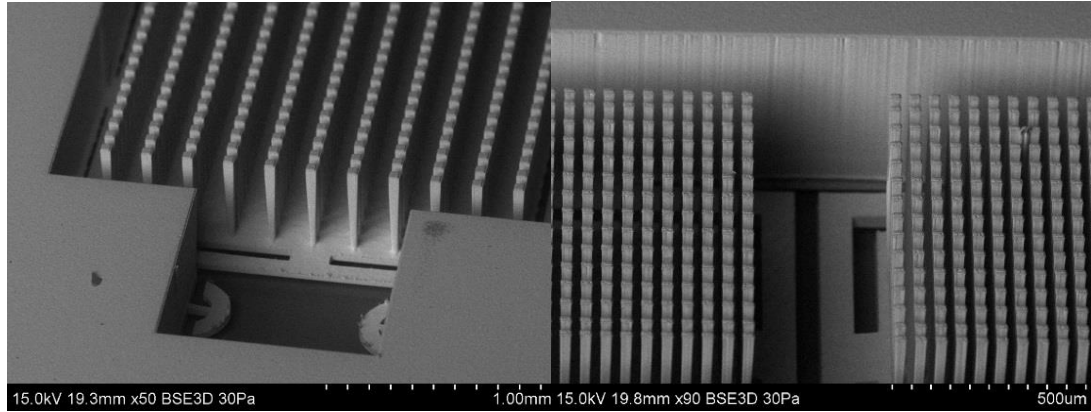


Figure 83 - SEM images of a released 1 mm x 1 mm pre-concentrator with pillar-type structures imaged from back surface. These initial devices were fabricated with an improved DRIE recipe but without the use of an etch stop, resulting in membranes that were approximately 35 μm thick and with poor thickness uniformity across the wafer.

Despite these drawbacks, the successful fabrication of initial devices demonstrated basic viability of the modified process sequence. Subsequent processing commenced on true SOI substrates, which soon resulted in successfully processed devices with uniform 25 μm thick membranes as illustrated in Figure 84.

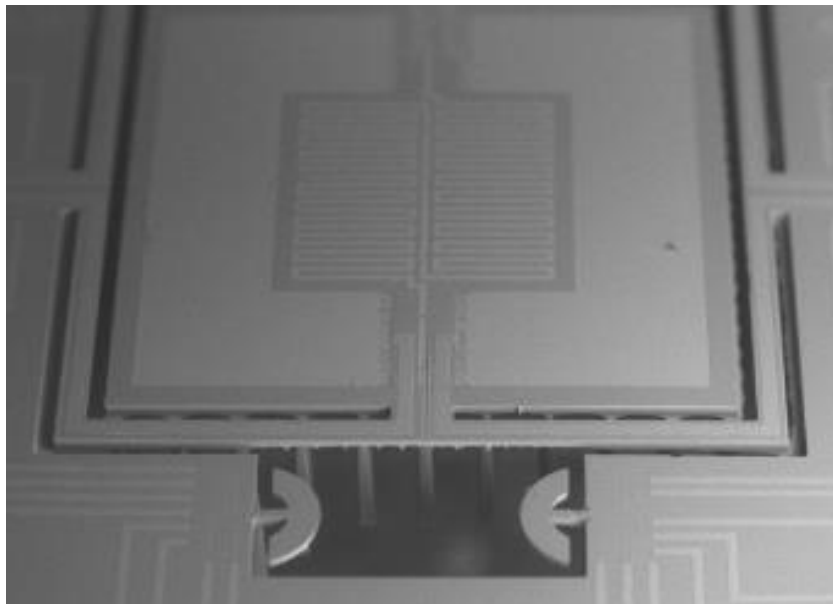


Figure 84 - SEM image of a released 2 mm x 2 mm pre-concentrator with pillar-type structures imaged from top surface. Also visible are the mass-sensitive resonator structures at the bottom of the image. These improved devices were fabricated from SOI substrates where the BOX layer was used as an etch stop for DRIE, resulting in membranes that were precisely 25 μm thick.

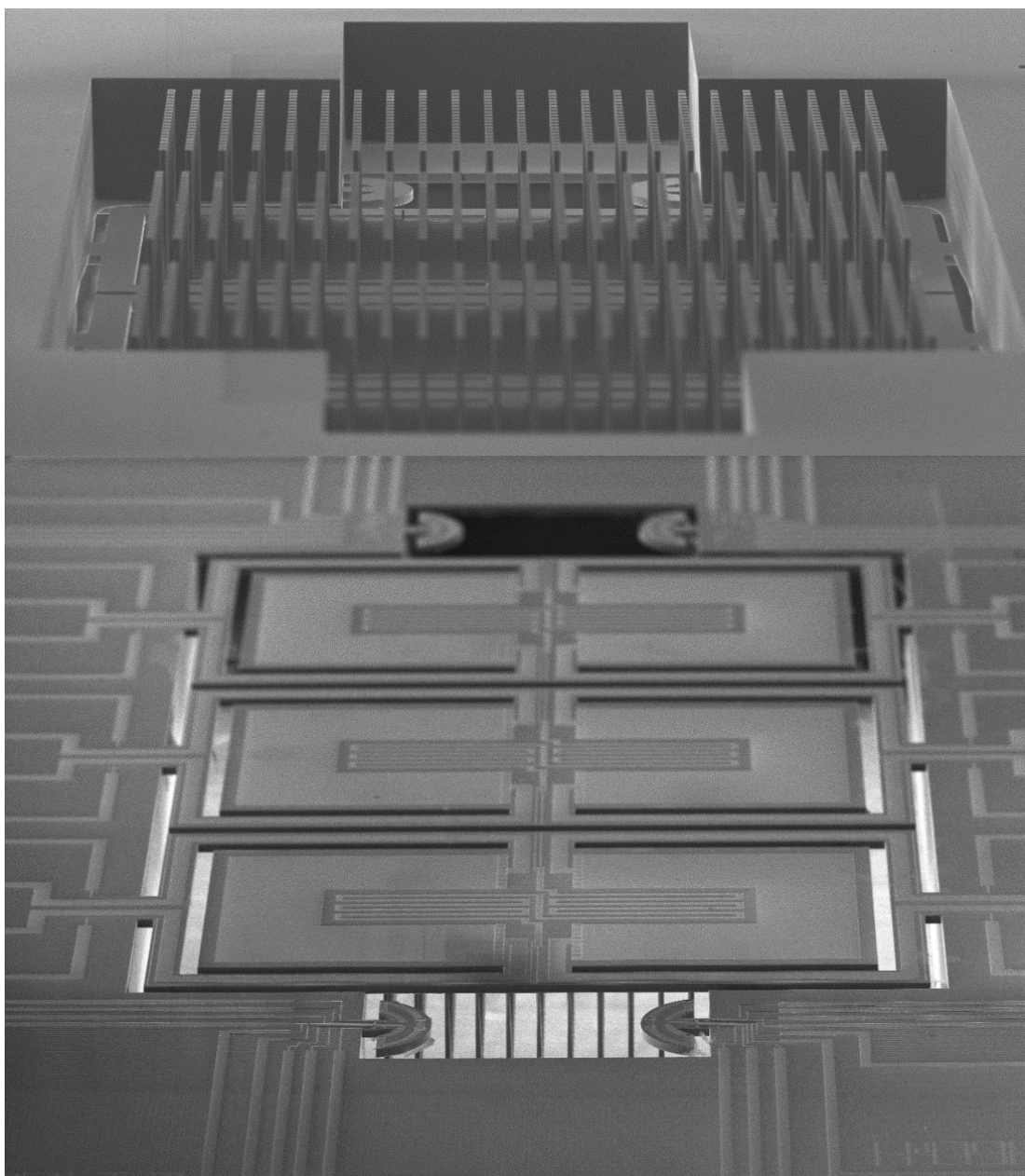


Figure 85 - SEM image of array of released 2 mm x 1 mm μ TPC devices with pillar-type structures imaged from top (top) and back (bottom) surfaces. These improved devices were fabricated from SOI substrates where the BOX layer was used as an etch stop for DRIE, resulting in membranes that were precisely 25 μ m thick.

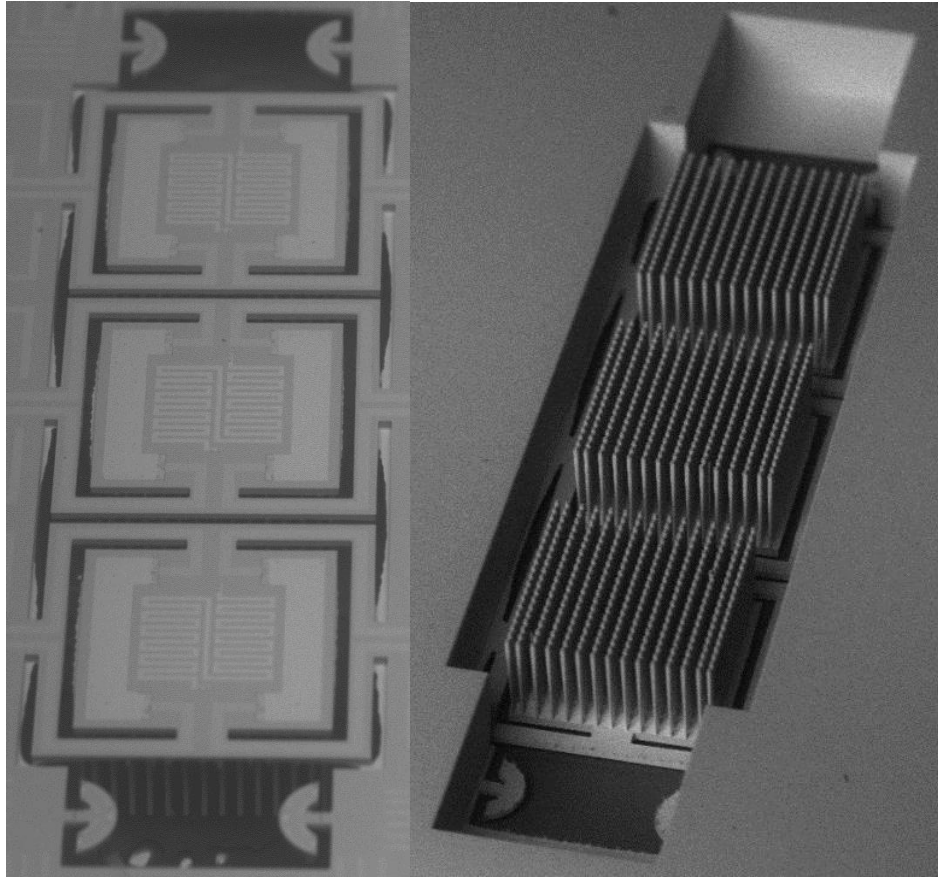


Figure 86 - SEM image of array of released 1 mm x 1 mm μ TPC devices with pillar-type structures imaged from top (left) and back (right) surfaces. These improved devices were fabricated from SOI substrates where the BOX layer was used as an etch stop for DRIE, resulting in membranes that were precisely 25 μ m thick.

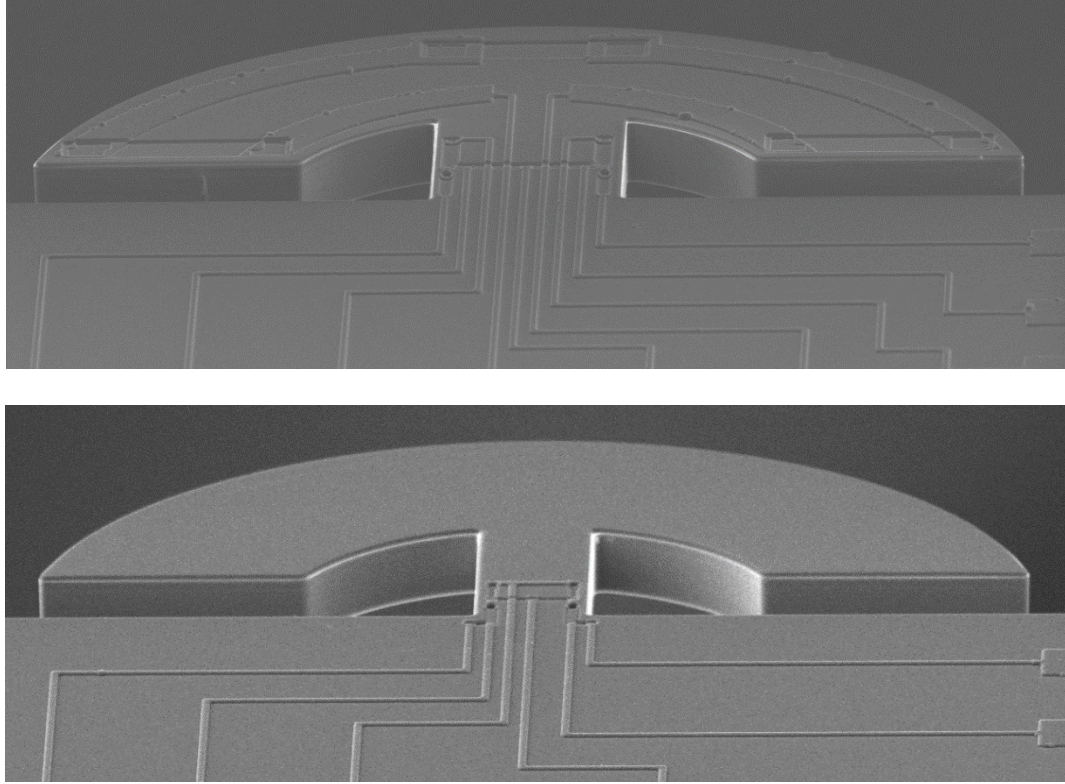


Figure 87 - SEM image of heated (top) and non-heated (bottom) integrated chemical sensors. The sensors were fabricated on-chip with the μ TPCs, resulting in a device thickness of precisely 25 μ m.

CH 7 – PRE-CONCENTRATOR CHARACTERIZATION

Following successful fabrication in the Georgia Tech Institute for Electronics and Nanotechnology (IEN) cleanroom facilities, performance for the various designs was first evaluated *via* electrical and thermal characterization. To facilitate this process, die from each design were mounted into 28-pin DIL ceramic packages and wire-bonded to connect each die electrically to each package (Figure 88).

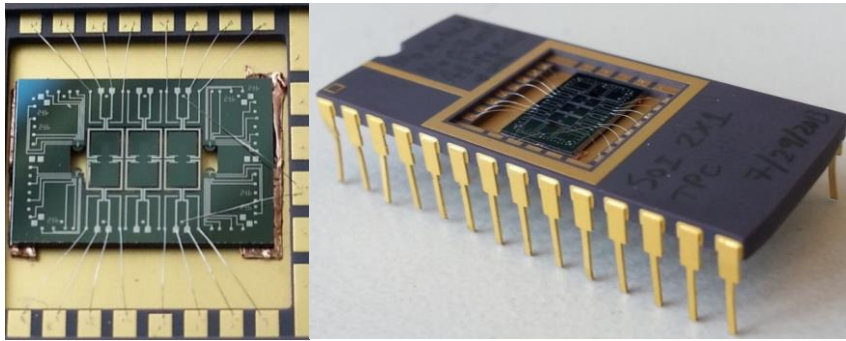


Figure 88 - Photographs of a 2 mm x 1 mm μ TPC die mounted in ceramic DIL package.

Electrical Measurements

Once mounted into the packages, the resistances of both the heating and measurement resistors were measured for each design, at room temperature in air. The results of these measurements are summarized in Table 4, and represent approximate values as the resistances varied slightly from die to die and from wafer to wafer. Examination of these

results reveals the measured resistances to lie within 10-28% of the designed specifications, with the exception of the measurement resistors for the 2 mm x 2 mm devices (47%).

Table 4 - Summary of electrical and thermal measurement results, compared with the values expected from simulation and theory.

Device	1 mm x 1 mm		2 mm x 1 mm		2 mm x 2 mm	
	Designed	Measured	Designed	Measured	Designed	Measured
Heating Resistance [Ohms]	500	593	500	604	500	553
Measurement Resistance [Ohms]	25k	32k	35k	44k	75k	110k
τ_{therm} [15]	0.2	0.35	0.4	0.8	0.6	1.3
Temp. Increase ΔT [°C]	265	194	229	188	271	155
P_{applied} [mW]	500	276	500	287	1000	309
$\Delta T/P_{\text{applied}}$ [°C/mW]	0.53	0.70	0.46	0.66	0.27	0.50

Oven Measurements

Once baseline resistance values were established, the relative and absolute resistance changes due to temperature were evaluated by placing each packaged μTPC in a temperature-controlled chamber and ramping the temperature while monitoring the resistance of each resistor. A Keithley 2400 source-meter was used to apply +10 V of DC

bias to the substrate (to reverse-bias the pn-junction between p-type resistors and n-type device layer), and an Agilent 34401A DMM was used to measure resistance. To enable relatively high temperatures up to 150 °C, a specialized circuit board was designed with temperature-resistant components and wires. This circuit board contained a socket for holding the ceramic DIL package, and served to interface between the packaged μ TPCs and external measurement equipment by way of electronic feed-through ports on the side of the temperature chamber (Figure 89).

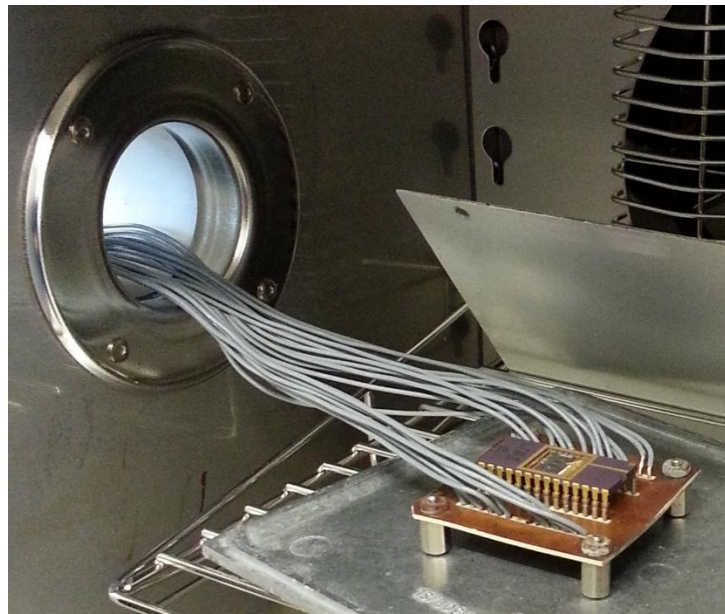


Figure 89 - Photograph of custom-built temperature-resistant PCB, connected to external measurement equipment by way of a feedthrough in the environmental chamber.

In this way, a plot of resistance as a function of temperature was generated for each design, as shown in Figures 90-94. Analysis of the data taken without substrate bias revealed that the resistance of the measurement resistor actually begins to *decrease* when the membrane temperature reaches approximately 120 °C. It is believed that this phenomenon occurs due to expansion of the PN-junction's depletion regions at elevated temperature, which causes overlap of the junctions to occur among the narrow bends in the long, thin resistor, thereby

reducing the effective resistance. In anticipation of this possibility, electrical contacts to the substrate were added during the mask layout design stage so that a reverse-bias voltage could be applied between the n-type substrate and the p-type doping as a way of improving electrical isolation within the devices. With the application of a reverse-bias voltage to the substrate contacts, the change in slope sign of the measurement resistor's resistance vs. temperature could be avoided and a monotonically-increasing temperature calibration curve results (Figure 90). The application of the substrate bias in case of the heating resistors, however, was found to have no effect on the relative resistance change as a function of temperature. In all subsequent measurements, a DC substrate bias of +10 V was applied *via* the substrate contacts between the n-type substrate and the p-type diffused resistors.

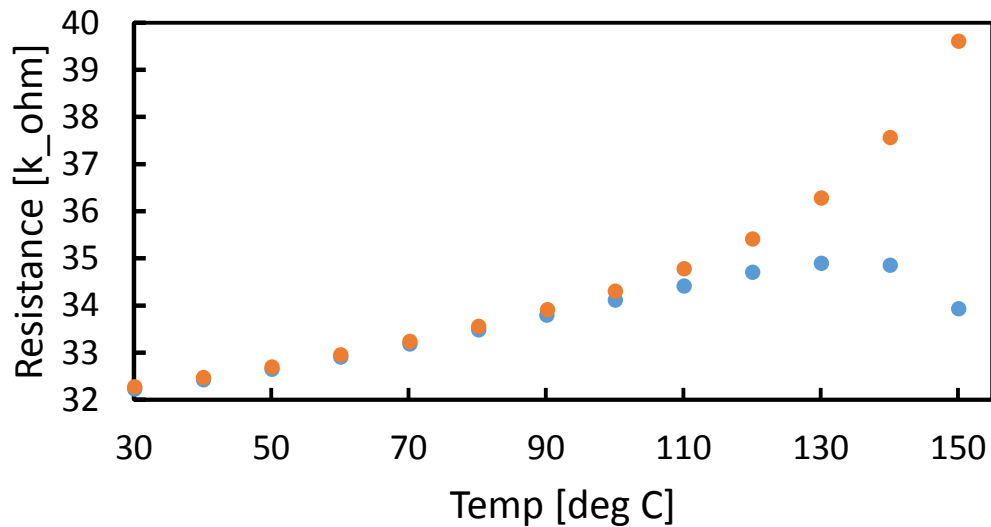


Figure 90 - Measured resistance as a function of ambient temperature for the measurement resistor of a 1 mm x 1 mm μ TPC device. The resistance was measured both with (orange) and without (blue) a +10 V DC bias applied to the substrate.

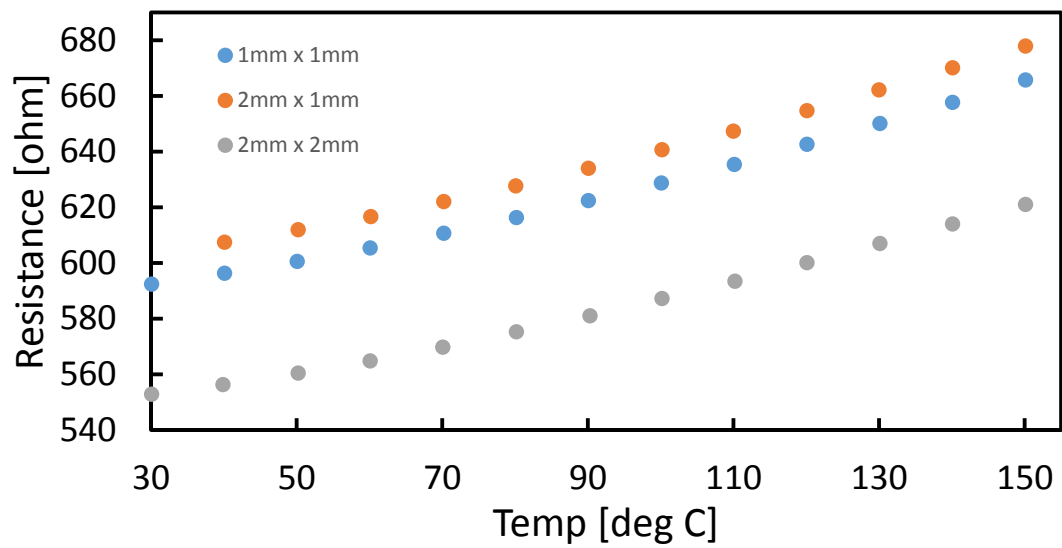


Figure 91 - Calibration data for the heating resistors on 1 mm x 1 mm, 2 mm x 1 mm, and 2 mm x 2 mm μ TPC devices, measured with no bias applied to the substrate.

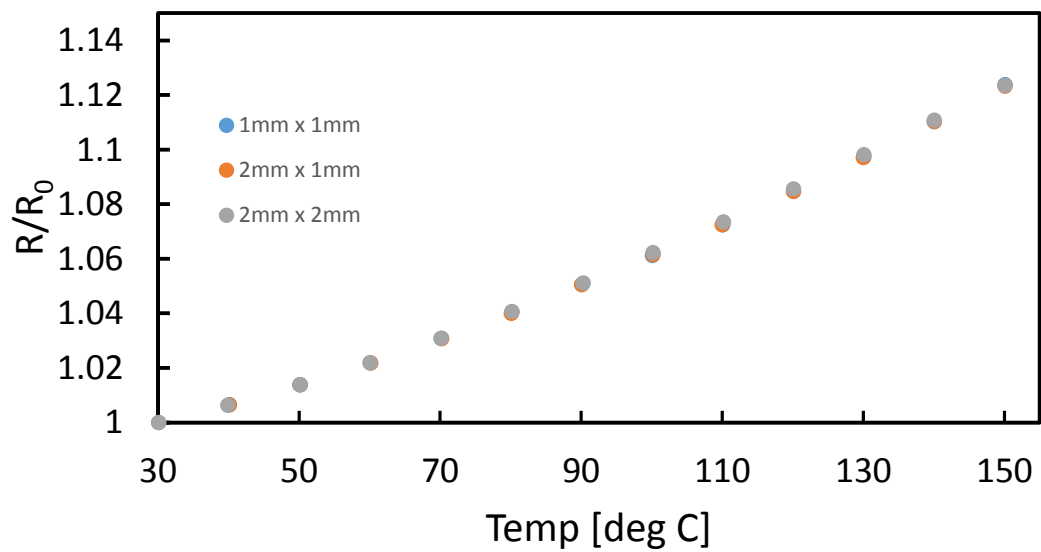


Figure 92 - Normalized resistance change as a function of the chamber temperature for all three heater designs (using data from Figure 43).

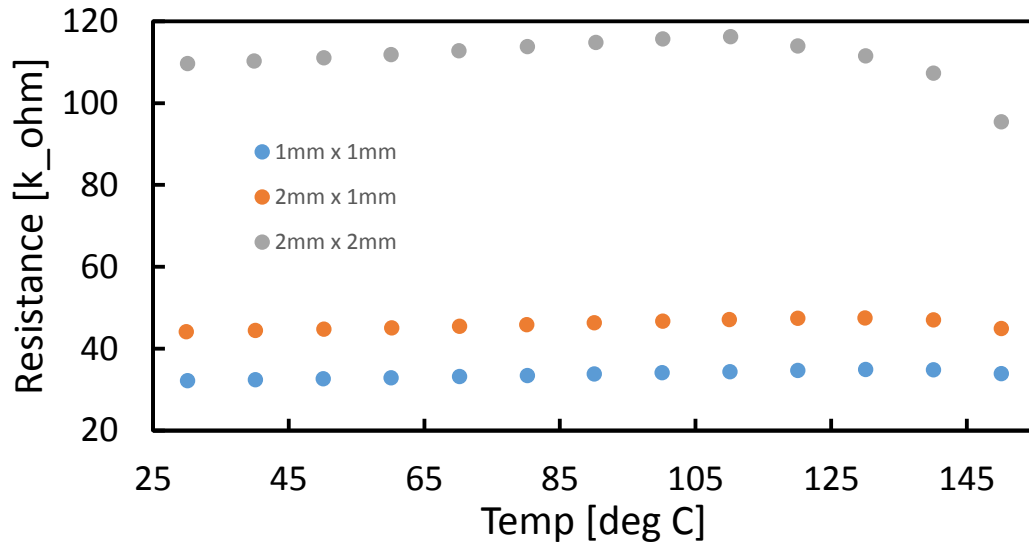


Figure 93 – Absolute resistances as a function of chamber temperature for all three measurement resistors, without applied substrate bias.

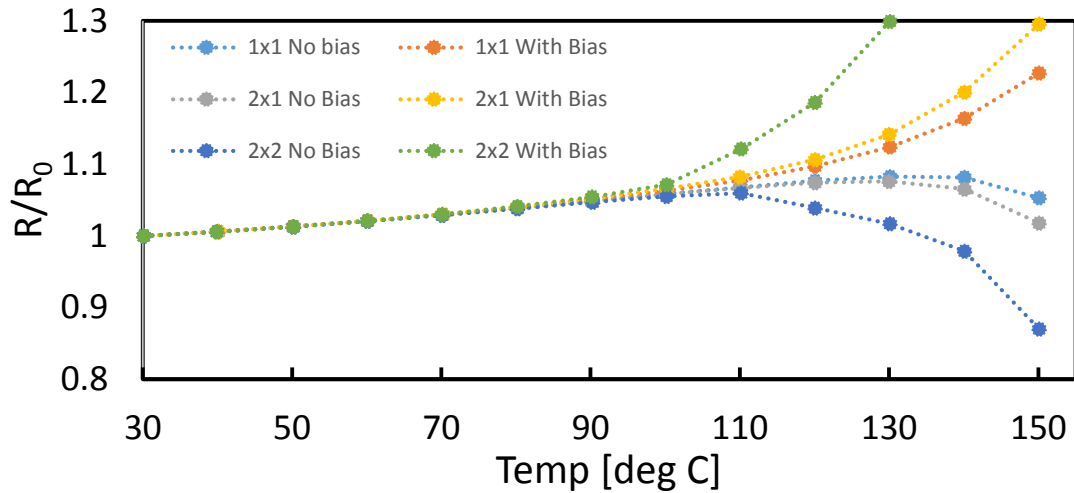


Figure 94 - Calibration data for the measurement resistors on 1 mm x 1 mm, 2 mm x 1 mm, and 2 mm x 2 mm μ TPC devices, measured with and without bias applied to the substrate.

A comparison of the temperature calibration curves for the measurement resistors with those of the heating resistors reveals that the heating resistor response with respect to temperature is independent of the biasing voltage. This is not the case for the measurement resistors, however, which are more susceptible to changes in PN-junction depletion region

because of the many tight, narrow bends in their geometries. It is suggested that future designs examine removing the meandering bends from the measurement resistors, so that they will respond predictably and without the need for a substrate bias voltage. Because the temperature dependence of the heating resistors (Figure 91) is more consistent across the three designs and independent of the substrate bias, it was decided to use the heater resistance for temperature monitoring going forward. For the heating resistors, the normalized resistance change as a function of temperature is well described by a quadratic dependence,

$$\frac{R}{R_0} = 0.982 + 4.99 \times 10^{-4} \cdot T + 3.02 \times 10^{-6} \cdot T^2$$

Equation 16 – Equation of fit for normalized heating resistance change as a function of temperature (in degrees Celsius).

Self-Heating

After quantifying the effect of ambient temperature on resistance change, heating power was applied directly to the membranes while monitoring the change in resistance for the various embedded resistors (Figures 95-98). These measurements were performed with a Keithley 2400 SourceMeter, by applying a voltage to the heating resistors (connected in parallel) and measuring the current flow. From the obtained I-V data, the heating power $P = I V$ and the heating resistance $R = V/I$ are readily extracted. In all cases, a +10 V bias was applied to the substrate contacts.

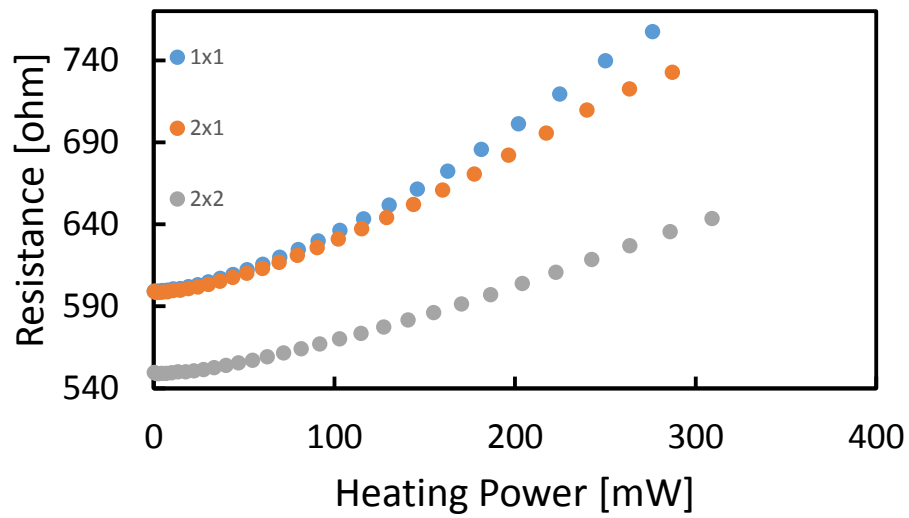


Figure 95 – Absolute resistance values for all three heaters as a function of heating power.

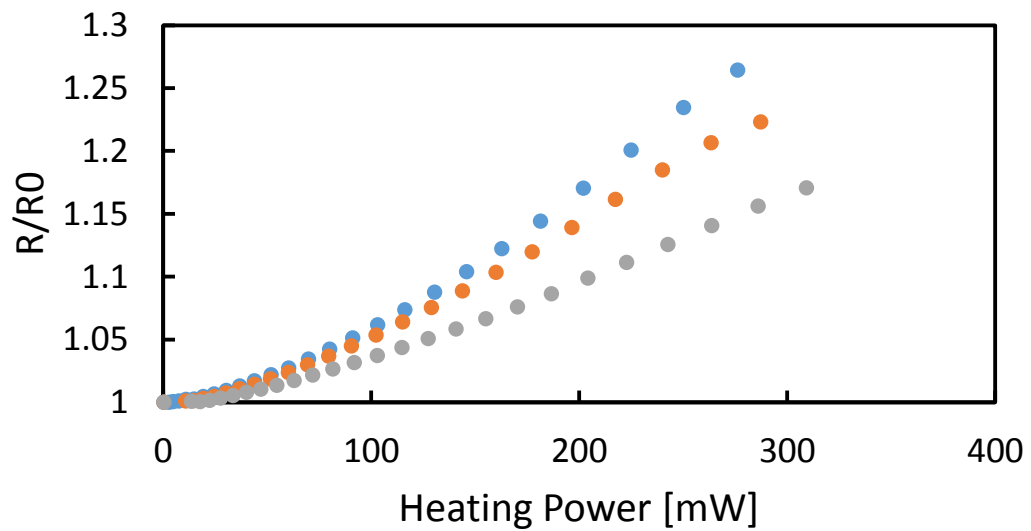


Figure 96 - Normalized resistance values for all three heaters as a function of heating power.

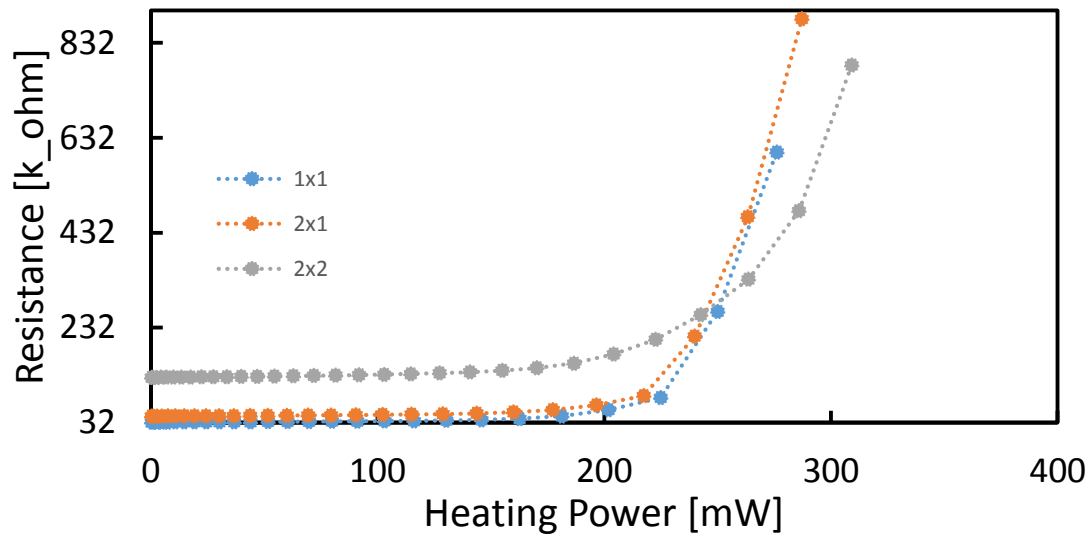


Figure 97 – Absolute resistance values for all three measurement resistors as a function of applied heating power.

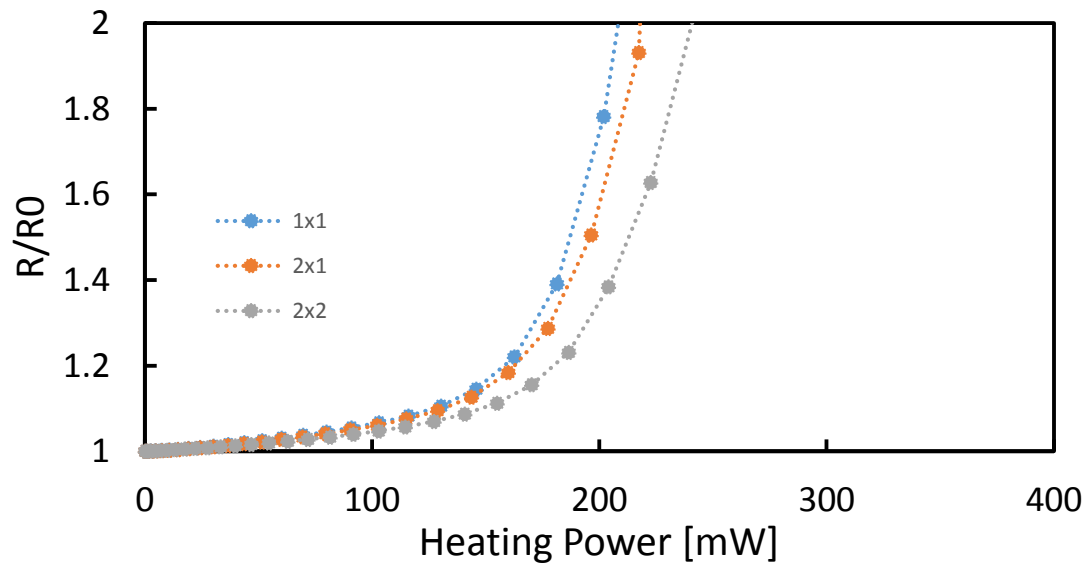


Figure 98 - Normalized resistance values for all three measurement resistors as a function of applied heating power.

By utilizing the temperature calibration data from Figures 90-94, the membrane temperature can now be estimated by measuring the resistance change during self-heating and calculating the membrane temperature from the (normalized) resistance change using

Equation 16; it was assumed that the quadratic fit can be extrapolated up to 250°C. Figure 99 shows the resulting membrane temperature for each design as a function of the applied heating power. For example, a heating power of 287 mW applied to the 2 mm x 1 mm device results in a membrane temperature increase of 188°C. As expected, the membrane temperature increases linearly with the applied heating power (Equation 13).

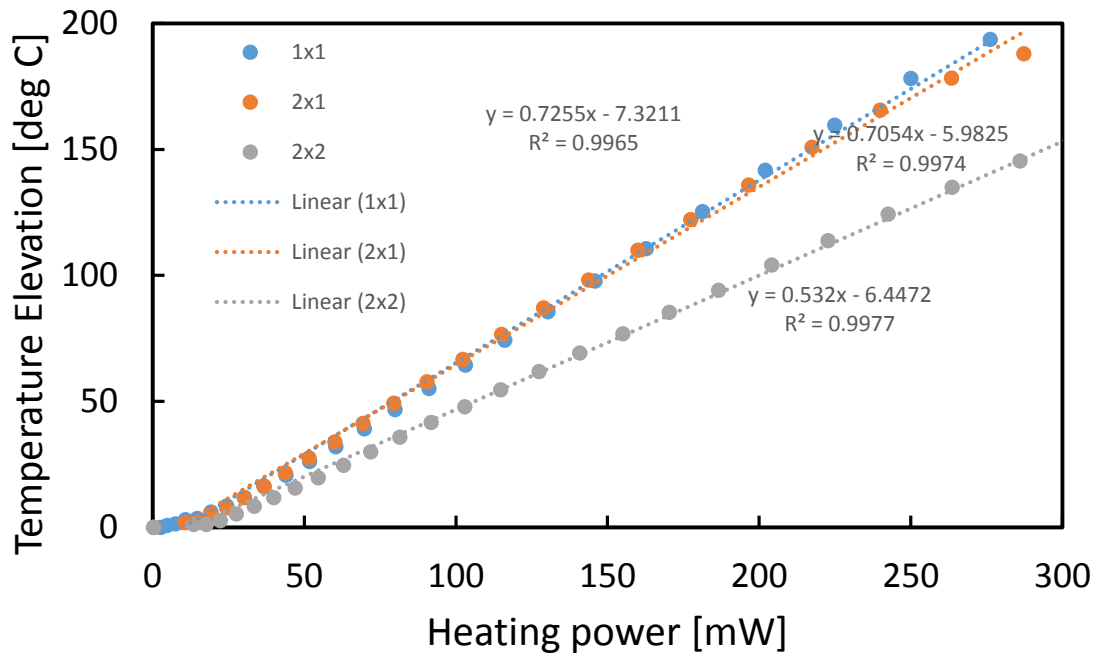


Figure 99 - Estimated membrane temperatures for 1 mm x 1 mm (blue), 2 mm x 1 mm (orange), and 2 mm x 2 mm (gray) μ TPC devices, measured with a +10 V DC bias applied to the substrate. The temperatures are estimated by measuring the temperature-dependent resistance during self-heating and comparing this value with the temperature calibration data.

The measured temperature increases indicate that the simulations performed during the design stage underestimated the temperature elevation for a given heating power. For the 2 mm x 1 mm device with 20 μ m membrane thickness discussed in Chapter 5, simulations predicted a temperature increase of 229°C for a heating power of 500 mW (see Figure 58), but the experimental data indicate a temperature increase of 188°C for only 287 mW of applied heating power. Considering that the tested device is slightly thicker (25

μm) and is composed of additional materials (e.g. aluminum, SiO_2) compared to the pure silicon structure assumed in simulation, the measured temperature elevation should be even less (e.g. due to reduced thermal resistance in the thicker support legs and increased thermal conduction along the metal lines). It appears that the heat transfer to the air, simulated in form of a constant heat transfer coefficient of $h = 50 \text{ Wm}^{-2}\text{K}^{-1}$ applied to all surfaces, has been overestimated. In fact, it is likely that in-between the ridges and pillars the heat transfer to the air is much less effective than e.g. at the top of the ridges or the opposite side of the membrane. To improve the simulation results, heat transfer through the air would have to be modeled more accurately by considering heat conduction through the air with the chip simulated within its full package.

It should also be noted that small non-linearities in the dependence of the membrane temperature on the heating power can be expected. As an example, the thermal conductivity of silicon and of the surrounding air are temperature-dependent, which would introduce non-linearities into the estimated temperature curve. As a final note, the temperature calibration data were taken with the entire packaged chip mounted inside of a temperature-controlled chamber, resulting in there being no temperature gradient between the suspended membrane and the ceramic packaging. In the case of self-heating, however, the membrane alone is heated while the ceramic package remains at a much cooler temperature. This situation results in a temperature gradient across the suspended membrane – and between the membrane and substrate – which leads to certain regions of the resistors having cooler temperatures (and therefore reduced resistances). These effects are not accounted for in the method used to calibrate the change in resistance as a function of membrane temperature. It is suggested that future work explore the use of a thermal

imaging system as an independent verification of membrane temperature elevation during self-heating.

Thermal Transient Behavior

Following characterization of resistance change with respect to temperature, thermal transient measurements were performed. To extract the thermal time constant of the μ TPC devices, a DC bias current of 100 μ A was applied to the measurement resistor. A 200-mW heating pulse was then applied to the heating resistors while simultaneously measuring the voltage change across the biased measurement resistor (Figure 100).

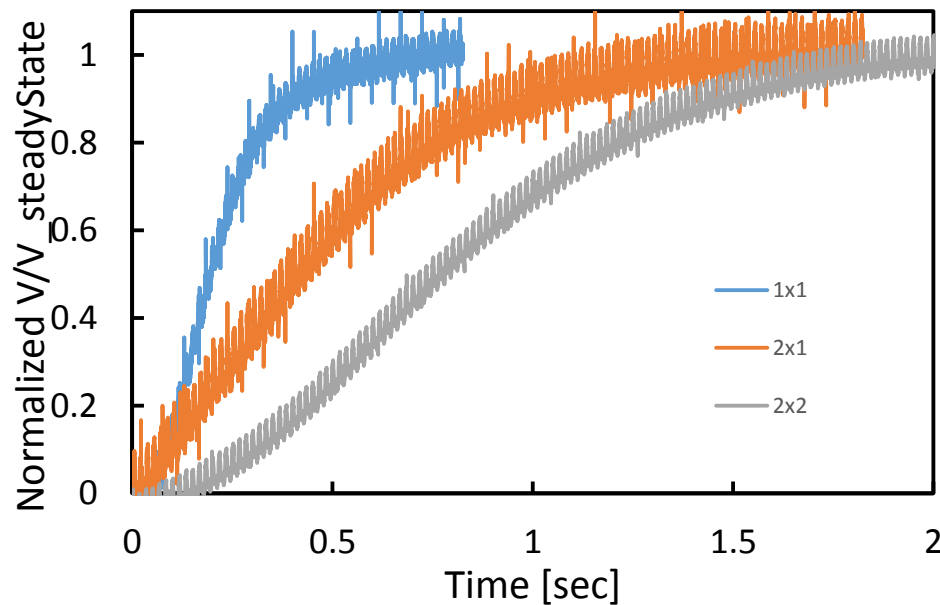


Figure 100 - Normalized thermal transients for all three designs. To extract the thermal time constant of the μ TPC devices, a DC bias current of 100 μ A was applied to the measurement resistor. A 200-mW heating pulse was then applied to the heating resistors while simultaneously measuring the voltage change across the biased measurement resistor.

The resulting normalized transients recorded for each design indicate thermal time constants below 1.5 seconds for all three designs. As expected the temperature exponentially approaches a steady state value when the heating pulse is applied, with the

thermal rise time increasing as a function of the thermal mass of the suspended membranes.

A comparison of the measured thermal time constants with the simulated predictions is summarized in Table 4.

CH 8 – PRE-CONCENTRATOR PACKAGING & CHEMICAL TESTING

Sorbent Coating

While the pre-concentrator designs have thus far been successfully fabricated and experimentally validated for proper electrical and thermal performance, application of a suitable sorbent layer is necessary for chemical functionality. For optimal chemical pre-concentration capacity, only the suspended membranes and high-surface-area 3-D ridge/pillar structures on the membranes would be (uniformly) coated with sorbent. Motivated by this requirement, various deposition techniques were investigated, which allow for individual devices in the array to be locally coated with separate sorbent materials. The exploration of sorbent coating techniques commenced with the following methods, which are available in the laboratory and cleanroom facilities of Georgia Tech:

- Drop-coating from pipette
- Inkjet printing
- Spray-coating with air brush

Due to the relatively large size of the membrane structures – and the correspondingly large sorbent masses required for full coverage – the possibility of drop coating the sorbent solutions directly from a micro-pipette was the first method to be investigated. Initial tests were performed by drop-casting 4 μL droplets of PIB dissolved

in toluene (0.2wt%) with a micro-pipetter onto ridge test structures (Figure 101) remaining from the DRIE process development discussed in Chapter 6.

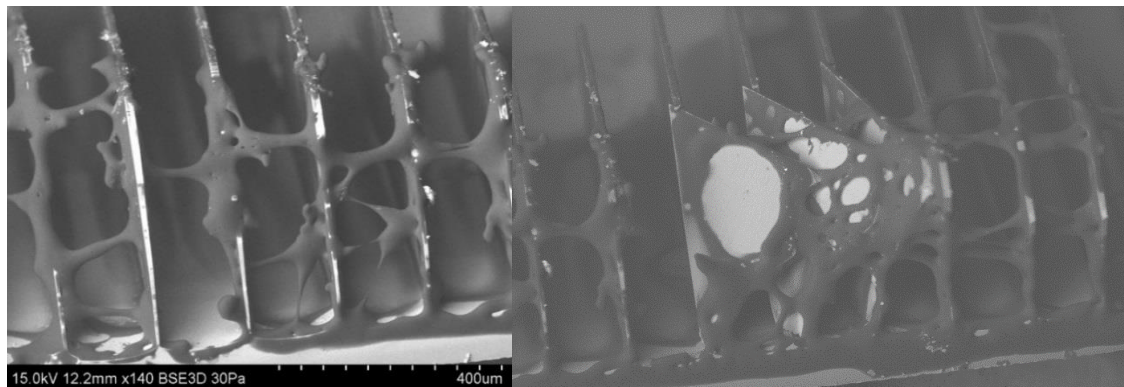


Figure 101 – SEM micrographs of silicon ridge structures coated with PIB by drop-coating of the polymer solution (toluene was used as solvent) from a micro-pipette.

This approach offers simplicity and speed, as entire devices can be coated in a matter of seconds, but resulted in layers that were inconsistent from device to device. As can be seen in the SEM images (Figure 101), the polymer solution does not properly wet the silicon surfaces inside the trenches, resulting in non-uniform deposition. In some cases, drop-coating even resulted in damage to the ridge/pillar structures. Additionally, drop-casting of the sorbent layers proved indiscriminant and difficult to constrain the layers within the boundaries of individual membranes, resulting in unwanted coating of adjacent membranes and much of the supporting substrate. This situation is non-ideal, as the substrate's thermal response is markedly different from that of the suspended membranes. Thus, sorbent coatings deposited on the substrate will capture a portion of the sample analyte concentration, but will not release the captured molecules during thermal desorption, as the substrate is thermally isolated from the self-heating membranes and remains relatively cool. Ultimately, this scenario contributes to a diminished pre-concentration factor. It is suggested that future work revisit this technique, and explore the possibility of utilizing

different solvent systems and surface modifications that could render the device surface more amenable to wetting for the dissolved sorbent.

Inkjet printing of the sorbent polymer layers was also investigated as a technique for achieving localized deposition onto the μ TPC membranes. To this end, inkjet printing was utilized in various tests onto both planar substrates and substrates with significant high aspect-ratio features. As discussed in Chapter 2, however, it was apparent that inkjet printing can suffer from a host of difficulties and limitations, especially when depositing substantially thick polymer layers over the relatively large surface areas of the suspended μ TPC membranes.

For the reasons discussed above, spray coating was chosen as the preferred coating technique due to its simplicity and immediate effectiveness. As discussed in Chapter 2, spray coating was accomplished by the use of a solvent atomizer in conjunction with laser-cut shadow masks. The use of the shadow masks enabled localized polymer deposition onto the membranes only, preventing sorbent from being deposited in undesirable regions on the devices. With the use of high concentration solutions and multiple coating steps, film thicknesses in excess of 200 μ m on the membrane surfaces can be achieved in less than an hour (Figure 104).

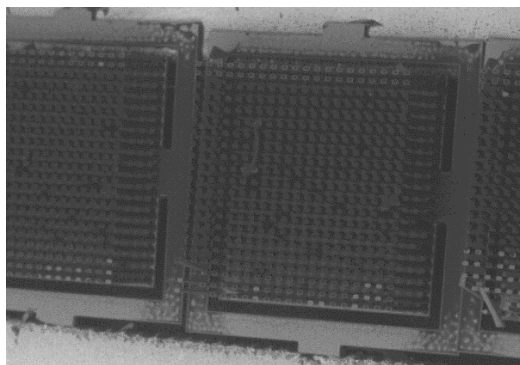


Figure 102 –SEM image of an array of 1 mm x 1 mm μ TPC membranes spray-coated with PIB.

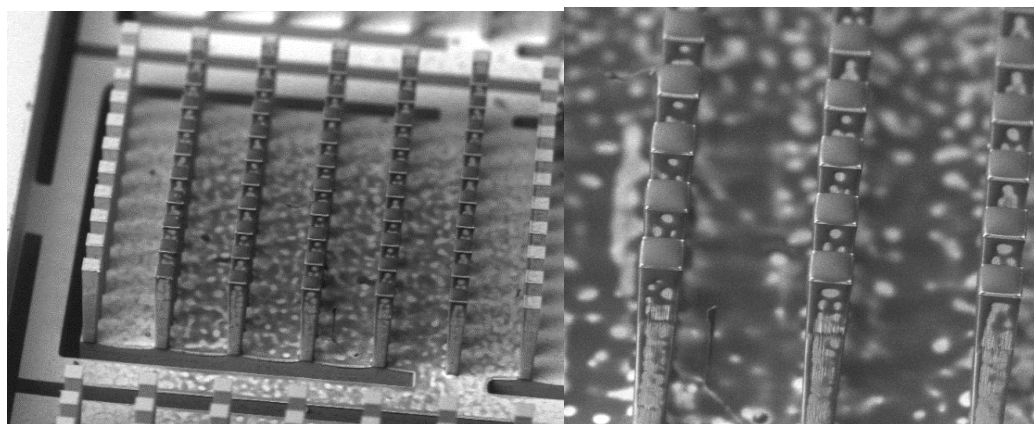


Figure 103 - SEM image of thin PIB coating, which was deposited with a shadow mask onto a suspended 2 mm x 1 mm μ TPC membrane. As seen in the figure, the location of the coating can be precisely controlled, allowing sorbent to be deposited only in regions useful for pre-concentration.

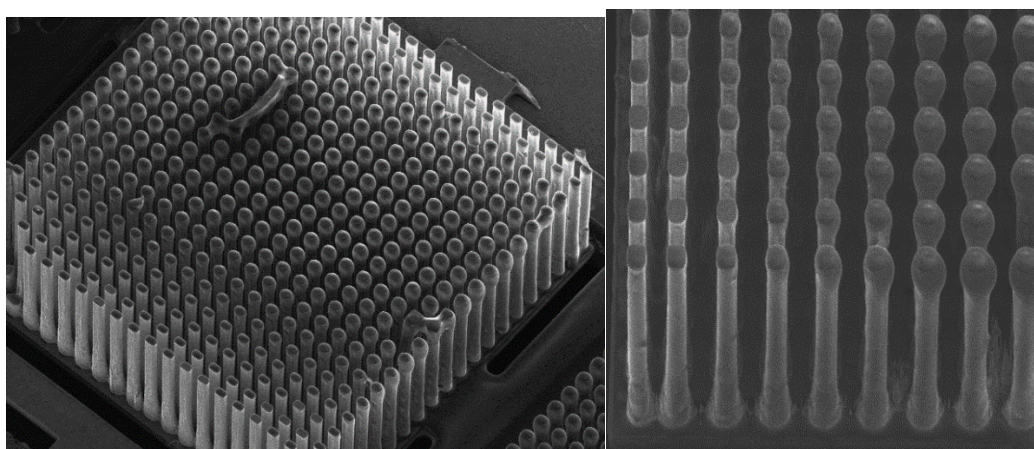


Figure 104 - SEM image of thick (approximately 50 μ m) OV-1 sorbent coating deposited by shadow masking onto a suspended 2 mm x 2 mm μ TPC membrane. As shown in the image on the right, the location of the coating can be precisely controlled.

Future work should revisit the other coating techniques more in depth, and also explore the possibility of using plasma deposition to deposit uniform polymer films. In the research group of Prof. D. Hess at Georgia Tech, plasma deposition has been used to deposit fluorocarbons [151]. While uniform films result, this technique generally yields highly cross-linked polymer films, which might in their current form not be suitable for TPCs (polymers like PIB are rubbery and act similar to sponges for VOCs). The use of multi-sorbent films (e.g. DVB/PDMS/Carbowax) and activated carbon particles – such as those used in conventional SPME [20, 44] and other μ TPC systems [1, 3, 18, 107, 119] – is suggested as a fruitful investigation for future work. In anticipation of this possibility, several of the μ TPC designs implemented wide ridge and pillar spacings that could accommodate relatively large activated carbon granules.

Packaging Concept

With a viable coating technique in place, development shifted to a suitable packaging strategy. As touched on during the mask layout stage, external circuit interface specifications require the chips to be mounted into a 28-pin ceramic DIL package. Furthermore, the packaging design has a significant influence on the pre-concentration factor, as the effective dead volume is directly determined by the packaged chamber and interconnect volumes. With these requirements in mind, a custom packaging approach was designed that minimizes the total dead volume to approximately 10 μ L and simultaneously forces the analyte-loaded gas stream through the high surface-area, sorbent-coated regions of the μ TPC on the back surface of the suspended membranes (Figure 105). In this case, a uniform coating thickness of 50 μ m results in a total sorbent volume of 2.5 μ L for an array

of the 2 mm x 2 mm devices. With a partition coefficient of 1000x for toluene into PIB, release of the sorbed toluene into a 10 μ L chamber volume would result in a pre-concentration factor of 250x. If, however, the chamber volume were 200 μ L, the pre-concentration factor would be reduced to only 12.5x which clearly demonstrates the importance of the packaged dead volume. The packaging process has been designed so that the packaged dies interface seamlessly with both the existing gas testing platform and measurement circuitry, as illustrated in Figure 105.

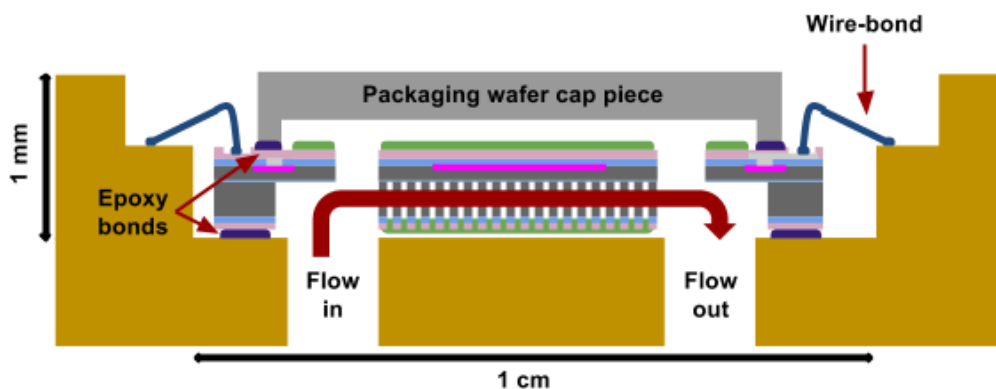


Figure 105 - Profile view of μ TPC packaging concept. A silicon capping piece (light gray) diced from a separately-processed packaging wafer is bonded to a μ TPC die (dark gray) with epoxy. The bottom surface of the μ TPC die is bonded with epoxy to the ceramic DIL package (gold) with the inlet/outlet ports on the die aligned to the laser-cut vias on the ceramic DIL package. The packaging results in a dead volume of approximately 10 μ L and is designed to be gas-tight with chamber walls that are inert with respect to VOC sorption.

In anticipation of the final packaging requirements, a packaging wafer mask set was designed during the mask layout stage. The packaging wafer process sequence requires two additional photomasks and was designed to allow the front surface of the μ TPC arrays to be capped and sealed with an inert, gas-tight, low-volume chamber.

To accomplish this, each die on the packaging wafer consists of a raised silicon ring that encircles the μ TPC array on the corresponding device wafer (Figure 106), while maintaining access to the wire-bonding pads around the perimeter of the die. Due to the necessary tolerances associated with bonding the capping piece, the introduction of additional setbacks between the ring, μ TPC array, and wire-bond pads were required. Ultimately, this design choice, in conjunction with the limit to maximum die size, introduced the most significant constraints on the footprints for the μ TPC arrays.

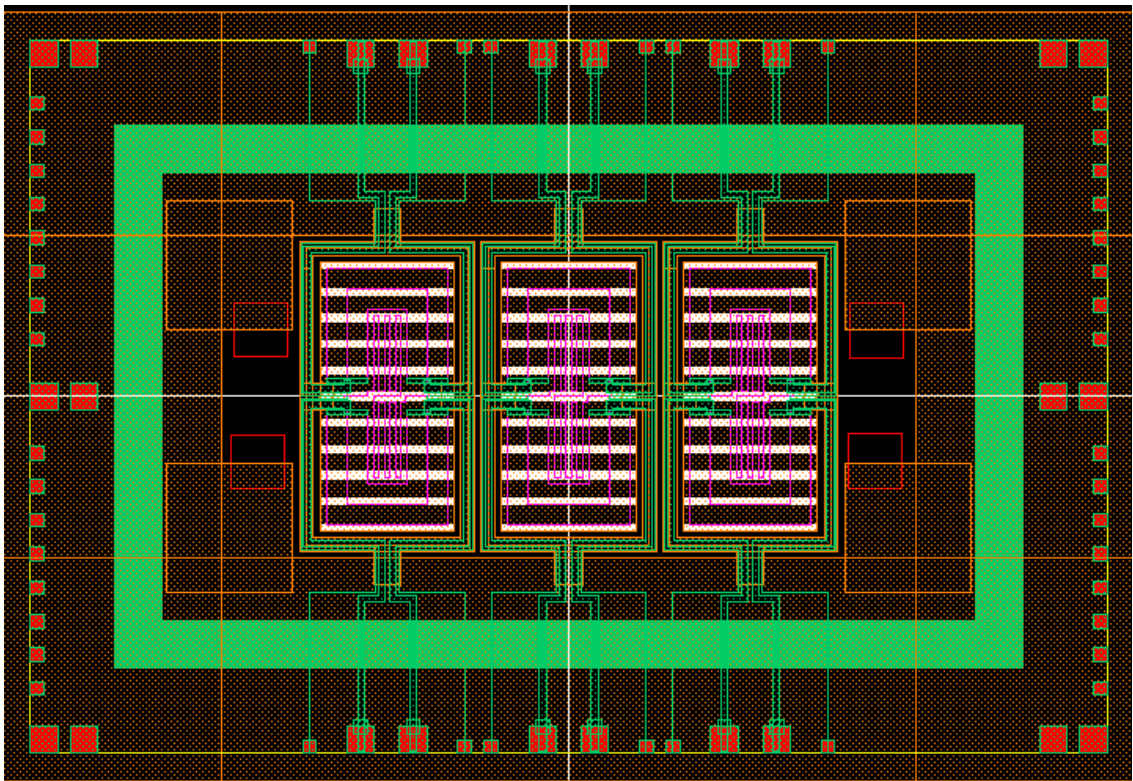


Figure 106 - Detail from mask layout for 2 mm x 1 mm μ TPC die, showing placement of the packaging wafer die onto the μ TPC die. The green ring surrounding the μ TPC array represents the raised silicon ridge on the packaging wafer capping piece.

The full fabrication sequence of the packaging wafer requires three mask steps (Figure 107), and represents new process development. Processing begins with the deposition and patterning of a thin metal layer onto a bare silicon wafer. The patterning of the metal layer re-uses Mask 3 from the SOI process flow, and is used only to aid in

alignment of the packaging die (i.e. not for electrical connections) to the device wafer. Next, several microns of dielectric are deposited and patterned on the front surface of the wafer for use as a DRIE hard mask. The wafer is then etched *via* DRIE partially through its bulk thickness, but stops short of reaching the back surface. At this point, additional dielectric layers are deposited onto the back surface and patterned to serve as a DRIE hard mask for forming the raised silicon rings. A final DRIE etch from the back surface creates the raised ring structures, and the completed wafer is ready for bonding to the device wafer. The etched through-holes from the front surface are used as windows to see through to the device wafer below during alignment. With the full 3-mask processing sequence, the packaging wafer is capable of being aligned to the underlying device layer and bonded at the wafer level (i.e., all die bonded simultaneously), which lends itself to large-scale manufacturing.

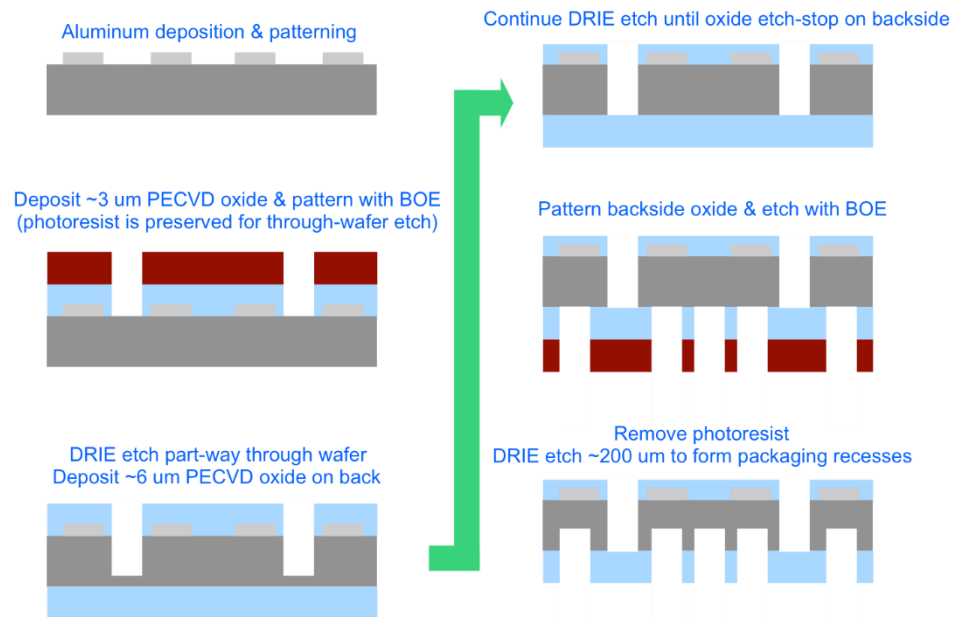


Figure 107 - Process flow diagram showing full fabrication sequence for μ TPC packaging wafer. If the capping pieces are to be bonded individually by hand, the process sequence can be simplified to a single mask step where DRIE of silicon is used to form the raised silicon rings.

If individual die are required to be bonded separately, however, the processing sequence can be simplified to just a single mask step with a DRIE etch to form the raised circular rings. This approach is more suitable for rapid prototyping and proof-of-concept work, and is the method employed in the presented packaging results. Figure 108 shows photographs of several diced capping die from a completed packaging wafer, and an individual capping die that has been bonded to a glass slide with epoxy placed on top of the raised ring structure.



Figure 108 - Photographs of several diced die (left) from completed packaging wafer, and single die bonded to glass slide with epoxy (right). To seal the top surface of the μ TPC die, epoxy is applied to the raised silicon ring of a capping die, which is subsequently bonded to the μ TPC die.

While the silicon capping pieces produced by the packaging wafer serve to seal the μ TPC chamber from the top, the chamber must also be sealed from the back surface. To achieve this goal, fluidic vias were laser-cut directly into the ceramic DIL package as shown in Figure 109.

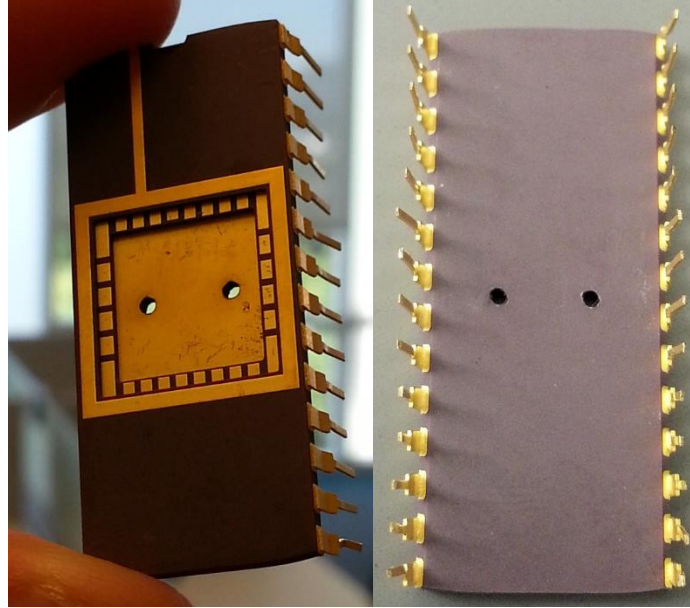


Figure 109 - Views from the top surface (left) and bottom surface (right) of ceramic DIL package, which has been laser-cut in preparation for packaging of a μ TPC die. The laser-cut vias are designed to align with the inlet and outlet ports on the μ TPC die.

The vias were arranged so that they are located directly beneath the inlet and outlet ports on the μ TPC die. In this way, the μ TPC chip – already sealed from the top with the silicon capping piece – can be directly bonded to the gold surface of the ceramic DIL package and the vias act as extensions of the on-chip inlet and outlet ports. Figure 110 is a photograph of a completely packaged device.

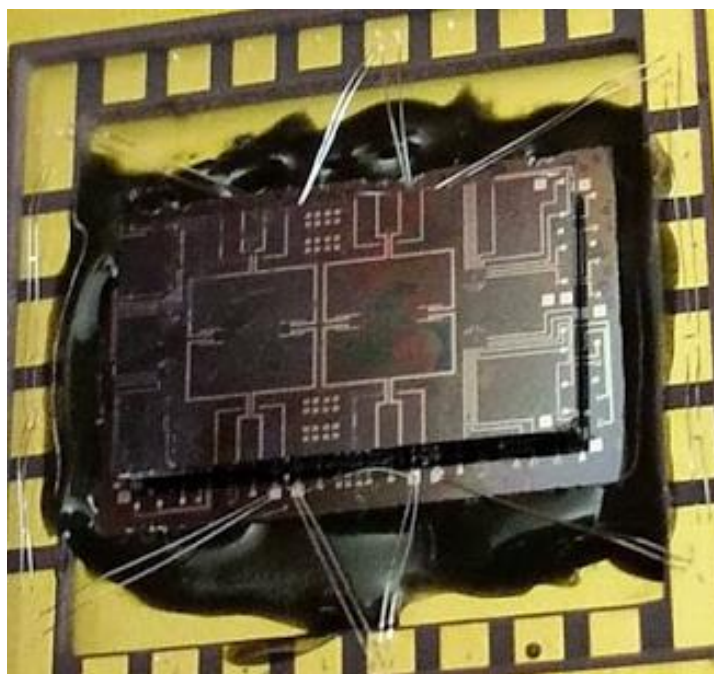


Figure 110 - Photograph of fully-packaged μ TPC die, which has been placed over the laser-cut vias and bonded with epoxy on the bottom surface. The top surface of the die has been sealed by bonding a silicon capping piece with epoxy. As can be seen from the figure, the packaging has been designed to allow wire-bonding between the die and package.

When applying the epoxy during bonding, care was taken to ensure that minimal epoxy enters the inside of the μ TPC chamber, as illustrated in Figure 108. In this way, the chamber walls exposed to gas samples are essentially composed of inert materials (e.g. silicon, gold, ceramic) and should not contribute significantly to sorption of VOC concentrations during measurement.

Furthermore, it is assumed that the partition coefficient of the epoxy is orders of magnitude less than the partition coefficients of the sorbent coatings, which minimizes the risk of unwanted sorption even further. However, the partition coefficient for the epoxy has not yet been verified by experiment, but is suggested for future work. If the epoxy is found to interfere with μ TPC sorption, the use of alternative epoxies based on inert materials (e.g. ceramics, PTFE) can be explored. Following packaging, the entire fluidic

pathway was tested for leaks and was found to be gas-tight for both nitrogen and air flows of up to 100 ml/min.

Chemical Measurements

With packaging complete, the devices were ready to interface with the existing gas flow system (Figure 111) for initial evaluation of chemical performance. Measurements commenced with testing of the integrated chemical sensors, which were controlled by an amplifying feedback loop and exposed alternately to pure nitrogen carrier gas and defined concentrations of VOCs in the custom gas set-up.

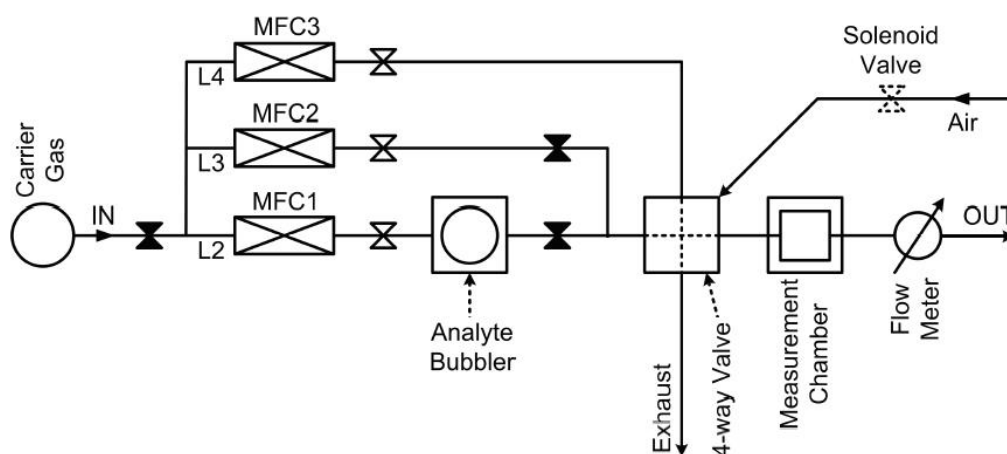
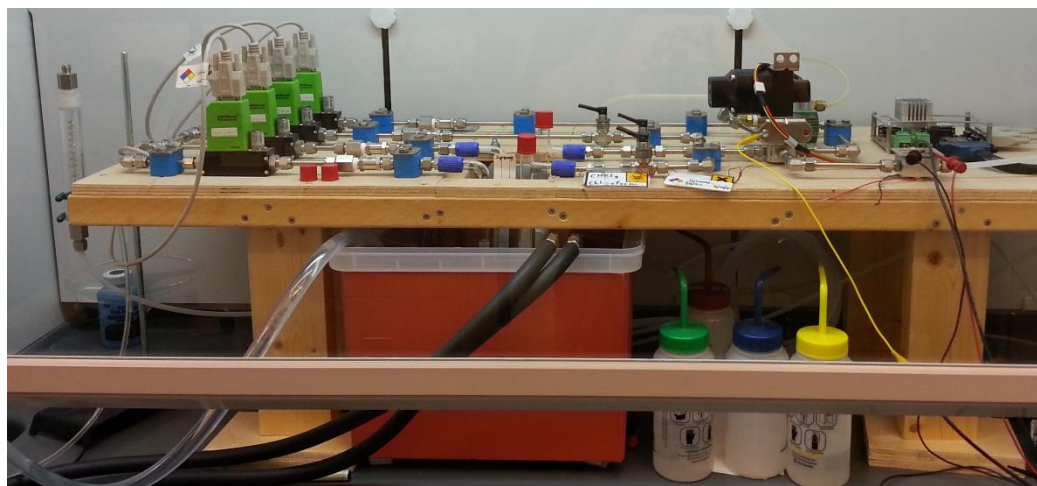


Figure 111 - Photograph (top) and schematic diagram (bottom) of custom gas setup. Flow rates are controlled by precision mass flow controllers (MFCs) and known VOC concentrations are generated by flowing carrier gas through a temperature-controlled bubbler and diluting with carrier gas. A pneumatic 4-way valve enables rapid switching between reference carrier and analyte gas streams.

As an example, Figure 112 shows the frequency response of a PECH-coated ($2\ \mu\text{m}$ thickness) resonator to different concentrations of toluene. The data were collected at a constant temperature of $20\ ^\circ\text{C}$ and a flow rate of $80\ \text{ml/min}$ through the measurement chamber. Between successive exposures to the analyte-loaded gas stream, the gas flow over the resonator is changed to pure nitrogen carrier gas. A four-way valve enables fast switching and allows the investigation of signal transients [55, 90]. From the baseline

frequency data, a short-term frequency stability of 3×10^{-8} was extracted using the Allan variance method.

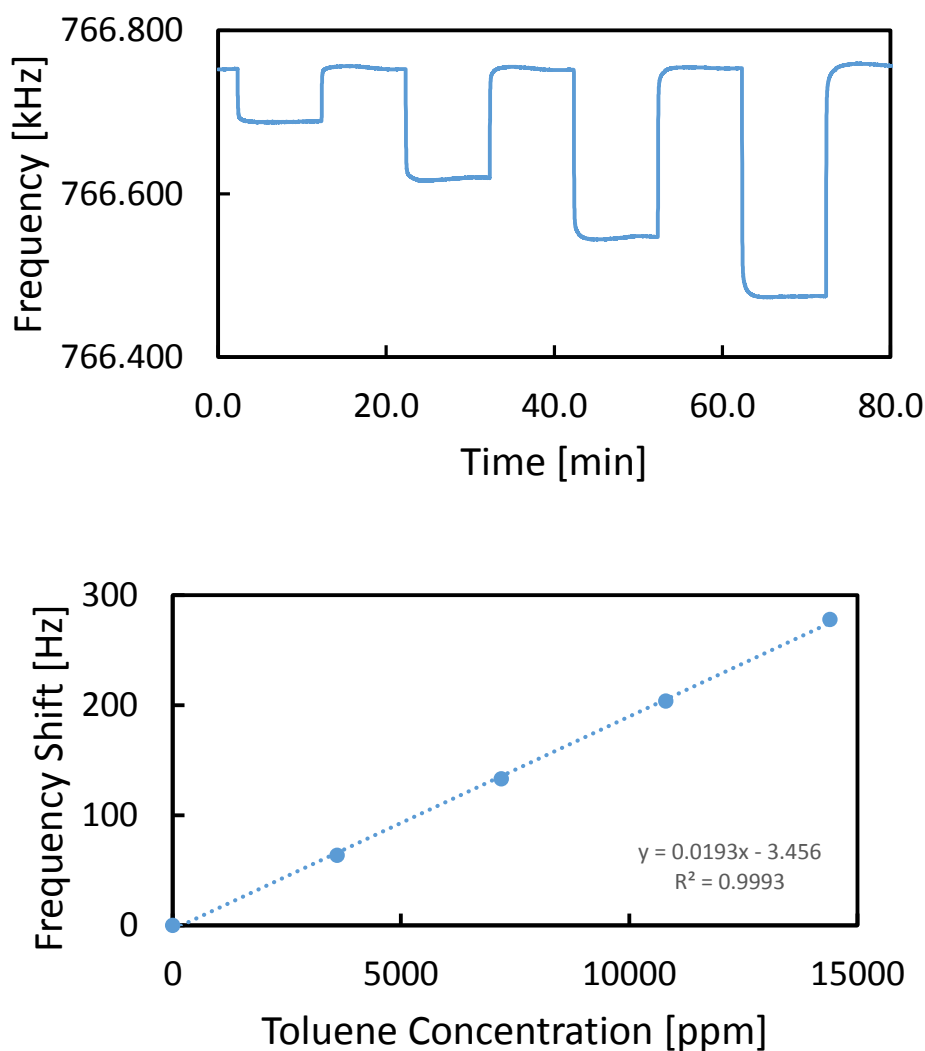


Figure 112 - Experimentally observed frequency shift of PECH-coated resonator as a function of time (top); the microsensor is subsequently exposed to different toluene concentrations (3600-7200-10800-14400 ppm). Between successive toluene exposures, the chamber is flushed with nitrogen as carrier gas. The response of the sensor with respect to toluene concentration is reversible and very linear (bottom).

An analysis of the measured frequency data reveals that the sensors exhibit a linear response with respect to toluene concentration (Figure 112, right). Using the observed chemical sensitivity of 0.019 Hz/ppm for toluene and the Allan variance of 3×10^{-8} , limits

of detection below 5 ppm for toluene can be expected for this device. However, these LoD values need to be confirmed by measurements at ppm-level analyte concentrations. Another important observation from the gas measurement data is that the sensor's response is fully reversible with time constants well below 1 minute even for relatively thick polymer films.

With suitable operation of the integrated chemical sensors confirmed, chemical testing shifted toward observation of the pre-concentration effect. In order to highlight the novel design of the μ TPC – which allows for measurements to take place in a static, non-flowing environment – an experimental setup was constructed which was capable of trapping a fixed volume of sample gas inside the μ TPC chamber. This setup consisted of utilizing the custom gas flow setup to flow a known concentration of analyte over the μ TPC until the analyte concentration in the sorbent was in equilibrium with the analyte concentration in the environment. Once at equilibrium, the inlet/outlet ports to the μ TPC were quickly sealed with a mechanical clamp (Figure 113). Initial experiments were carried out with a μ TPC chip that had been mounted into a ceramic DIL package, but not bonded to the package with epoxy. The μ TPC die was not sealed from the top surface with a capping piece, but was sealed into a larger chamber with the use of a second ceramic DIL package (containing an array of chemical sensors) and a thin nitrile gasket (Figure 113).

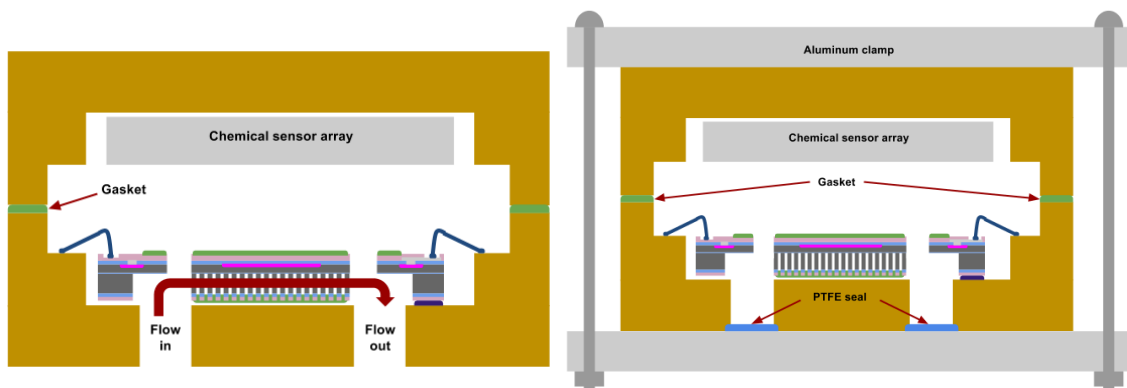


Figure 113 - Experimental test setup for measuring pre-concentration factor. The μ TPC and chemical sensors are first exposed (left) to a constant toluene concentration until equilibrium is reached. Once in equilibrium, the inlet/outlet ports to the chamber are quickly sealed (right) with a mechanical clamp, trapping a fixed volume of toluene inside the chamber. Applying heating power to the μ TPC during thermal desorption drives sorbed analyte molecules out of the μ TPC sorbent, which raises the ambient toluene concentration inside the chamber. Analyte uptake into the chemical sensors then increases due to the increased ambient concentration.

The experiment was performed by first exposing a μ TPC and chemical sensors coated with PEUT to a constant 5000 ppm concentration of toluene until equilibrium was reached. Once in equilibrium, the inlet/outlet ports into the chamber were quickly sealed with a mechanical clamp, trapping a fixed volume of gas inside the chamber. Due to the condition prior to clamping, all sorption into the sorbent layers on both the chemical sensors and the μ TPC was presumed to be in equilibrium with the analyte concentration in the gas phase. Once the chamber was sealed, application of heating power to the μ TPC drives sorbed analyte molecules out of the μ TPC sorbent (i.e. thermal desorption), which raises the analyte concentration inside the chamber. Analyte uptake into the chemical sensors then increased due to the increased ambient concentration. After several seconds, the entire package heats up (due to the power generated in the μ TPC), which begins to reduce the temperature-dependent sorption capacity of the sorbent layer on the chemical sensors. At this point, sorbed analyte desorbs from the chemical sensor and a new equilibrium (based on the elevated temperature) is established inside the chamber.

By first performing an initial control experiment – where only pure N₂ (i.e. no analyte) is introduced into the chamber – the response of the system to temperature alone can be recorded. This response is then subtracted from the total response due to both temperature and analyte effects (Figure 114), resulting in a plot of the system's response to analyte only. As can be seen from the figure, the aggregate sensor response shows the sensor shifting in frequency due to the increased mass uptake – as if it had been exposed to a higher gas concentration than that which was originally introduced into the chamber.

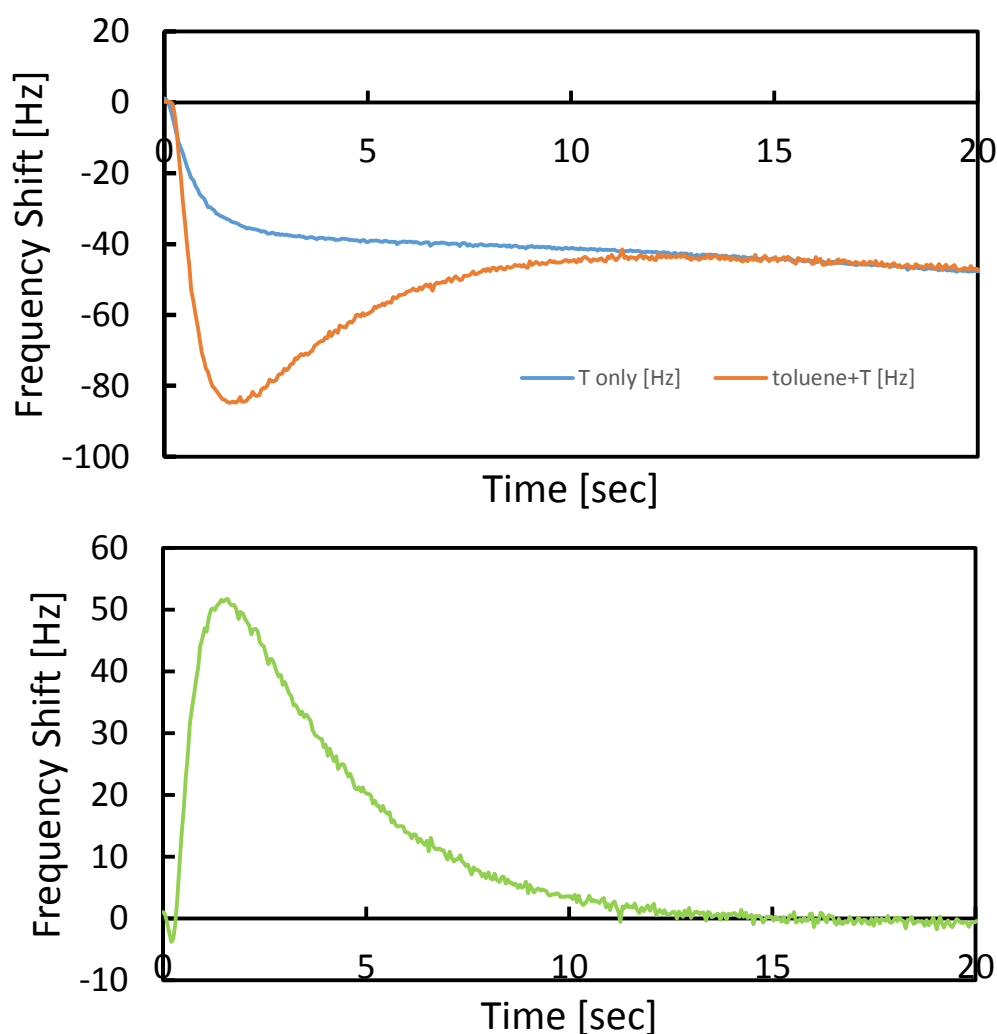


Figure 114 - Experimentally observed pre-concentration factor. (Top) shows a comparison between the sensor signal when the μ TPC is exposed to N₂ only for (blue curve) and 5000 ppm of toluene for (orange curve). The plot (bottom) shows the aggregate response, where temperature effects have been removed leaving only the response to toluene. The response of the sensor alone (i.e. without the μ TPC

connected) was approximately 100 Hz when exposed to 5000 ppm of toluene; thus, an additional increase of 50 Hz due to pre-concentration has boosted the signal by 50%. Thermal desorption was performed by applying 100mW of heating power to the μ TPC for 30 sec.

While significant as a proof-of-concept demonstration, the observed PC factor of 50% is considerably lower than expected. This is almost certainly a result of the large dead volumes introduced by interfacing with the cantilever-based sensors on a separate DIL package. In the experimental setup used to collect these data, the total dead volume inside of the sealed chamber is approximately 200 μ L, nearly twenty times larger than the 10 μ L volume possible with the more sophisticated packaging detailed in Chapter 7. As the increased ambient concentration experienced by the chemical sensor during thermal desorption is a function of the volume into which the sorbed molecules are released, reducing the dead volume is critical. Thus, the pre-concentration factor is expected to increase to at least 20 with use of the improved packaging. Furthermore, the experiment described above involved pre-concentration of a relatively high-concentration sample, where the chemical sensor might be saturated after thermal desorption. The μ TPC system, however, was designed for optimal operation of very low-concentration samples (e.g. ppb), and it is expected that the pre-concentration factor will increase further when the capability of testing at these concentration levels is available. Future work will involve installing a calibrated gas permeation tube delivery system capable of reaching these low concentrations.

CH 9 – OUTLOOK & FUTURE WORK

Integrated Recess Structure

Different techniques for improving the quality and uniformity of deposited sorbent polymer films onto MEMS-based micro-cantilever chemical sensors were presented. A novel integrated recess structure for constraining the sorbent polymer layer to a fixed volume with uniform thickness was developed. The recess structure was used in conjunction with localized polymer deposition techniques, such as inkjet printing and spray coating in combination with shadow masking, to deposit controlled, uniform sorbent layers onto specific regions of chemical sensors, enhancing device performance. By constraining the deposited sorbent layer away from high-strain regions, device stability is enhanced, and by replacing chemically-inert silicon mass with ‘active’ sorbent mass, device sensitivity is increased. Additionally, localized polymer deposition enables arrays, where each device in the array is coated with a different polymer, improving overall selectivity of the sensor system. The integrated recess structure represents improvement over prior state-of-the art by addressing the sorbent coating challenge at the sensor design stage, i.e. as a priority from the beginning, rather than as an afterthought.

It is suggested for future work that an optical technique to determine film thickness on coated devices be explored. As the integrated recess structure discussed in Chapter 2 can be utilized to constrain the film to a readily measurable known volume, the process of determining the volume of deposited sorbent should be straightforward. For example, the integrated recess structure has a well-known fixed volume determined by precision

processing and easily verified by independent measurement prior to coating. Once coated, it is clear to see when the volume of the recess structure has been completely filled, allowing one to know precisely the volume of sorbent polymer occupying the space. It is also suggested for future work that improvements be made to the measurement setup. For example, the expected LoDs for the sensors are extrapolated down to the low-ppm range, but these need to be confirmed by challenging the sensors with actual low-ppm analyte concentrations.

Transient Signal Generation & Analysis

In addition to localized polymer deposition, the investigation of transient signal generation and analysis was presented for mass-sensitive chemical sensing of volatile organic compounds (VOCs) in the gas phase. It was demonstrated that transient signal analysis can be employed to enhance the selectivity of individual sensors leading to improved analyte discrimination. Transient signals were generated by the rapid switching of mechanical valves, and also by thermal methods. Thermally-generated transients utilize a novel sensor design which incorporates integrated heating units onto the cantilever and enables transient signal generation without the need for an external fluidic system. When compared with prior state-of-the-art, transient signal generation and analysis represents a distinct improvement, especially to sensor selectivity. The ability of a single sensor to distinguish closely-related analytes, e.g. different alcohols or aromatic hydrocarbons, has been demonstrated successfully using transient signals generated by the heated cantilevers.

It is suggested for future work that improvements to the temporal resolution of the measurement system be performed, so that frequency measurements can be obtained less

than 1 ms apart. This is important due to the fast thermal rise time of the heated cantilevers, so that the entire transient signal can be sampled quickly enough. Additionally, pulsed operation schemes could be investigated, which could remove the requirement of driving the resonator continuously, enabling lower power consumption per measurement and potentially improving stability. As discussed previously, it is also suggested that the thermal properties of the packaging be improved to avoid undesirable heating of the chip during thermal transient generation. For example, the chip could be connected to a heat sink capable of effectively sinking the heating power from the pulses, or the measurement protocol could be modified to work with shorter heating pulses. Also, as discussed previously, laminar flow in the measurement chamber might further impede the rate with which the concentration changes at the surface of the sensing film. The effect of this concentration step with finite slope in the measurement chamber was not observed during initial data collection, as data were only recorded every 1 s and due to the slower diffusion of toluene into PIB. Thus, the heating-induced transients likely represent a more accurate representation of the diffusion in the sensing film. It is suggested for future work that additional measurements be taken to confirm the conclusions of this result.

Pre-Concentration

Finally, the development of a MEMS-based μ TPC system for enhanced detection of VOCs in the gas phase has been demonstrated. The novel system features integrated chemical sensing technology, and can be used to improve the sensitivity of previously developed cantilever-based resonant micro-sensors by temporarily increasing the effective concentration seen by the sensors. The system features arrays of suspended, thermally-

isolated μ TPC devices and offers the potential for coarse pre-filtering of complex gas mixtures, leading to enhanced selectivity. Experimental measurements confirm that even the largest hotplates (2 mm x 2 mm) can be heated to 200°C with less than 500mW of heating power, and exhibit thermal time constants below 1 second. Additionally, the design of the system enables novel modes of operation without the need of an external fluidic system, with initial tests of the system demonstrating a pre-concentration factor of 50% for toluene in a static, no-flow configuration.

While significant milestones have already been achieved, this endeavor is a multi-generational one, which will require several years to reach full maturity. Future work will focus on increasing the pre-concentration factor of the system through various means. For example, improved techniques for the localized deposition of sorbent materials will be investigated, with an emphasis on utilizing plasma-deposited and activated carbon-based sorbents. The implementation of multi-layer sorbents comprised of several different sorbent types may also prove fruitful in this regard. The viability of the drop-casting technique may be improved by exploring the possibility of different solvent systems and surface modifications that could render the device surface more amenable to wetting. Also, the effect of sorbent coating thickness on device performance can be explored and optimized.

In addition to sorbent layer improvements, the packaging design must also be enhanced. For example, it became clear during the thermal evaluation of the devices that there was evidence of the package itself heating up more than expected. To mitigate this undesirable effect, a heatsink could be coupled to the ceramic package with thermally conductive paste, or active cooling could be employed to ensure the ceramic package stays

at a more stable temperature during measurement. Additionally, it is yet unclear if the bonding epoxy is sufficiently inert to the sorption of VOCs, especially at elevated temperatures. If this epoxy proves unsuitable, other epoxies based on ceramic or PTFE chemistries could be employed as more inert alternatives. If even these epoxies do not render the μ TPC chamber sufficiently inert, it could even be possible to coat the walls of the chamber with parylene. Deposition of parylene over the sorbent-coated membrane surfaces could be prevented by heating the μ TPC membranes during parylene coating, as parylene deposition is inhibited onto hot surfaces. Such a technique holds substantial possibility for increasing the pre-concentration factor by truly rendering all other surfaces inside the chamber inert.

Perhaps the richest area for improvement is in the testing setup. While it was important to first demonstrate the system's novel measurement capabilities in a static, no-flow arrangement, all other μ TPCs encountered in the literature utilized some sort of flow system with zero dead-volume valves that allowed for sharp injection into a GC column or measurement chamber. Such an approach could be explored with this system as well, along with an investigation of optimal flow rates, desorption heating powers, and heating durations. Along these lines, it will also be essential to minimize the μ TPC dead volume by improving system packaging. The effect of more sophisticated heating patterns could also improve system performance, in both a static, no-flow arrangement as well as a forced-flow setup. Low-cost, low-power microcontrollers in a feedback arrangement could generate the desired heating patterns, and could even improve the total system's portability, allowing automatic operation on mobile platforms for extended periods of time. Such microcontrollers could further be used to remove temperature effects in real-time by

comparing the output of a sensor to that of an uncoated, reference device. This type of support circuitry would be necessary to fully realize the system's capability of operating in real-time with all four integrated sensors.

In addition to circuit improvements, challenging the system with much lower analyte concentrations is also likely to improve performance, as the integrated sensors will be able to operate far away from their saturation points. To accomplish this, however, will require significant modification to the existing gas flow setup and will likely require the installation and calibration of a gas permeation tube delivery system for generating such low concentrations in a reliable and consistent manner. Clearly, much work remains for the system demonstrated here to reach its full potential, but the possibilities are very exciting.

APPENDIX A – SUPREME SIMULATION CODE

SUPREM OUTPUT FILE

```
*****
***                               TSUPREM-4  (TM)                               ***
***      Version D-2010.03-0, System K (AMD64: Linux)      ***
***                               Copyright (C) 1988-2007                               ***
***                               Synopsys, Inc.                               ***
***                               ***                               ***
*** This software and the associated documentation are ***
*** confidential and proprietary to Synopsys, Inc. Your ***
*** use or disclosure of this software is subject to the ***
*** terms and conditions of a written license agreement ***
*** between you, or your company, and Synopsys, Inc. ***
***                               ***                               ***
***                               Compiled: February 09, 2010                               ***
***                               TSUPREM-4 is a trademark of Synopsys, Inc. ***
*****
```

17-Mar-2015 16:35:01

Entering source file modifiedStanfordDoping.sup.

assign name=length n.val=0.01

assign name=pwidth n.val=0.005

Establish the mesh

Use default X spacing for 1-D

Specify a finer mesh in the Y-direction for more accuracy

line y loc=0.0 spacing=0.01 tag=top

line y loc=10.0 spacing=0.10 tag=bottom

initialize the silicon

initialize <100> impurity=phosphorus i.resistivity=10

** Automatic X grid generation: lines at X=0 and X=1 micron.

2 lines in the x direction.

256 lines in the y direction.

make plots on the screen (instead of postscript file)

```

option device=X

# use detailed oxidation model
method vertical pd.full

##

# Processing

# perform a pre dep diffusion
diffusion time=40 temperature=930 boron=3.82e20
diffusion continue time=90 temperature=930 t.final=600
select z=boron title="Predep Boron"
plot.1d x.val=0
pause

# plot the results of the predepimplant
select z=log10(abs(doping)) title="Doping Profile, before and after drive-in"
plot.1d x.val=0 y.min=13 y.max=21 x.min=-0.2 x.max=2.0

# drive-in
diffusion time= 60 temperature= 600 t.final=950 inert
diffusion continue time= 5 dryo2
diffusion continue time=30 weto2
diffusion continue time=30 t.final=1000 inert
diffusion continue time=30 dryo2
diffusion continue time=20 inert
diffusion continue time=100 t.final=600

# plot results after the anneal
select z=log10(abs(doping))
plot.1d x.val=0 color=2 ^axes ^clear

#Annealing Metal in Lindberg Furnace
diffusion time=40 temperature=30 t.final=350 inert

*** Warning: Temperature (30 C) is below 400 degrees; impurity diffusion may
*** be inaccurate and program may have numerical difficulties.

diffusion continue time=33 t.final=450 inert

```

```

diffusion continue temperature = 450 time=150 inert
diffusion continue time=120 t.final=33 inert
select z=log10(abs(doping))
plot.1d x.val=0 color=3 ^axes ^clear
# print the results
select z=doping
print.1d x.val=0 layers

```

Num	Material	Top	Bottom	Thickness	Integral
1	oxide	-0.0895	0.0687	0.1582	-2.3372e+14
2	silicon	0.0687	1.2972	1.2285	-2.7373e+14
3	silicon	1.2972	10.0000	8.7028	3.9028e+11

```

select z=doping
extract silicon x.val=0 value=0 d.extrac assign name=Dj
    Extracted result: 1.22849
electric x.val=0
***** STRUCTURE INFORMATION *****

```

LAYER	MATERIAL	THICKNESS	REGION	DIFTYP	THICKNESS	TOP	BOTTOM
2	oxide	0.1582			0.1582	-0.0895	0.0687
1	silicon	9.9313	2	p	1.2083	0.0687	1.2770
			1	n	8.7013	1.2987	10.0000

```

*****
Bias step 1: 0.00 (Volts)
*****

```

Material	Thickness	Type	Junction Depth	Sheet Resistance
oxide	1580 A			
silicon	9.93 um	P	1.23 um	248 ohm/sq
		N	9.93 um	13.8 K ohm/sq

```

*****
Exiting source file modifiedStanfordDoping.sup.
*** END TSUPREM-4 ***

```

APPENDIX B – COMSOL SIMULATION CODE EXAMPLE

```
function out = model
%
% MT_1mmx1mmx20um_100umLegs_Ridges_h15_p500mW.m
%
% Model exported on Jun 20 2015, 18:42 by COMSOL 4.4.0.195.

import com.comsol.model.*
import com.comsol.model.util.*

model = ModelUtil.create('Model');

model.modelPath('C:\Users\cantilever\Desktop\MT_COMSOL\CodeModels');

model.modelNode.create('mod1');

model.geom.create('geom1', 3);
model.geom('geom1').feature.create('BLK1', 'Block');
model.geom('geom1').feature.create('BLK10', 'Block');
model.geom('geom1').feature.create('BLK11', 'Block');
model.geom('geom1').feature.create('BLK12', 'Block');
model.geom('geom1').feature.create('BLK13', 'Block');
model.geom('geom1').feature.create('BLK14', 'Block');
model.geom('geom1').feature.create('BLK15', 'Block');
model.geom('geom1').feature.create('BLK16', 'Block');
model.geom('geom1').feature.create('BLK17', 'Block');
model.geom('geom1').feature.create('BLK18', 'Block');
model.geom('geom1').feature.create('BLK19', 'Block');
model.geom('geom1').feature.create('BLK2', 'Block');
model.geom('geom1').feature.create('BLK20', 'Block');
model.geom('geom1').feature.create('BLK21', 'Block');
model.geom('geom1').feature.create('BLK22', 'Block');
model.geom('geom1').feature.create('BLK23', 'Block');
model.geom('geom1').feature.create('BLK24', 'Block');
model.geom('geom1').feature.create('BLK25', 'Block');
model.geom('geom1').feature.create('BLK26', 'Block');
model.geom('geom1').feature.create('BLK27', 'Block');
model.geom('geom1').feature.create('BLK28', 'Block');
model.geom('geom1').feature.create('BLK29', 'Block');
model.geom('geom1').feature.create('BLK3', 'Block');
model.geom('geom1').feature.create('BLK30', 'Block');
model.geom('geom1').feature.create('BLK31', 'Block');
model.geom('geom1').feature.create('BLK32', 'Block');
model.geom('geom1').feature.create('BLK33', 'Block');
model.geom('geom1').feature.create('BLK34', 'Block');
model.geom('geom1').feature.create('BLK35', 'Block');
model.geom('geom1').feature.create('BLK36', 'Block');
model.geom('geom1').feature.create('BLK4', 'Block');
model.geom('geom1').feature.create('BLK5', 'Block');
model.geom('geom1').feature.create('BLK6', 'Block');
model.geom('geom1').feature.create('BLK7', 'Block');
model.geom('geom1').feature.create('BLK8', 'Block');
model.geom('geom1').feature.create('BLK9', 'Block');
model.geom('geom1').feature('BLK1').set('axis', {'0' '0' '1'});
model.geom('geom1').feature('BLK1').set('size', {'4.0E-4' '9.0E-4' '2.0E-6'});
model.geom('geom1').feature('BLK10').set('pos', '-4.5E-4,-4.5E-4,-2.0E-6');
model.geom('geom1').feature('BLK10').set('axis', {'0' '0' '1'});
model.geom('geom1').feature('BLK10').set('size', {'2.0E-5' '0.0010' '2.0E-4'});
model.geom('geom1').feature('BLK10').set('pos', '-4.2E-4,-5.0E-4,0.0');
model.geom('geom1').feature('BLK11').set('axis', {'0' '0' '1'});
model.geom('geom1').feature('BLK11').set('size', {'4.0E-4' '9.0E-4' '2.0E-6'});
model.geom('geom1').feature('BLK11').set('pos', '5.0E-5,-4.5E-4,-2.0E-6');
model.geom('geom1').feature('BLK12').set('axis', {'0' '0' '1'});
model.geom('geom1').feature('BLK12').set('size', {'0.0012' '1.0E-4' '2.0E-5'});
model.geom('geom1').feature('BLK12').set('pos', '-6.0E-4,6.0E-4,-2.0E-5');
model.geom('geom1').feature('BLK13').set('axis', {'0' '0' '1'});
model.geom('geom1').feature('BLK13').set('size', {'0.0012' '1.0E-4' '2.0E-5'});
model.geom('geom1').feature('BLK13').set('pos', '-6.0E-4,-7.0E-4,-2.0E-5');
```

[illegible]


```

model.geom('geom1').feature('BLK35').set('pos', '2.2E-4,-5.0E-4,0.0');
model.geom('geom1').feature('BLK36').set('axis', {'0' '0' '1'});
model.geom('geom1').feature('BLK36').set('size', {'2.0E-5' '0.0010' '2.0E-4'});
model.geom('geom1').feature('BLK36').set('pos', '2.6000000000000003E-4,-5.0E-4,0.0');
model.geom('geom1').feature('BLK4').set('axis', {'0' '0' '1'});
model.geom('geom1').feature('BLK4').set('size', {'2.0E-5' '0.0010' '2.0E-4'});
model.geom('geom1').feature('BLK4').set('pos', '3.0000000000000003E-4,-5.0E-4,0.0');
model.geom('geom1').feature('BLK5').set('axis', {'0' '0' '1'});
model.geom('geom1').feature('BLK5').set('size', {'2.0E-5' '0.0010' '2.0E-4'});
model.geom('geom1').feature('BLK5').set('pos', '3.4E-4,-5.0E-4,0.0');
model.geom('geom1').feature('BLK6').set('axis', {'0' '0' '1'});
model.geom('geom1').feature('BLK6').set('size', {'2.0E-5' '0.0010' '2.0E-4'});
model.geom('geom1').feature('BLK6').set('pos', '3.8E-4,-5.0E-4,0.0');
model.geom('geom1').feature('BLK7').set('axis', {'0' '0' '1'});
model.geom('geom1').feature('BLK7').set('size', {'2.0E-5' '0.0010' '2.0E-4'});
model.geom('geom1').feature('BLK7').set('pos', '4.2E-4,-5.0E-4,0.0');
model.geom('geom1').feature('BLK8').set('axis', {'0' '0' '1'});
model.geom('geom1').feature('BLK8').set('size', {'2.0E-5' '0.0010' '2.0E-4'});
model.geom('geom1').feature('BLK8').set('pos', '4.6E-4,-5.0E-4,0.0');
model.geom('geom1').feature('BLK9').set('axis', {'0' '0' '1'});
model.geom('geom1').feature('BLK9').set('size', {'2.0E-5' '0.0010' '2.0E-4'});
model.geom('geom1').feature('BLK9').set('pos', '-4.6E-4,-5.0E-4,0.0');
model.geom('geom1').setGeom('C:\Users\cantilever\Desktop\MT_COMSOL\CodeModels\MT_1mmx1mmx
20um_100umLegs_Ridges_h15_p500mW_geom1.mphbin');

model.material.create('mat1');
model.material('mat1').propertyGroup.create('Enu', 'Young's modulus and Poisson's
ratio');
model.material('mat1').propertyGroup.create('RefractiveIndex', 'Refractive index');

model.physics.create('ht', 'HeatTransfer', 'geom1');
model.physics('ht').feature.create('hs1', 'HeatSource', 3);
model.physics('ht').feature('hs1').selection.set([8 23]);
model.physics('ht').feature.create('templ', 'TemperatureBoundary', 2);
model.physics('ht').feature('templ').selection.set([1 324]);
model.physics('ht').feature.create('hf1', 'HeatFluxBoundary', 2);
model.physics('ht').feature('hf1').selection.set([2 3 4 5 6 7 8 9 11 12 14 15 16 17 18 20
21 22 23 24 25 26 27 28 30 31 32 33 34 35 36 38 39 45 46 47 48 49 50 52 55 56 57 58 59 60
61 63 66 67 68 69 70 71 72 74 77 78 79 80 81 82 83 85 88 89 90 91 92 93 94 96 99 100 101
102 103 104 105 107 110 111 112 113 114 115 116 118 121 122 123 124 125 126 127 129 132 133
134 135 136 137 139 140 142 143 145 148 150 151 152 154 155 156 157 158 159 161 163 165 166
167 168 170 171 172 173 174 175 177 178 179 180 184 186 187 189 192 193 194 195 196 197 198
199 200 201 203 206 207 208 209 210 211 212 213 214 215 217 220 221 222 223 224 225 226 228
231 232 233 234 235 236 237 239 242 243 244 245 246 247 248 250 253 254 255 256 257 258 259
261 264 265 266 267 268 269 270 272 275 276 277 278 279 280 281 283 286 287 288 289 290 291
292 294 297 298 299 300 302 303 305 306 307 308 309 311 312 313 314 316 317 319 320 321 322
323]);

model.mesh.create('mesh1', 'geom1');
% The mesh object below is lost and cannot be exported
model.mesh('mesh1').feature.create('obj', 'MeshObject');
model.mesh.create('mesh2', 'geom1');
model.mesh('mesh2').feature.create('ftet1', 'FreeTet');

model.material('mat1').name('Silicon');
model.material('mat1').propertyGroup('def').set('heatcapacity', '703[J/(kg*K)]');
model.material('mat1').propertyGroup('def').set('thermalexpansioncoefficient', {'4.15e-
6[1/K]' '0' '0' '0' '4.15e-6[1/K]' '0' '0' '0' '4.15e-6[1/K]'});
model.material('mat1').propertyGroup('def').set('relpermittivity', {'12.1' '0' '0' '0'
'12.1' '0' '0' '0' '12.1'});
model.material('mat1').propertyGroup('def').set('thermalconductivity', {'163[W/(m*K)]' '0'
'0' '0' '163[W/(m*K)]' '0' '0' '0' '163[W/(m*K)]'});
model.material('mat1').propertyGroup('def').set('relpermeability', {'1' '0' '0' '0' '1' '0'
'0' '0' '1'});
model.material('mat1').propertyGroup('def').set('density', '2330[kg/m^3]');
model.material('mat1').propertyGroup('def').set('electricconductivity', {'1e-12[S/m]' '0'
'0' '0' '1e-12[S/m]' '0' '0' '0' '1e-12[S/m]'});
model.material('mat1').propertyGroup('Enu').set('youngsmodulus', '131E9[Pa]');
model.material('mat1').propertyGroup('Enu').set('poissonsratio', '0.27');
model.material('mat1').propertyGroup('RefractiveIndex').set('n', '');
model.material('mat1').propertyGroup('RefractiveIndex').set('ki', '');

```

```

model.material('mat1').propertyGroup('RefractiveIndex').set('n', {'3.48' '0' '0' '0' '3.48'
'0' '0' '0' '3.48'});
model.material('mat1').propertyGroup('RefractiveIndex').set('ki', {'0' '0' '0' '0' '0' '0'
'0' '0' '0'});

model.physics('ht').feature('solid1').set('minput_frequency', 'freq');
model.physics('ht').feature('osl').set('minput_frequency', 'freq');
model.physics('ht').feature('init1').set('T', '293.15');
model.physics('ht').feature('hs1').set('Q', '250e-3/(0.4e-3*0.9e-3*2e-6)');
model.physics('ht').feature('temp1').set('T0', '293.15');
model.physics('ht').feature('hfl').set('HeatFluxType', 'InwardHeatFlux');
model.physics('ht').feature('hfl').set('h', '50');
model.physics('ht').feature('hfl').set('Text', '293.15');

model.mesh('mesh1').feature('obj').set('filename', '$FILENAME$_mesh1_obj.mphbin');
model.mesh('mesh1').run;
model.mesh('mesh2').feature('size').set('hauto', 8);
model.mesh('mesh2').run;

model.study.create('std1');
model.study('std1').feature.create('time', 'Transient');

model.sol.create('sol1');
model.sol('sol1').study('std1');
model.sol('sol1').attach('std1');
model.sol('sol1').feature.create('st1', 'StudyStep');
model.sol('sol1').feature.create('v1', 'Variables');
model.sol('sol1').feature.create('t1', 'Time');
model.sol('sol1').feature('t1').feature.create('fc1', 'FullyCoupled');
model.sol('sol1').feature('t1').feature.create('d1', 'Direct');
model.sol.create('sol2');
model.sol('sol2').study('std1');

model.study('std1').feature('time').set('initstudyhide', 'on');
model.study('std1').feature('time').set('initsolhide', 'on');
model.study('std1').feature('time').set('notstudyhide', 'on');
model.study('std1').feature('time').set('notsolhide', 'on');

model.result.create('pg1', 'PlotGroup3D');
model.result('pg1').feature.create('vol1', 'Volume');

model.study('std1').feature('time').set('rtolactive', true);
model.study('std1').feature('time').set('mesh', {'geom1' 'mesh1'});
model.study('std1').feature('time').set('tlist', 'range(0,0.1,3)');

model.sol('sol1').attach('std1');
model.sol('sol1').feature('st1').name('Compile Equations: Time Dependent');
model.sol('sol1').feature('st1').set('studystep', 'time');
model.sol('sol1').feature('v1').set('control', 'time');
model.sol('sol1').feature('t1').set('storeudot', false);
model.sol('sol1').feature('t1').set('control', 'time');
model.sol('sol1').feature('t1').set('tlist', 'range(0,0.1,3)');
model.sol('sol1').feature('t1').set('bwinitstepfrac', '1.0');
model.sol('sol1').feature('t1').set('atolglobalmethod', 'unscaled');
model.sol('sol1').feature('t1').set('solfile', false);
model.sol('sol1').feature('t1').feature('fc1').active(false);
model.sol('sol1').feature('t1').feature('fc1').set('damp', '1.0');
model.sol('sol1').feature('t1').feature('fc1').set('ratelimitactive', true);
model.sol('sol1').feature('t1').feature('d1').set('linsolver', 'spooles');
model.sol('sol1').feature('t1').feature('d1').set('errorchk', 'off');
model.sol('sol2').name('COMSOL 3.5a Solution');
model.sol('sol2').runAll;

model.result('pg1').set('data', 'dset2');
model.result('pg1').set('solnum', '31');
model.result('pg1').set('solrepresentation', 'solnum');

model.name('CADENCE_1mmx1mmx20um_100umLegs_Ridges_CONVECTION.mph');

model.geom('geom1').feature('BLK10').setIndex('size', '5.0E-4', 2);
model.geom('geom1').runPre('fin');

```

```

model.geom('geom1').feature('BLK14').setIndex('size', '5.0E-4', 2);
model.geom('geom1').feature('BLK15').setIndex('size', '5.0E-4', 2);
model.geom('geom1').feature('BLK17').setIndex('size', '5.0E-4', 2);
model.geom('geom1').feature('BLK18').setIndex('size', '5.0E-4', 2);
model.geom('geom1').feature('BLK19').setIndex('size', '5.0E-4', 2);
model.geom('geom1').feature('BLK2').setIndex('size', '5.0E-4', 2);
model.geom('geom1').runPre('fin');
model.geom('geom1').feature('BLK20').setIndex('size', '5.0E-4', 2);
model.geom('geom1').feature('BLK24').setIndex('size', '5.0E-4', 2);
model.geom('geom1').feature('BLK26').setIndex('size', '5.0E-4', 2);
model.geom('geom1').feature('BLK28').setIndex('size', '5.0E-4', 2);
model.geom('geom1').feature('BLK3').setIndex('size', '5.0E-4', 2);
model.geom('geom1').feature('BLK30').setIndex('size', '5.0E-4', 2);
model.geom('geom1').feature('BLK31').setIndex('size', '5.0E-4', 2);
model.geom('geom1').feature('BLK32').setIndex('size', '5.0E-4', 2);
model.geom('geom1').feature('BLK33').setIndex('size', '5.0E-4', 2);
model.geom('geom1').feature('BLK34').setIndex('size', '5.0E-4', 2);
model.geom('geom1').feature('BLK35').setIndex('size', '5.0E-4', 2);
model.geom('geom1').feature('BLK36').setIndex('size', '5.0E-4', 2);
model.geom('geom1').feature('BLK4').setIndex('size', '5.0E-4', 2);
model.geom('geom1').feature('BLK5').setIndex('size', '5.0E-4', 2);
model.geom('geom1').feature('BLK6').setIndex('size', '5.0E-4', 2);
model.geom('geom1').feature('BLK7').setIndex('size', '5.0E-4', 2);
model.geom('geom1').feature('BLK8').setIndex('size', '5.0E-4', 2);
model.geom('geom1').feature('BLK9').setIndex('size', '5.0E-4', 2);
model.geom('geom1').runPre('fin');
model.geom('geom1').run;

model.mesh.remove('mesh1');
model.mesh.remove('mesh2');
model.mesh.create('mesh1', 'geom1');
model.mesh('mesh1').run;

model.result('pg1').run;
model.result('pg1').run;
model.result.dataset.create('cpt1', 'CutPoint1D');
model.result.create('pg2', 'PlotGroup1D');
model.result('pg2').run;
model.result.dataset('cpt1').set('pointx', '0');
model.result('pg2').run;
model.result('pg2').set('ylabelactive', 'on');
model.result('pg2').set('ylabel', 'Temperature [K]');
model.result('pg2').set('xlabelactive', 'on');
model.result('pg2').set('xlabel', 'Time [15]');
model.result.numerical.create('av1', 'AvSurface');
model.result.numerical('av1').selection.set([26]);
model.result.dataset.remove('cpt1');
model.result('pg2').run;
model.result.remove('pg2');
model.result('pg1').run;
model.result('pg1').run;
model.result.remove('pg1');

model.sol('sol1').runAll;

model.result.export.create('img1', 'Image3D');
model.result.export('img1').set('unit', 'px');
model.result.export('img1').set('height', '600');
model.result.export('img1').set('width', '800');
model.result.export('img1').set('lockratio', 'off');
model.result.export('img1').set('resolution', '96');
model.result.export('img1').set('size', 'manual');
model.result.export('img1').set('antialias', 'on');
model.result.export('img1').set('title', 'on');
model.result.export('img1').set('legend', 'on');
model.result.export('img1').set('logo', 'on');
model.result.export('img1').set('options', 'off');
model.result.export('img1').set('fontsize', '9');
model.result.export('img1').set('customcolor', [1 1 1]);
model.result.export('img1').set('background', 'color');
model.result.export('img1').set('qualitylevel', '92');

```

```

model.result.export('img1').set('qualityactive', 'off');
model.result.export('img1').set('imagetype', 'png');
model.result.export('img1').set('axisorientation', 'on');
model.result.export('img1').set('grid', 'on');
model.result.export.create('plot1', 'Plot');
model.result.export.remove('img1');
model.result.export.remove('plot1');
model.result.create('pg1', 'PlotGroup3D');
model.result('pg1').run;
model.result('pg1').set('data', 'dset1');
model.result('pg1').feature.create('voll', 'Volume');
model.result('pg1').run;
model.result('pg1').run;

model.physics('ht').feature('hf1').set('h', 1, '5');

model.sol('sol1').runAll;

model.result('pg1').run;

model.physics('ht').feature('hf1').set('h', 1, '500');

model.sol('sol1').runAll;

model.result('pg1').run;

model.physics('ht').feature('hf1').set('h', 1, '100');

model.sol('sol1').runAll;

model.result('pg1').run;
model.result('pg1').run;
model.result('pg1').run;

model.physics('ht').feature('hf1').set('h', 1, '223');

model.sol('sol1').runAll;

model.result('pg1').run;

model.physics('ht').feature('hf1').set('h', 1, '75');

model.sol('sol1').runAll;

model.result('pg1').run;

model.physics('ht').feature('hf1').set('h', 1, '25');

model.sol('sol1').runAll;

model.result('pg1').run;

model.physics('ht').feature('hf1').set('h', 1, '20');

model.sol('sol1').runAll;

model.result('pg1').run;

model.physics('ht').feature('hf1').set('h', 1, '10');

model.sol('sol1').runAll;

model.result('pg1').run;

model.physics('ht').feature('hf1').set('h', 1, '15');

model.sol('sol1').runAll;

model.result('pg1').run;

model.physics('ht').feature('hs1').set('Q', 1, '0.5*275e-3/(0.4e-3*0.9e-3*2e-6)');

```

```

model.sol('sol1').runAll;

model.result('pg1').run;

model.name('MT_1mmx1mmx20um_100umLegs_Ridges.mph');

model.result('pg1').run;
model.result.table.create('tbl1', 'Table');
model.result.table('tbl1').comments('Surface Average 1 (T)');
model.result.numerical('av1').set('table', 'tbl1');
model.result.numerical('av1').setResult;
model.result.create('pg2', 1);
model.result('pg2').set('data', 'none');
model.result('pg2').feature.create('tblp1', 'Table');
model.result('pg2').feature('tblp1').set('table', 'tbl1');
model.result('pg2').run;

model.physics('ht').feature('hs1').set('Q', 1, '250e-3/(0.4e-3*0.9e-3*2e-6)');

model.sol('sol1').runAll;

model.result('pg1').run;
model.result('pg2').run;
model.result('pg2').feature('tblp1').set('linestyle', 'dotted');
model.result('pg2').feature('tblp1').set('linecolor', 'blue');
model.result('pg2').feature('tblp1').set('linestyle', 'cycle');
model.result('pg2').feature('tblp1').set('linewidth', '1');
model.result('pg2').feature('tblp1').set('linemarker', 'none');
model.result('pg2').feature('tblp1').set('legend', 'on');
model.result('pg2').run;
model.result('pg2').run;
model.result('pg1').run;
model.result('pg2').run;
model.result.table('tbl1').save('C:\Users\cantilever\Desktop\MT_COMSOL\Figures\MT_1x1_Tau
Plot_h15.txt');
model.result.table('tbl1').save('C:\Users\cantilever\Desktop\MT_COMSOL\Figures\MT_1x1_Tau
Plot_h15.csv');
model.result('pg1').run;
model.result('pg1').run;

model.name('MT_1mmx1mmx20um_100umLegs_Ridges.mph');

model.result('pg1').run;
model.result('pg2').run;
model.result.numerical('av1').set('table', 'tbl1');
model.result.numerical('av1').appendResult;
model.result('pg2').run;
model.result('pg1').run;
model.result('pg2').run;
model.result('pg2').run;
model.result('pg2').run;
model.result('pg2').run;
model.result('pg2').run;
model.result.remove('pg2');
model.result.numerical('av1').set('table', 'tbl1');
model.result.numerical('av1').appendResult;
model.result('pg1').run;
model.result.create('pg2', 1);
model.result('pg2').set('data', 'none');
model.result('pg2').feature.create('tblp1', 'Table');
model.result('pg2').feature('tblp1').set('table', 'tbl1');
model.result('pg2').run;
model.result('pg2').run;
model.result.remove('pg2');
model.result.table.create('tbl2', 'Table');
model.result.table('tbl2').comments('Surface Average 1 (T)');
model.result.numerical('av1').set('table', 'tbl2');
model.result.numerical('av1').setResult;
model.result.create('pg2', 1);
model.result('pg2').set('data', 'none');
model.result('pg2').feature.create('tblp1', 'Table');

```

```

model.result('pg2').feature('tblp1').set('table', 'tbl2');
model.result('pg2').run;

model.physics('ht').feature('hfl').set('h', 1, '50');

model.sol('sol1').runAll;

model.result('pg1').run;
model.result('pg2').run;
model.result('pg1').run;
model.result('pg2').run;
model.result.remove('pg2');
model.result.table.create('tbl3', 'Table');
model.result.table('tbl3').comments('Surface Average 1 (T)');
model.result.numerical('av1').set('table', 'tbl3');
model.result.numerical('av1').setResult;
model.result.create('pg2', 1);
model.result('pg2').set('data', 'none');
model.result('pg2').feature.create('tblp1', 'Table');
model.result('pg2').feature('tblp1').set('table', 'tbl3');
model.result('pg2').run;
model.result('pg1').run;
model.result.table('tbl3').save('C:\Users\cantilever\Desktop\MT_COMSOL\Figures\MT_1x1_Tau
Plot_h50_p500mW.csv');

model.physics('ht').feature('hfl').set('h', 1, '15');

model.result('pg2').run;
model.result.remove('pg2');

model.sol('sol1').runAll;

model.result('pg1').run;
model.result.table.create('tbl4', 'Table');
model.result.table('tbl4').comments('Surface Average 1 (T)');
model.result.numerical('av1').set('table', 'tbl4');
model.result.numerical('av1').setResult;
model.result.create('pg2', 1);
model.result('pg2').set('data', 'none');
model.result('pg2').feature.create('tblp1', 'Table');
model.result('pg2').feature('tblp1').set('table', 'tbl4');
model.result('pg2').run;
model.result.table('tbl4').save('C:\Users\cantilever\Desktop\MT_COMSOL\Figures\MT_1x1_Tau
Plot_h15_p500mW.csv');
model.result('pg1').run;

out = model;

```

APPENDIX C – ARDUINO CODE USED FOR THERMAL PULSES

```
//Map input bits (to DAC) to physical output pins (on ARDUINO)
const int bit0 = 52;      // MSB
const int bit1 = 50;
const int bit2 = 48;
const int bit3 = 46;
const int bit4 = 44;
const int bit5 = 42;
const int bit6 = 40;
const int bit7 = 38;      //LSB

int switchPin = 10;        //used to begin running program
int indicatorPin = 13;

//Converts a decimal integer into binary and returns as a string
String decimal_to_binary_converter(int dec_num){
  int zeros = 8 - String(dec_num,BIN).length();
  String bin_num_as_string;
  for (int i=0; i<zeros; i++) {
    bin_num_as_string = bin_num_as_string + "0";
  }
  bin_num_as_string = bin_num_as_string + String(dec_num,BIN);
  return bin_num_as_string;
}
//Accepts binary number as a string, and sets corresponding output on ARDUINO PINS
//assumes 8 bit DAC
void write_to_DAC_pins (String bin_num){
  if (String(bin_num[0]).equals("0")){ //bit 0
    digitalWrite(bit0, LOW);}
  else{
    digitalWrite(bit0, HIGH);}
  if (String(bin_num[1]).equals("0")){ //bit 1
    digitalWrite(bit1, LOW);}
  else{
    digitalWrite(bit1, HIGH);}
  if (String(bin_num[2]).equals("0")){ //bit 2
    digitalWrite(bit2, LOW);}
  else{
    digitalWrite(bit2, HIGH);}
  if (String(bin_num[3]).equals("0")){ //bit 3
    digitalWrite(bit3, LOW);}
  else{
    digitalWrite(bit3, HIGH);}
  if (String(bin_num[4]).equals("0")){ //bit 4
    digitalWrite(bit4, LOW);}
  else{
    digitalWrite(bit4, HIGH);}
  if (String(bin_num[5]).equals("0")){ //bit 5
    digitalWrite(bit5, LOW);}
  else{
    digitalWrite(bit5, HIGH);}
  if (String(bin_num[6]).equals("0")){ //bit 6
    digitalWrite(bit6, LOW);}
  else{
    digitalWrite(bit6, HIGH);}
  if (String(bin_num[7]).equals("0")){ //bit 7
    digitalWrite(bit7, LOW);}
  else{
    digitalWrite(bit7, HIGH);}
}
void blink_indicator_led(int delayTime){ //delayTime in millisec
  digitalWrite(indicatorPin, HIGH);
  delay(delayTime);
  digitalWrite(indicatorPin, LOW);
  delay(delayTime);
}
```

```

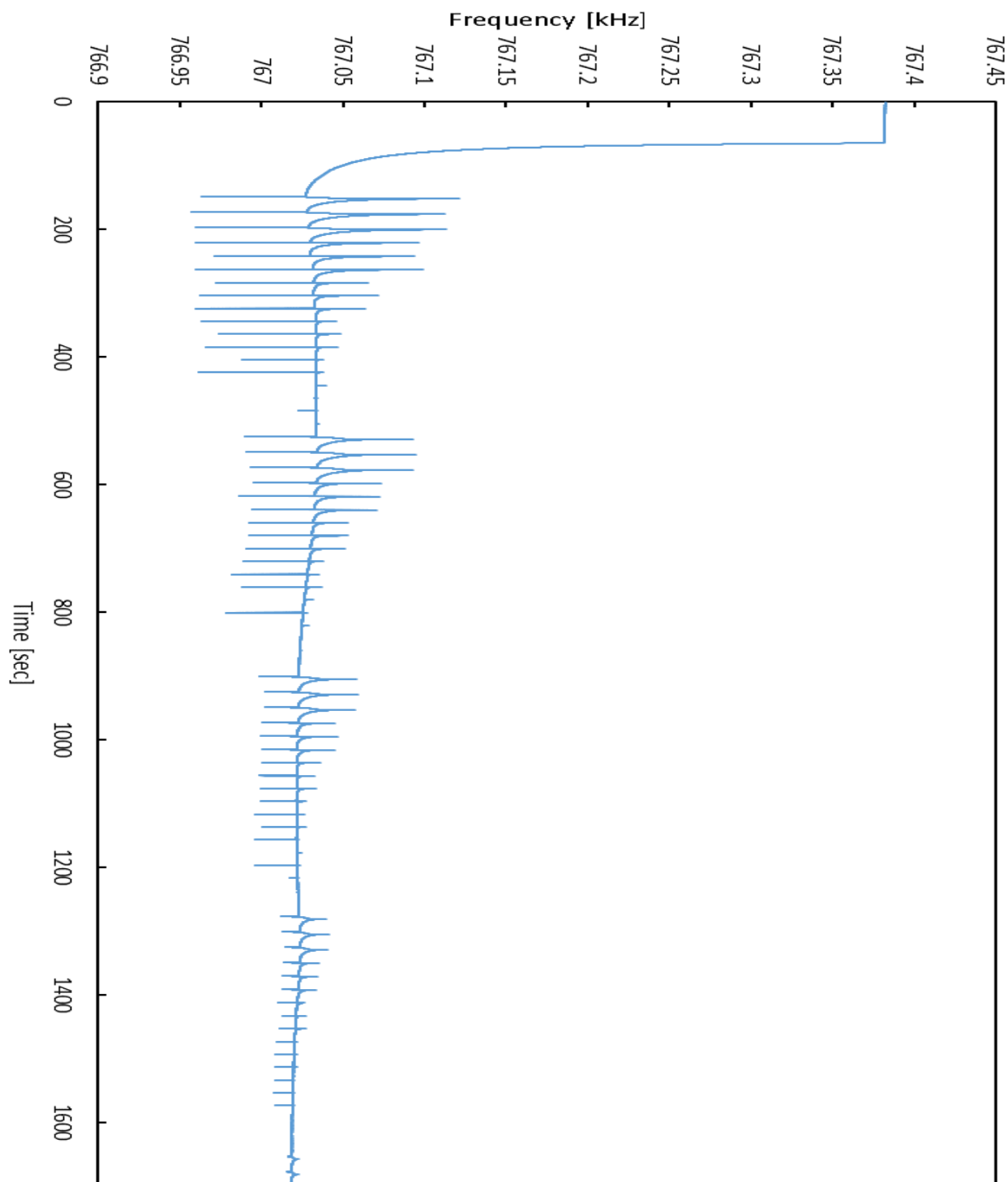
}
void setup() {
  Serial.begin(9600);
  pinMode(bit0, OUTPUT);
  pinMode(bit1, OUTPUT);
  pinMode(bit2, OUTPUT);
  pinMode(bit3, OUTPUT);
  pinMode(bit4, OUTPUT);
  pinMode(bit5, OUTPUT);
  pinMode(bit6, OUTPUT);
  pinMode(bit7, OUTPUT);
  pinMode(switchPin, INPUT);
  pinMode(indicatorPin, OUTPUT);
  write_to_DAC_pins ("00000000");
}
void loop(){
  write_to_DAC_pins ("00000000");          //set DAC output voltage back to zero immediately
  if (digitalRead(switchPin) == HIGH){    //blink indicator led rapidly to show that program
is starting (program starts when switchPin is flipped to HIGH, otherwise just idles)
    for (int i=0; i<10; i++){
      blink_indicator_led(200);
    }
    digitalWrite(indicatorPin, HIGH);
    delay(2000);                          //wait 2 sec

    unsigned long time_wait = 20e3; //20 sec...10*30 sec = 300e3 = 5 min
    double time_heat = 0;
    String bin_string = decimal_to_binary_converter(0);
    for (int h=100; h>=20; h=h-20){
      for (int n=12; n>=2; n=n-2){
msec
        for( int i=1; i<=3; i=i+1){          //repeat 3 times for each
power, duration
          time_heat = pow(2,n);              //pow(<base>,<exponent>);
so heating duration doubles every cycle
          bin_string = decimal_to_binary_converter(h);
          write_to_DAC_pins (bin_string);    //turn on heater
          delay(time_heat);
          write_to_DAC_pins ("00000000");    //turn off heater
          delay(time_wait);                  //wait between heating
pulses
        }
      }
    }
    write_to_DAC_pins ("00000000"); //set DAC output voltage back to zero once program
has finished
    for (int i=0; i<5; i++){                //slow blink LED on pin 13 once program has finished
      blink_indicator_led(200);
    }
  }
  blink_indicator_led(1000);
}

```


APPENDIX D – EXAMPLE RAW DATA OF THERMALLY-GENERATED TRANSIENTS

Raw data captured from a PECH-coated resonator exposed to 10,800 ppm of toluene.



REFERENCES

- [1] M. Li, S. Biswas, M. H. Nantz, and R. M. Higashi, "A microfabricated preconcentration device for breath analysis," *Sensors and Actuators B: Chemical*, vol. 180, pp. 130–136, April 2013.
- [2] I. Voiculescu, "Multiparametric MEMS Biosensors With Integrated Impedance Spectroscopy and Gravimetric Measurements for Water Toxicity Sensing," *ASME 2013 2nd Global Congress on NanoEngineering for Medicine and Biology*, vol. Boston, Massachusetts, USA, p. V001T02A001, Feb 4-6 2013.
- [3] H. Lahlou, X. Vilanova, and X. Correig, "Gas phase micro-preconcentrators for benzene monitoring: A review," *Sensors and Actuators B: Chemical*, vol. 176, pp. 198–210, Jan 2013.
- [4] G. Korotcenkov and B. K. Cho, "Engineering approaches for the improvement of conductometric gas sensor parameters: Part 1. Improvement of sensor sensitivity and selectivity (short survey)," *Sensors and Actuators B: Chemical*, vol. 188, pp. 709–728, Nov 2013.
- [5] J. Foulletier and P. Fabry, *Chemical and biological microsensors : applications in liquid media*. London, Hoboken, NJ: ISTE ;Wiley, 2010.
- [6] N. Lazarus, S. S. Bedair, and C. C. Lo, "CMOS-MEMS capacitive humidity sensor," *Microelectromechanical Systems*, vol. 19, pp. 183 - 191, Feb 2 2010.
- [7] S. Zampolli, I. Elmi, F. Mancarella, and P. Betti, "Real-time monitoring of sub-ppb concentrations of aromatic volatiles with a MEMS-enabled miniaturized gas-chromatograph," *Sensors and Actuators B: Chemical*, vol. 141, pp. 322–328, Aug 18 2009.
- [8] A. Boisen and T. Thundat, "Design & fabrication of cantilever array biosensors," *Materials today*, vol. 12, pp. 32–38, Sept 2009.
- [9] L. Senesac and T. G. Thundat, "Nanosensors for trace explosive detection," *materials today*, vol. 11, pp. 28–36, Mar 2008.
- [10] I. Elmi, S. Zampolli, E. Cozzani, and F. Mancarella, "Development of ultra-low-power consumption MOX sensors with ppb-level VOC detection capabilities for emerging applications," *Sensors and Actuators B: Chemical*, vol. 135, pp. 342–351, Dec 10 2008.
- [11] H. P. Lang and C. Gerber, "Microcantilever sensors," *STM and AFM studies on (bio) molecular systems*, vol. 285, pp. 1-27, 2008.
- [12] J. H. Seo and O. Brand, "High-Factor In-Plane-Mode Resonant Microsensor Platform for Gaseous/Liquid Environment," *Microelectromechanical Systems*, vol. 17, pp. 483 - 493, April 4 2008.
- [13] C. McDonagh, C. S. Burke, and B. D. MacCraith, "Optical chemical sensors," *Chemical reviews*, vol. 108, pp. 400-422, 2008.
- [14] E. T. Zellers, S. Reidy, and R. A. Veeneman, "An integrated micro-analytical system for complex vapor mixtures," *Solid-State Sensors*, vol. Lyon, pp. 1491 - 1496, June 10-14 2007.
- [15] J. Lisec, N. Schauer, J. Kopka, L. Willmitzer, and A. R. Fernie, "Gas chromatography mass spectrometry–based metabolite profiling in plants," *Nature protocols*, vol. 1, pp. 387-96, 2006.
- [16] G. Chiavari and G. C. Galletti, "Pyrolysis—gas chromatography/mass spectrometry of amino acids," *Journal of Analytical and Applied Pyrolysis*, vol. 24, pp. 123-137, Dec 1992.

- [17] S. Berijani, Y. Assadi, and M. Anbia, "Dispersive liquid–liquid microextraction combined with gas chromatography-flame photometric detection: Very simple, rapid and sensitive method," *Journal of Chromatography A*, vol. 1123 pp. 1–9, 4 August 2006.
- [18] G. Serrano, T. Sukaew, and E. T. Zellers, "Hybrid preconcentrator/focuser module for determinations of explosive marker compounds with a micro-scale gas chromatograph," *Journal of Chromatography A*, vol. 1279, pp. 76–85, 76–85 2013.
- [19] M. Akbar, S. Narayanan, M. Restaino, and M. Agah, "A purge and trap integrated microGC platform for chemical identification in aqueous samples," *Analyst*, vol. 139(13), pp. 3384-92, Jul 7 2014.
- [20] H. Lai, A. Leung, M. Magee, and J. R. Almirall, "Identification of volatile chemical signatures from plastic explosives by SPME-GC/MS and detection by ion mobility spectrometry," *Analytical and bioanalytical chemistry*, vol. 396, pp. 2997-3007, Apr 2010.
- [21] C. Ho, A. Robinson, D. Miller, and M. Davis, "Overview of Sensors and Needs for Environmental Monitoring," *Sensors*, vol. 5, pp. 4-37, 2005.
- [22] M. Ashraf-Khorassani, L. T. Taylor, and M. Agah, "MEMS-based multi-inlet/outlet preconcentrator coated by inkjet printing of polymer adsorbents," *Sensors and Actuators B: Chemical*, vol. 133, pp. 24–32, July 28 2008.
- [23] M. Agah, G. R. Lambertus, and R. Sacks, "High-speed MEMS-based gas chromatography," *Microelectromechanical Systems*, vol. 15, pp. 1371 - 1378, 30 October 2006.
- [24] J. J. Whiting, C. J. Lu, E. T. Zellers, and R. D. Sacks, "A portable, high-speed, vacuum-outlet GC vapor analyzer employing air as carrier gas and surface acoustic wave detection," *Analytical chemistry*, vol. 73, pp. 4668-75, Oct 1 2001.
- [25] A. J. Grall, E. T. Zellers, and R. D. Sacks, "High-speed analysis of complex indoor VOC mixtures by vacuum-outlet GC with air carrier gas and programmable retention," *Environmental science & Technology*, vol. 35, pp. 163-9, Jan 1 2001.
- [26] L. Renaghan, Z. Hasnain, and M. Agah, "A fabrication technology for three-dimensional micro total analysis systems," *Journal of Micromechanics*, vol. 20, Mar 2010.
- [27] B. Alfeeli and M. Agah, "Toward handheld diagnostics of cancer biomarkers in breath: Micro preconcentration of trace levels of volatiles in human breath," *Sensors Journal*, vol. 11, pp. 2756 - 2762, June 23 2011.
- [28] B. Alfeeli and M. Agah, "Micro preconcentrator for handheld diagnostics of cancer biomarkers in breath," *Sensors*, vol. Kona, HI, pp. 2490 - 2493, Nov 1-4 2010.
- [29] S. Roach, D. Atkinson, and A. Waters, "Primary health care in the Kimberley: Is the doctor shortage much bigger than we think?," *Australian Journal of Medicine*, vol. 15, pp. 373-9, Dec 2007.
- [30] S. Narayanan, A. Garg, and M. Agah, "Matrix GC: Multi-dimensional Analysis/Detection using Integrated Columns," *MicroGC: Of Detectors and ...*, vol. Blacksburg, VA, March 26 2014.
- [31] J. W. Grate, "Acoustic wave microsensor arrays for vapor sensing," *Chemical reviews*, vol. 100, pp. 2627–2648, Mar 28 2000.
- [32] Q. Zhong, W. H. Steinecker, and E. T. Zellers, "Characterization of a high-performance portable GC with a chemiresistor array detector," *Analyst*, vol. 134, pp. 283-93, Feb 2009.
- [33] S. K. Kim, H. Chang, and E. T. Zellers, "Prototype micro gas chromatograph for breath biomarkers of respiratory disease," *Solid-State Sensors, Actuators and Microsystems Conference, 2009. TRANSDUCERS 2009. International*, vol. Denver, CO, pp. 128 - 131, June 21-25 2009.
- [34] M. Li, S. Biswas, and M. H. Nantz, "A microfabricated preconcentrating device for exhaled breath analysis," *Solid-State Sensors, Actuators and Microsystems Conference*,

2011. *TRANSDUCERS 2011. International*, vol. Beijing, China, pp. 1148 - 1151, June 5-9 2011.
- [35] T. Paixão and M. Bertotti, "Development of a breath alcohol sensor using a copper electrode in an alkaline medium," *Journal of Electroanalytical Chemistry*, vol. 571, pp. 101–109, Sept 15 2004.
 - [36] H. Chang, J. Bryant-Genevier, and E. T. Zellers, "Microfabricated gas chromatograph for on-site determination of trichloroethylene in indoor air arising from vapor intrusion. 1. Field evaluation," *Journal of environmental science & technology*, vol. 46, pp. 6073–6080, May 22 2012.
 - [37] T. Sukaew, H. Chang, G. Serrano, and E. T. Zellers, "Multi-stage preconcentrator/focuser module designed to enable trace level determinations of trichloroethylene in indoor air with a microfabricated gas chromatograph," *Analyst*, vol. 136, pp. 1664-1674, 2011.
 - [38] C. J. Lu, C. Jin, and E. T. Zellers, "Chamber evaluation of a portable GC with tunable retention and microsensor-array detection for indoor air quality monitoring," *Journal of Environmental Monitoring*, vol. 8, pp. 270-8, Feb 2006.
 - [39] C. J. Lu and E. T. Zellers, "A dual-adsorbent preconcentrator for a portable indoor-VOC microsensor system," *Analytical chemistry*, vol. 73, pp. 3449–3457, June 6 2001.
 - [40] M. D. Martin, T. J. Roussel, and S. Cambron, "Performance of stacked, flow-through micropreconcentrators for portable trace detection," *International Journal for ...*, vol. 13, pp. 109-119, Dec 2010.
 - [41] C. Jia, S. A. Batterman, and E. T. Zellers, "Rapid determination of ETS markers with a prototype field-portable GC employing a microsensor array detector," *Journal of Environmental Monitoring*, vol. 9, pp. 440-8, May 2007.
 - [42] A. B. A. Dow and W. Lang, "Design and fabrication of a micropreconcentrator focuser for sensitivity enhancement of chemical sensing systems," *Sensors Journal*, vol. 12, pp. 2528 - 2534, June 1 2012.
 - [43] B. Alfeeli, D. Hogg, and M. Agah, "Solid-phase microextraction using silica fibers coated with tenax-TA films," *Procedia Engineering*, vol. 5, pp. 1152–1155, Sept 5-8 2010.
 - [44] M. Y. Wong, W. R. Cheng, M. H. Liu, W. C. Tian, and C. J. Lu, "A preconcentrator chip employing μ -SPME array coated with in-situ-synthesized carbon adsorbent film for VOCs analysis," *Talanta*, vol. 101, pp. 307-13, Nov 15 2012.
 - [45] A. M. Dietrich, B. Alfeeli, and M. Agah, "The possibilities will take your breath away: breath analysis for assessing environmental exposure," *Environmental science & Technology*, vol. 45, pp. 8167–8175, Aug 12 2011.
 - [46] M. Akbar and M. Agah, "A microfabricated propofol trap for breath-based anesthesia depth monitoring," *Microelectromechanical Systems*, vol. 22, pp. 443 - 451, April 2013.
 - [47] M. A. Zareian-Jahromi and M. Agah, "Selective micro preconcentration of propofol for anesthetic depth monitoring by using seedless electroplated gold as adsorbent," *Engineering in Medicine*, vol. 2009, pp. 2763-6, 2009.
 - [48] W. A. Groves, E. T. Zellers, and G. C. Frye, "Analyzing organic vapors in exhaled breath using a surface acoustic wave sensor array with preconcentration: Selection and characterization of the preconcentrator," *Analytica Chimica Acta*, vol. 371, pp. 131-143, 5 October 1998.
 - [49] I. D. Kim, A. Rothschild, and H. L. Tuller, "Advances and new directions in gas-sensing devices," *Acta Materialia*, pp. 974–1000, February 2013.
 - [50] C. J. Lu, J. Whiting, R. D. Sacks, and E. T. Zellers, "Portable gas chromatograph with tunable retention and sensor array detection for determination of complex vapor mixtures," *Analytical chemistry*, vol. 75, pp. 1400–1409, Feb 15 2003.
 - [51] B. Wang and E. V. Anslyn, *Chemosensors : principles, strategies, and applications*. Hoboken, N.J.: John Wiley and Sons, 2011.

- [52] Z. Long, L. Kou, M. J. Sepaniak, and X. Hou, "Recent advances in gas phase microcantilever-based sensing," *Reviews in Analytical Chemistry*, vol. 32, pp. 135–158, April 2013.
- [53] J. Jiri, J. Mira, and D. M. DeVaney, "Chemical Sensors," *Analytical Chemistry*, vol. 66, pp. 207R–228R, June 1994.
- [54] F.-G. Banica, *Chemical sensors and biosensors : fundamentals and applications*. Chichester, West Sussex, U.K.: John Wiley and Sons Incorporated, 2012.
- [55] A. M. Kummer, T. P. Burg, and A. Hierlemann, "Transient signal analysis using complementary metal oxide semiconductor capacitive chemical microsensors," *Analytical chemistry*, vol. 78, pp. 279–290, Dec 2 2006.
- [56] D. Lange, C. Hagleitner, and A. Hierlemann, "Complementary metal oxide semiconductor cantilever arrays on a single chip: mass-sensitive detection of volatile organic compounds," *Analytical Chemistry*, vol. 74, pp. 3084–3095, May 18 2002.
- [57] S. Narayanan, B. Alfeeli, and M. Agah, "Two-port static coated micro gas chromatography column with an embedded thermal conductivity detector," *Sensors Journal*, vol. 12, pp. 1893 - 1900, April 24 2012.
- [58] S. Narayanan, B. Alfeeli, and M. Agah, "A micro gas chromatography chip with an embedded non-cascaded thermal conductivity detector," *Procedia Engineering*, vol. 5, pp. 29–32, Sept 5-8 2010.
- [59] E. T. Zellers, S. A. Batterman, and M. Han, "Optimal coating selection for the analysis of organic vapor mixtures with polymer-coated surface acoustic wave sensor arrays," *Analytical chemistry*, vol. 67, pp. 1092–1106, Mar 1995.
- [60] J. D. Adams, "Self-sensing array of microcantilevers for chemical detection," *US Patent* 8, 2013.
- [61] S. Subhashini and A. Vimala, "Toxic gas sensor using resonant frequency variation in micro-cantilever," *Sustainable Utilization*, vol. Kuala Lumpur, pp. 87 - 91, Oct 6-9 2012.
- [62] L. A. Beardslee, S. Aravamudhan, C. Carron, and P. Joseph, "Detection of Anti-IgG Using Cantilever-type Resonant Microstructures Vibrating in In-plane Flexural Modes," *Sensors, 2012 IEEE*, vol. Taipei, Taiwan, Oct 28-31 2012.
- [63] I. Basu, R. V. Subramanian, and A. Mathew, "Solid state potentiometric sensor for the estimation of tributyrin and urea," *Sensors and Actuators B: Chemical*, vol. 107, pp. 418–423, May 27 2005.
- [64] A. Wisitsoraat, P. Sritongkham, and C. Karuwan, "Fast cholesterol detection using flow injection microfluidic device with functionalized carbon nanotubes based electrochemical sensor," *Biosensors and Bioelectronics*, vol. 26, pp. 1514–1520, Dec 15 2010.
- [65] V. Palmisano, L. Boon-Brett, C. Bonato, F. Harskamp, W. J. Buttner, M. B. Post, *et al.*, "Evaluation of selectivity of commercial hydrogen sensors," *International Journal of Hydrogen Energy*, vol. 39, pp. 20491-20496, 12/3/ 2014.
- [66] S. Kommandur, A. MahdaviFar, P. J. Hesketh, and S. Yee, "A microbridge heater for low power gas sensing based on the 3-Omega technique," *Sensors and Actuators A: Physical*, vol. 233, pp. 231-238, 9/1/ 2015.
- [67] A. MahdaviFar, M. Navaei, R. Aguilar, P. J. Hesketh, G. Hunter, M. W. Findlay, *et al.*, "Transient Thermal Response of Micro TCD for Identification of Gases," *Meeting Abstracts*, vol. MA2013-02, pp. 2795-2795, 2013.
- [68] M. V. Chistiakova, S. Ce, and A. M. Armani, "Label-Free, Single Molecule Resonant Cavity Detection: A Double-Blind Experimental Study," *Sensors (14248220)*, vol. 15, pp. 6324-6341, 2015.
- [69] E. T. Zellers and M. Han, "Effects of temperature and humidity on the performance of polymer-coated surface acoustic wave vapor sensor arrays," *Analytical chemistry*, vol. 68, pp. 2409–2418, July 15 1996.

- [70] G. Z. Zhang and E. T. Zellers, "Portable instrument employing a surface acoustic wave sensor with a regenerable reagent coating for direct measurement of 1, 3-butadiene and styrene," *Review of scientific instruments*, vol. 66, pp. 239-246, Jan 1995.
- [71] E. T. Zellers, R. M. White, and S. M. Rappaport, "Use of a surface-acoustic-wave sensor to characterize the reaction of styrene vapor with a square-planar organoplatinum complex," *Analytical chemistry*, vol. 62, pp. 1222-7, July 1 1990.
- [72] A. Boisen, S. Dohn, S. S. Keller, and S. Schmid, "Cantilever-like micromechanical sensors," *Reports on Progress in Physics*, vol. 74, Feb 28 2011.
- [73] S. B. Truax, K. S. Demirci, and L. A. Beardslee, "Mass-sensitive detection of gas-phase volatile organics using disk microresonators," *Analytical Chemistry*, vol. 83, pp. 3305–3311, April 6 2011.
- [74] L. A. Beardslee, A. M. Addous, and S. Heinrich, "Thermal excitation and piezoresistive detection of cantilever in-plane resonance modes for sensing applications," *Microelectromechanical Systems*, vol. 19, pp. 1015 - 1017, July 29 2010.
- [75] D. Lange, A. Kummer, N. Kerness, O. Brand, and H. Baltes, "Smart single-chip gas sensor microsystem," *Nature*, vol. 414, pp. 293-296, Nov 15 2001.
- [76] L. Junwoo, C. Wook, Y. Yong Kyoung, H. Kyo Seon, L. Sang-Myung, K. Sungchul, *et al.*, "A Micro-Fabricated Force Sensor Using an All Thin Film Piezoelectric Active Sensor," *Sensors (14248220)*, vol. 14, pp. 22199-22207, 2014.
- [77] P. S. Waggoner and H. G. Craighead, "Micro-and nanomechanical sensors for environmental, chemical, and biological detection," *Lab on a Chip*, vol. 7, pp. 1238-1255, May 15 2007.
- [78] K. M. Goeders, J. S. Colton, and L. A. Bottomley, "Microcantilevers: sensing chemical interactions via mechanical motion," *Chemical reviews*, vol. 108, pp. 522–542, Jan 30 2008.
- [79] J. L. Arlett, E. B. Myers, and M. L. Roukes, "Comparative advantages of mechanical biosensors," *Nature nanotechnology*, vol. 6, pp. 203–215, Mar 27 2011.
- [80] J. L. Hazel and V. V. Tsukruk, "Spring constants of composite ceramic/gold cantilevers for scanning probe microscopy," *Thin Solid Films*, vol. 339, pp. 249–257, Feb 8 1999.
- [81] R. Bashir, A. Gupta, and G. W. Neudeck, "On the design of piezoresistive silicon cantilevers with stress concentration regions for scanning probe microscopy applications," *Journal of Mechanics and Microengineering*, vol. 10, 2000.
- [82] N. Yazdi, F. Ayazi, and K. Najafi, "Micromachined inertial sensors," *Proceedings of the IEEE*, vol. 86, pp. 1640 - 1659, Aug 6 1998.
- [83] K. S. Demirci, L. A. Beardslee, S. Truax, J. J. Su, and O. Brand, "Integrated silicon-based chemical microsystem for portable sensing applications," *Sensors and Actuators B: Chemical*, vol. 180, pp. 50-59, 4// 2013.
- [84] A. Hierlemann, O. Brand, and H. Baltes, "Complementary metal oxide semiconductor cantilever arrays on a single chip: mass-sensitive detection of volatile organic compounds," *Analytical Chemistry*, vol. 74, pp. 3084–3095, May 18 2002.
- [85] B. T. Stuart, S. D. Kemal, A. B. Luke, L. Yulia, H. Andreas, M. Boris, *et al.*, "Mass-Sensitive Detection of Gas-Phase Volatile Organics Using Disk Microresonators," *Analytical Chemistry*, vol. 83, pp. 3305–3311, April 6 2011.
- [86] M. Rahimi, I. Chae, J. E. Hawk, S. K. Mitra, and T. Thundat, "Methane sensing at room temperature using photothermal cantilever deflection spectroscopy," *Sensors and Actuators B: Chemical*, vol. 221, pp. 564-569, 12/31/ 2015.
- [87] X. Bai, H. Hou, B. Zhang, and J. Tang, "Label-free detection of kanamycin using aptamer-based cantilever array sensor," *Biosensors and Bioelectronics*, vol. 56, pp. 112-116, 6/15/ 2014.
- [88] C. Carron, P. Getz, J. Su, L. Beardslee, S. Heinrich, F. Josse, *et al.*, "CANTILEVER-BASED RESONANT MICROSENSOR WITH INTEGRATED TEMPERATURE

- MODULATION," *Hilton Head Solid-State Sensors, Actuators and Microsystems Workshop*, June 6-8 2014.
- [89] C. Carron, P. Getz, J. J. Su, and D. S. Gottfried, "Cantilever-based resonant gas sensors with integrated recesses for localized sensing layer deposition," *Sensors*, vol. Baltimore, MD, pp. 1 - 4, Nov 3-6 2013.
 - [90] J. Su, C. Carron, S. Truax, and K. S. Demirci, "Assessing polymer sorption kinetics using micromachined resonators," *TRANSDUCERS, Solid-State Sensors, Actuators and Microsystems, 12th International Conference on, 2011 (Volume:1)*, vol. Beijing, China, June 5-9 2011.
 - [91] S. D. Senturia, "Microsystem design," *Microsystem design*, 2001.
 - [92] M. J. Vellekoop, "Acoustic wave sensors. Theory, design and physicochemical applications: by D.S. Ballantine, R.M. White, S.J. Martin, A.J. Ricco, E.T. Zellers, G.C. Frye and H. Wohltjen, published by Academic Press, San Diego, 1997, ISBN 0-12-077460-7, 436 pages," *Sensors and Actuators A: Physical*, vol. 63, p. 79, Sept 1997.
 - [93] K. S. D. L.A. Beardslee, Y. Luzinova, J.J. Su, B. Mizaikoff, S. Heinrich, F. Josse, O. Brand, "IN-PLANE MODE RESONANT CANTILEVERS AS LIQUID-PHASE CHEMICAL SENSORS WITH PPB RANGE LIMITS OF DETECTION," *Hilton Head Solid-State Sensors, Actuators and Microsystems Workshop*, June 10-14 2010.
 - [94] H. Wasisto, Q. Zhang, S. Merzsch, A. Waag, and E. Peiner, "A phase-locked loop frequency tracking system for portable microelectromechanical piezoresistive cantilever mass sensors," *Microsystem Technologies*, vol. 20, pp. 559-569, 2014/04/01 2014.
 - [95] M. M. Mehta and V. Chandrasekhar, "A hybrid analog-digital phase-locked loop for frequency mode non-contact scanning probe microscopy," *Review of Scientific Instruments*, vol. 85, pp. 1-7, 2014.
 - [96] B. H. Kim, M. Maute, F. E. Prins, D. P. Kern, M. Croitoru, S. Raible, *et al.*, "Parallel frequency readout of an array of mass-sensitive transducers for sensor applications," *Microelectronic Engineering*, vol. 53, pp. 229-232, 6// 2000.
 - [97] A. Loui, T. V. Ratto, T. S. Wilson, S. K. McCall, E. V. Mukerjee, A. H. Love, *et al.*, "Chemical vapor discrimination using a compact and low-power array of piezoresistive microcantilevers," *Analyst*, vol. 133, pp. 608-615, 2008.
 - [98] B. Li, S. Santhanam, L. Schultz, M. Jeffries-El, M. C. Iovu, G. Sauvé, *et al.*, "Inkjet printed chemical sensor array based on polythiophene conductive polymers," *Sensors and Actuators B: Chemical*, vol. 123, pp. 651-660, 2007.
 - [99] N. Kim, S. Graham, W. J. Potscavage, Jr., B. Domercq, and B. Kippelen, "A hybrid encapsulation method for organic electronics," *Applied Physics Letters*, vol. 94, pp. 163-308, 2009.
 - [100] A. Hierlemann, A. J. Ricco, K. Bodenhöfer, and W. Göpel, "Effective Use of Molecular Recognition in Gas Sensing: Results from Acoustic Wave and in Situ FT-IR Measurements," *Analytical Chemistry*, vol. 71, pp. 3022-3035, 1999/08/01 1999.
 - [101] J. C. (ed.), "Polymer Permeability," *Elsevier*, 1985.
 - [102] J. Crank, *The Mathematics of Diffusion*, 1st ed.,: Oxford University Press, 1956.
 - [103] P. Chandra and W. J. Koros, "Sorption of lower alcohols in poly(ethylene terephthalate)," *Polymer*, vol. 50, pp. 4241-4249, 8/12/ 2009.
 - [104] M. C. Villet and G. R. Gavalas, "Measurement of concentration-dependent gas diffusion coefficients in membranes from a psuedo-steady state permeation run," *Journal of Membrane Science*, vol. 297, pp. 199-205, 7/5/ 2007.
 - [105] L. K. Wright, H. Chang, N. Nuño, and E. T. Zellers, "Microfabricated gas chromatograph for rapid, trace-level determinations of gas-phase explosive marker compounds," *Analytical Chemistry*, vol. 86, pp. 655-663, Nov 8 2013.

- [106] J. Park, D. Heldsinger, M. D. Hsieh, and E. T. Zellers, "Vapor recognition with an integrated array of polymer-coated flexural plate wave sensors," *Sensors and Actuators B: Chemical*, vol. 62, pp. 121–130, Feb 25 2000.
- [107] A. Hoover, G. Rice, J. R. Heflin, and M. Agah, "Improved performance of micro-fabricated preconcentrators using silica nanoparticles as a surface template," *Journal of Chromatography A*, vol. 1322, pp. 1–7, Dec 2013.
- [108] S. Narayanan and M. Agah, "Fabrication and characterization of a suspended TCD integrated with a gas separation column," *Microelectromechanical Systems*, vol. 22, pp. 1166 - 1173, May 14 2013.
- [109] M. Li, S. Biswas, M. H. Nantz, and R. M. Higashi, "Preconcentration and analysis of trace volatile carbonyl compounds," *Analytical chemistry*, vol. 84, pp. 1288–1293, Dec 7 2012.
- [110] Y. Mohsen, J. B. Sanchez, F. Berger, and H. Lahlou, "Selection and characterization of adsorbents for the analysis of an explosive-related molecule traces in the air," *Sensors and Actuators B: Chemical*, vol. 176, pp. 124–131, Jan 2013.
- [111] C. J. Lu, S. W. Pang, and E. T. Zellers, "Multiple-stage microfabricated preconcentrator-focuser for micro gas chromatography system," *Microelectromechanical Systems*, vol. 14, pp. 498 - 507, June 6 2005.
- [112] B. Alfeeli and M. Agah, "Selective preconcentration by temperature manipulation of cascaded Micro preconcentrators," *Solid-State Sensors, Actuators and Microsystems Conference, 2009. TRANSDUCERS 2009. International*, vol. Denver, CO, pp. 1662 - 1665, June 21-25 2009.
- [113] B. Alfeeli and M. Agah, "Micro preconcentrator with embedded 3D pillars for breath analysis applications," *Sensors*, vol. Lecce, pp. 736 - 739, Oct 26-29 2008.
- [114] S. W. Pang, C. J. Lu, and E. T. Zellers, "High sensitivity three-stage microfabricated preconcentrator-focuser for micro gas chromatography," *TRANSDUCERS, Solid-State Sensors, Actuators and Microsystems, 12th International Conference on, 2003 (Volume:1)*, pp. 131 - 134 vol.1, 8-12 June 2003 2003.
- [115] S. W. Pang, C. J. Lu, and E. T. Zellers, "Microfabricated preconcentrator-focuser for a microscale gas chromatograph," *Microelectromechanical Systems*, vol. 12, pp. 264 - 272, June 25 2003.
- [116] C. J. Lu and E. T. Zellers, "Multi-adsorbent preconcentration/focusing module for portable-GC/microsensor-array analysis of complex vapor mixtures," *Analyst*, vol. 127(8), pp. 1061-8, Aug 2002.
- [117] S. W. Pang, R. A. Veeneman, and E. T. Zellers, "Microfabricated preconcentrator for quantitative analysis of low concentration volatile organic compounds," *Solid-State Sensors*, vol. 2, pp. 2091 - 2094 Vol. 2, June 5-9 2005.
- [118] L. T. Taylor and M. Agah, "Design, modeling, and fabrication of MEMS-based multicapillary gas chromatographic columns," *Microelectromechanical Systems*, vol. 18, pp. 28 - 37, Feb 2009.
- [119] T. Sukaew, "Micro-scale Preconcentrators for Vapor-Phase Air Contaminants: Optimizing the Design and Operating Conditions for Integration with Micro-scale Gas," *Thesis*, vol. University of Michigan, June 13 2013.
- [120] H. Lahlou, J. B. Sanchez, Y. Mohsen, and X. Vilanova, "A planar micro-concentrator/injector for low power consumption microchromatographic analysis of benzene and 1, 3 butadiene," *Microsystem design*, vol. 18, pp. 489-495, Feb 7 2012.
- [121] Y. Mohsen, J. B. Sanchez, F. Berger, and H. Lahlou, "Development of a gas micro-preconcentrator for the analysis of explosive traces: study and characterization of various adsorbing materials," *14th International Meeting on Chemical Sensors - IMCS 2012, 2012-05-20 - 2012-05-23*, vol. Nürnberg/Nuremberg, Germany, pp. 559 - 562, 2012.

- [122] R. Lalauze, *Chemical sensors and biosensors*. London, Hoboken, N.J.: Iste ; Wiley, 2012.
- [123] H. Shakeel and M. Agah, "High-performance multicapillary gas separation columns with MPG stationary phases," *Sensors*, vol. Limerick, pp. 1909 - 1912, Oct 28-31 2011.
- [124] P. Kurzawski, A. Hierlemann, and E. T. Zellers, "Evaluation of multitransducer arrays for the determination of organic vapor mixtures," *Analytical chemistry*, vol. 80, pp. 227-36, Jan 1 2008.
- [125] C. Jin and E. T. Zellers, "Limits of recognition for binary and ternary vapor mixtures determined with multitransducer arrays," *Analytical chemistry*, vol. 80, pp. 7283-93, Oct 1 2008.
- [126] D. Barrettino, M. Graf, C. Hagleitner, and A. Kummer, "Monolithic CMOS multi-transducer gas sensor microsystem for organic and inorganic analytes," *Sensors and Actuators B: Chemical*, vol. 126, pp. 431-440, Oct 1 2007.
- [127] J. Park, G. Z. Zhang, and E. T. Zellers, "Personal monitoring instrument for the selective measurement of multiple organic vapors," *AIHAJ*, vol. 61(2), pp. 192-204, Mar-Apr 2000.
- [128] S. K. Kim, H. Chang, and E. T. Zellers, "Microfabricated gas chromatograph for the selective determination of trichloroethylene vapor at sub-parts-per-billion concentrations in complex mixtures," *Analytical chemistry*, vol. 83, pp. 7198-7206, Aug 22 2011.
- [129] B. Alfeeli and M. Agah, "MEMS-based selective preconcentration of trace level breath analytes," *Sensors Journal*, vol. 9, pp. 1068 - 1075, Sept 2009.
- [130] M. D. Hsieh and E. T. Zellers, "Adaptation and evaluation of a personal electronic nose for selective multivapor analysis," *Journal of occupational and environmental science*, vol. 1, pp. 149-60, Mar 2004.
- [131] M. Akbar and M. Agah, "A golden micro-trap for anesthetic depth monitoring using human breath samples," *Micro Electro Mechanical Systems (MEMS), 2012 IEEE 25th International Conference on*, pp. 906 - 909, 2012.
- [132] M. Akbar and M. Agah, "A cascaded micro preconcentration approach for extraction of volatile organic compounds in water," *Sensors*, vol. Taipei, Taiwan, pp. 1 - 4, Oct 28-31 2012.
- [133] V. Jain, R. K. Johnson, F. L. Beyer, J. R. Heflin, and M. Agah, "Characterization of poly (2, 6-diphenyl-p-phenylene oxide) films as adsorbent for microfabricated preconcentrators," *Microchemical ...*, vol. 98, pp. 240-245, July 2011.
- [134] B. Alfeeli, L. T. Taylor, and M. Agah, "Evaluation of Tenax TA thin films as adsorbent material for micro preconcentration applications," *Microchemical Journal*, vol. 95, pp. 259-267, July 2010.
- [135] J. H. Seo, S. K. Kim, E. T. Zellers, and K. Kurabayashi, "Microfabricated passive vapor preconcentrator/injector designed for microscale gas chromatography," *Lab on a Chip*, vol. 12, pp. 717-724, Jan 9 2012.
- [136] D. Paul, S. J. Kim, K. Kurabayashi, and E. T. Zellers, "Comprehensive two-dimensional gas chromatographic separations with a microfabricated thermal modulator," *Analytical Chemistry*, vol. 84, pp. 6973-6980, July 31 2012.
- [137] K. A. Gorder, E. M. Dettenmaier, and E. T. Zellers, "Microfabricated gas chromatograph for on-site determinations of TCE in indoor air arising from vapor intrusion. 2. spatial/temporal monitoring," *Journal of environmental science & technology*, vol. 46, pp. 6073-6080, May 22 2012.
- [138] E. T. Zellers, G. Serrano, and H. Chang, "A micro gas chromatograph for high-speed determinations of explosive markers," *Solid-State Sensors*, vol. Beijing, China, pp. 2082 - 2085, June 5-9 2011.
- [139] J. Driscoll, R. D. Sacks, K. D. Wise, S. W. Pang, and E. T. Zellers, "First-generation hybrid MEMS gas chromatograph," *Lab on a Chip*, vol. 5, pp. 1123-1131, Aug 10 2005.

- [140] J. Lovette, G. W. Rice, J. R. Heflin, and M. Agah, "Highly stable surface functionalization of Microgas chromatography columns using layer-by-layer self-assembly of silica nanoparticles," *Analytical Chemistry*, vol. 85, pp. 8135–8141, 2013.
- [141] B. Alfeeli, M. A. Zareian-Jahromi, and M. Agah, "Micro preconcentrator with seedless electroplated gold as self-heating adsorbent," *Sensors*, vol. Christchurch, pp. 1947 - 1950, Oct 25-28 2009.
- [142] S. W. Pang, C. J. Lu, and E. T. Zellers, "Microfabricated preconcentrator-focuser for a microscale gas chromatograph," *Microelectromechanical Systems*, vol. 1, pp. 264 - 272, June 25 2003.
- [143] S. Reidy, D. George, M. Agah, and R. Sacks, "Temperature-programmed GC using silicon microfabricated columns with integrated heaters and temperature sensors," *Analytical chemistry*, vol. 79, pp. 2911–2917, Feb 21 2007.
- [144] H. Smith, E. T. Zellers, and R. Sacks, "High-speed, vacuum-outlet GC using atmospheric-pressure air as carrier gas," *Analytical Chemistry*, vol. 71, pp. 1610–1616, Mar 6 1999.
- [145] W. R. Collin, G. Serrano, L. K. Wright, and H. Chang, "Microfabricated gas chromatograph for rapid, trace-level determinations of gas-phase explosive marker compounds," *Analytical Chemistry*, vol. 86, pp. 655-663, November 8 2013.
- [146] E. H. M. Camara, P. Breuil, D. Briand, and N. F. De, "A micro gas preconcentrator with improved performance for pollution monitoring and explosives detection," *Analytica chimica acta*, vol. 688, pp. 175-82, March 2011.
- [147] I. Voiculescu, R. A. McGill, and M. E. Zaghloul, "Micropreconcentrator for enhanced trace detection of explosives and chemical agents," *Sensors Journal*, vol. 6, pp. 1094 - 1104, Oct 2006.
- [148] R. P. Manginell, D. R. Adkins, and M. W. Moorman, "Mass-sensitive microfabricated chemical preconcentrator," *Microelectromechanical Systems*, vol. 17, pp. 1396 - 1407, Dec 2 2008.
- [149] P. Zellner and M. Agah, "A SINGLE-MASK SINGLE-ETCH PROCESS FOR CONSTRUCTING THREE DIMENSIONAL MICRO TOTAL ANALYSIS SYSTEMS," *Twelfth International Conference on Miniaturized Systems for Chemistry and Life Sciences*, October 12 - 16 2008.
- [150] F. Tassi, F. Capecchiacci, A. Bucciatti, and O. Vaselli, "Sampling and analytical procedures for the determination of VOCs released into air from natural and anthropogenic sources: A comparison between SPME (Solid Phase Micro Extraction) and ST (Solid Trap) methods," *Applied Geochemistry*, vol. 27, pp. 115-123, 1// 2012.
- [151] S. Vaswani, J. Koskinen, and D. W. Hess, "Surface modification of paper and cellulose by plasma-assisted deposition of fluorocarbon films," *Surface and Coatings Technology*, vol. 195, pp. 121-129, 5/31/ 2005.